POLITECNICO DI MILANO

Scuola di Ingegneria Civile, Ambientale e Territoriale

Corso di Laurea in Ingegneria per l'Ambiente ed il Territorio

ASSESSMENT OF CONTINUUM MODELS

FOR REACTIVE TRANSPORT IN POROUS MEDIA

Relatore: Dott. Giovanni Michele PORTA

Correlatori: Prof. Alberto GUADAGNINI

Prof. Martin Julian BLUNT

Tesi di Laurea di:

Giulia CERIOTTI

Matricola n° 782692

Anno Accademico 2012/2013

ABSTRACT

This thesis focuses on reactive transport modeling of bimolecular homogeneous irreversible reactions of the kind A+B→C at Darcy scale. The state of the art model adopted in this situation is advection dispersion reaction equation (ADRE). This, assuming the complete mixing between reactant concentrations at pore-scale, leads to over-prediction fo the reaction product formation. Here we investigate five different continuum models proposed in recent literature. These include single (Porta et al. ,2012; Sanchez-Vila et al. ,2010; Hochstetler and Kitanidis, 2013) and multicontinuum (double rate mass transfer, DRMT) approximations . The appropriateness of these models is investigated upon performing a quantitative comparison with the results of avaliable pore-scale numerical simulations of the reactive transport process for two porous medium scenarios characterized by different degree of geometry complexity (Porta et al. 2013). The assessment for single continuum models is performed through the following three-steps procedure: i) different values for each parameter included in the model are selected; ii) model is solved for each possible combination of parameter values selected; iii) the appropriateness of each computed solution is evaluated through different criteria which quantify the error between pore-scale and continuum-scale simulation results. The models assessment provides a detailed study which provides key information in view of model calibration. Main results of this work show that the pore-scale geometry complexity has a key influence on model performances. Moreover, we show that the quantification of incomplete mixing effect through an effective parameter is necessary to capture system behavior at the continuum scale, in the presence of complex porous scenarios.Our results suggest that the theoretically-based model proposed by Porta et al. (2012) is able to reproduce the key behaviors observed in pore scale simulations.Finally, the implementation of a double rate mass transfer model shows promising features that lead to overcome single continuum models limitations.

ABSTRACT (ITA)

L'argomento di questa tesi è la modellazione alla scala di Darcy del trasporto reattivo caratterizzato da una reazione bimolecolare omogenea e irreversibile del tipo A+B→C. Attualmente, il modello ADRE (Advection Dispersion Reaction Equation) viene comunemente utilizzato in questo contesto. Tale modello assume che, alla scala di poro, le concentrazioni dei reagenti si mescolino completamente portando ad una sovrastima della formazione del prodotto di reazione. In questo lavoro vengono analizzati cinque diversi modelli continui proposti in letteratura. Tra questi ci sono modelli a continuo singolo (Porta et al. 2012; Sanchez-Vila et al. 2010; Hochstetler and Kitanidis 2013) e multiplo (Double Rate Mass Transfer Model, DRMTM). Confrontando quantitativamente i risultati di simulazioni numeriche eseguite alla microscala su geometrie più o meno complesse (Porta et al 2013), viene verificata l'attendibilità dei modelli. Questa valutazione, per modelli a continuo singolo, viene effettuata con la seguente procedura: i) vengono selezionati diversi valori per ogni parametro presente nel modello; ii) il modello viene risolto con ogni combinazione dei valori scelti dei parametri, iii) l'attendibilità di ogni risoluzione viene valutata quantificando, con diversi criteri, l'errore commesso nell'approssimare i risultati delle simulazioni numeriche. Questa valutazione fornisce un'analisi dettagliata che consente di dedurre informazioni importanti per la calibrazione dei modelli. Da questo studio si evince che la complessità della geometria del mezzo ha un'influenza importante sulle performance dei modelli. Inoltre, per riprodurre il comportamento del sistema alla scala di continuo in scenari porosi complessi è necessario quantificare l'effetto del mescolamento incompleto tramite parametri effettivi. Le analisi effettuate suggeriscono che il modello proposto da Porta et al (2012) è in grado di riprodurre alcuni comportamenti cruciali del sistema che sono osservati nelle simulazioni alla microscala. Infine l'implementazione del modello DMRTM ha rivelato caratteristiche promettenti che permetterebbero di superare alcuni dei limiti caratterizzanti i modelli a continuo singolo.

CONTENTS

LIST OF FIGURES

LIST OF TABLES

INTRODUCTION

The term "reactive transport" is commonly used in Environmental and Earth sciences to indicate all the subsurface flow processes in which transport of dissolved species is coupled with chemical, mechanical, physical and biological transformations. That means that reactive transport definition includes a wide variety of complex natural processes occurring in subsurface flows. Nowadays, understanding reactive transport dynamics is becoming an important task due to the fact that many processes of practical interest depend on these natural phenomena. In particular, reactive transport has a crucial role in the following applicative fields:

- Environmental contamination: groundwater pollutants normally undergo to reactive transport and understanding it is crucial in order to control, monitor and forecast contaminats spreading in acquifers (*Bear and Cheng, 2010*).
- Global change: CO_2 storage provides one of the possible techniques to mitigate CO_2 and possible related effects on global climate changes. This technique consists in injecting CO_2 into geological formations. Saline acquifers appear particularly interesting for their important storage capacity. When CO_2 is injected into the acquifer it undergoes to a complex rective transport. Understanding this process is fundamental for evaluating the feasibility of this technique and possible connected risks (*Zengh at al. 2008; Audigane et al. 2007*)
- Oil reservoir efficient exploitation: an established practice in oil extraction is to inject chemical species (e.g. surfactants) that are able to reduce the oil surface tension and improve oil recovery. A solution of reactive matter is injected into the reservoir and flows interacting with fluid and solid phases in the subsurface. Understanding this process is very important in order to optimize oil recovery (see e.g. *Delshad et al., 2002*).

The reactive processes which are coupled to flows in natural subsurface environments, as the ones exemplified above, are very complex and they can be hardly reproduced through laboratory experiments. Moreover, the direct monitoring of their evolutions in space and time is hardly feasible due to the difficulties and costs of field data retrieval. Thus, conceptual and mathematical models for reactive transport description are required both for practical and research purposes. A reliable reactive transport model, indeed, would allow not only forecasting the natural phenomena and controlling

contaminant spreading, but it is also a crucial research tool for understanding the evolving dynamics of coupled natural processes (*Steefel et al., 2005*).

In order to develop conceptual and mathematical models, the key processes that characterize reactive transport must be identified and understood. Due to their complexity, actual natural phenomena do not represent the most suitable reference cases for basic theoretical, numerical and experimental investigations. As a consequence, many studies presented in literature (*Gramling et al., 2002; Porta et al. 2013; Edery et al.,2010, Kapoor et al., 1997; Anmala and Kapoor, 2013;Hochstetler and Kitanidis, 2013, Sanchez-Vila et al., 2010; Rubio et al., 2008, Raje and Kapoor, 2000; De Anna et al., 2013*) have focused on a very simple benchmark problem, an homogeneous bimolecular irreversible reaction of the kind A+B→C in a fully saturated domain. This is also the problem setting that is considered in this work. In spite of its simplicity, this setting allows investigating the coupled effect of flow and reaction processes inside the porous domain.

In this simple case, observing reactive transport at pore-scale level, three physical processes are identified: advection, diffusion and reaction. These processes have been modeld pore-scale and different modeling approaches are already successfully implemented. In principle, if the geometry of the system was known, we would be able to completely model the reactive transport in porous domain. However the limitations in computer power and characterization techniques do not allow implementing pore-scale modeling approaches at Darcy or field scale. As a consequence, for practical purposes, macro-scale models are formulated in order to capture the average evolution of the system neglecting the detailed description of the porous medium geometry. On the other hand, these models cannot neglect the effects of pore-scale structure on the coupled transport and reaction processes. Indeed, the reactive transport evolution observed in heterogeneous systems is significantly different from the one observed in homogeneous ones. In particular, and the pore scale flow field typilcally includes local velocity fluctuations, which may yield to segregate reactants plumes and limit the reaction occurrence. This phenomenon is usually referred as incomplete mixing effect. Neglecting this effect generally yields overestimation of the reaction rate observed in real systems and to inaccurately represent average features of reactive transport phenomena. Indeed, this represents the main limitation of the Advection Dispersion Reaction Equation model (ADRE) which is the state of the art tool for macro-scale modeling of reactive transport.

Moving from this, many alternative models relying on different conceptual approaches have been proposed in order to provide a formulation able to embed the incomplete mixing effects. As a consequence of this vital research activity, the investigation of reactive transport modeling tools appears multifaceted and this topic is still a open field of discussion. In this context a structured comparisons among the different available model formulations is currently lacking and is the primary scope of this work. This analysis is valuable in order to identify the most promising directions for future research efforts. According on this purpose, this work is focused on five different models which rely on a common conceptual approach including the classical ADRE: the continuum approach.

This approach allows describing the spatial and temporal solutes concentration distributions according to a system of partial differential equations (PDEs) which represents the mass balances of chemical species. In this way, an approximate description of reactive transport processes can be obtained using established numerical methods normally implemented for PDEs systems. The effects of pore-scale processes, e.g., incomplete mixing and solute spreading due to hydrodynamic dispersion, are then embedded into the equation formulation through one or more effective parameters.. Each model included in our study presents a different formulation of the reaction term and as rendered by an incomplete mixing model. Using a set of pore-scale numerical simulation performed for different porous scenarios, the solutions yielded by different models are analyzed in order to:

- Evaluate the importance of embedding the incomplete mixing effect into the formulations;
- Investigate the importance of pore-scale structure on model performances;
- Assess the capability of different reactive term formulations to capture the reactive transport dynamic features;
- Compare solutions given by different models in order to discriminate which one allows to better performances.

In this work we consider a comparison among several continuum approximation, where the porous medium is treated as a single homogeneous continuum characterized by effective parameters. In addition to these modeling options we consider a double continuum approximation, i.e. a modeling framework. This yields an alternative conceptualization of incomplete mixing effect: the Double Rate Mass Transfer model (DRMT) which has been little explored, so far.

Our analysis allows identifying the main strengths and limitations of each of the considered models and assessing which are the most promising modeling options for continuum representation of pore-scale reactive processes. As a consequence, our work provides a significant and innovative contribution to reactive transport modeling research: it provides the first structured assessment of different models and identifies the most promising directions to follow for further advancements.

The structure of this thesis is here described. In the first part (Chapter 1) we introduce the framework and the state of the art of the field in which our work is contextualized. In Chapter 2 materials and methods are presented and in particular: i) the specific problem setting and the description of the validation data; ii) the analysis of conceptual and mathematical formulation of each continuum model evidencing the differences in reaction term definition, iii) the numerical tools for model solution. The results presentation is gathered in Chapter 3-Chapter 5 and is divided in three different sections: the first one (Chapter 3) is dedicated to validation and comparison of the model for a simple and ordered porous medium domain; the second one is addressed to models assessment in a complex and disordered porous medium domain (Chapter 4); the third is focused on a quantiative comparison between all the considered models limited to the challenging case of a disoredered pore-scale geometry. Conclusion and future possible research direction highlighted by our work are reported at the end of the thesis.

Chapter 1 BIMOLECULAR REACTIVE TRANSPORT IN POROUS MEDIA: CONCEPTUAL FRAMEWORK AND STATE OF THE ART

1.1 Types of chemical reactions

Physical, chemical, and biological processes influence and control solute and particle matter fate and transport in the subsurface. In Earth and environmental sciences, the term "reactive transport" generally indicates all the processes through which a chemical is transported and simultaneously physically or chemically transformed. Many different types of reactive processes can take place in an aquifer and ; these fall into three broad categories: physical, chemical and biochemical transformation. We define a physical transformation a process in which the substance chemical composition remains unchanged while its physical properties change (e.g. phase transitions). A chemical transformation, instead, implies that the reactants evolve into new chemical substances. Finally, a transformation is "biochemical" if it is mediated by organisms. Among chemical reactions, *Rubin (1983)* classifies the group of "sufficiently fast" reversible reactions and "insufficiently fast" and/or irreversible reactions. The first group of reactions proceeds very fast and equilibrium is essentially immediately reached compared to the other system processes. As a consequence, assuming that local chemical equilibrium always exists at every point of the system leads to negligible error in process modeling. On the other hand, the "insufficiently fast" and/or irreversible reactions evolutions are function of time through a kinetic law. Note that a reaction rate is not absolutely slow or fast, but it depends on the problem that we are considering. A reaction can be fast compared to a process or slow compared to another one. The kinetic rate (k) quantifies the amount of mass transformed as function of time and it is an important parameter in order to understand the velocity of the reaction compared to other processes. Both sufficiently fast/reversible and insufficiently fast/irreversible reactions can be homogeneous or heterogeneous. A reaction in which the reactants are in the same phase are called homogeneous, while heterogeneous reactions involve reactants in different phases. Finally heterogeneous reactions, may or may not involve or not the solid grain surface: reactions such as adsorption or ionic exchange take place on the grain surface, while classical heterogeneous reactions (precipitation, complex formation, reduction, dissolution and oxidation) involve different phases without necessarly interacting with the solid grains. This classification proposed by *Rubin (1983)* is summarized in Figure 1.1.

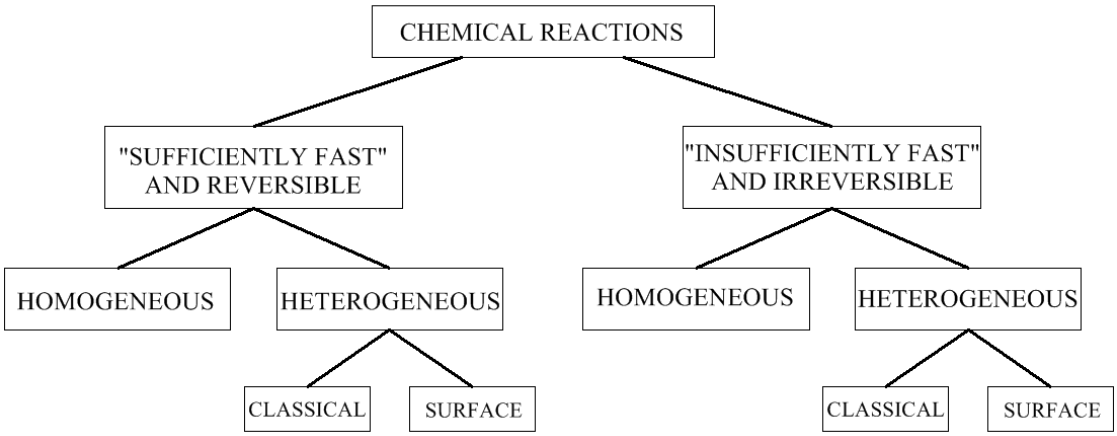

Figure 1.1 Classification of chemical reactions useful in solute transport analyses (Rubin, 1983).

In this wide and multifaceted scenario, we will deal with the specific problem of a chemical, homogeneous and irreversible reaction. A detailed explanation of the problem setting chosen is provide in section 2.1. First though, we will review the literature associated with modelling these processes to help frame the novel contributions of this thesis.

1.2 Introduction to benchmark problem and motivations

In this work we consider a column of porous domain fully saturated with a solution of a chemical A. A solution of B is injected from a boundary of the column. A bimolecular irreversible homogeneous reaction takes at the interface between A and B producing C. A more detailed explanation of the problem setting is provided in section 2.1.

This configuration is interesting for two reasons:

- It is representative of a replacement scenario which may describe practical remediation techniques. For example, the in situ injection of remedial reactants has shown remarkable results for its efficiency and low costs. It consists in injecting a reactant that can transform the contaminant which is present in the groundwater into a harmless substances as for example oxidation of hydrocarbons (e.g. *Kluck and Achari, 2004*)
- It is often considered in experimental and modeling works as benchmark problem (*Gramling et al., 2002; Porta et al. 2013; Edery et al.,2010, Kapoor et al., 1997; Anmala and Kapoor, 2013;Hochstetler and Kitanidis, 2013, Sanchez-Vila et al., 2010; Rubio et al., 2008, Raje and Kapoor, 2000; De Anna et al., 2013*)

1.3 Pore-scale processes and governing equations

At the pore-scale, the solutes undergo three different processes:

- *Advection:* since the liquid phase flows, the solutes are transported by the flow along streamlines.
- *Molecular Diffusion:* advection alone does not capture the solute behavior at a local level since the solute spreads tranverse to the fluid direction as consequence of molecular diffusion which arises from the random thermal motion of the solute. The net flux follows the concentration gradient resulting in chemical migration from regions of higher to lower concentraions.
- *Reaction:* when the reactants meet, they undergo to a chemical reaction. The reactants A and B are consumed while the product C is generated.

The three processes listed before are simultaneous phenomena and affect local concentration distributions of the three chemical species. Advection and diffusion regulate the mixing of the solutes allowing the reaction to take place. Mathematically the problem can be described by:

$$\begin{aligned}
&\frac{\partial \hat{c}_A}{\partial \hat{t}} + \vec{\hat{u}} \cdot \hat{\nabla} \hat{c}_A = \hat{D}_A \hat{\nabla}^2 \hat{c}_A - \hat{r}_{AB} \\
&\frac{\partial \hat{c}_B}{\partial \hat{t}} + \vec{\hat{u}} \cdot \hat{\nabla} \hat{c}_B = \hat{D}_B \hat{\nabla}^2 \hat{c}_B - \hat{r}_{AB} \\
&\frac{\partial \hat{c}_C}{\partial \hat{t}} + \vec{\hat{u}} \cdot \hat{\nabla} \hat{c}_C = \hat{D}_C \hat{\nabla}^2 \hat{c}_C + \hat{r}_{AB}
\end{aligned} \tag{1.1}$$

The symbol ^ indicates that the variable is dimensional; $\hat{c}_i (i = A, B, C)$ [mol/m^3] represents the dissolved solute concentration; $\hat{D}_i (i = A, B, C)$ [m^2/s] is the molecular diffusion coefficient which is assumed to be equal for A, B and C ($\hat{D}_A = \hat{D}_B = \hat{D}_C = \hat{D}_m$). The term $\vec{\hat{u}} \cdot \hat{\nabla} \hat{c}_i$ indicates the advective term; indeed it is proportional to the advective velocity field $\vec{\hat{u}}$ [m/s]. The latter is governed by the Navier-Stokes equation (*Citrini and Noseda, 1987*). However, flow in porous media can be often assumed to be laminar and the fluid density constant. In these conditions, the Navier-Stokes equation reduces to the Stokes equation:

$$\begin{aligned}
&\hat{\nabla} \hat{p} = \hat{\mu} \hat{\nabla}^2 \vec{\hat{u}} - \hat{\rho} \vec{\hat{g}} \\
&\hat{\nabla} \cdot \vec{\hat{u}} = 0
\end{aligned} \tag{1.2}$$

where $\hat{p}$ [Pa] is the fluid pressure; $\hat{\mu}$ [Ns/m^2] is the viscosity; $\hat{\rho}$ [kg/m^3] is the density and $\vec{\hat{g}}$ [m/s^2] is the gravity vertically directed. The term $\hat{D}\hat{\nabla}^2\hat{c}_i$ models molecular diffusion employing Fick's law. The reaction term $\hat{r}_{AB}$ is modeled as sink/source term into the equations: it is always negative for reactant species while it is always positive for the product since the reaction is irreversible. Here, it is assumed that the reactants are locally completely and instantaneously well mixed and so that we can model $\hat{r}_{AB}$ as:

$$r_{AB} = \hat{k}\hat{c}_A\hat{c}_B \tag{1.3}$$

where $\hat{k}$ [m^3/(mol s)] is the intrinsic reaction rate as measured in well-stirred batch reactor. Equation (1.1) needs to be completed with appropriate initial and boundary conditions. The Equation (1.1) can eventually be recast into a dimensionless form by introducing the following dimensionless quantities:

$$Pe = \frac{\hat{U}\hat{w}}{\hat{D}_m}; Da = \frac{\hat{k}\hat{w}^2\widehat{c_0}}{\hat{D}_m}; t = \hat{t}\frac{\hat{U}}{\hat{w}}; \widehat{c_i} = \widehat{c_0}c_i; \vec{\hat{u}} = \hat{U}\vec{u}; \frac{\partial}{\partial\hat{x}} = \frac{\partial}{\partial x}\frac{1}{\hat{w}} \tag{1.4}$$

where:

- Pe is the Péclet number which is the ratio between the advective characteristic timescale and diffusive characteristic timescale;
- Da indicates the Damköhler number which is the ratio between the reaction characteristic timescale and diffusion characteristic timescale;
- t is the dimensionless time;
- $\hat{U}$ [m/s] indicates the modulus of the averaged seepage velocity vector in the fluid phase;
- $\vec{u}$ is a unitary vector directed as the averaged fluid velocity;
- $\hat{w}$ [m] indicates the characteristic pore-scale spatial dimension;
- $\hat{D}_m$ [m^2/s] is the diffusion coefficient and it is supposed to be equal for all the solutes for the sake of simplicity;
- $\hat{k}$ [m^3/(s mol)] is the intrinsic reaction kinetic constant;

- $\left\langle \widehat{C_0} \right\rangle^l$ [mol/m^3] is the characteristic concentration value fixed with boundary or initial conditions inside the liquid phase.

Introducing the quantities of Eq. (1.4), the dimensionless formulation of Eq. (1.1) is:

$$\begin{aligned}
\frac{\partial c_A}{\partial t} + \vec{u}\nabla c_A &= \frac{1}{Pe}\nabla^2 c_A - \frac{Da}{Pe} c_A c_B \\
\frac{\partial c_B}{\partial t} + \vec{u}\nabla c_B &= \frac{1}{Pe}\nabla^2 c_B - \frac{Da}{Pe} c_A c_B \\
\frac{\partial c_C}{\partial t} + \vec{u}\nabla c_C &= \frac{1}{Pe}\nabla^2 c_C + \frac{Da}{Pe} c_A c_B
\end{aligned} \tag{1.5}$$

In addition, we introduce the definition of advection ($\hat{t}_A$ [s]), diffusion ($\hat{t}_D$[s]) and reaction ($\hat{t}_R$ [s]) timescales:

$$\hat{t}_A = \frac{\hat{w}}{\hat{U}}; \hat{t}_D = \frac{\hat{w}^2}{\hat{D}_m}; \hat{t}_R = \frac{1}{\hat{k}\left\langle \hat{c}_0 \right\rangle^l} \tag{1.6}$$

Using Eq. (1.6) , we can define *Pe*, *Da* and t differently from Eq. (1.4):

$$Pe = \frac{\hat{t}_D}{\hat{t}_A}; Da = \frac{\hat{t}_D}{\hat{t}_A}; t = \frac{\hat{t}}{\hat{t}_A} \tag{1.7}$$

Equations (1.1) and (1.5) well describe the physical processes observed in a homogenous liquid domain and can be considered in principle correct inside the single pores. Modeling difficulties arise when these local processes are observed from a up-scaled point of view in which liquid and solid phases cohexist and interact. Rective processes observed in a porous domain at Darcy-scale or field scale evolve in every different way compared to pore-scale level. Advection, diffusion and reaction processes are influenced by the presence of the porous domain and the pore-scale chemical species and local velocity distributions affect the phenomena evolution at upper-scale levels. As a consequence up-scaling model from pore-scale is not trivial since the local effects must be embedded into the up-scaled model in order to interpret the reactive process observed in real porous domain.

The first model proposed was the Advection-Dispersion-Reaction Equation (ADRE) which assumes that reactant are locally well mixed and the reaction evolves similar to a well-mixed batch reactor.

However, the limitations of this model have been soon identified since it leads to overestimation of the reaction rate when chemical reactive species are segrated due to the presence of porous domain (*Gramling et al .2002; Raje and Kapoor, 2000*).

Considerable research effort has been spent in order to understand which are the significant local effects that govern the reaction processes from a physical point of view and must be embedded in up-scaled model. In the literature, the two main approaches are used to investigate reactive mechanisms and the governing phenomena at pore-scale: physical experiments and pore-scale modeling.

1.3.1 Experimental results

Running a physical experiment is an immediate way to explore the dynamics and evolution of reactive processes. *Raje and Kapoor (2000)* and *Gramling et al. (2002)* proposed two different techniques and their results have been often used as validation/calibration data for up-scaled reactive transport models (e.g. *Sanchez-Vila et al., 2010; Rubio et al., 2008; Edery et al, 2010*). More recently, *De Anna et al. (2013)* developed a new experimental setting in which concentration and product formation can be measured with high spatial resolution. The problem setting is common and similar to one considered in this thesis, i.e. an homogenous irreversible bimolecular reaction.

Raje and Kapoor (2000) studied reactive transport in a glass bead pack with a fixed radius of 1.5 mm. The column was cylindrical where the length is 18 cm and the diameter is 4.5 cm. Two runs were performed:

- Run 1: the column is initially saturated with a solution of 1,2-naphthoquinone-4-sulfonic acid (NQS) while a solution of aniline (AN) is injected by the left boundary of the domain; the initial concentration of both the solution is equal to 0.5 mM (Pe= 442.3 and Da= 492.3).
- Run 2: the setting is turned upside down compared to Run 1, i.e. the AN solution fills the column while NQS solution is injected; the initial concentration of the solutions is 0.25 mM (Pe= 1046.5, Da= 245.9).

The reaction between AN and NQS is bimolecular and irreversible and the reaction product is 1,2-naphthoquinone-4-aminobenzene (NQAB). The color changes during the reaction. As a consequence it is possible to measure the chemical concentrations at the end of the column. Even if the experiments results are provided in terms of averaged concentrations at column end , *Raje and Kapoor (2000)* first

pointed out the distance between the well-mixed assumption and the real process taking place into the column. Moreover the different flux and reaction conditions allowed exploring the influence of *Pe* and *Da* on reactive transport evolution.

Gramling et al. (2002) designed a different experimental apparatus which could acquire more information than *Raje and Kapoor (2000),* as average chemical species distribution within the domain. *Gramling et al. (2002)* investigated the reaction between N_2EDTA and $CuSO_4$ which change color. Images at different times are captured in which the change in light absorbance is measured and is related to the concentration of different species. Indeed, images are discretized in pixels (0.3x0.3 mm) and each pixel color intensity (from 0 to 4095) is converted into relative light absorbance value (A/A0) using the Scanalytics, Inc. software program IP Lab. In this way, *Gramling et al. (2002)* established a proportionality between absorbance and the amount of product generated and reaction product profiles as function of time are obtained. *Gramling et al. (2002)* conducted different experiments for diverse flow conditions (Q=2.7 ml/s, Q=16 ml/s, Q=150 ml/s) in glass chamber filled with grains of pure cryolite. The cryolite diameter is 1.19-1.41 mm. The chamber is 30 cm long , 5.5 cm high and 1.8 deep. The chamber is initially saturated with a solution of N_2EDTA (C_0=0.02 M). a solution of $CuSO_4$. The imaging of the experiment at different times is reported in Figure 1.2. Confirming the results of *Raje and Kapoor (2000)*, it is observed that the product profiles estimated assuming the complete mixing of reactants are overestimated compared to experimental results.

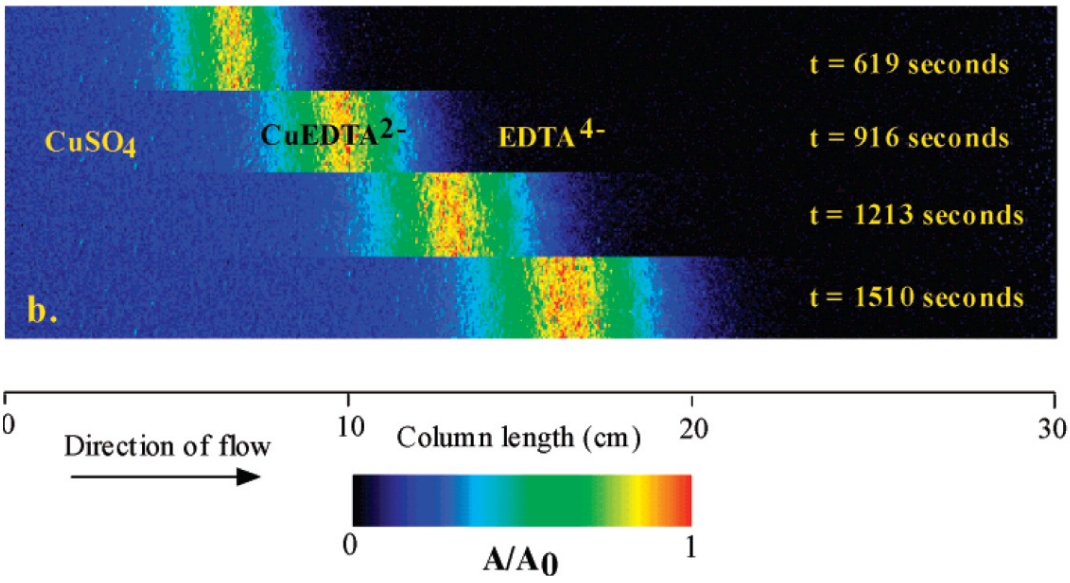

Figure 1.2 Reaction between 0.02 M CuSO4 and 0.02 M EDTA,4- producing a zone of CuEDTA2- in the chamber (Gramling et al. 2002).

Recently, *De Anna et al. (2013)* performed two experiments in a very small synthetic column porous domain (160x100 mm) with very high spatial resolution leading to very detailed knowledge of pore-scale spatial concentration distributions. The first run investigated non-reactive transport using a solution of Fluorescein sodium salt which emits photons if invested by radiation with a wave length of 494 nm. The solute spatial concentration is detectable through a high resolution camera since it is proportional to the photons emitted.

The second run concerned to the reactive transport between bis (2,4,6-trichlorophenyl) oxalate (TCPO) and 3-aminofluoranthene (3-AFA) and hydrogen peroxide (H_2O_2). This reaction is particularly interesting since it is chemiluminescent and the light produced is proportional to the amount of reaction that takes place.each reaction produces a photon and photons locations are captured using a camera which is very sensible to light and high resolution. Recording the spatial light distribution provides the spatial distribution of reaction rate.

The results produced by *De Anna et al. (2013)* are particularly interesting since they are able to characterize mixing and reactive transport at intra-pore level providing better understanding of the basic mechanisms. All these experience are used to contextualize the problem we are dealing with and to provide a physical counterpart in order to explain the results.

1.3.2 Pore-scale modeling

Pore-scale modeling solves Eq. (1.1) numerically in the pore space. The great advantage of this approach is to provide more detailed information on the solute concentration fields compared to experiments where local values are difficult to measure. Experimental observations are usually limited reporting only averaged data (see *Gramling et al.,2002* and *Raje and Kapoor, 2000*) or investigating very small systems (see *De Anna et al. ,2013*). Then pore scale simulations configures as a complementary approach to physical experiments in order to test and chellenge different theories. The pore-scale modeling uses one of two different methods: Eulerian and Lagrangian.

The Eq. (1.1) describes the solute mass balances referring to an infinitesimal volume and it is function of continuous variables in space and time. The Eulerian method approach recasts the Eq. (1.1) into a numerical model, written in terms of many discrete values of these variables, defined at specified points in space and time. The solution of the system in every point of the domain is then approximated interpolating the discrete values computed. In other words, a partial differential equations system is approximated by a set of linear algebraic equations which computes the system solution only on discrete points of space and time (*Bear and Chen, 2010*). Eulerian methods are nowadays well-established techniques and are commonly implemented to solve flow (Navier-Stokes and Stokes equations). They have also been employed in literature to solve reactive transport at pore-scale level avoiding physical experiments.

For example *Anmala and Kapoor (2013)* presented solutions to Eq. (1.1) using a standard, centered, finite difference method (*Ames, 1992*) while *Hochstetler and Kitanidis (2013)* performed the reactive transport through finite element multiphysics software COMSOL 4.1.

In constrast, in the Lagrangia approach, the equations are solved on a coordinate system that moves with the fluid. Typically it is not possible to model each solute molecule, so the solute plume is represented by set of particles moving in the flow domain. Each one of these particles represents a given solute mass and the process is described from the prospective of the single particle. Typically the Lagrangian method is called particle tracking random walk, although other types of Lagrangian approach are possible – such as using streamlines (*Crane and Blunt*, 2000).

Here we report a detailed explanation of a particle tracking random walk method since the validation data used in this thesis (see section 2.2) are simulated through this technique.

The solute concentration plume is outlined as a collection of N particles and each particle is associated to a fraction of the total mass of the chemical specie. The time is discretized into M time-steps. We assume that the velocity field $\vec{u}(\vec{\hat{x}})$ is known (i.e. the flow field has been previously solved). Each particle moves due to advection and diffusion. Advection is model as a deterministic process since particle moves along the velocity streamlines, as the velocity field is known. The diffusion process, instead, is conceptually modeled as a stochastic process similar to the Brownian motion. As a consequence the step in space done by each particle is made by a deterministic step along the streamline and a random step as showed in Figure 1.3 and expressed by the following equation:

$$\vec{\hat{x}}(\hat{t}_i + \partial\hat{t}) = \vec{\hat{x}}(\hat{t}_i) + \vec{\hat{u}}(\vec{\hat{x}})\partial\hat{t} + \vec{P}(\vec{\hat{x}}) \tag{1.8}$$

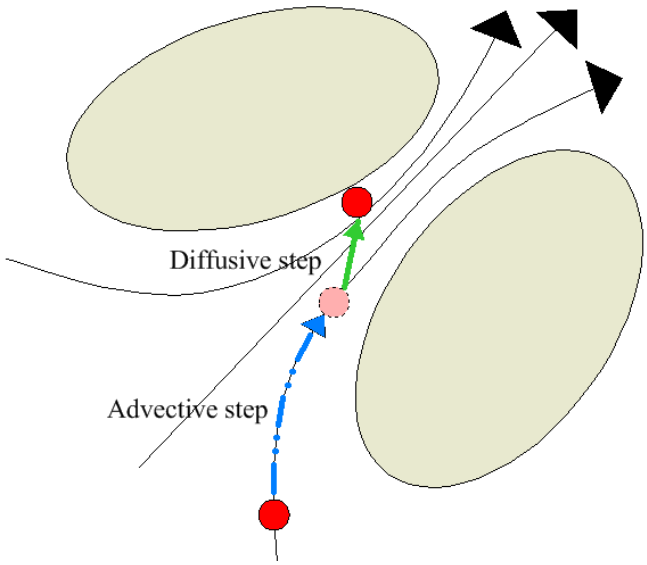

Figure 1.3. Outline of random walk transport modeling.

Here, $\vec{\hat{x}}$ is the particle position referred to a fixed coordinate system; $\hat{t}_i$ is the time at the i-th timestep; $\partial\hat{t}$ is the length of the time-step; $\vec{\hat{u}}(\vec{\hat{x}})\partial\hat{t}$ is the particle movement due to advection and $\vec{P}(\vec{\hat{x}})$ indicates the particle displacement due to diffusion. Different expressions have been proposed for computing the diffusive step $\vec{P}(\vec{\hat{x}})$ appearing in Eq.(1.8). For example, *Bijeljic et al. (2004)* modeled the diffusion as a random step in a random direction defined by the coordinates of a the spherical coordinate system:

$$\begin{aligned} P(\hat{x}) &= \hat{\lambda}\cos(\theta)\sin(\varphi) \\ P(\hat{y}) &= \hat{\lambda}\sin(\theta)\sin(\varphi) \\ P(\hat{z}) &= \hat{\lambda}\cos(\varphi) \end{aligned} \tag{1.9}$$

where $\hat{\lambda}$ indicates the random length of the diffusive step centered on the mean value of $\sqrt{2\hat{D}_m\partial\hat{t}}$ ($\hat{D}_m = molecular\ diffusion, \partial\hat{t} = length\ of\ timestep$) in a Cartesian coordinate system; φ and θ are randomly chosen angles.

A slightly different, although mathematically equivalent, approach for diffusion modeling is employed in *Porta et al. (2012b)*, *Porta et al. (2013)* and *Chaynikov (2013)* previously proposed (*e.g Salles et al., 1993*):

$$\vec{P}(\vec{\hat{x}}) = \hat{\delta}\vec{d} \tag{1.10}$$

where $\hat{\delta}$ is the module of the diffusive displacement equal to $\sqrt{6\hat{D}_m\partial\hat{t}}$. The direction of the diffusive step is random and defined by the vector $\vec{d}$.

Bimolecular reaction can be modeled defining a probability that the reaction takes place between two reactant particles which encounter each other, as in *Porta et al. (2012b)*, *Porta et al. (2013)* and *Chaynikov (2013)*. Here we briefly recall this modeling approach. These authors discretized the domain into a regular cubic mesh and correlated the reaction probability to the reactant concentrations, particles residence time in a cube and the reaction kinetic coefficient using:

$$\begin{aligned} RP_A &= \hat{k}\hat{c}_0 c_B(K_i)T_C(K_i)\delta\hat{t} \\ RP_B &= \hat{k}\hat{c}_0 c_A(K_i)T_C(K_i)\delta\hat{t} \end{aligned} \tag{1.11}$$

where $RP_i(i = A, B)$ represents the reaction probability of component *i*; the factor $T_C(K_i)$ is the fraction of the time step $\delta\hat{t}$ spent by the particle in cube K_i; $\hat{c}_0$ is the initial concentration while $c_i(K_i)(i = A, B)$ is the dimensionless ratio among the reactant concentration and its initial value inside the cube K_i.

They derived Eq.(1.11) by integrating the reactants evolution in time:

$$\begin{aligned} \frac{d\hat{c}_A}{d\hat{t}} &= -\hat{k}\hat{c}_0 c_B(\hat{t})\hat{c}_A \\ \frac{d\hat{c}_B}{d\hat{t}} &= -\hat{k}\hat{c}_0 c_A(\hat{t})\hat{c}_B \end{aligned} \tag{1.12}$$

After computing the advective and diffusive displacement, for each particle of A at each time-step, a number (RN) is randomly generated using an uniform distribution:

- If $RN > RP_A$ the reaction doesn't take place:
- If $RN < RP_A$ the reaction takes place and the particle of A is replaced by a particle of C randomly assigned to a position along the previous step of A.

This approach is an interesting tool since it conceptually very simple and easy to implement; moreover we are able to follow the fate of each particle allowing a better understanding of the processes that are taking place in the porous medium. As a consequence, it could be a valid alternative to complex experiments for the investigations and simulations of reactive transport in different conditions and porous medium scenarios.

On the other hand, the random walk approach suffers of some problems (*Salamon et al., 2006*). Concentrations computed through the random walk approach are characterized by random fluctuations. This limitation can be overcome increasing the number of particles, but this can be computationally expensive, or by introducing a smoothing function to estimate concentrations. Errors due to concentrations computation are propagated step by step.

1.3.3 Evidence of experiments and pore-scale modeling investigations

Integrating the results obtained though the different approaches proposed in previous section, it is possible to determine how the presence of porous medium affects the evolution of bimolecular reactive transport.

Raje and Kapoor (2000) verifed that the intrinsic kinetic rate provides a good description of the reaction evolution in a well-mixed system. However, *Raje and Kapoor (2000)* and *Gramling et al. (2002)* registered a significant discrepancy between the expected amount of mass product in condition

of complete mixing and the real mass product recorded. The conclusion is that incomplete mixing takes place and the effective kinetic rate in real porous media differs from the intrinsic one measured in a batch reactor. The incomplete mixing (or "segregation") can more or less affect the experiment depending on the relative importance of reaction process compared to advection-diffusion spreading. *Raje and Kapoor (2000)* showed that the assumption of complete mixing induces bigger error for reaction-dominated transports (*Da>Pe*) as opposed to advection dominated ones (*Da<Pe*), as depicted in Figure 1.4.

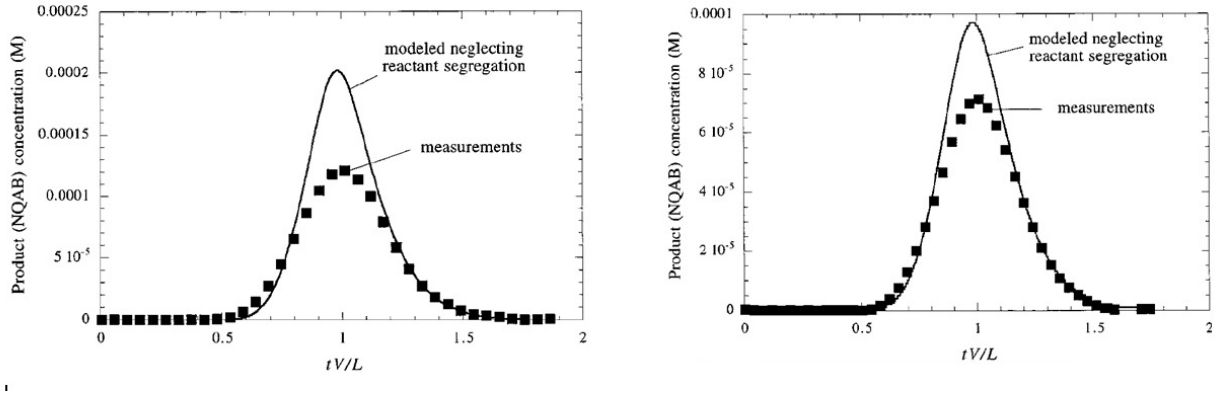

Figure 1.4 Variation of the product concentration at the end of the column for Da>Pe (left) and for Da<Pe (right), (Raje and Kapoor, 2000)

De Anna et al., 2013 provided further insight into the observations of *Raje and Kapoor (2000)* and *Gramling et al. (2002)*. They observed the spreading of the non-reactive plume which is commonly represented by a phenomenon called hydrodynamic dispersion. Through this, we lump the effects of three different phenomena, depicted in Figure 1.5, that arise due to the presence of the pore-system (*Bear and Cheng, 2010*):

- Molecular diffusion inside the pore channels;
- The effect of velocity gradient along the pore channel traverse directions to the advective direction;
- The change in magnitude and direction of velocity streamlines in pore channels due to the diverse diameters of the microscopic tubes and the pore-structure.

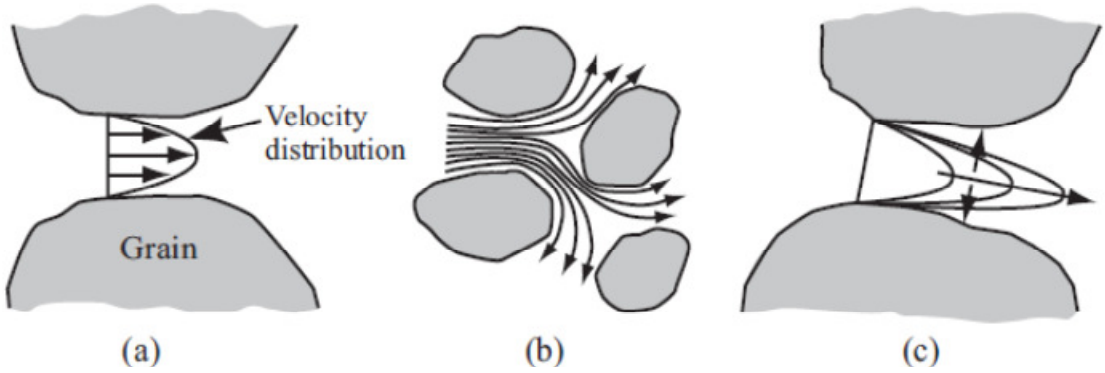

Figure 1.5. Dispersion due to mechanical spreading (a,b), and molecular diffusion (c), (Bear and Cheng, 2010).

Hydrodynamic dispersion is classically assumed to be a Fickian process similar to molecular diffusion. However, for times shorter than the characteristic transport time over a typical scale of heterogeneity, *De Anna et al., 2013* clearly showed that the behavior of solute spreading cannot be captured by a Fickian hydrodynamic dispersion mechanism. Indeed, the solute plumes tend to be distorted but not mixed. Figure 1.6 shows that the solute front has a lamellar shape: the solute rapidly spread but it is not well mixed since the solute concentration presents significant variations in a single pore-space. The importance and evidence of this irregular front shape mainly depends on the flow field and porous medium heterogeneities features (*Chen and Meiburg,1998*).

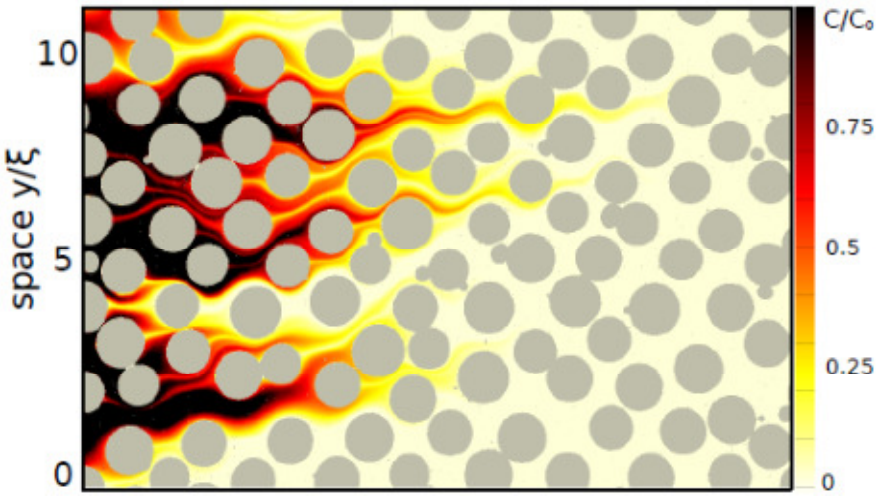

Figure 1.6 The concentration field of a conservative tracer (De Anna et al., 2013).

De Anna et al. (2013) also showed, through their experiments, that the fingering of solutes influences the reaction inside the pore spaces. Figure 1.7 shows that the irregular shape of reactants limits the reactive process in stretched regions where A and B are in conctact.

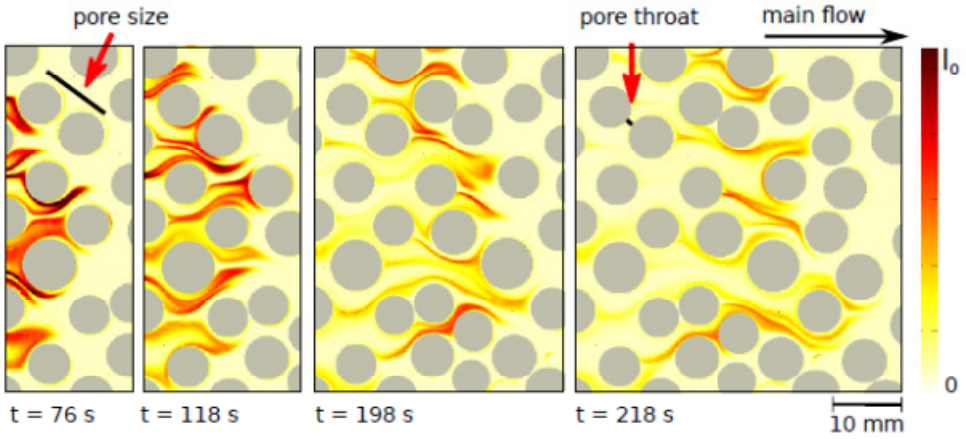

Figure 1.7. Field of light intensity produced by chemiluminescent reactions at the reactants fronts, (De Anna et al. 2013)

Numerical simulations provide further insight into the analysis provided by the experimental results. Pore-scale numerical simulations confirm the irregular shape of solute fronts and, as a consequence of the reactive zone (see Figure 1.8).

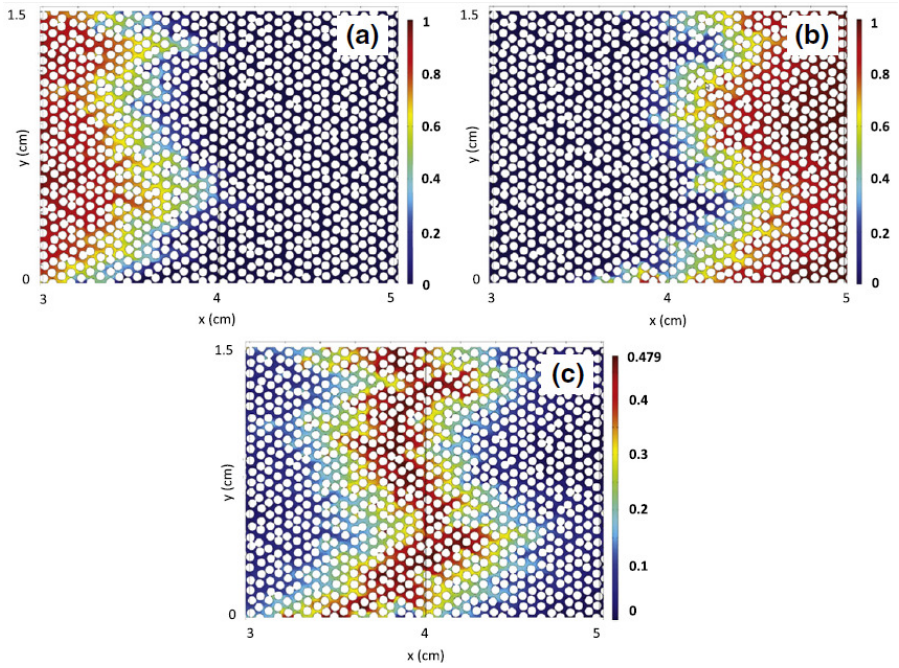

Figure 1.8. Snapshots of normalized concentrations of the reactants A (a) and B (b) and the product C (c) (Hochstetler and Kitanidis, 2013).

Thanks to pore-scale modeling, the concentration fields are accurately known in each point of the domain and this allows us to analyze fluctuations in reactant concentrations. A negative cross-correlation between reactant concentrations has been observed for the specific problem setting of

homogeneous irreversible bimolecular reaction. This is particularly well depicted in *Porta et al. (2013)* who computed the logarithm of the reactant product. Figure 1.9 and Figure 1.10 show that this quantity is not homogeneously distributed at the interface between the two reactants meaning that inside the porous medium the degree of mixing varies significantly. *Anmala and Kapoor (2013)* analyzed the time evolution of concentration fluctuations. They found that these fluctuations progressively vanish with time and the velocity of this process is macroscopically governed by the dispersion which characterizes the reactant concentration spreading.

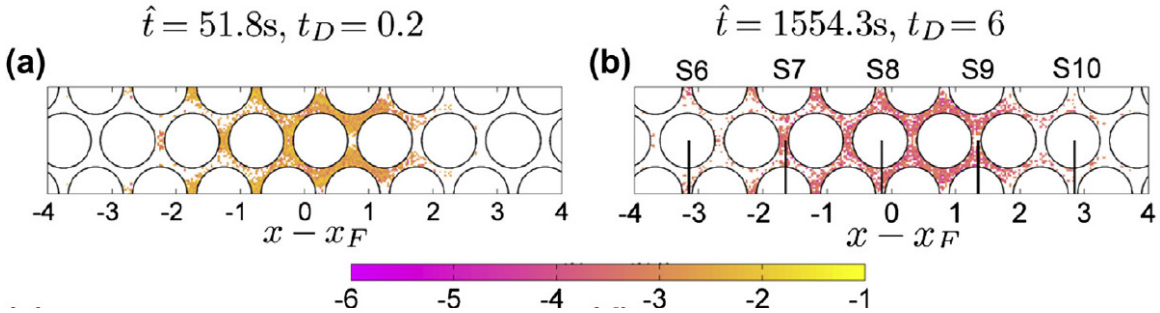

Figure 1.9 pore-scale distribution of mixing intensity, log (C_AC_B), for Pe=96, Da=1038, and ϕ =0.36 at t_D=0.2 (left), t_D=6 (right). Solid lines indicate the position of the cross sections considered in Figure 1.10 (Porta et al.,2013).

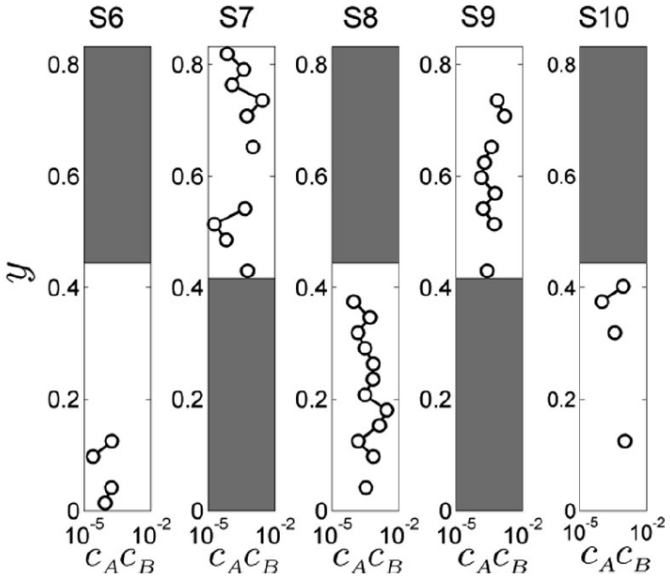

Figure 1.10 Traverse profiles of the product C_AC_B for t_D =6, Pe=96 and Da=1038. Location of the different cross sections is indicated in Figure 1.9 (Porta et al.,2013).

1.4 Darcy-scale modeling

Practical problems involving reactive transport processes at field or Darcy scale usually cannot be modeled using a direct pore-scale solution. Indeed, complete knowledge of the soil pore geometry is impossible and pore-scale transport simulation at field or Darcy scale is not affordable from a computational viewpoint (*Dentz et al., 2011*). As a consequence, continuum- scale models are needed in which the relevant pore scale processes are lumped into up-scaled parameters. These are typically difficult to characterize due to multi-scale heterogeneities. In particular, in reactive transport a key point is played by the parameterization of mixing and reaction: this entails the representation of dispersive process and mixing behavior to quantify effective reaction observe in real media. Indeed, the difference between mixing and spreading, as pointed out by *De Anna et al. (2013)*, assumes a crucial role in up-scaled reactive modeling: while spreading indicates the spatial extent of the of the concentration field, mixing is the quantification of the homogeneity inside the plume (*Dentz et al., 2011*). Darcy/field scale models need to take into account these coupled processes quantifying the effects of incomplete mixing and non-Fickian dispersion behavior on effective rate kinetics.

Diverse approaches have been proposed to tackle this issue. In the following we summarize the results related to two main conceptual approaches which have been applied at the Darcy-scale: continuum models and continuous time random walks (CRTW). An alternative approach, which hasn't been explored in the case of bimolecular homogeneous irreversible reaction, is the Dual Rate Mass Transfer model (DRMT) and it presented in section 1.4.3.

1.4.1 Continuum approach

The continuum approach is based on the assumption that the porous medium is replaced by an effective continuum. As a consequence of this assumption, the porous medium is outlined as a series of overlapping and interacting continua which represent the different phases present in the real domain (Figure 1.11). In this framework, it is possible to describe the behavior of each phase in terms of continuous variables (for example solute concentrations, fluids velocity, fluids pressures, etc) which are functions of space and time. Since the variables describing each phase are assumed to be continuous in space and time, it is possible to associate an averaged value of these variables over a representative elementary volume (REV) at each point of the domain.

The pore-scale features are embedded into up-scaled effective parameters. Through this approach we lose information about the microscopic values of the variables and geometrical configuration within each phase (*Bear and Cheng, 2010*).

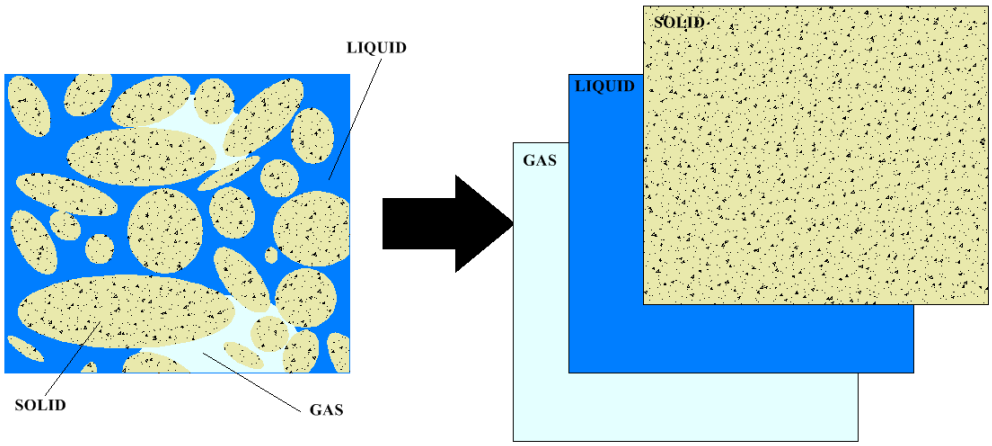

Figure 1.11. Continuum models assumption is outlined: the different phases present in the porous medium are schemed as overlapping continua. Each one of the continua represents one of the phases included in the actual domain.

According to the continuum approach, reactive transport is modeled using a system of coupled Partial Differential Equations (PDEs): each PDE represents the mass balance of a solute involved in the transport for each continuum. The following equation indicates the general mathematical structure of the mass balance referred to the *i-th* solute in the *j-th* continuum (or *j-th* phase):

$$\frac{\partial(\varphi_j \left\langle \hat{C}_i \right\rangle^j)}{\partial \hat{t}} = \hat{\nabla} \hat{f}(\hat{t}, \hat{x}, \hat{y}, \hat{z}) \pm \hat{s}(\hat{t}, \hat{x}, \hat{y}, \hat{z}) \tag{1.13}$$

where:

- The hat (^) means that the variables are dimensional while the absence of the hat means that the variables are dimensionless;
- $\left\langle \hat{C}_i \right\rangle^j$ indicates the volume averaged concentrations in *j-th* phase of *i-th* solute;
- $\hat{f}$ represents a flux term describing and dispersive transport of the *i-th* solute in the *j-th* continuum;
- $\hat{s}$ is a source term which includes all the chemical or physical transformations that generate an increment or decrement of the solute concentrations. This term measures, for example, the

effects of adsorption on solid, exchange of solute mass between different continua, chemical and biochemical reactions and so on;

- $\hat{t}$ indicates time;
- $\hat{x}$, $\hat{y}$ and $\hat{z}$ indicate spatial coordinates;
- $\langle \vec{u}_j \rangle$ indicates the averaged velocity vector that characterized the *j-th* phase;
- φ_j represents the volume fraction occupied by the *j-th* phase over the entire domain.

The $\hat{s}$ and $\hat{f}$ are expressed as function of effective parameters which lump the microscopic velocity field variations and local concentration distributions and, as consequence, they describe the hydrodynamic dispersion and incomplete mixing processes. Considering a bimolecular irreversible and homogeneous reactions in fully saturated porous medium Eq. (1.13) reduces to:

$$\frac{\partial(\langle \hat{C}_i \rangle^l)}{\partial \hat{t}} = \phi \hat{\nabla} \left[\hat{f}(\hat{t}, \hat{x}, \hat{y}, \hat{z}) \right] \pm \phi \hat{s}(\hat{t}, \hat{x}, \hat{y}, \hat{z}) \quad i = A, B, C \tag{1.14}$$

The symbol ϕ indicates the porosity of the porous medium and $\langle \hat{C}_i \rangle^l$ is the volume averaged concentration of solute $i (i = A, B, C)$ in the liquid phase.

As stated before, the ADRE model is the standard model for reactive transport and it relies on the continuum approach. This model assumes that reactants undergo a complete and instantaneous mixing within the REV which is much bigger than the characteristic pore-scale dimension. As a consequence the source term is function only of the intrinsic reaction rate (the one observed in a batch reactor). The dispersion term is assumed to be Fickian and the dispersion coefficient of all reactive species is assumed equal to conservative tracer. *Gramling et al. (2002)* tested the ADRE model against experimental data revealing its limits, a discussed above. The comparison is shown in Figure 1.12. *Gramling et al. (2002)* showed that the ADRE model over-predicts product concentrations since the complete pore-scale mixing does not occur; neglecting incomplete mixing can significantly affect model predictions.

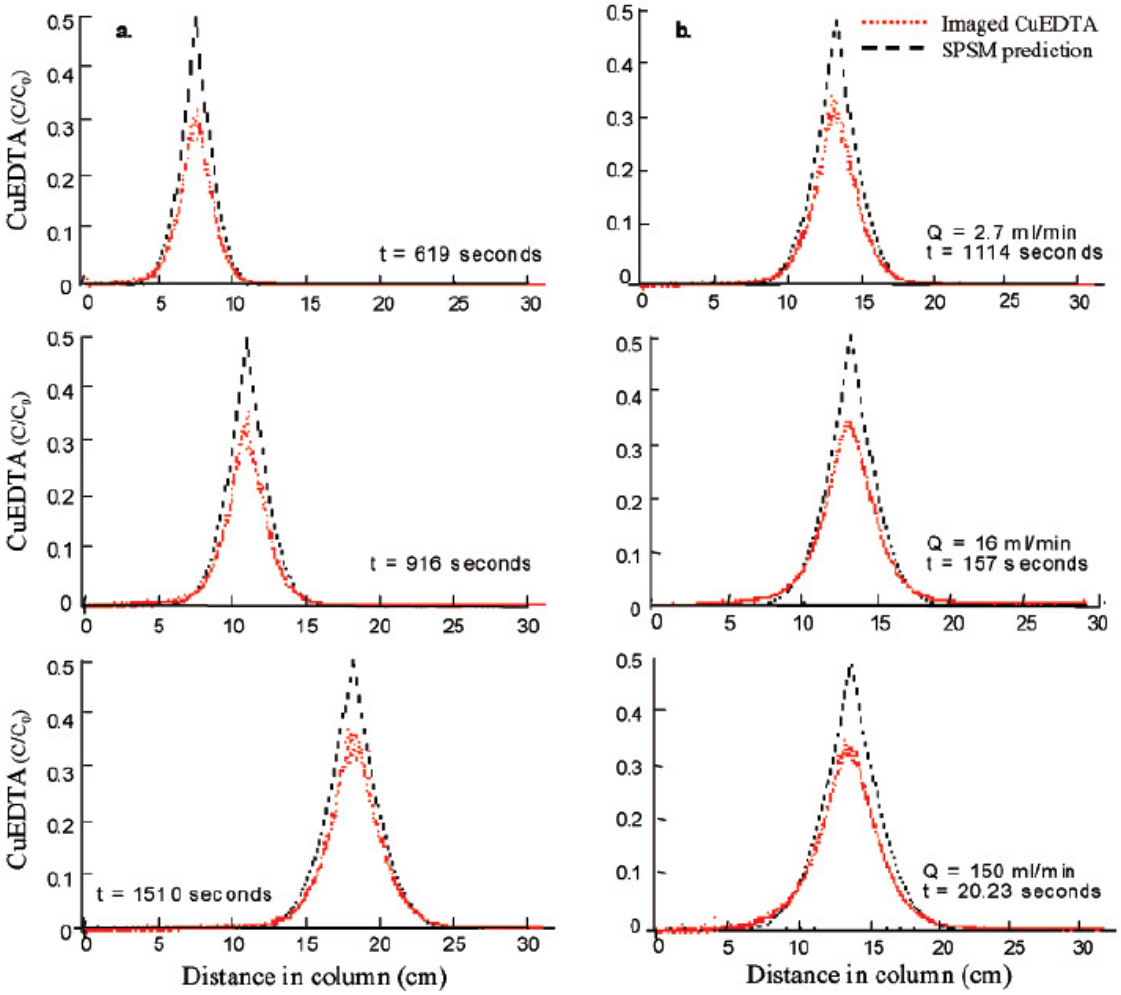

Figure 1.12 Model predicted and imagined CuEDTA-2 (relative to the initial reactant concentration C0=0.02 M) in the chamber. (a) Three times at flow rate Q) 2.67 mL/min. (b) Three flow rates at pore volume) 0.45, (Gramling et al., 2002).

However, in some cases, the ADRE can be considered a reliable model for describing the averaged behavior of a reactive process. *Battiato et al. (2011)* demonstrated that the ADRE model adequately represents narrow range of situations which are often not satisfied in practical conditions. This scenario have stimulated researchers to look for new continuum models. Two are the possible approaches: theoretical up-scaling and effective models.

1.4.1.1 Theoretical up-scaling

While different effective models based on empirical formulations have been largely proposed (see section 1.4.1.2), a theoretical up-scaling of reactive transport continuum model has been recently proposed by the work of *Porta et al. (2012a)* filling a gap in the reactive transport literature. *Porta et al. (2012a)* relied on the Volume Averaging technique to derive continuum equations starting

from balances valid at the pore-scale within a specific phase (*Whitaker, 1999*). In this work the authors upscaled Eq. (1.1) and formally derived a continuum model formulation. They proposed a non-local continuum model where the dispersive term embeds the non-Fickian behavior of dispersion and the reaction term takes into account the small scale concentration fluctuations and the incomplete mixing effect. However these non-local effects vanish at late time and the *Porta et al. (2012a)* model turns into the ADRE model. Up to now the appropriateness of this model has been tested only for a plane channel flow in *Porta et al. (2012b)* and for a regular porous medium scenario in *Porta et al. (2013)*.

Thanks to this theoretical analysis, *Porta et al. (2012a)* underlined that the time-dependency of the dispersive process can't be neglected and the Fickian analogy does not capture the actual behavior of the system, at least for short times, in agreement with the observations of *De Anna et al. (2013)*. Then the authors showed that the formulation of the up-scaled model depends on relative importance of the reaction process compared to advection. Indeed, the transport is coupled with reactant fluctuations when Da>>Pe, i.e in reaction-dominated transport, as already observed in experimental and micro-scale simulations. *Porta et al. (2012a)* formally demonstrated that the intrinsic reaction rate and a constant dispersion coefficient do not properly model the reactive transport, while a time dependent effective reaction rate (*Rubio et al, 2008 ; Sanchz-Vila, 2010*) is consistent with these theoretical analysis. Moreover, *Porta et al.(2012a)* suggested that possible dispersion and reaction time-dependent parameters can properly approximate the non-local terms which are not computationally trivial. The up-scaled model formally validates the finding of *Anmala and Kappor (2013)* who observed from numerical pore-scale simulations that the macroscopic kinetic is dependent on averaged concentration gradient. In *Porta et al. (2013)*, the up-scaled model derived is compared against pore-scale numerical simulations and the experimental observations derived in effective models. Non-local effects vanish for long times as already observed in previous numerical pore-scale simulations (*Kapoor et al. 1997*, *Anmala and Kapoor, 2013*, *Hochstetler and Kitanidis, 2013*) and the long-term product generation is independent of *Da*; it is controlled only by *Pe*. Moreover, if *Da* is sufficiently small the impact of incomplete mixing is not evident since the mixing is not the limiting process and the ADRE model properly reproduces the transport. Finally, *Porta et al. (2013)* concluded that considering a steady formulation of the theoretical model leads to negligible or modest error (less than 10%) on reaction rate predictions compared to pore-scale numerical simulation in a regular and homogeneous porous medium.

1.4.1.2 Effective models

Hochstetler and Kitanidis (2013) and *Rubio et al. (2008)* proposed two different models both based on the previous analyses driven by *Kappor et al. (1997)* who investigated reactive transport through numerical simulations. Kapoor et al. observed the evolution of solute concentration fields in the presence of a bimolecular second-order reaction and explored the concept of "Segregation Intensity", first introduced by *Danckwerts (1952)*. The Segregation Intensity is defined as a quantification of incomplete mixing, due to the presence of porous medium, and it depends on space and time. *Kapoor et al (1997)* proposed the following definition for the Segregation Intensity (S):

$$S = \frac{\left\langle \hat{\hat{C}}_A^l \hat{\hat{C}}_A^l \right\rangle}{\left\langle \hat{C}_A \right\rangle^l \left\langle \hat{C}_B \right\rangle^l} \tag{1.15}$$

Hochstetler and Kitanidis (2013) empirically modeled Segregation Intensity as a constant while *Rubio et al. (2008)* defined Segregation Intensity as a function of time. They both used S as reducing correcting factor for the ADRE kinetics term to take into account the incomplete mixing process. Focusing on *Rubio et al. (2008)*, they proposed a heuristic model for the S as a function of time with four free parameters. The dispersion coefficient considered is the one proposed by *Gramling et al. (2002)* for a conservative tracer, while the fitting parameters for S model are estimated by trial and error using the *Gramling et al. (2002)* experimental results. As shown in Figure 1.13, the inclusion of segregation effects in the reactive term leads to a better predictions of experimental data. However it must be taken into account that they introduced several free parameters and that increases the complexity of the calibration and optimization procedure.

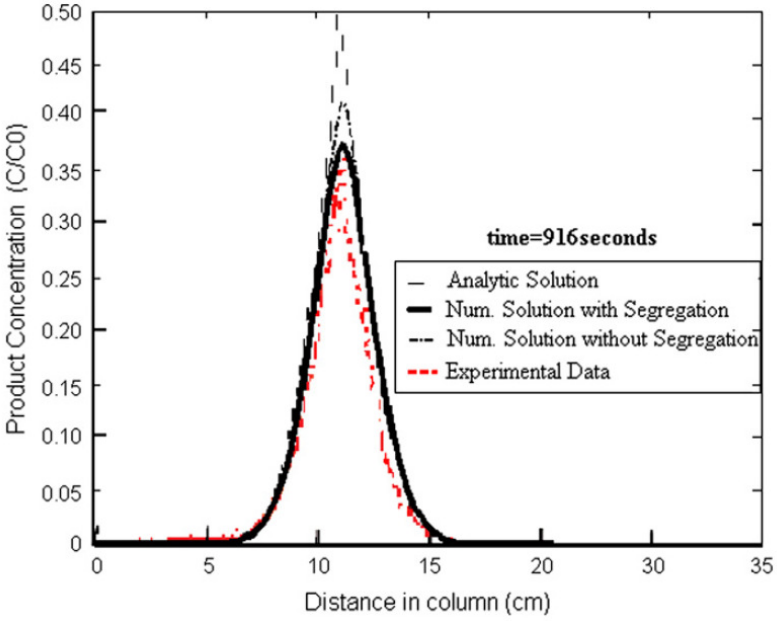

Figure 1.13. Concentration of product as a function of the position inside the tube at 916 s. Experimental data were taken from Gramling et al. (2002) ,(Rubio et al . 2008). In this figure, the analytic solution corresponds to solution of ADRE; Num. Solution without Segregation refers to a numerical solution of ADRE with a new integration scheme proposed by Rubio et al. (2008); Num. Solution with Segregation indicates the numerical solution of the new continuum model proposed by Rubio et al. (2008).

Hochstetler and Kitanidis (2013) solved the reactive transport in a virtual two-dimensional pore-scale porous medium using a finite element multiphysics software. In analogy to *Rubio et al. (2008)* and *Gramling et al. (2002)*, the dispersion coefficient is estimated independently from reactive process solving a non-reactive tracer transport in the chosen domain. Using the numerical solution they estimated an effective up-scaled kinetic constant (k_{eff}) and analyzed the relationship between the intrinsic kinetic rate (k) and k_{eff} which is expression of the Segregation Intensity. The result of this analysis is an empirical relationship between k and k_{eff} through two fitting parameters. Their work confirms once again that the intrinsic kinetic constant clearly overestimates real product concentrations and an effective parameter that models incomplete mixing is necessary for a good agreement between experimental/numerical data and up-scaled model predictions .

Sanchez-Vila et al. (2010), matched the experimental results of *Gramling et al. (2002)*, using another ADRE based continuum model. They assumed that: i) the dispersion term is Fickian, as in the ADRE, but the effective dispersion is no longer calibrated through a non-reactive tracer experiment; ii) the reactive term is proportional to the reactant concentrations product and it depends on time according to a power law. As it is shown in Figure 1.14, the Sanchez-Vila et al. model well reproduces the reaction

product concentration profiles apart from the tails; it also captures the main feature of global product evolution against time (Figure 1.15).

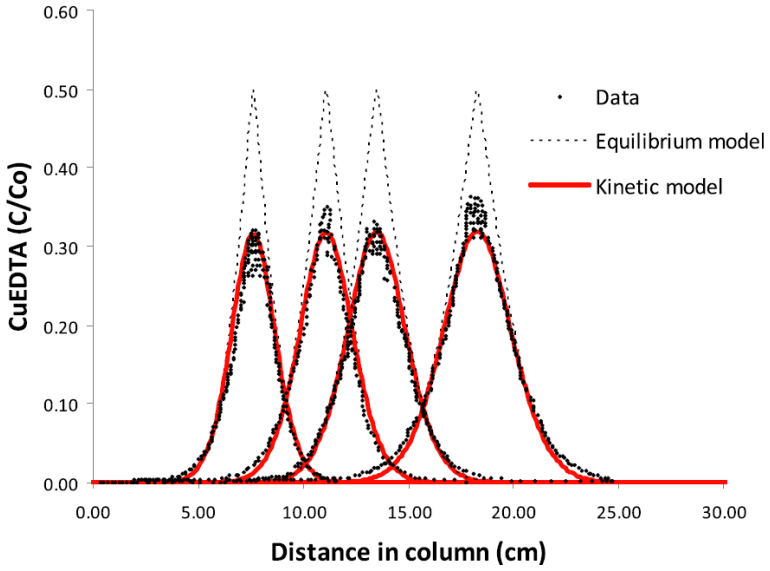

Figure 1.14. Best fit (of Gramling et al. (2002) experiment) obtained with the kinetic reactive transport model for four different times (610, 916, 1114, and 1510 s). $CuEDTA^{2-}$ concentration for the experiment conducted with a flow rate of 2.67 mL/min. the first and third curves starting from the left are used for calibration . the remaining two curves are predictions, used for model validation. The curves corresponding to ADRE model considering instantaneous equilibrium are reported for comparative purposes (Sanchez-Vila et al. 2010).

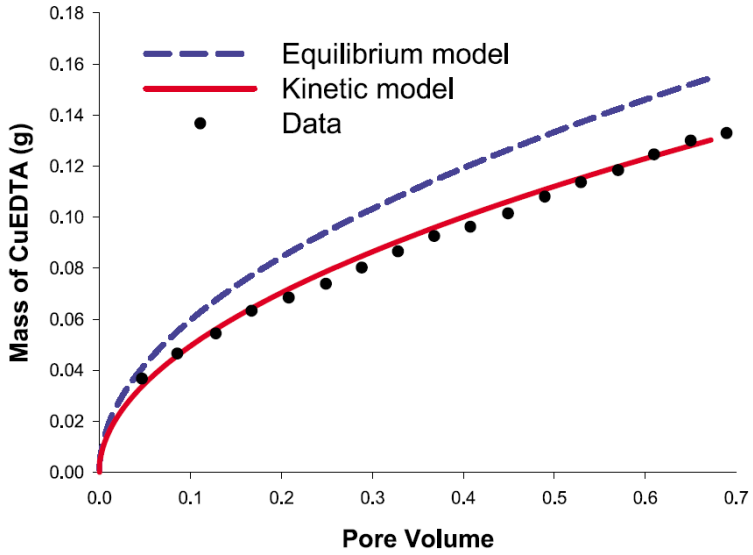

Figure 1.15. Total mass of $CuEDTA^{2-}$ produced as a function of time compared to that predicted by our Sanchez-Vila et al. model for a flow rate of 2.7 mL/min. The curve corresponding to the ADRE model considering instantaneous equilibrium is reported for comparative purposes. (Sanchez-Vila et al. 2010).

All the models reported provide a way to explore the reactive transport modeling problem. However these formulations are all affected by the same limitation: they all involve matching parameters which are not obtained through a rigorous theoretical derivation.

1.4.2 Continuous time random walk (CTRW) approach

This approach is a generalization of the particle tracking random walk techniques introduced in section 1.3.2. The solute transport is modeled in a Lagrangian framework where space-time particle transitions are characterized by probably density functions (pdfs). In this way, it possible to model slow and fast reaction (*Dentz et al, 2011*). The crucial point of this methodology is the definition of the pdf to use for spatial and time description. In literature, this approach has been first implemented for non-reactive transport. For example, *Berkowitz and Scher (1997)* analyzed the evolution of a solute plume in a fractured medium finding good agreement between CTRW results, experimental data measured in real fractured medium and particle tracking random walk simulations. *Cortis et al. (2004a)* tested the CRTW approach for conservative transport in a homogenous medium focusing attention on the predictability of early and late-time behavior. Analyzing a series of tracer breakthrough experiments in a one-dimensional (1D) flow field, they showed that the CRTW method can be helpful in capturing the solute tails compared to the Advection-Diffusion-Equation model (i.e. the classical continuum Darcy scale model for non-reactive transport) as illustrated in Figure 1.16.

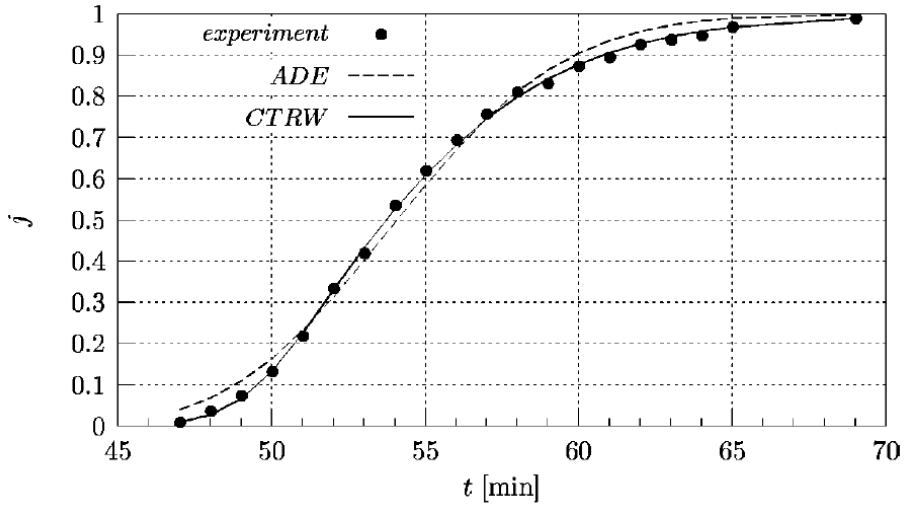

Figure 1.16. Comparison of measured vs fitted breakthrough curves for a typical short column experiment. The quantity *j* represents the normalized flux-averaged concentration. Dots: measured chloride breakthrough curve, for a fine sand. (Cortis et al, 2004a)

For reactive transport, *Dentz and Berkovitz (2005)* and *Dentz and Castro (2009)* applied the CRTW to describe the effect of adsorption in porous media solute transport while *Edery et al. (2010)* focused on the same benchmark problem analyzed in this thesis, i.e. homogeneous irreversible bimolecular reactive transport. In *Edery et al. (2010)* each particle motion is governed by the following equations:

$$s^{(N+1)} = s^{(N)} + \xi^{(N)}, t^{(N+1)} = t^{(N)} + \tau^{(N)} \tag{1.16}$$

Where s identifies the particle space coordinates and t is the time; N counts the simulation steps; ξ and τ are random increments of space and time respectively. The spatial step is computed as function of a random length and random angle. The pdf laws for space and time increments distribution are assumed independent and equal to:

$$\begin{aligned} p(s) &= \lambda_s^2 \exp(-\lambda_s s) \\ \Omega(\theta) &= N(\mu, \sigma^2) \\ \psi(t) &= C \frac{\exp(-t/t_2)}{(1+t/t_1)^{1+\beta}} \end{aligned} \tag{1.17}$$

where:

- $p(s)$ indicates the length of spatial increment; it depends on λ_s which is an unknown parameter which can be estimated starting from the first and second moment of particle spatial location in time;
- $\Omega(\theta)$ defines the angle distribution and it is assumed to be Gaussian with μ and σ as mean and standard deviation respectively;
- $\Psi(t)$ is the pdf chosen for time distribution and it assumed to be a truncated power law (TPL) to simulate non-Fickian transport; it depends on β and C: the first two are fitting parameters while t_1 and t_2 are characteristic transition time and cutoff time to Fickian transport, respectively, as defined in *Berkovitz et al. (2006)*.

At each simulation step, the distance among all possible couples of reactant particles are checked and if the distance is less than a fixed value R the reaction takes place; A and B are removed from the simulation and a new particle of C is placed in the average location between A and B positions.

We can observe good agreement between TPL-CRTW and *Gramling et al. (2002)* experiments: the TPL-CRTW matches both the peaks and the tails of product profiles (Figure 1.17) and it captures the global features of the system since it captures the total mass production (Figure 1.18).

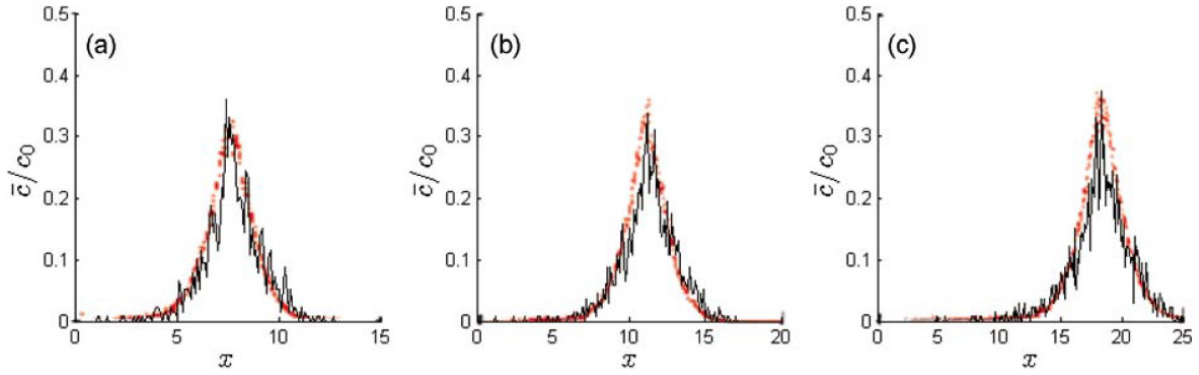

Figure 1.17. Particle tracking simulations (jagged line) with the slight Fickian TPL time distribution of $\beta = 1.96$, $t_1 = 6.6$ s, $t_2 = 10^5$ s, $l_s = 18.2$ cm^{-1}, and R = 0.3 cm, compared to the experimental measurements (dotted profile) of Gramling et al. (2002), showing the relative concentration of C particles at times (a) t = 619 s, (b) t = 916 s, and (c) t = 1510 s, (Edery et al., 2010)

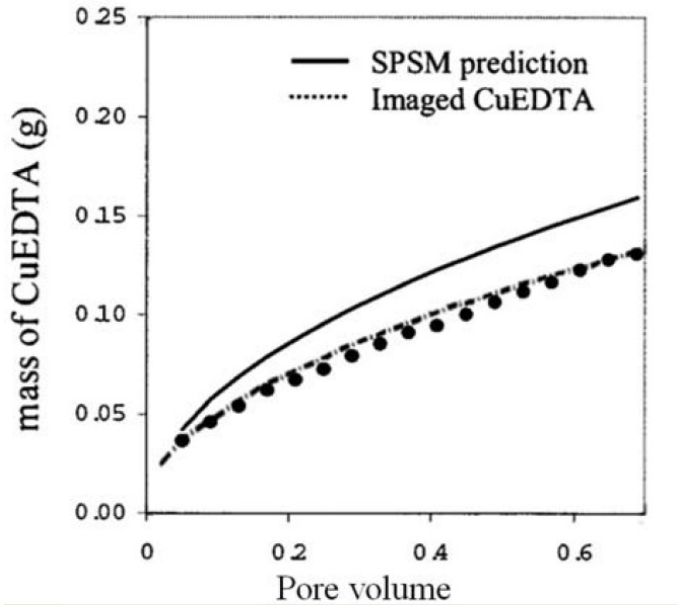

Figure 1.18 Total mass production given from the particle tracking simulations (dash - dotted line) with the marginally Fickian TPL time distribution of $\beta = 1.96$, $t_1 = 6.6$ s, $t_2 = 10^5$ s, $l_s = 18.2$ cm^{-1}, and R = 0.3 cm, compared to the experimental measurements (dotted profile) and the ADRE (solid line) standard pore - scale mixed (SPSM) model of Gramling et al. (2002), (Edery et al., 2010)

The implementation of two pdf functions, that can be freely chosen, guarantees high flexibility to CRTW approach. It has been shown that TPL works well to interpret a large set of experimental

results; however, these results are not supported by theoretical analysis. Moreover, the link between pore-scale dynamics and effective parameter R, which needs to be calibrated against experimental data, is not established yet.

1.4.3 Dual Rate Mass Transfer Model (DRMTM)

The Dual Rate Mass Transfer Model (DRMTM) was first proposed to describe the transport in fractured porous media. In these systems, the fractures are preferential channels for the fluid advective flux. In the porous medium, due to its low porosity compared to the fractures, the fluid is practically immobile and dissolved species move only due to diffusion processes. Even as the liquid phase is physically a single phase, it is worthy to represent the liquid phase within the pore-space through two apparent phases: the immobile phase and the mobile phase. The two apparent phases can exchange solute mass through diffusion process since they are in contact. At the continuum-scale, two different overlapping continua correspond to the apparent phases since a single continuum could not capture the deeply different behavior of the two apparent phases (*Huang at al., 2003*). Heterogeneous porous media are comparable to fractured systems. Figure 1.19 shows that the velocity inside the real porous media channels varies enormously. Looking at Figure 1.19, we can identify channels which correspond to preferable pathways for contaminant and solutes transport. This fact is due to the pore sizes and geometrical configuration of the system: some pores, which are dead-end or very small, are almost inaccessible to advective flux and "stagnant"; some others are larger and easily permeable.

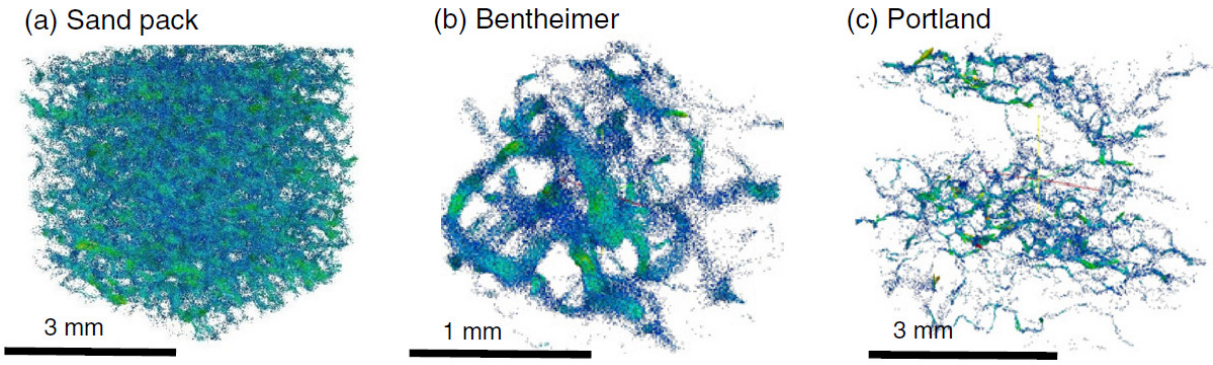

Figure 1.19. The flow field computed on: (a) a sand pack;(b) a Bentheimer sandstone; (c) Portaland limestone. The colour scale indicates the normalized flow field: blue is slow, while green and red are fast from Blunt et al. (2012).

This type of approach has been already implemented to describe evolution of sorpion processes and surface reactions (e.g.*Van Genuchten et al,1976*; *Haggerty and Gorelik, 1995*). However, this modeling

approach seems, in theory, suitable also to describe bimolecular homogeneous irreversible reactions in heterogeneous domain where the segregation of reactant between the mobile and immobile phases yields to incomplete mixing effect and limits the product generation.

1.5 Contribution of the thesis

The overview presented above shows that many different approaches and models are available for Darcy-scale reactive transport. Continuum and CRTW are two popular- and sometimes competing-approaches to this problem. In particular, *Edery et al. (2010)* affirmed that an ADRE based continuum model can not appropriately capture the main features of incomplete mixing processes. For these reasons, we focus our attention on five continuum models in different porous scenarios to explore if the reactive transport can be effectively described through this type of model. Particular attention is given to the model presented in *Porta et al. (2012a)* since it is supported by a formal and rigorous formulation. We test this model for a disordered porous medium case study and compare it to other empirical ADRE-based models. In addition to that, we present a first application of Double Rate Mass Transfer Model (DRMTM), explained in section 2.4, to the case of bimolecular reactions.

We first investigate how each model embeds the effects of incomplete mixing into effective parameters. Then we face the parameter calibration problem. We develop a preliminary analysis in which we explore how up-scaled effective parameters can be conditioned relying on diverse information on the system behavior. Our calibration data set is pore-scale numerical simulations, so in practice we have access to very detailed information, typically not available in laboratory experiments. This allows us to test the significance of different kinds of calibration data for parameter estimation. We analyze the impact of different pore-scale structures on continuum models parameters. The different models are compared in terms of their capability to depict features of reactive transport.

Chapter 2 MATERIALS AND METHODS: PROBLEM SETTING AND MODELS IMPLEMENTATION

In this chapter we illustrate the methodological structure and framework of the work in five parts:

- We introduce the context to the problem (section 2.1);
- We present the data that we use to assess continuum-scale reactive transport model included in our work. The data chosen are the micro-scale numerical simulation results performed by *Porta et al. (2013)* and by *Chaynikov (2013)* which consider bimolecular reaction (section 2.2).
- As shown in the previous Chapter, different approaches have been formulated to model bimolecular reactive transport. In our work we focus on four single-porosity continuum models (section 2.3). In addition we want to explore the suitability of Dual Rate Mass Transfer Model (DRMTM). This type of model is conceptually different from single-porosity continuum models but it is always based on the continuum approach (see section 2.4). Then, we provide a detailed conceptual and the mathematical framework of these models.
- In section 2.5, we clarify the procedure used to numerically implement and solve the models.
- Finally, we present a summary of methodologies (section 2.6) in which we describe how the puzzling elements presented before contribute to the thesis results development. The quantities and the criteria used for model assessment are definite.

2.1 Problem setting

We focus the attention on a simple reactive transport case study: a homogeneous and irreversible reaction. We consider a generic bimolecular reaction of the kind A+B→C that is often referred in scientific literature as benchmark problem. We assume that initially a porous domain is fully saturated by a solution of component A with a spatially homogeneous concentration. Fluid containing a homogenously dissolved chemical B is injected through the left domain boundary (Γ_{in}). Both the solutions are dilute, meaning that the fluid density is constant and equal to the water density. The fluid phase flows in the pore space under the action of a steady and laminar velocity field $\vec{\hat{u}}$. When A and B meet, C is produced at the interface in the liquid phase. The velocity field and the solid phase are not affected by the reaction. The upper (Γ_{up}) and lower (Γ_{low}) boundaries of the column and the solid-

liquid interface (Γ_{s-l}) are impermeable to the flux and to solutes. A concise sketch of the case study described is presented in Figure 2.1.

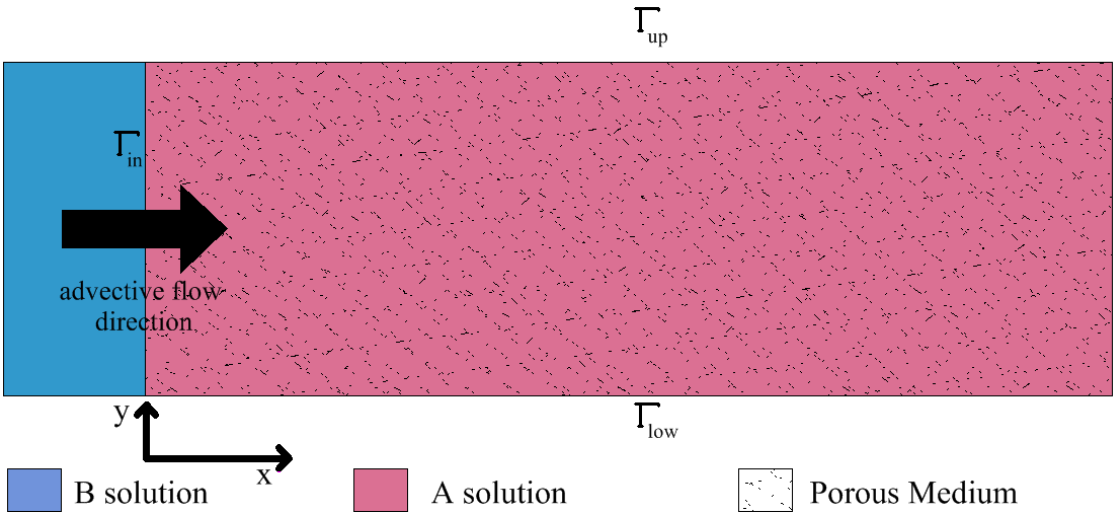

Figure 2.1 Sketch of the case study initial and boundary conditions and system coordinates.

2.2 Pore-scale validation data

Micro-scale numerical simulation results performed by *Porta et al. (2013)* and *Chaynikov (2013)* are here used to validate a continuum-scale reactive transport model. Pore-scale data refer to particle tracking simulations of reactive transport in two-dimensional disaggregated porous media for different combinations of *Da* and *Pe*. The reaction is of the kind A+B→C where A, B and C are three different dilute chemical species. The porous media are fully saturated with a solution containing the reactant A while a solution containing B is progressively injected. C in generated at the interface . The grains of the porous media are outlined as arrays of cylinders and the medium is constituted of periodic cells. We consider two structures:

- Porous medium scenario 1: The porous medium in which the reaction takes place is very simple and regular as shown in Figure 2.2. The porosity is fixed at the value of 0.36. the symbol *w* indicates the characteristic length of the porous medium which represents the averaged distance between the centers of two consecutive cylinders along the x direction. Table 2.1 reports the combinations of *Da* and *Pe* which have been investigated with this geometry: the results of these simulations have been presented in *Porta et al. (2013)* and *Chaynikov (2013)*. Results of simulations with nonreactive tracers are also available for the investigated *Pe* numbers.

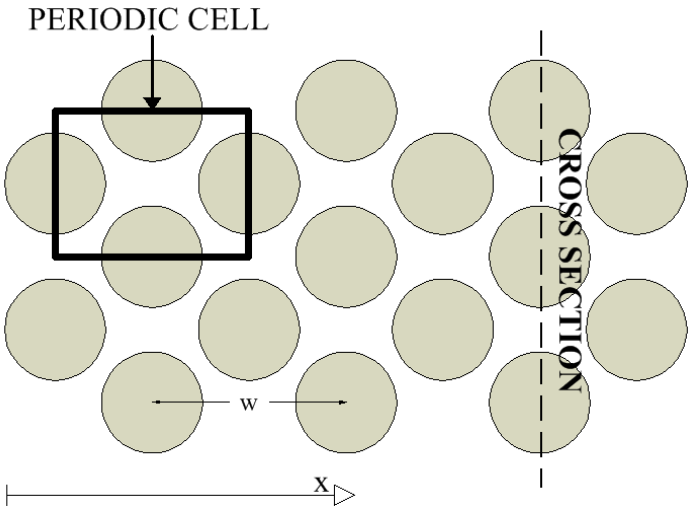

Figure 2.2. Outline of porous medium scenario 1.

Table 2.1. Combination of *Da* and *Pe* numbers which have been investigated with porous medium scenario 1.

Pe=6, *Da*=8	*Pe*=6, *Da*=64.8	*Pe*=6, *Da*=1038
Pe=24, *Da*=8	*Pe*=24, *Da*=64.8	*Pe*=24, *Da*=1038
Pe=96, *Da*=8	*Pe*=96, *Da*=64.8	*Pe*=96, *Da*=1038

- Porous medium scenario 2: The porous medium is no longer regular but the cylinders are irregularly distributed in space as shown in Figure 2.3. The porosity is fixed at the value of 0.6. This is a more complicated geometry in which both cavities and fast flowing channels influence the reaction and the transport evolutionary features. Table 2.2 reports the combinations of *Da* and *Pe* which have been investigated with this geometry: the results of these simulations have not yet been presented. The particle tracking algorithm is analogous to the one applied to the porous scenario 1. A non reactive tracer simulation was also run.

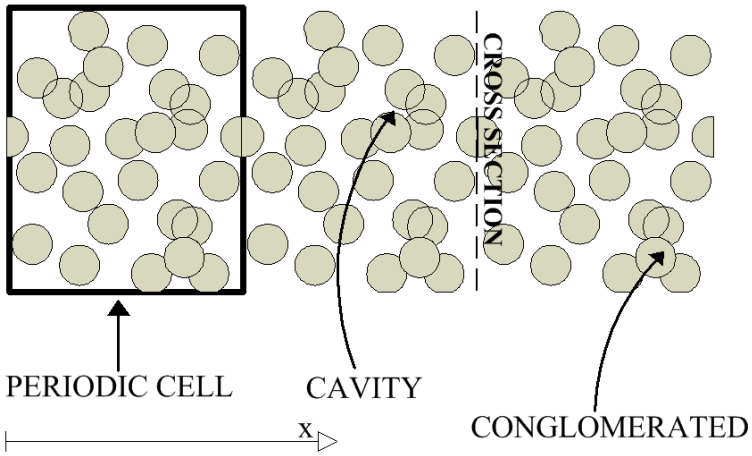

Figure 2.3. Outline of porous medium scenario 2.

Table 2.2. Combination of *Da* and *Pe* numbers which have been investigated with porous medium scenario 2.

Pe=6, *Da*=8	*Pe*=6, *Da*=64.8	*Pe*=6, *Da*=1038
Pe=24, *Da*=8	*Pe*=24, *Da*=64.8	*Pe*=24, *Da*=1038

Since we are considering 1D continuum models, the pore-scale simulation results have been averaged along the cross-sectional sections indicated in Figure 2.2 and Figure 2.3 through dashed black lines. In the following discussion, the pore-scale cross sectional averaged data will be referred as "pore-scale data".

2.3 Single-porosity continuum models

We consider a porous medium that is fully saturated and the fraction of volume occupied by the liquid phase corresponds to the porosity of the porous medium (ϕ); adsorption and biochemical reactions are supposed to be absent and the solid grain are impenetrable to water and to solutes. The latter implies that no solute concentration is expected into solid phase and the model is limited to liquid phase. Moreover the solid grains geometry is not affected by the reaction that takes place only in the liquid phase; hence the porosity can be considered constant in time. In our case study, the domain is one-dimensional (along the axis x) and only three solutes are involved in the reactive process: the reactants A and B and the reaction product C. As a consequence, the PDEs system presents three 1-D equations:

$$\begin{aligned}
\phi\frac{\partial(\left\langle \hat{C}_A \right\rangle^l)}{\partial \hat{t}} &= \phi\frac{\partial}{\partial x}\left[f(\hat{t},\hat{x})\right] - \phi s(\hat{t},\hat{x}) \\
\phi\frac{\partial(\left\langle \hat{C}_B \right\rangle^l)}{\partial \hat{t}} &= \phi\frac{\partial}{\partial x}\left[f(\hat{t},\hat{x})\right] - \phi s(\hat{t},\hat{x}) \\
\phi\frac{\partial(\left\langle \hat{C}_C \right\rangle^l)}{\partial \hat{t}} &= \phi\frac{\partial}{\partial x}\left[f(\hat{t},\hat{x})\right] + \phi s(\hat{t},\hat{x})
\end{aligned} \tag{2.1}$$

where ϕ indicates the porosity and $\left\langle \hat{C}_i \right\rangle^l$ is the volume averaged concentration of solute *i* in liquid phase. We associate the following set of boundaries and initial conditions related to the case study analyzed:

$$\begin{aligned}
&\left\langle \hat{C}_A \right\rangle^l (x,0) = \hat{C}_{A0} && \forall x \geq 0 \\
&\left\langle \hat{C}_B \right\rangle^l (0,0) = \hat{C}_{B0} && \\
&\left\langle \hat{C}_B \right\rangle^l (x,0) = 0 && \forall x > 0 \\
&\left\langle \hat{C}_C \right\rangle^l (x,0) = 0 && \forall x \geq 0 \\
&\frac{\partial \left\langle \hat{C}_B \right\rangle^l (-\infty,t)}{\partial x} = 0 && \forall t \geq 0 \\
&\frac{\partial \left\langle \hat{C}_A \right\rangle^l (-\infty,t)}{\partial x} = 0 && \forall t \geq 0 \\
&\frac{\partial \left\langle \hat{C}_C \right\rangle^l (-\infty,t)}{\partial x} = 0 && \forall t \geq 0 \\
&\frac{\partial \left\langle \hat{C}_A \right\rangle^l (+\infty,t)}{\partial x} = 0 && \forall t \geq 0 \\
&\frac{\partial \left\langle \hat{C}_B \right\rangle^l (+\infty,t)}{\partial x} = 0 && \forall t \geq 0 \\
&\frac{\partial \left\langle \hat{C}_C \right\rangle^l (+\infty,t)}{\partial x} = 0 && \forall t \geq 0
\end{aligned} \tag{2.2}$$

The *s* term is defined positive for the product while it is negative for the reactants. Indeed, since the reaction is irreversible, C can only be formed while A and B are always consumed. For the sake of simplicity of numerical implementation, we define two conservative components D=B-A and E=B+C which allow us rewriting Eq. (2.1) in the following form that will be often used in the next paragraphs:

$$\begin{aligned}
\phi\frac{\partial(\left\langle \hat{C}_E \right\rangle^l)}{\partial \hat{t}} &= \phi\frac{\partial}{\partial \hat{x}}\left[f(\hat{t},\hat{x}) \right] \\
\phi\frac{\partial(\left\langle \hat{C}_D \right\rangle^l)}{\partial \hat{t}} &= \phi\frac{\partial}{\partial \hat{x}}\left[f(\hat{t},\hat{x}) \right] \\
\phi\frac{\partial(\left\langle \hat{C}_B \right\rangle^l)}{\partial \hat{t}} &= \phi\frac{\partial}{\partial \hat{x}}\left[f(\hat{t},\hat{x}) \right] - s(\hat{t},\hat{x})
\end{aligned} \tag{2.3}$$

with the following boundaries and initial conditions:

$$\begin{aligned}
&\left\langle \hat{C}_E \right\rangle^l (x,0) = 0 && \forall x \geq 0 \\
&\left\langle \hat{C}_B \right\rangle^l (x,0) = 0 && \forall x > 0 \\
&\left\langle \hat{C}_B \right\rangle^l (0,0) = 0 && \\
&\left\langle \hat{C}_D \right\rangle^l (x,0) = \hat{C}_{B0} - \hat{C}_{A0} && \forall x \geq 0 \\
&\frac{\partial \left\langle C_E \right\rangle^l (+\infty,t)}{\partial x} = 0 && \forall t \geq 0 \\
&\frac{\partial \left\langle C_B \right\rangle^l (+\infty,t)}{\partial x} = 0 && \forall t \geq 0 \\
&\frac{\partial \left\langle C_D \right\rangle^l (+\infty,t)}{\partial x} = 0 && \forall t \geq 0 \\
&\frac{\partial \left\langle C_E \right\rangle^l (-\infty,t)}{\partial x} = 0 && \forall t \geq 0 \\
&\frac{\partial \left\langle C_B \right\rangle^l (-\infty,t)}{\partial x} = 0 && \forall t \geq 0 \\
&\frac{\partial \left\langle C_D \right\rangle^l (-\infty,t)}{\partial x} = 0 && \forall t \geq 0
\end{aligned} \tag{2.4}$$

Notice that the mass balances of D and E can be solved separately.

We investigate four different continuum models reviewed in literature that are all based on a system of PDEs structured as Eq. (2.1) or equivalently as Eq. (2.3):

- MODEL 1: the advection-dispersion-reaction model (ADRE);
- MODEL 2: the model formulated by *Porta et al. (2012a)*;
- MODEL 3: the model formulated by *Sanchez-Vila et al (2010);*
- MODEL 4: the model formulated by *Hochstetler and Kitanidis (2013).*

Each one of the listed models provides a different formulation. In the next paragraphs the conceptual formulations of these models will be explored: the dimensional and the dimensionless formulations will be presented pointing out the hypotheses assumed.

2.3.1 MODEL 1: ADRE

The advection-dispersion-reaction equation (ADRE) is a standard continuum model for reactive transport. Starting from the pore scale mass balance equations defined in Eq. (1.1),we can derive the ADRE formulation implementing the volume averaging method (*Whitaker, 1999*) and imposing the following hypotheses:

- Spatial scale separation;
- $Da \ll Pe$ that means that the reaction process is slow compared to advection and dispersion processes;
- Time is assumed sufficiently large to consider a steady state closure (*Porta et al.,2012*).

In the ADRE model the cross-correlation between the reactants concentration fluctuations in the reactive term is assumed to be negligible and the reactive term is then approximated by:

$$\hat{k}\left\langle \left\langle \hat{C}_A \right\rangle^l \left\langle \hat{C}_B \right\rangle^l + \hat{\tilde{C}}_B^l \hat{\tilde{C}}_A^l \right\rangle \simeq \hat{k} \left\langle \hat{C}_A \right\rangle^l \left\langle \hat{C}_B \right\rangle^l \tag{2.5}$$

where $\hat{k}$ represents the intrinsic kinetic reaction rate derived from well-mixed batch tests.

As we can see the structure of the ADRE model reflects the general continuum model structure Eq. (2.1) where the *f* and *s* terms are:

$$f = \hat{D}\frac{\partial \langle C_i \rangle^l}{\partial \hat{x}} \tag{2.6}$$

$$s = \hat{k}\left\langle \hat{C}_A \right\rangle^l \left\langle \hat{C}_B \right\rangle^l \tag{2.7}$$

The parameter $\hat{D}$ is the dispersion coefficient that embeds the effect of molecular diffusion and the hydrodynamic solute dispersion. The effective parameter $\hat{D}$ is constant in space and time.

We rewrite Model 1 using the dimensionless quantities reported in Eq. (1.4) and employing the conservative components D and E:

$$\begin{aligned}
&\frac{\partial \langle C_i \rangle^l}{\partial \hat{t}} = \frac{1}{Pe}(D+1)\frac{\partial^2 \langle C_i \rangle^l}{\partial x^2} - \langle u \rangle \frac{\partial \langle C_i \rangle^l}{\partial \hat{x}} \quad \text{i=D,E} \\
&\frac{\partial \langle C_B \rangle^l}{\partial \hat{t}} = \frac{1}{Pe}(D+1)\frac{\partial^2 \langle C_B \rangle^l}{\partial x^2} - \langle u \rangle \frac{\partial \langle C_B \rangle^l}{\partial \hat{x}} - \frac{Da}{Pe}\langle C_B \rangle^l (\langle C_B \rangle^l - \langle C_D \rangle^l)
\end{aligned} \tag{2.8}$$

where the D is the ratio between the dimensional dispersion coefficient and the dimensional diffusion coefficient.

2.3.2 MODEL 2: Porta et al. (2012a)

In this work we dedicate particular attention to the model presented by *Porta et al. (2012a)*. This model is particularly interesting since it is formally derived by up-scaling the pore-scale system equation (1.1) using the volume averaging method. For details about the volume averaging implementation, see *Porta et al. (2012a)*.

Referring to the conservative components, the s term is absent and the format of f term is the following one:

$$f = \frac{1}{Pe}\left[D_U^* * \frac{\partial}{\partial t}\left(\frac{\partial \langle C_i \rangle^l}{\partial x}\right) \right] \quad i = D, E \tag{2.9}$$

where * indicates the convolution and D_U^* is:

$$D_U^* = 1 + \frac{1}{V\phi}\int_{A_{ls}} b_i dA + \left\langle \tilde{u} b_i \right\rangle^l \qquad i = D, E \tag{2.10}$$

V is the averaging volume, A_{ls} is the liquid-solid interface within the averaging volume and b_i is a closure variable (*Porta et al. 2012a; Porta et al.,2013*). Regarding the reactive specie B the format of f and s depends on the relative importance of *Da* compared to *Pe*:

- If $Da \ll Pe$

$$f = \frac{1}{Pe} D_U^* * \frac{\partial}{\partial t}\left(\frac{\partial}{\partial x} \left\langle C_B \right\rangle^l \right) \tag{2.11}$$

$$s = \frac{Da}{Pe} \left\langle C_B \right\rangle^l \left(\left\langle C_B \right\rangle^l - \left\langle C_D \right\rangle^l \right) \tag{2.12}$$

- If $Da \gg Pe$

$$f = \frac{1}{Pe}\left[\frac{\partial \left\langle C_B \right\rangle^l}{\partial x} + M\left(D_U^* - 1 \right) * \frac{\partial}{\partial t}\left(\frac{\partial \left\langle C_D \right\rangle^l}{\partial x} \right) \right] \tag{2.13}$$

$$s = -\frac{Da}{Pe}\left[\left\langle C_B \right\rangle^l \left(\left\langle C_B \right\rangle^l - \left\langle C_D \right\rangle^l \right) + M\left(M - 1 \right) \left\langle \left(b_D * \frac{\partial \left\langle C_D \right\rangle^l}{\partial x} \right)^2 \right\rangle^l \right] \tag{2.14}$$

where $M = \dfrac{\left\langle C_B \right\rangle^l}{\left\langle C_B \right\rangle^l + \left\langle C_A \right\rangle^l} = \dfrac{\left\langle C_B \right\rangle^l}{2\left\langle C_B \right\rangle^l - \left\langle C_D \right\rangle^l}$.

Following *Porta et al. (2013)* we can break Eq. (2.14) into two parts r_1 and r_{2U} :

$$r_1 = -\frac{Da}{Pe} \left\langle C_B \right\rangle^l \left(\left\langle C_B \right\rangle^l - \left\langle C_D \right\rangle^l \right) \tag{2.15}$$

$$r_{2U} = -\frac{Da}{Pe} M\left(M - 1 \right) \left\langle \left(b_D * \frac{\partial \left\langle C_D \right\rangle^l}{\partial x} \right)^2 \right\rangle^l \tag{2.16}$$

The term r_{2U} includes the closure variable b_D which embeds the effects of small scale fluctuations and, as a consequence, the effects of incomplete mixing. Due to the convolutions, the equations are non local in time meaning that the transport and the reaction at time *t* depend on the previous history of the system. *Porta et al. (2012a)* demonstrated that nonlocal effects tend to vanish with time and the standard formulation of Advection-Dispersion Equation (ADE) for conservative components and ADRE (see Eq. (2.8)) for reactive species are recovered in long times for $Da \ll Pe$.

The inclusion of the convolution in the equations turns them into integral-differential equations the solution of which is computationally expensive. In this work, we do not include a fully nonlocal solution, but we resort to two simplified approximations of Equations (2.11)-(2.14) . The two simplified formulations will be referred as Model 2 and Model 2b in the following.

MODEL 2

A first possible simplification of *Porta et al. (2012a)* model can be done if we assume that the system parameters attained an asymptotic value. In this case, the convolution can be substituted by a Fickian term. The conservative components are then described by the ADE model. Concerning the reactive specie B, if $Da \ll Pe$ the ADRE model is recovered while if $Da \gg Pe$:

$$f = \frac{1}{Pe}\left[\frac{\partial \langle C_B \rangle^l}{\partial x} + M\left(D-1\right)\left(\frac{\partial \langle C_D \rangle^l}{\partial x}\right)\right] \tag{2.17}$$

$$s = -\frac{Da}{Pe}\left[\langle C_B \rangle^l \left(\langle C_B \rangle^l - \langle C_D \rangle^l\right) + M\left(M-1\right)B\left(\frac{\partial \langle C_D \rangle^l}{\partial x}\right)^2\right] \tag{2.18}$$

where B is the asymptotic value of $\langle b_D^2 \rangle^l$ in the asymptotic regime.Since we approximate the convolution of Model 2 reaction term to a constant parameter, it is possible that for short times the absolute value r_2 is bigger than r_1 leading to a negative reaction rate. In order to avoid this physically impossible result, we solve Model 2 imposing that:

- If $|r_2| > r_1$ then $s = 0$, i.e. reactants do not mix at all;
- If $|r_2| < r_1$ then $s = r_1 + r_2$.

MODEL 2B

In Model 2b, we simplify *Porta et al. (2012a)* model formulation (reported in Eq. (2.11)-(2.14)) assuming that the flux and the reaction terms are function of time but they don't depend on the previous history of the system. In this case convolutions are approximated as follows:

$$\left\langle \left(b_D * \frac{\partial \langle C_D \rangle^l}{\partial x} \right)^2 \right\rangle^l = B(t) \left(\frac{\partial \langle C_D \rangle^l}{\partial x} \right)^2 \tag{2.19}$$

$$\left(D_U^* - 1 \right) * \frac{\partial}{\partial t} \left(\frac{\partial \langle C_D \rangle^l}{\partial x} \right) = D(t) \frac{\partial \langle C_D \rangle^l}{\partial x} \tag{2.20}$$

where $B(t)$ and $D(t)$ are:

$$\begin{aligned} B(t) &= B(1 - \exp(-a_1 t)) \\ D(t) &= D(1 - \exp(-a_2 t)) \end{aligned} \tag{2.21}$$

Substituting Eq.(2.19)-(2.21) into Eq. (2.9)-(2.14) we obtain the formulation of Model 2b for conservative and reactive solutes. The exponential formulation of Eq. (2.21) is suggested by the analyses done by *Porta et al. (2013)*. In Figure 2.4 we can observe that *B* and *D* present an exponential growth for short times and then they reach a steady asymptotic value and, as consequence Eq. (2.21) can well interpret the time evolution of the parameters. In Figure 2.4, *B* and *D* trends are expressed as function of diffusive timescale (t_D).

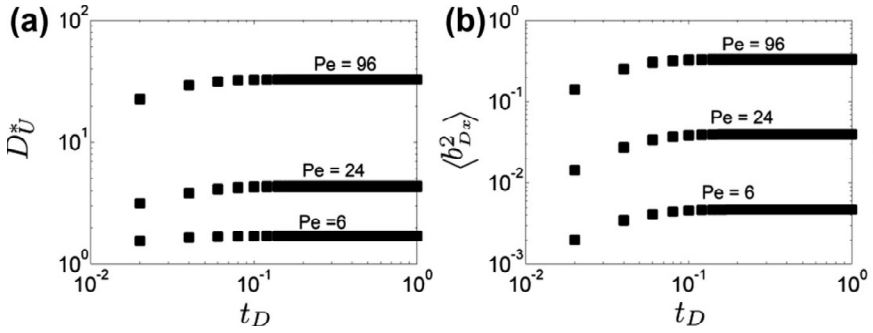

Figure 2.4 Evolution of the (a) longitudinal dispersion coefficient D_U*and (b) b^2_D with t_D for ϕ=0.25 (Porta et al., 2013). Here b^2_{Dx} is the square value of the closure variable along the x-axis and corresponds to B(t).

2.3.3 MODEL 3: Sanchez-Vila et al. (2010)

Model 3 was proposed in *Sanchez-Vila et al. (2010)* after pointing out the limitations of ADRE model. We will first report the original dimensional formulation, then we provide its dimensionless counterpart. *Sanchez-Vila et al. (2010)* defined a new continuum model based on the ADRE aiming at interpreting the experimental data reported in *Gramling et al (2002)*. While the f term remains unchanged compared to Model 1, they assumed that the s term can be modeled as:

$$s = \hat{\beta}\left\langle \hat{C}_A \right\rangle^l \left\langle \hat{C}_B \right\rangle^l \tag{2.22}$$

where $\hat{\beta}$ is a time dependent coefficient expressed by the following equation:

$$\hat{\beta} = \hat{\beta}_0 \hat{t}^{-m} \tag{2.23}$$

and it embeds the effect of incomplete mixing. Parameters $\hat{\beta}_0$ and m are explicitly defined as calibration parameters. Contrasting other approaches (*Gramling et al.,2002, Rubio et al., 2008; Hochstetler and Kitanids, 2013*), *Sanchez-Vila et al. (2010)* considered the dispersion coefficient as a calibration parameter. The authors presented a conceptual explanation of their model that is briefly reported here. Since the fluid velocity can exhibit large variations at the pore-scale, a real porous medium can be schemed as a two regions mass transfer model (introduced in section 1.4.3): the immobile zones are constituted by dead-end pores and relative slow fluid velocity conduits (compared to the mean Darcy velocity) while the mobile zones are represented by the fast flowing conduits. Immobile and mobile zones exchange mass due to advection and diffusion processes and, depending on the importance of these processes, the mixing between reactants can be more or less fast. Because of that, the presence of these immobile zones delays the mixing processes between the reactants and influences the entity of reaction rate. As a consequence the mass transfer rate between the immobile and mobile zones assumes a key role in the reactive transport. In this framework, *Sanchez-Vila et al. (2010)* include the effect of the mass transfer rate into the reaction term through the parameter $\hat{\beta}$. The mathematical form of $\hat{\beta}$ is based on *Haggerty et al.(2004)*.

Sanchez-Vila et al. (2010) performed the calibration and validation process as follows:

- Among the experimental results proposed by *Gramling et al. (2002)*, two sampling product profiles are selected (at t=610 s and t=1114 s);
- The parameters $\hat{D}$, $\hat{\beta}_0$ and m are adjusted manually against the two sampling profiles;
- Using the calibrated parameters (reported in Table 2.3), a validation of the model is performed against the product profiles at t=916 s and t=1510 s.

Sanchez-Vila et al. (2010) observed agreement between their model predictions and experimental data and demonstrated that continuum models are able to capture reactive transport features. Moreover, they highlighted that the calibrated dispersion coefficient is lower than the conservative one proposed by *Gramling et al. (2002)*.

Table 2.3. Parameters calibrated by Sanchez-Vila et al. (2919) for the experiment performed by Gramling et al. (2002).

$\hat{D}$	$1.30*10^{-3}$
$\hat{\beta}_0$	240 L/(mol s)
m	0.93

The parameter $\hat{\beta}$ has the same dimension of $\hat{k}$, the intrinsic reaction rate. We can define a dimensionless form of $\hat{\beta}$ as:

$$\beta = \frac{\hat{\beta}}{\hat{k}} \tag{2.24}$$

We rewrite Model 3 using the dimensionless quantities reported in Eq. (1.4) and in Eq. (2.24) and employing the conservative components D and E:

$$\begin{aligned} &\frac{\partial \langle C_i \rangle^l}{\partial \hat{t}} = \frac{1}{Pe}(D+1)\frac{\partial^2 \langle C_i \rangle^l}{\partial x^2} - \langle u \rangle \frac{\partial \langle C_i \rangle^l}{\partial \hat{x}} \quad \text{i=E,D} \\ &\frac{\partial \langle C_B \rangle^l}{\partial \hat{t}} = \frac{1}{Pe}(D+1)\frac{\partial^2 \langle C_B \rangle^l}{\partial x^2} - \langle u \rangle \frac{\partial \langle C_B \rangle^l}{\partial \hat{x}} - \frac{Da}{Pe}\beta \langle C_B \rangle^l (\langle C_B \rangle^l - \langle C_D \rangle^l) \end{aligned} \tag{2.25}$$

2.3.4 MODEL 4: Hochstetler and Kitanidis (2013)

Model 4 is based on the Segregation Intensity concept formulated by *Kapoor et al. (1997)*. Starting from the Segregation Intensity (S) reported in Eq. (1.15), *Hochstetler and Kitanidis (2013)* defined the effective reaction rate ($\hat{k}_{eff}$) and the effectiveness factor (E) as:

$$\hat{k}_{eff} = (1 - S)\hat{k} \tag{2.26}$$

$$E = \frac{\hat{k}_{eff}}{\hat{k}} = 1 + S \tag{2.27}$$

Introducing the effective reaction rate, *Hochstetler and Kitanidis (2013)* recasted the ADRE model into the following model:

$$\frac{\partial \left\langle \hat{C}_i \right\rangle^l}{\partial \hat{t}} = -\hat{u}_{eff} \frac{\partial \left\langle \hat{C}_i \right\rangle^l}{\partial \hat{x}} + \hat{D}_{eff} \frac{\partial^2 \left\langle \hat{C}_i \right\rangle^l}{\partial \hat{x}^2} \pm \hat{k}_{eff} \left\langle \hat{C}_A \right\rangle^l \left\langle \hat{C}_B \right\rangle^l \quad i = A, B, C \tag{2.28}$$

Hochstetler and Kitanidis (2013) developed an empirical formulation of E applying this procedure:

- A conservative transport problem is solved in a virtual two-dimension domain with the following features (Figure 2.5): the system dimensions are L=7.45 cm and H=1.54 cm, the grains are represented as circles with a fixed diameter of 0.5 mm, the circles are first placed in space according to a regular grid and then randomly displaced around their original locations, if any overlapping of cylinders occurs a conglomeration is formed;
- The Break-Through Curves (BTCs) of cross-sectionally averaged concentrations are measured at different distances from the inlet;
- Using the tracer BTCs at a distance equal or bigger than 4 cm from the inlet, the BTCs data are fitted to the ADE model where the Darcy velocity ($\hat{u}_{eff}$) and the dispersion coefficient ($\hat{D}_{eff}$) are the fitting parameters; *Hochstetler and Kitanidis (2013)* assumed that the transport regime can be considered asymptotic at that distance from the inlet;
- The reactive transport problem described by Eq. (1.1) is solved in the same virtual two-dimension domain for different values of constant intrinsic rate ($\hat{k}$);

- The BTCs of the averaged cross sectional reaction product concentrations are computed at different distances from the inlet boundary;
- The BTCs of reaction product concentrations are fitted to Eq. (2.28) using $\hat{k}_{eff}$ as fitting parameter while $\hat{u}_{eff}$ and $\hat{D}_{eff}$ are the ones estimated for non-reactive transport;
- The evolution of $\hat{k}_{eff}$ as function of $\hat{k}$ and the cross section distance from the inlet is analyzed (Figure 2.6a) and the evolution of the effectiveness factor *E* as function of *Da* is derived (Figure 2.6b);
- Looking at Figure 2.6b, *Hochstetler and Kitanidis (2013)* finally proposed this empirical formulation of *E*:

$$E = \frac{\gamma\lambda}{Da + \lambda} \tag{2.29}$$

where γ and λ are dimensionless calibration parameters.

- *Hochstetler and Kitanidis (2013)* calibrated the parameters γ and λ against the curve reported in Figure 2.6b obtaining the values reported in Table 2.4 for the specific case study analyzed in their work.

Table 2.4 Calibrated parameters for the specific case analyzed by Hochstetler and Kitanidis, (2013).

$\hat{u}_{eff}$	$2.88*10^{-5}$ [m/s]
$\hat{D}_{eff}$	$1.08*10^{-8}$ [m^2/s]
γ	0.94
λ	11.2

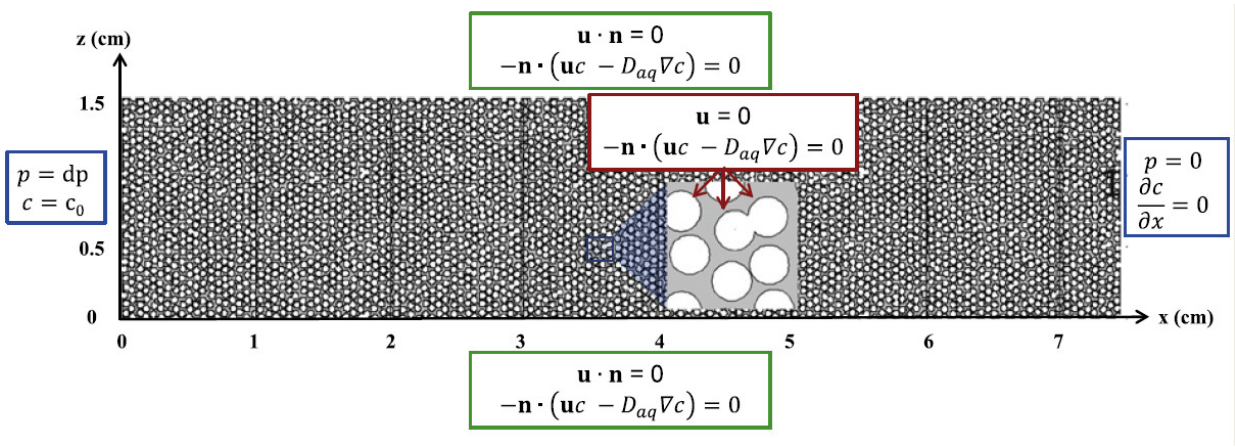

Figure 2.5 Porous medium domain with flow and transport boundary condition. The grains are with and the pore-space is gray.

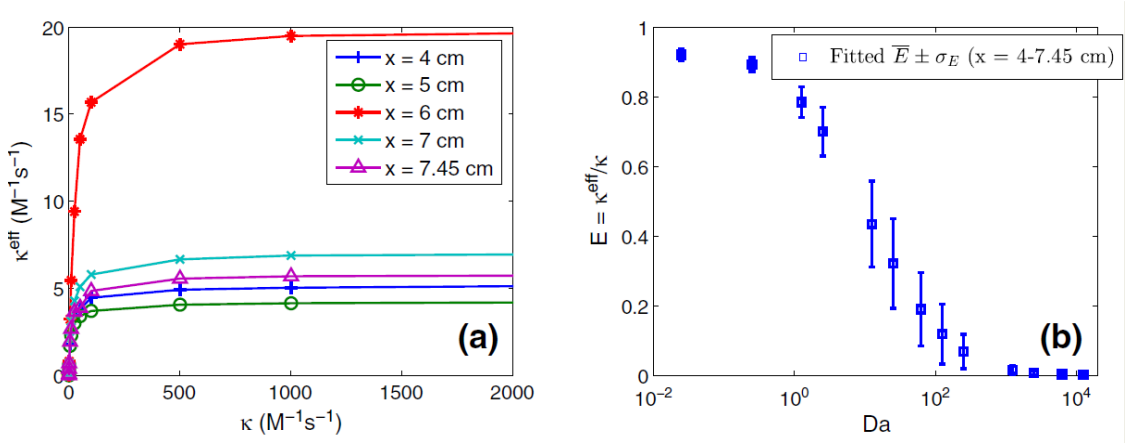

Figure 2.6. The effective reaction rate constants fitted from product (C) BTCs for a range of intrinsic rate constants (from 0.01 $M^{-1}s^{-1}$) computed at different cross sections. The effective rate constant versus the intrinsic rate constants (a),and the mean effectiveness factor plus/minus one standard deviation versus the Damkhöler number (b), from Hochstetler and Kitanidis (2013).

According to Eq. (2.28), the f term is analogous to Eq. (2.6), i.e. the ADRE flux term. Introducing the correcting factor E as defined in (2.27), we express the s term as:

$$s = E\hat{k}\left(\langle C_A \rangle^l \langle C_B \rangle^l\right) \tag{2.30}$$

We rewrite Model 4 using the dimensionless quantities reported in Eq. (1.4) and employing the conservative components D and E:

$$\begin{aligned}
&\frac{\partial \langle C_i \rangle^l}{\partial \hat{t}} = \frac{1}{Pe}(D+1)\frac{\partial^2 \langle C_i \rangle^l}{\partial x^2} - \langle u \rangle \frac{\partial \langle C_i \rangle^l}{\partial \hat{x}} \quad \text{i=E,D} \\
&\frac{\partial \langle C_B \rangle^l}{\partial \hat{t}} = \frac{1}{Pe}(D+1)\frac{\partial^2 \langle C_B \rangle^l}{\partial x^2} - \langle u \rangle \frac{\partial \langle C_B \rangle^l}{\partial \hat{x}} - \frac{Da}{Pe} E \langle C_B \rangle^l (\langle C_B \rangle^l - \langle C_D \rangle^l)
\end{aligned} \tag{2.31}$$

2.4 MODEL 5: Dual Rate Mass Transfer Model

We have introduced the concenptual framework of this model in section 1.4.3. At the continuum-scale, we can model reactive transport within a double porosity medium as a system of coupled PDEs (labeled here as Model 5). Two equations are needed to describe the space-time evolution of each dissolved specie, i.e. one in the mobile and one in the immobile region. We adopt here the following mathematical formulation (*Bear and Cheng, 2010*):

$$\begin{aligned}
&\phi_m \frac{\partial \left\langle \hat{C}_{i_m} \right\rangle^m}{\partial \hat{t}} = -s_{m\to im} - \phi_m \langle \hat{v}_m \rangle \frac{\partial \left\langle \hat{C}_{i_m} \right\rangle^m}{\partial \hat{x}} + D_{Mob} \hat{D}_m \phi_m \frac{\partial^2 \left\langle \hat{C}_{i_m} \right\rangle^m}{\partial \hat{x}^2} - \hat{k} \left\langle \hat{C}_{A_m} \right\rangle^m \left\langle \hat{C}_{B_m} \right\rangle^m \quad \text{i=A}_m\text{,B}_m \\
&\phi_m \frac{\partial \left\langle \hat{C}_{C_m} \right\rangle^m}{\partial \hat{t}} = -s_{m\to im} - \phi_m \hat{v}_m \frac{\partial \left\langle \hat{C}_{C_m} \right\rangle^m}{\partial \hat{x}} + D_{Mob} \hat{D}_m \phi_m \frac{\partial^2 \left\langle \hat{C}_{C_m} \right\rangle^m}{\partial \hat{x}^2} + \hat{k} \left\langle \hat{C}_{A_m} \right\rangle^m \left\langle \hat{C}_{B_m} \right\rangle^m \\
&\frac{\partial \left\langle \hat{C}_{i_{im}} \right\rangle^{im}}{\partial \hat{t}} = s_{m\to im} - \hat{k} \left\langle \hat{C}_{A_{im}} \right\rangle^{im} \left\langle \hat{C}_{B_{im}} \right\rangle^{im} \quad \text{i=A}_{im}\text{,B}_{im} \\
&\frac{\partial \left\langle \hat{C}_{C_{im}} \right\rangle^{im}}{\partial \hat{t}} = s_{m\to im} - \hat{k} \left\langle \hat{C}_{A_{im}} \right\rangle^{im} \left\langle \hat{C}_{B_{im}} \right\rangle^{im}
\end{aligned} \tag{2.32}$$

where:

- The transport and the reaction for the species in the mobile phase are modeled as in the ADRE model, i.e. we assume that the reactants are well mixed within the rwo separated phases;
- In the low velocity region, advection and dispersion are assumed neglected;
- The two continua can exchange solutes and the mass transfer is modeled as a source term $s_{m\to im}$ which measures the amount of solute mass that moves from mobile region (*m*) to immobile (*im*) one;

- D_{Mob} is the ratio between the dispersion coefficient in the mobile region and the diffusion coefficient;
- ϕ_m represents the fraction of void volume in the porous medium associated to mobile phase, i.e. the mobile porosity;
- $\langle \hat{v}_m \rangle$ indentifies the average seepage velocity in the mobile region;
- $\left\langle \hat{C}_{i_m} \right\rangle^m$ and $\left\langle \hat{C}_{i_{im}} \right\rangle^{im}$ are the volume averaged solute concentrations in the mobile phase and in the immobile phase respectively.

The mass transfer process ($s_{m\to im}$) is commonly expressed as (*Bear and Cheng, 2010*):

$$s_{m\to im} = \phi_{im}\hat{Z}\left(\left\langle \hat{C}_{i_m} \right\rangle^m - \left\langle \hat{C}_{i_{im}} \right\rangle^{im}\right) \text{ i=A,B,C} \tag{2.33}$$

where ϕ_{im} represents the fraction of void volume in the porous medium associated to immobile regions. The parameter $\hat{Z}$ is the mass transfer rate and it quantifies the mass transfer velocity between the immobile and mobile phases. As $\hat{Z}$ increases, the system tends to behave a single-domain model where the porosity tends to ϕ and, on the other hand, when $\hat{Z}$ gets close to zero the system can be modeled as a single-domain model where the porosity is equal to ϕ_m (*Zheng and Wang, 1999*).

We define the dimensionless volume averaged seepage velocities in mobile ($\langle v_m \rangle$) and in immobile ($\langle v_{im} \rangle$) regions as:

$$\langle v_m \rangle = \frac{\langle \hat{v}_m \rangle}{\hat{U}} \tag{2.34}$$

$$\langle v_{im} \rangle = \frac{\langle \hat{v}_{im} \rangle}{\hat{U}} \tag{2.35}$$

where $\langle \hat{v}_{im} \rangle$ is the averaged dimensional seepage in the immobile water and it is has been assumed equal to zero.

We define the dimensionless characteristic fluid velocity ($\langle \hat{u} \rangle$) of the porous medium as:

$$\langle u \rangle = \frac{\langle v_m \rangle \phi_m + \langle v_{im} \rangle \phi_{im}}{\phi} = \frac{\langle v_m \rangle \phi_m}{\phi} \tag{2.36}$$

We will now reformulate the Eq.(2.32)-(2.33) using the dimensionless quantities of Eq. (1.4) and Eq. (2.36) and the conservative components E and D.

$$\begin{aligned}
&\frac{\partial \langle C_{i_m} \rangle^m}{\partial t} = -\beta_{IM} Z \left(\langle C_{i_m} \rangle^m - \langle C_{i_{im}} \rangle^{im} \right) - \langle u \rangle (\beta + 1) \frac{\partial \langle C_{i_m} \rangle^m}{\partial x} + \frac{D_{Mob}}{Pe} \frac{\partial^2 \langle C_{i_m} \rangle^m}{\partial x^2} \quad \text{i=E}_m,\text{D}_m \\
&\frac{\partial \langle C_{B_m} \rangle^m}{\partial t} = -\beta_{IM} Z \left(\langle C_{B_m} \rangle^m - \langle C_{B_{im}} \rangle^{im} \right) - \langle u \rangle (\beta + 1) \frac{\partial \langle C_{B_m} \rangle^m}{\partial x} + \frac{D_{Mob}}{Pe} \frac{\partial^2 \langle C_{B_m} \rangle^m}{\partial x^2} + \frac{Da}{Pe} \langle C_{B_m} \rangle^m \left(\langle \hat{C}_{B_m} \rangle^m - \langle \hat{C}_{D_m} \rangle^m \right) \\
&\frac{\partial \langle C_{i_{im}} \rangle^{im}}{\partial t} = \phi_{im} Z \left(\langle C_{i_m} \rangle^m - \langle C_{i_{im}} \rangle^{im} \right) \quad \text{i=E}_{im},\text{D}_{im} \\
&\frac{\partial \langle \hat{C}_{B_{im}} \rangle^{im}}{\partial \hat{t}} = \phi_{im} Z \left(\langle C_{B_m} \rangle^m - \langle C_{B_{im}} \rangle^{im} \right) - \frac{Da}{Pe} \langle C_{B_{im}} \rangle^{im} \left(\langle \hat{C}_{B_{im}} \rangle^{im} - \langle \hat{C}_{D_{im}} \rangle^{im} \right)
\end{aligned} \tag{2.37}$$

where β_{IM} is the ratio between the immobile porosity and mobile porosity while Z is the mass transfer $\hat{Z}$ multiplied to $\hat{t}_A$ in order to get an dimensionless mass transfer.

2.5 Model implementation

In this section we illustrate the numerical code used for models implementation. The PDEs systems are solved through the implementation of the PDEPE Matlab function. This member of the Matlab toolbox is suggested in Matlab User's Guide for solving flows in porous media and diffusive problems (Partial Differential Equation Toolbox™ User's Guide, 2013). The PDEPE function solves initial-boundary value systems of parabolic-elliptic PDEs in 1-D. The user is required to define the PDEs structure, the spatial mesh (*xmesh*) and the times (*tspan*) at which he/she is interested to the solution of the problem. The PDEPE Matlab function operates a discretization in space of the PDEs to obtain Ordinary Differential Equations (ODEs). The resulting ODEs are then integrated to obtain the solution at the *tspan* required by the user. The time integration is done by the ode15s Matlab function. Notice that the

ode15s does not integrate the solution on the time steps required by the user but it adapts the time step and the formula automatically for the integration. The code ode15s is a quasi-constant step size implementation of the Numerical Differentiation Formulas (NDFs). This family of numerical methods is a modification of Backward Differentiation Formulas (BDFs), (*van Schijndel et al, 2000*). The BDFs are implicit and linear multi-steps methods: they approximate the derivative of the solution at time-step *h* using the information computed at the time-step *h* itself and at *n* previous time-steps.

Before implementing this code for solving the models, we verified the suitability of the code to the simulation of transport codes. In particular, we compared the solution given by the PDEPE function against analytical solutions of:

- *Ogata and Banks (1961)* in section 2.5.1;
- *Huang et al.(2000)* analytical solution for double porosity model in section 2.5.2.

The results showed in the next paragraphs confirmed the suitability of this tool for the problems of transport in porous media.

2.5.1 Ogata and Banks (1961)

Ogata and Banks proposed the analytical solution in 1961 for the Advection-Diffusion Equation (ADE) with the following assumptions (*Ogata and Banks, 1961*):

- the porous medium is homogeneous and isotropic and no mass transfer takes place between the liquid phase and the solid phase;
- the porous medium is fully saturated;
- the flow is considered unidirectional and the velocity is constant along the flow field;
- the solute is conservative.

Then the problem is formulated as:

$$\frac{dC}{dt} = D\frac{\partial^2 C}{\partial x^2} - v\frac{\partial C}{\partial x} \tag{2.38}$$

The following boundaries and initial conditions are associated to Eq. (2.38):

$$\begin{aligned} &C(0,t) = C_0 \quad \forall t \geq 0 \\ &C(x,0) = 0 \quad \forall x \geq 0 \\ &\frac{\partial C(+\infty,t)}{\partial x} = 0 \quad \forall t \geq 0 \\ &\frac{\partial C(-\infty,t)}{\partial x} = 0 \quad \forall t \geq 0 \end{aligned} \tag{2.39}$$

where D [m^2/s] is the dispersion coefficient, $C(t,x)$ [mol/m^3] is the solute concentration in the fluid, v [m/s] is the average fluid velocity while x [m] and t [s] are the spatial and temporal coordinates.

The analytical solution proposed by the authors is:

$$\frac{C(x,t)}{C_0} = \frac{1}{2}\left\{ erfc\left(\frac{x-vt}{\sqrt{4Dt}}\right) + \exp\left(\frac{vx}{D}\right) erfc\left(\frac{x+vt}{\sqrt{4Dt}}\right)\right\} \tag{2.40}$$

We implement the problem Eq. (2.38)-(2.39) with the PDEPE Matlab function for different values of *D* and different *x* step lengths (Δx) while v is constant and equal to 0.6 m/s. Table 2.5 reports the combinations of *D* and *x* step lengths investigated.

Table 2.5. Combination of D and x step lengths analyzed in the comparison between the Ogata-Banks analytical solution and PDEPE Matlab function solution.

D=2×10^{-2} cm^2/s; Δx =0.01 cm;	D=5×10^{-2} cm^2/s; Δx =0.01 cm;	D=10×10^{-2} cm^2/s; Δx =0.01 cm;
D=2×10^{-2} cm^2/s; Δx =0.05 cm;	D=5×10^{-2} cm^2/s; Δx =0.05 cm;	D=10×10^{-2} cm^2/s; Δx =0.05 cm;
D=2×10^{-2} cm^2/s ; Δx =0.1 cm;	D=5×10^{-2} cm^2/s; Δx =0.1 cm;	D=10×10^{-2} cm^2/s; Δx =0.1 cm;

We computed the error (*err*) between the Ogata-Banks analytical solution ($C_{ANALYTICAL}$) and the PDEPE solution (C_{PDEPE}) at *t=5* s using:

$$err = \Delta x \sum_{j=1}^{nx} \left(C_{jPDEPE} - C_{jANALYTICAL} \right)^2 \tag{2.41}$$

where Δx is the x step length; nx is the number of x-steps in the domain; $C_{jANALYTICAL}$ .and C_{jPDEPE} are the concentration solute value computed at *j-th* x step for Ogate-Banks solution and PDEPE solution respectively.

Figure 2.7 shows the error trend as function of Δx and D. We can observe the PDEPE solution converges to the analytical solution with the Δx decrement with almost quadratic convergence. For $\Delta x = 0.01$ cm the error is very small and can be considered a digital error.

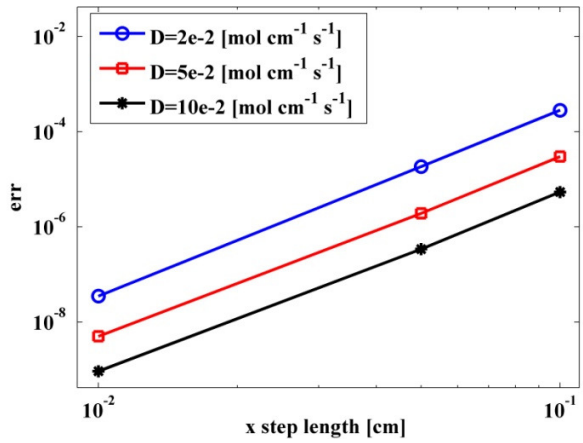

Figure 2.7. Error trends as function of D and x step-length.

2.5.2 Ciriello et al (2013)

Ciriello et al. (2013) implemented the analytical solution for the dual porosity model proposed by *Huang et al.(2000)* in which a conservative solute undergoes to advection and dispersion process. A 1D computational domain is considered where a conservative solute is injected from the left boundary as depicted in Figure 2.8. The mathematical description of the problem is the following one:

$$\begin{aligned} f\frac{\partial C(x,t)}{\partial t} + (1-f)\frac{\partial C^*(x,t)}{\partial t} &= D'\frac{\partial^2 C(x,t)}{\partial x^2} - q\frac{\partial C(x,t)}{\partial x} \\ (1-f)\frac{\partial C^*(x,t)}{\partial t} &= K\left[C(x,t) - C^*(x,t)\right] \end{aligned} \tag{2.42}$$

Here we adopted the symbols used in *Ciriello et al.(2013)*:

- K [1/s] is the rate mass transfer between the mobile and immobile phases;
- f is the fraction of mobile pore space in the porous medium;

- C [mol/m^3] and C^* [mol/ m^3] are the mobile and immobile concentrations respectively;
- D' [m^2/s] is the longitudinal dispersion;
- t [s] and x [m] are the temporal and space coordinates;
- q [m/s] is the Darcy velocity.

The following boundaries and initial conditions are associated with Eq. (2.42):

$$\begin{aligned} &C(x,0)=0 \qquad \forall x>0 \\ &C(0,t)=C_0 \qquad \forall t\geq 0 \\ &\left.\frac{\partial C(x,t)}{\partial x}\right|_L=0 \quad \forall t\geq 0 \\ &C^*(x,0)=0 \qquad \forall x\geq 0 \\ &\left.\frac{\partial C^*(x,t)}{\partial x}\right|_L=0 \quad \forall t\geq 0 \end{aligned} \tag{2.43}$$

where L is the domain length and it is supposed to be long enough in order to avoid that the right boundary condition affects the evolution of concentration in space.

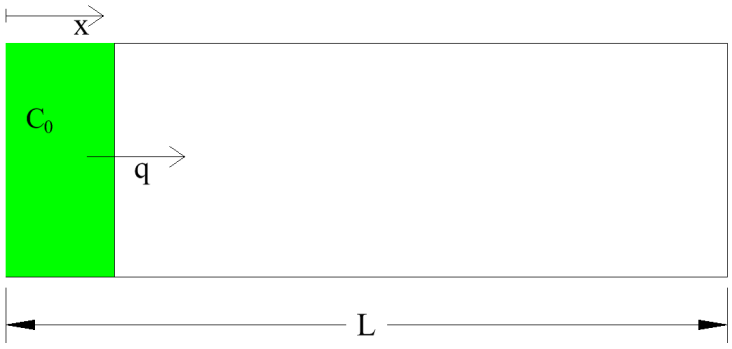

Figure 2.8. Double porosity problem scheme.

To obtain the analytical solution, Equations (2.42)-(2.43) are transformed into Laplace space:

$$\begin{aligned} &D'\frac{d^2\tilde{c}(x,u)}{dx^2}-q\frac{d\tilde{c}(x,u)}{dx}-\xi\tilde{c}(x,u)=0 \\ &\tilde{c}^*(x,u)=\frac{K\tilde{c}(x,u)}{(1-f)u+K} \end{aligned} \tag{2.44}$$

Equation (2.44) is completed by the following boundary conditions:

$$\begin{aligned} \tilde{c}(0,u) &= \frac{c_0}{u} \\ \tilde{c}^*(0,u) &= \frac{c^*_0}{u} \\ \tilde{c}'(L,u) &= \tilde{c}^{*\prime}(L,u) = 0 \end{aligned} \tag{2.45}$$

where $\tilde{c}$ and $\tilde{c}^*$ are the transformed variables of c and c^* respectively; u is the Laplace parameter and $\xi = u\frac{f(1-f)u+K}{(1-f)u+K}$.

The analytical solution of Eq. (2.44) is:

$$\begin{aligned} \tilde{c}(x,u) &= k_1 e^{\lambda_+ x} + k_2 e^{\lambda_- x} \\ \tilde{c}^*(x,u) &= \frac{K(k_1 e^{\lambda_+ x} + k_2 e^{\lambda_- x})}{(1-f)u+K} \end{aligned} \tag{2.46}$$

where:

- $\lambda_\pm = \frac{q}{2D'} \pm \sqrt{\frac{q^2}{4D'^2} + \frac{\xi}{D'}}$;
- $k_1 = -\frac{c_0 UR}{u(1-UR)}$ and $k_2 = -\frac{c_0}{u(1-UR)}$ in which $R = \frac{e^{\lambda_- L}}{e^{\lambda_+ L}}$ and $U = \frac{\lambda_-}{\lambda_+}$.

The analytical solution in the Laplace space is then numerically inverted using the algorithm of *Stehfest (1970)*.

We implement the Eq. (2.42)-(2.43) with the PDEPE Matlab function for different values of K and different x step lengths (Δx) while the others parameters are constant and representative of a real laboratory scale setting . Table 2.6 reports the combinations of K and x step lengths investigated while Table 2.7 indicates the constant values of the others considered parameters.

Table 2.6. Values of K and *x* step lengths analyzed in the comparison between the Ciriello et al. (2013) analytical solution and PDEPE Matlab function solution.

K=1×10^{-5} 1/s; Δx =0.001 m	K=5×10^{-5} 1/s; Δx =0.001 m;	K=2×10^{-6} 1/s Δx =0.001 m;
K=1×10^{-5}1/s; Δx =0.0005 m;	K=5×10^{-5} 1/s; Δx =0.0005 m;	K=2×10^{-6} 1/s; Δx =0.0005 m;
K=1×10^{-5} 1/s; Δx =0.00001 m;	K=5×10^{-5} 1/s; Δx =0.00001 m;	K=2×10^{-6} 1/s; Δx =0.00001 m;
K=1×10^{-5}1/s; Δx =0.00005 m;	K=5×10^{-5} 1/s; Δx =0.00005 m;	K=2×10^{-6} 1/s; Δx =0.00005 m;

Table 2.7. Ciriello et al. (2013) model parameters.

Parameters	Value
D'	6.31×10^{-8}m^2/s
q	4.356×10^{-5}m/s
f	0.36

We compute the error (err) between the analytical solution ($C_{ANALYTICAL}$)and the PDEPE solution (C_{PDEPE}) at *t=40 s* using (2.41) where Δx is the *x* step length; nx is the number of x-step in the domain; $C_{jANALYTICAL}$.and C_{jPDEPE} are the concentration solute value computed at *j-th x* step for analytical solution and PDEPE solution respectively. Figure 2.9 and Figure 2.10 show the error trends as function of Δx and K for the mobile and the immobile phase respectively. We can observe the PDEPE solution converges to the analytical solution with the Δx decrement. For $\Delta x = 0.01$ cm the error attains negligible values. In Figure 2.9, we observe that the rate of convergence to the analitycal solution decreases for small Δx. This can be explained considering that the analytical solution to which we are referring, is actually obtained through Laplace solution numerical inversion.

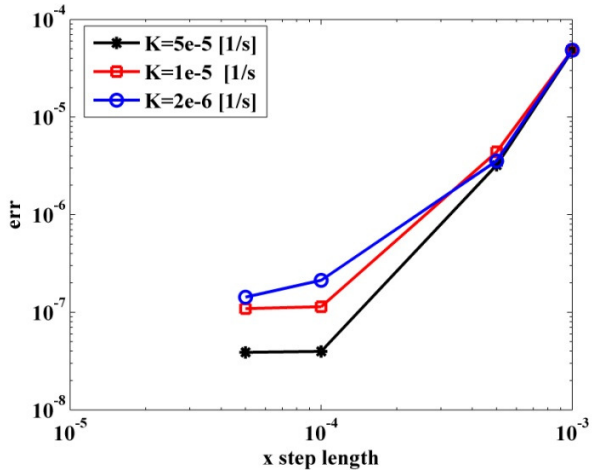

Figure 2.9. Error trends as function of K and x step-length for the mobile solute concentration.

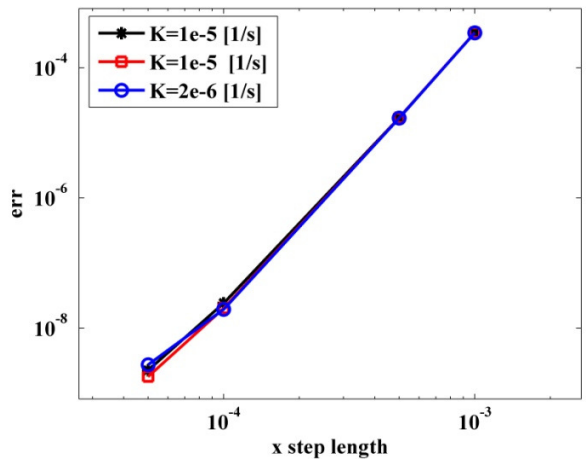

Figure 2.10. Error trends as function of K and x step-length for the immobile solute concentration.

2.6 Summary of methodologies

All the elements presented in this chapter are necessary to obtain the desired results proposed in section 1.5. A scheme of the thesis methodological procedure is outlined in Figure 2.11.

First model mathematical and conceptual formulations are defined (in Figure 2.11 n=1,2,3,4,5). The models are then contextualized to the specific benchmark problem introducing some boundary and initial conditions inferred from the problem setting chosen. The models are then implemented and numerically solved using a Matlab tool (PDEPE function). The solution depends on the value assigned to the parameters (in Figure 2.11 generically identified by the symbol "p") included in the model formulation. Two different approaches are used to define the values of the parameters depending on the porous medium scenario analyzed:

- Porous medium scenario 1: the parameters values of Model 1 and Model 2 have already been computed by *Porta et al. (2013)* for this specific porous scenario. As a consequence, we solve Model 1 and Model 2 as function of the values suggested by *Porta et al. (2013).*
- Porous medium scenario 2: in this case different combinations of the parameters for each model have been proposed and each model is solved as many times as the number of parameter values combinations.

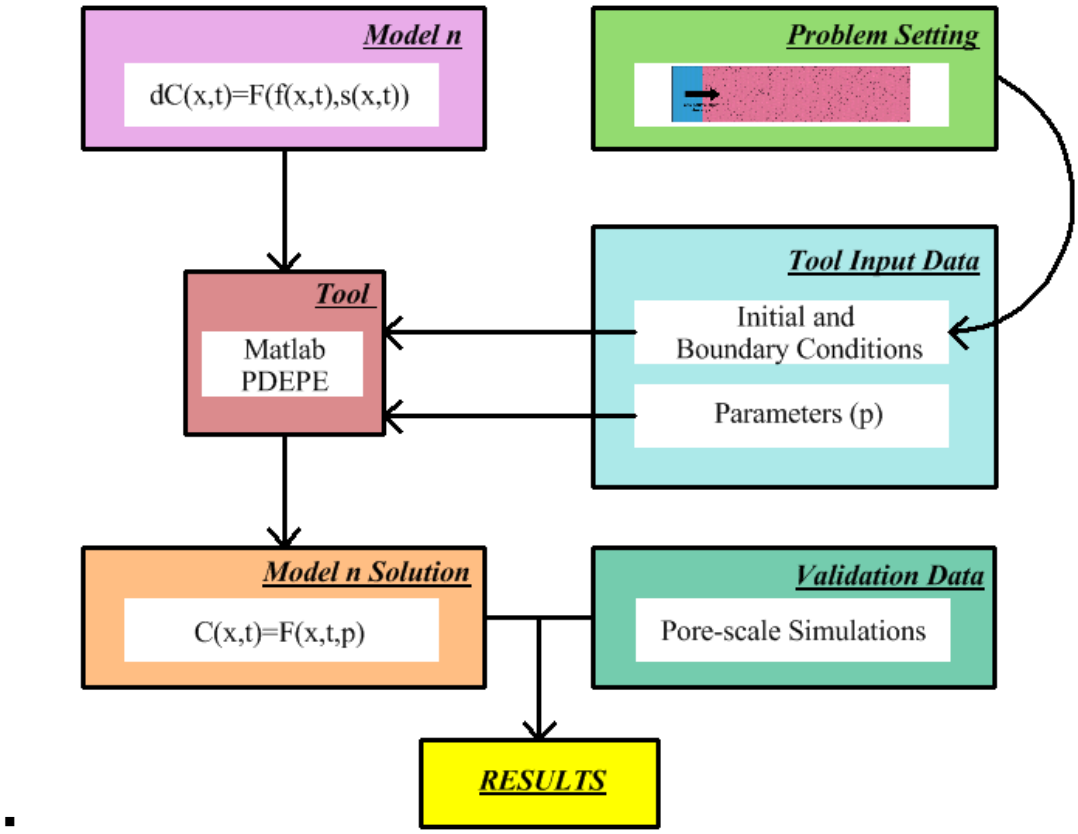

Figure 2.11 Outline of the methodological procedure.

2.6.1 Definition of pore-scale quantities for model assessment

As previously stated, the pore-scale simulations are run on a bidimensional domain indicated in Figure 2.1 and recalled in Figure 2.12. The geometrical dimensions of the domain are indicated in Figure 2.12 with the labels *H* (along the *y* coordinated) and *L* (along the *x* coordinate corresponding to the direction of the averaged fluid velocity).

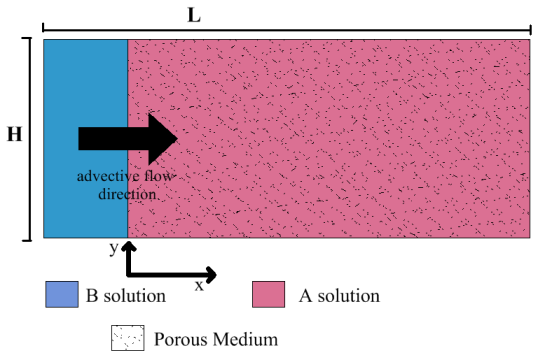

Figure 2.12 Outline of the problem setting and geometrical dimensions.

We assess the different model numerical solutions using the following quantities computed on pore-scale data:

- Concentration profiles (C_A, C_B, C_C): section averaged concentration distributions along x direction direction recorded at time $\tilde{t}$ computed as:

$$C_i(x,\tilde{t}) = \int_H c_i(x,y,\tilde{t})dy \quad i = A,B,C \tag{2.47}$$

  where H indicates the dimension of the 2D-domain along the y direction considered in pore-scale simulations;

- Global product (G_C): time-evolution of the integrated product concentration within the entire domain computed as:

$$G_C(t) = \int_L C_C(x,t)dx \tag{2.48}$$

  where L is the domain dimension alng the x direction;

- Global rate (R_C): time-evolution of the reaction rate integrated within the entire domain computed as:

$$R_C(t) = \frac{dG_C(t)}{dt} \tag{2.49}$$

- Peak product concentration ($C_{C\max}$): evolution maximum value of product concentration registered as function of time:

$$C_{\max}(t) = \max[C_C(t,x)] \tag{2.50}$$

  To smooth local oscillations of the concentration profile product concentration peak is computed by averaging 41 data centered around the maximum value.

2.6.2 Criteria for models assessment

The models assessment and comparison, on the basis of the quantities introduced in section 2.6.1, is done computing four different functions, which quantify the difference between continuum and pore-scale model results. We label those functions as "objective functions" in the following, as they are proposed as candidate objective function for reactive transport model calibration. The first objective function we consider (f_1) computes the means squared error yielded by continuum model concentration profile predictions with respect to pore-scale data:

$$f_{1i\_k}(t_j) = \frac{\sum_{n=1}^{N}\left[C_{ni\_k}(t) - C_{ni\_PS}(t)\right]^2}{N} \quad i = A, B, C \quad k = 1,2,3,4,5 \tag{2.51}$$

where $f_{1i\_k}(t)$ is the first objective function computed for the chemical species i profiles given by the Model k at time t; $C_{ni\_k}(t)$ is the concentration predicted by Model k for the chemical i at time t; $C_{ni\_PS}(t)$ is the concentration derived by pore-scale averaged data of the species i; N is the number of data considered. Eventually, the function f_1 definition is applied to global product (G_C) in the following form:

$$f_{1GC\_k} = \frac{\sum_{n=1}^{N}\left(G_{Cn\_k} - G_{Cn\_PS}\right)^2}{N} \tag{2.52}$$

where f_{1GC_k} is the first objective function computed for the global product given by the Model k at time; G_{Cn_k} is the global product given by the Model k; G_{Cn_PS} is the global product given by pore-scale data;

The second objective function (f_2) considered in this analysis is:

$$f_{2i\_k}(t) = \frac{\sum_{n=1}^{N}\left[\log(C_{ni\_k}(t)) - \log(C_{ni\_PS}(t))\right]^2}{N} \quad i = A, B, C \quad k = 1,2,3,4,5 \tag{2.53}$$

which is computed for the chemical species i profiles yielded by the Model k at time t. Eq. (2.53) is similar to Eq. (2.51) but, instead of linear concentrations, the mean squared error is computed on the logarithmic values of concentrations.

Then, we introduce a third objective function (f_3) which relies on the definition of the survival function (SF):

$$\begin{aligned} SF_i(t) &= 1 - C_{i\_k}(t) \quad i = A, B \text{ and } k = 1,2,3,4,5 \\ SF_{C\_k}(t) &= 0.5 - C_{C\_k}(t) \quad k = 1,2,3,4,5 \end{aligned} \tag{2.54}$$

where $SF_{i\_k}(t)$ indicates the survival function computed for the chemical species i profile predicted by Model k at time t and $C_{i\_k}(t)$ is the concentration profile of chemical i at time t predicted by the Model k at time t. Similarly, we can define the survival function computed on pore-scale cross sectional averaged concentrations:

$$\begin{aligned} SF_{B\_PS}(t) &= 1 - C_{i\_PS}(t) \quad i = A, B \\ SF_{C\_PS}(t) &= 0.5 - C_{C\_PS}(t) \end{aligned} \tag{2.55}$$

where $SF_{i\_PS}(t)$ indicates the survival function computed for the chemical i on pore-scale cross sectional averaged concentrations at time t and $C_{i\_PS}(t)$ is the pore-scale cross-sectional averaged concentration of chemical i at time t. The third objective function f_3 is defined including Eq. (2.55)-(2.54):

$$f_{3i\_k}(t) = \frac{\sum_{n=1}^{n} \left[\log(SF_{in\_k}(t)) - \log(SF_{in\_PS}(t)) \right]^2}{N} \quad i = A, B, C \quad k = 1,2,3,4,5 \tag{2.56}$$

where $f_{3i\_k}(t)$ is computed for the chemical species i profiles predicted by the Model k at time t.

Finally the fourth objective function is the sum of f_{2i_k} and f_{3i_k}:

$$f_{4i\_k}(t) = f_{2i\_k}(t) + f_{3i\_k}(t) \quad i = A, B, C \text{ and } k = 1,2,3,4,5 \tag{2.57}$$

Chapter 3 RESULTS 1: POROUS MEDIUM SCENARIO 1

We analyze here the pore-scale setting (see section 2.2) investigated in *Porta et al. (2013)*. The main findings of their analysis, are briefly recalled below, as they are useful for our successive results elaboration and discussion. Then, we compare the results obtained by implementation of Model 1 and Model 2 with those yielded by pore scale simulations

3.1 Summary of results by Porta et al. (2013)

Using the detailed numerical simulations performed on this porous medium scenario, the authors explored three main aspects: i) the evolving dynamics of reactive process in this porous medium; ii) the time evolution of D and B appearing in Model 2 formulation; iii) the reliability of Model 2 reaction term (Eq. (2.14)) in describing the reaction observed in pore-scale simulations.

The evolution in time of global quantities (global product and global reaction rate) shows that at early times the reaction process depends on Da value while for later times it is governed by Pe number becoming independent of reaction constant. In Figure 3.1, the time evolutions of global quantities is compared to expected evolutions in asymptotic regime which have been determinated in *Porta et al. (2012b)*:

- global product asymptotically evolves proportional to the to the square root of time ($G_C \propto \sqrt{t}$);
- global reaction rate is asymptotically inversely proportional to the square root of time ($R_C \propto \frac{1}{\sqrt{t}}$).

Through this comparison, *Porta et al. (2013)* showed that the system tends to the asymptotic behavior more or less quickly depending on the Da number (Figure 3.1).

Even as incomplete mixing process does not strongly affect global quantities, it has a key influence on the local fluctuations of reactants concentrations and on the shape of the mixing zone. *Porta et al. (2013)* showed that Da critically impacts the local reactant mixing degree and in particolar demonstrated that the incomplete mixing at the pore scale is proportional to both *Pe* and *Da* numbers.

In practice this means that the most interesting and challenging reactive transport setting for continuum scale models corresponds to combinations of high *Pe* and *Da* numbers.

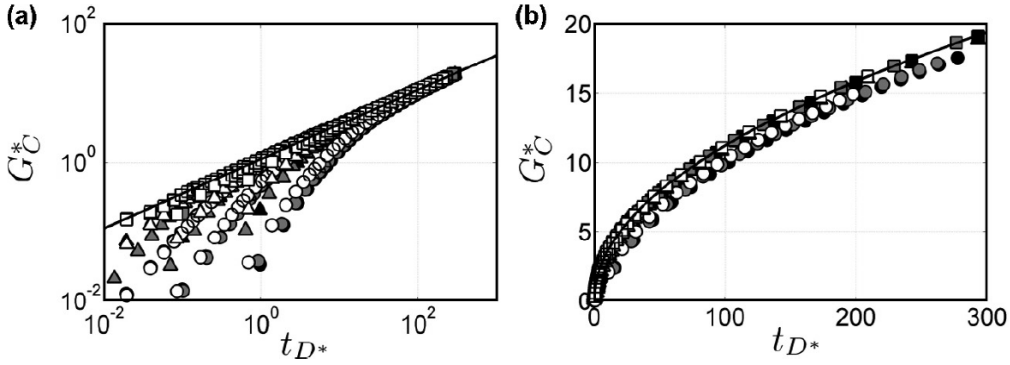

Figure 3.1 Global product (G^*_C) versus t_{D*} ($t_{D*} = \hat{t}\hat{D}/\hat{w}^2$) in logarithmic (a) and linear (b) scales. Numerical results are for *Da* =8.2 (○), 64.8 (□), 1038 (Δ). Black, grey and empty symbols are associated with =0.25, 0.36 and 0.5, respectively. the solid line corresponds to asymptotic behavior (Porta et al., 2013).

Porta et al. (2013) computed the time-evolution of *D* (Figure 3.2a) and *B* (Figure 3.2b) using pore-scale data showing that both the parameters increase with time and rapidly reach an asymptotic value. This suggests that non-local effects are negligible in this specific porous medium.

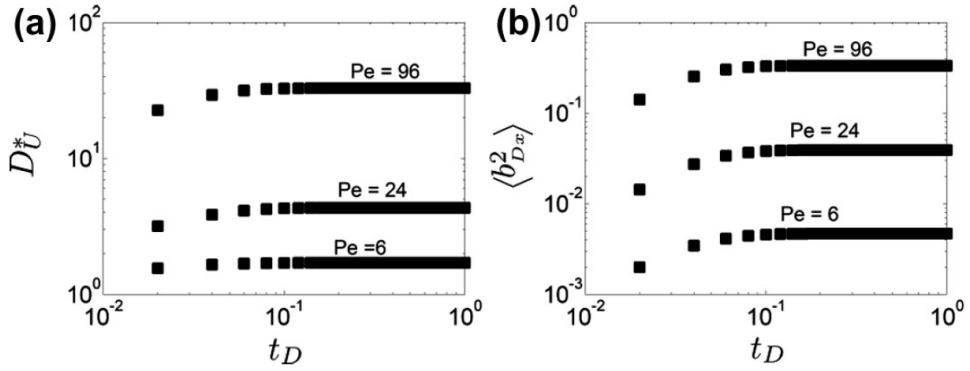

Figure 3.2 Evolution of the (a) longitudinal dispersion coefficient D_U*and (b) b^2_D with t_D for φ=0.25 (Porta et al., 2013). Here b_{2Dx} is the square value of the closure variable along the *x*-axis and corresponds to *B*.

Finally, *Porta et al. (2013)* demonstrated the appropriateness of the reaction rate term proposed in their model in capturing local and global features of reactive transport nevertheless nonlocal effects are neglected (see Eq.(2.18)). As explained in section 2.3.2, *Porta et al. (2013)* reaction term can be broken into two different parts: r_1 and r_{2U} (see Eq.(2.15) and Eq. (2.16)). The term r_{2U} can be computed by resolving a pore-scale closure problem, which is derived through Volume Averaging of pore scale

equations. This yields an approximation of the averaged reactant cross-covariance appearing in up-scaled reaction term:

$$r_2 = \frac{Da}{Pe}\left\langle \tilde{c}_A \tilde{c}_B \right\rangle^I \tag{3.1}$$

Porta et al. (2013) compared r_{2U} to r_2 computed on pore-scale data. Figure 3.3 shows that r_{2U} (Figure 3.3b) captures the salient features of r_2 (Figure 3.3a) local distribution. Hence *Porta et al. (2013)* showed that the global reaction rates obtained integrating r_1 and r_{2U} within the all domain well-approximated the ones computed through pore-scale data.

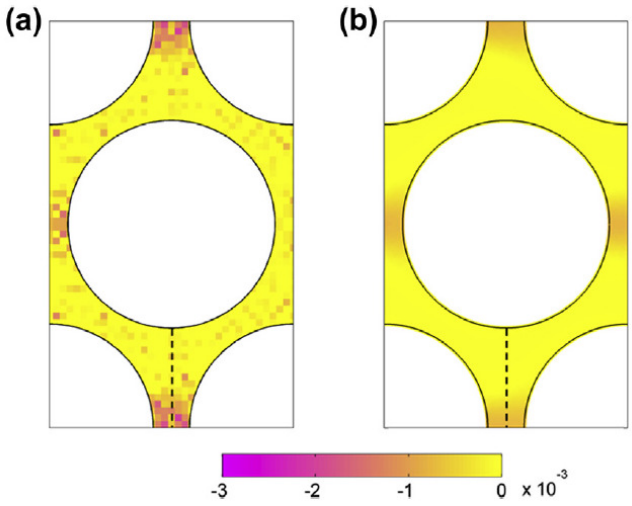

Figure 3.3 Spatial distribution of a) r_2 and b) its approximation r_{2U} in a unit cell at reaction front (Porta et al. 2013).

3.2 Qualitative Model 1 and Model 2 comparison

In this chapter we provide an advancement of the work presented in *Porta et al. (2013)* by providing the direct solutions of *Porta et al. (2012a)* model and Model 1 at the continuum-scale and comparing the results with those yielded by pore-scale simulations. Among the numerical simulations presented in *Porta et al. (2013)*, we focus here only on the one characterized by largest Pe=96 and Da=1038, i.e. the combination of maximum Pe and Da numbers. Indeed, as stated above, in this conditions, reactants exhibit an higher degree of incomplete mixing. As a consequence, this combination of parameters, among those considered in *Porta et al.* (2013), poses the greatest challenges to continuum models. The characteristics of the simulation considered in the following are reported in Table 3.1.

Since the analysis of *Porta et al. (2013)* demonstrated that dispersion and reaction convolutions have a limited impact in this specific problem setting, we solve the approximation of *Porta et al. (2012a)* model proposed in section 2.3.2 using the asymptotic values of dispersion (D) and B computed by *Porta et al. (2013)* and reported in Table 3.2.

Table 3.1 Numerical pore-scale simulation conditions in porous medium scenario 1.

Pe	96
Da	1038
ϕ	0.36
$\hat{D}_m$	2.0000e-9 [m^2/s]
$\hat{w}$	7.2000e-004 [m]
$\langle \hat{u} \rangle^l$	2.6667e-004 [m/s]
$\hat{k}$	4.0046 [m^3/(mol s)]

Table 3.2 Values of D and B computed by Porta et al. (2013) for porous medium scenario 1.

D^*	45.591
B	0.399

Model 2 predictions are then compared to pore-scale cross sectional data in order to assess the validity of the Volume Averaged formulation. We compare the results of Model 2 to those of Model 1 (i.e., the ADRE) solution in order to investigate the importance of incomplete mixing term on the modeling of process at continuum scale. The comparison between Model 1, Model 2 and pore-scale data is presented in term of the quantities introduced in section 2.6: global mass of the reaction product (G_C)indicated in Eq. (2.48), chemical concentration profiles (C_A, C_B, C_C) definted in Eq. (2.47); time-evolution of product peak concentration ($C_{\max}$) according to Eq.(2.50) and the global reaction rate (R_C) computed as reported in Eq. (2.49).

3.3 Qualitative analysis of Models results against pore-scale simulations

We move from the analysis of global quantities such as global product and global reaction rate, as defined in Eq. (2.48)-(2.49). As shown in Figure 3.4**,** Model 1 and Model 2 predictions of G_C are almost indistinguishable for $t > 10^0$ and tend to diverge when t approaches to zero. Even as Model 1 and Model 2 global products present different behaviors for short times, we cannot discriminate which one of the two solutions better interprets the pore-scale data since these are available only for dimensionless times larger than 1. Model 1 global product is consistently bigger than Model 2 global product for short times. For $t > 10^0$, Model 1 and Model 2 both well predict the pore-scale global product. Similar considerations can be drawn from Figure 3.5 where global reaction rate R_C is depicted. Model 1 global reaction rate starts to increase earlier and reaches an higher peak compared to Model 2 global reaction rate. For $t > 10^0$, both the Models recover the asymptotic behavior $R_C \propto \frac{1}{\sqrt{t}}$ and well reproduce the results yielded by pore-scale simulation.

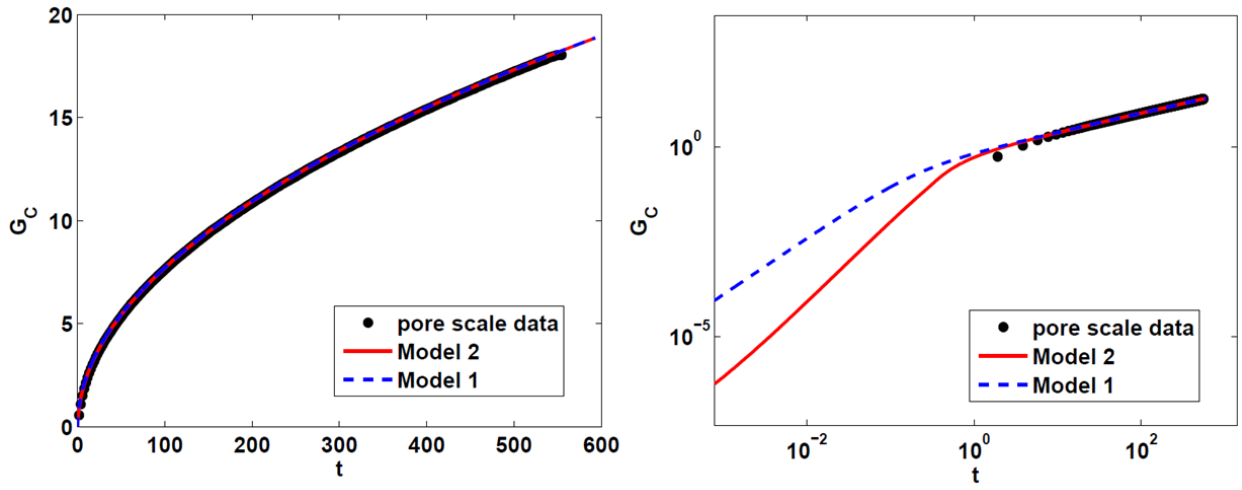

Figure 3.4 Model 1 and Model 2 global product predictions compared to pore-scale sectional averaged data. The graph on the right is equivalent to the one on the left but axes are expressed in logarithmic scale in order to give relevance to short times global product behavior.

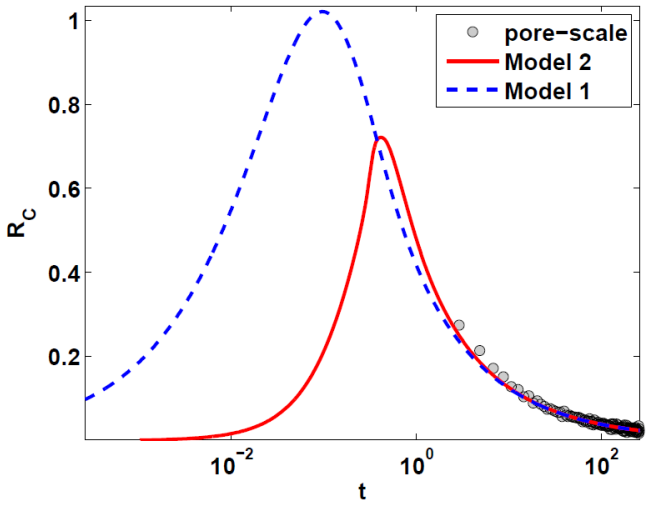

Figure 3.5 Model 1 and Model 2 global reaction rate compared to pore-scale sectional averaged data.

In Figure 3.6 we depict the Model 2 global reaction rate decomposed in:

$$R1_C = \int_L r_1 dx = \int_L -\frac{Da}{Pe}\langle C_B \rangle^l \left(\langle C_B \rangle^l - \langle C_D \rangle^l \right) dx \tag{3.2}$$

$$R2_C = \int_L |r_{2U}| dx = \int_L \left| M(M-1) B \frac{\partial^2 \langle C_D \rangle^l}{\partial x^2} \right| dx \tag{3.3}$$

The difference between $R1_C$ and $R2_C$ leads to Model 2 global reaction rate already plotted in Figure 3.5. Even as the mathematical formulations of Model 1 reaction term and r_1 are equivalent, they lead to different global reaction rates time-evolutions since reactants concentrations rendered by two models are different. As we can see in Figure 3.6, when $R2_C > R1_C$, Model 2 global reaction rate is zero otherwise it is equivalent to $R1_C - R2_C$. For $t \to 0$, $R2_C$ tends to infinite since it is proportional to $\left(\frac{\partial C_D}{\partial x} \right)^2$ which is infinite at $t = 0$ according to the initial conditions of the problem at hand.

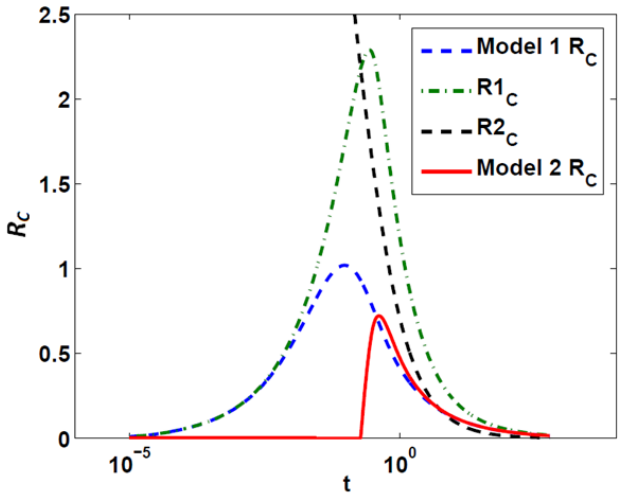

Figure 3.6 Model 1 compared to Model 2 global reaction rates time-evolutions. For the latter the contribute of *R1* and *R2* are depicted.

The detailed pore-scale numerical simulations allow to test Model 1 and Model 2 predictions against cross section-averaged concentration profiles, computed through Eq.(2.47). In Figure 3.7-Figure 3.10, we present reactant concentration profiles at four different times ($t = 1.93; 9.63; 57.77; 481.40$). For each time we report a zoomed image of reactant mixing zone (i.e., where the two reactants coexist). The following Figure 3.7-Figure 3.10 display the concentration profiles in a coordinate system integral to the advective front (x_{AD}) defined as:

$$x_{AD} = x - \frac{\langle \hat{u} \rangle^{l} \hat{t}}{\hat{w}} \tag{3.4}$$

According to (3.4), the origin of *x*-axis identifies the position of the advective front in dimensionless coordinates.

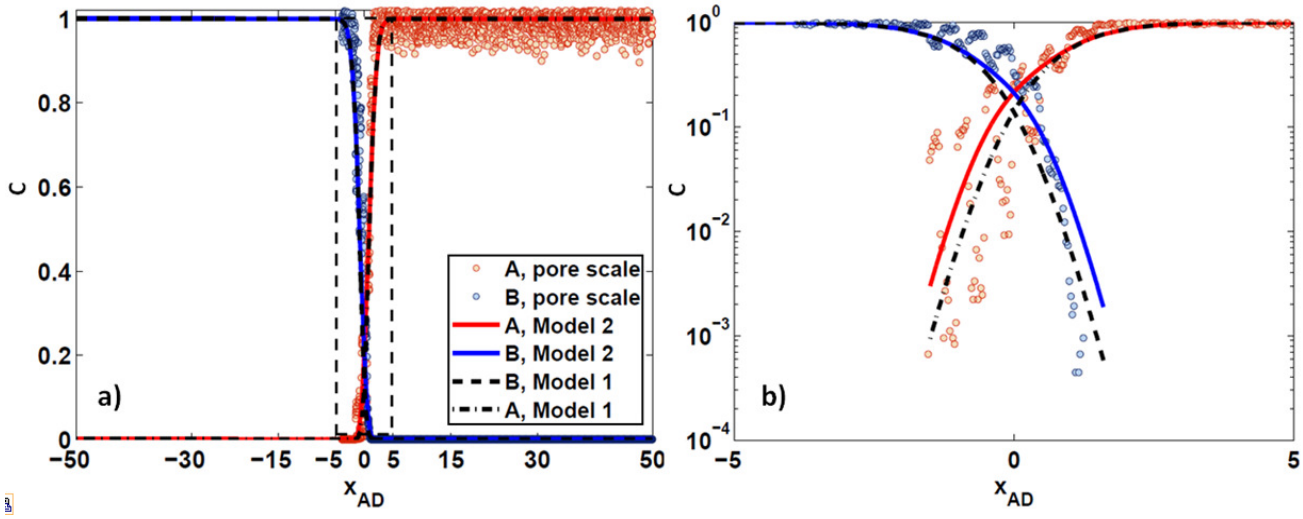

Figure 3.7 a) Reactant concentration profiles given by Model 1 and Model 2 at t=1.93 comapred to pore-scale cross sectional averaged data. b) A zoomed image of reactant mixing front delimited by dashed black line in figure a).

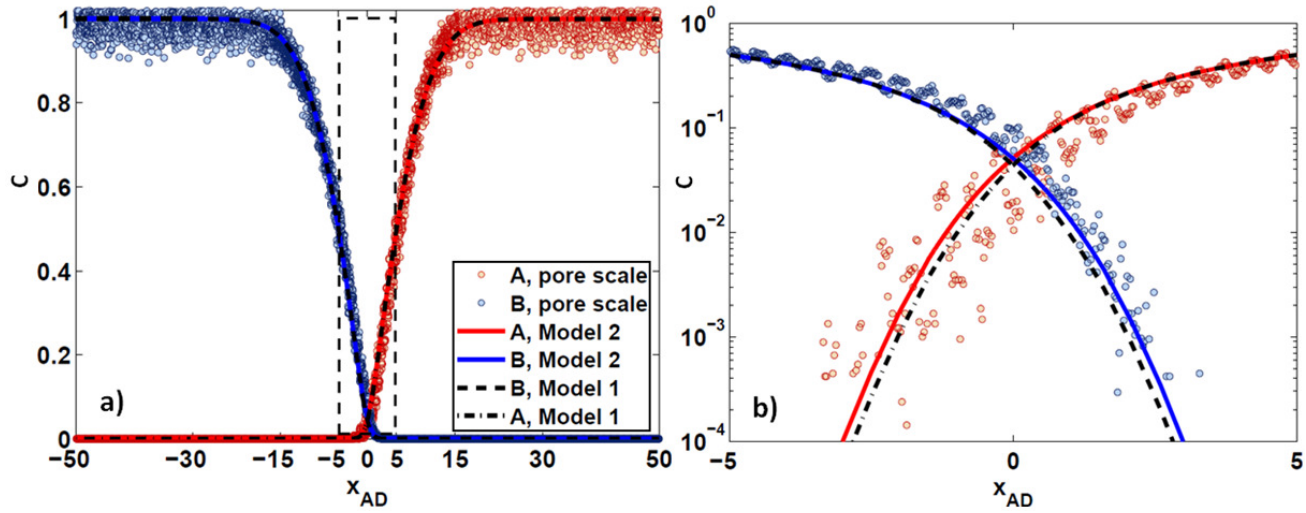

Figure 3.8 a) Reactant concentration profiles given by Model 1 and Model 2 at t=9.63 comapred to pore-scale cross sectional averaged data. b) A zoomed image of reactant mixing front delimited by dashed black line in figure a).

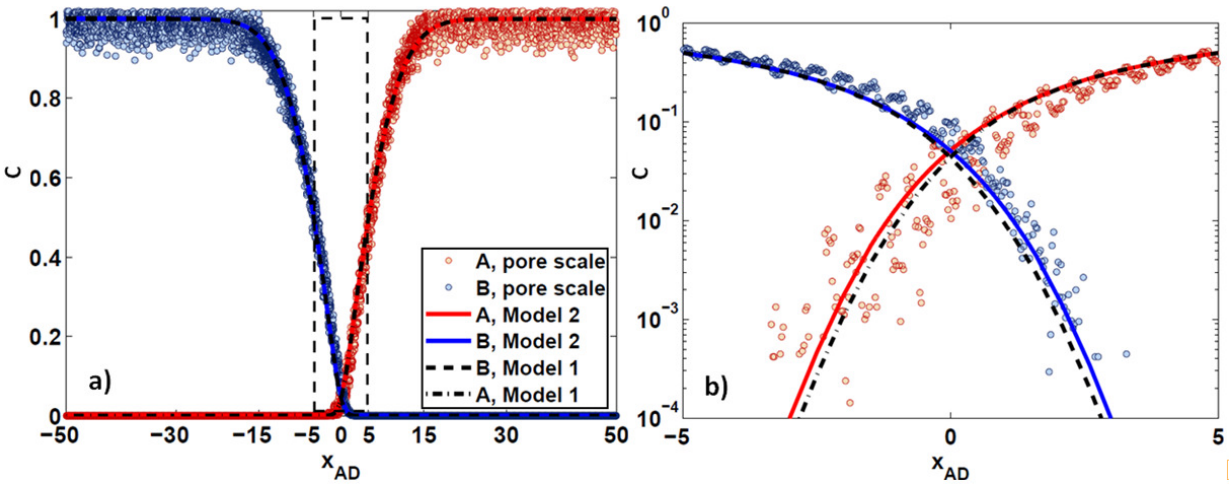

Figure 3.9 a) Reactant concentration profiles given by Model 1 and Model 2 at t=57.77 comapred to pore-scale cross sectional averaged data. b) A zoomed image of reactant mixing front delimited by dashed black line in figure a).

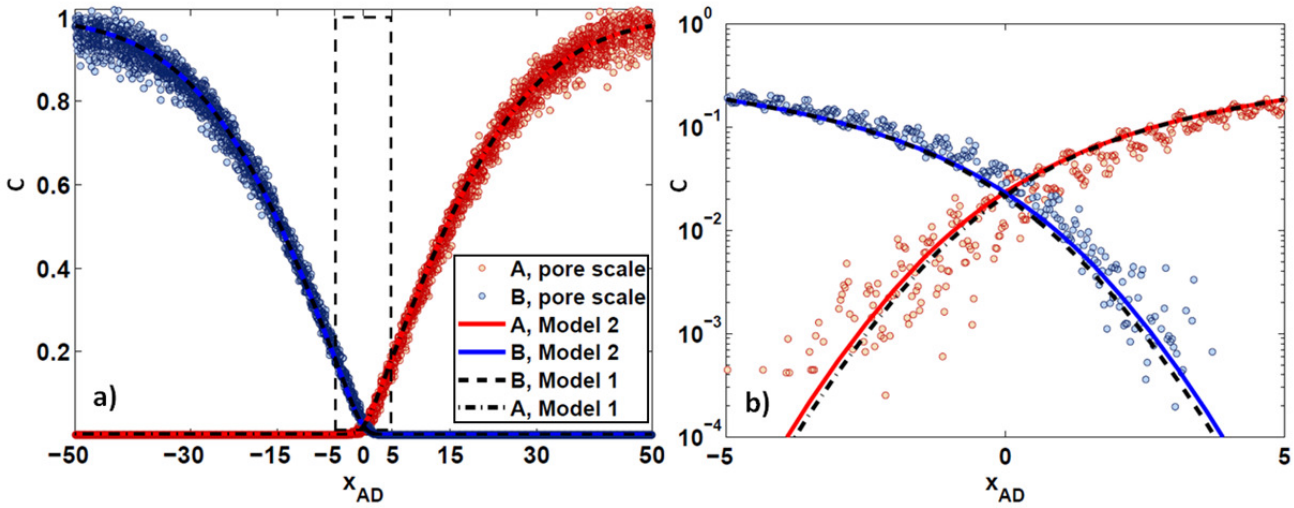

Figure 3.10 a) Reactant concentration profiles given by Model 1 and Model 2 at t=481.40 comapred to pore-scale cross sectional averaged data. b) A zoomed image of reactant mixing front delimited by dashed black line in figure a).

The linear profiles depicted in Figure 3.7a-Figure 3.10a at different times show that outside the mixing zone the reactant profiles yielded by Model 1 and Model 2 are superimposed for all considered time levels. Those both well describe the evolution in space of the two reactant concentrations. On the other hand, within the mixing zone, where the reaction takes place, the difference between Model 1 and Model 2 results is detectable as shown by Figure 3.7b-Figure 3.10b. The comparison of Figure 3.7b-Figure 3.10b highlights that the difference between reactant profiles given by Model 1 and Model 2 progressively reduces until becoming negligible for long times, as the system trends to the asymptotic regime. In Figure 3.7b, which depicts reactant profiles within the mixing for short times (i.e., t=1.96),

even as the two model show different behaviors, it is not possible to discriminate between the two model performances. Indeed, comparing C_B pore-scale cross sectional averaged data to profiles given by the two models, we observe that both Models do not capture the system behavior within the mixing zone for short times. Concerning C_A profiles, it is hard to qualitatively establish if the Models are capturing its evolutions and which one of those better interprets pore-scale cross sectional averaged data. Indeed the backward tail of the concentration C_A exhibits larger oscillations than C_B. These oscillations are due to the amount of particles which are entrapped in dead end pores characterized by low fluid velocity (*Porta et al. 2013*). Figure 3.8 and Figure 3.9 , which display reactants profiles at intermediate times (t=9.63 and t=57.77), suggest that Model 2 solution better interprets pore-scale cross sectional averaged data since it provides better fitting of data compared to Model 1. In Figure 3.10b, at late time, the difference between reactant profiles yielded by Model 1 and Model 2 has almost completely vanished and the two model performances are comparable in reproducing pore-scale cross sectiona averaged data.

These results show that the two models are equivalent outside the mixing zone. This can be explained by observing that the formulation of dispersive transport which is identical in the two models. The continuum models results differ in the mixing region, due to the different formulation of the reaction term.

Figure 3.11- Figure 3.14 display the product concentration profiles (C_C) at the same times considered in Figure 3.7-Figure 3.10 (i.e., $t = 1.93; t = 9.63; t = 57.77; t = 481.40$). Results are shown by considering both linear and logarithmic axes scales. The linear ones depict only a limited area around the product peak indicated in the red broken lines in Figure 3.11a- Figure 3.14a. Model 2 differs from Model 1 only in a very limited region around product concentration peak mainly detectable for short times. As time increases, the difference between Model 1 and Model 2 product concentration profile predictions becomes negligible. Logarithmic plots in Figure 3.11 and Figure 3.12 suggests that the dispersion parameter used in Models solutions overestimates the effective dispersion observed for earliest times.

Figure 3.15 clarifies the difference between concentration peak yielded by Model 1 and Model 2. Those are compared to pore-scale averaged data one computed by Eq. (2.50). In Figure 3.15, we observe that Model 1 peak evolution is always above the Model 2 one for short times refleticting the

differences observed in Figure 3.11b-Figure 3.14b. Even as the discrepancy between the two model peak evolutions for short times, those both approach the same asymptotic value for long times. The comparison between the curves yielded by the two models suggests that Model 2 shows a better performance in interpreting C_{max} data for $t < 10^2$. Even as the overall Model 2 peak prediction is better, a overestimation of pore-scale cross sectional averaged data is yielded by Model 2 for few initial times.

This qualitative analysis suggests that the solutions of the two Models are good at reproducing pore-scale simulation data apart from short times features. However, some figures (e.g. Figure 3.8b, Figure 3.9b and Figure 3.15) show that Model 2 yields to a better fit of pore-scale cross sectional averaged data.

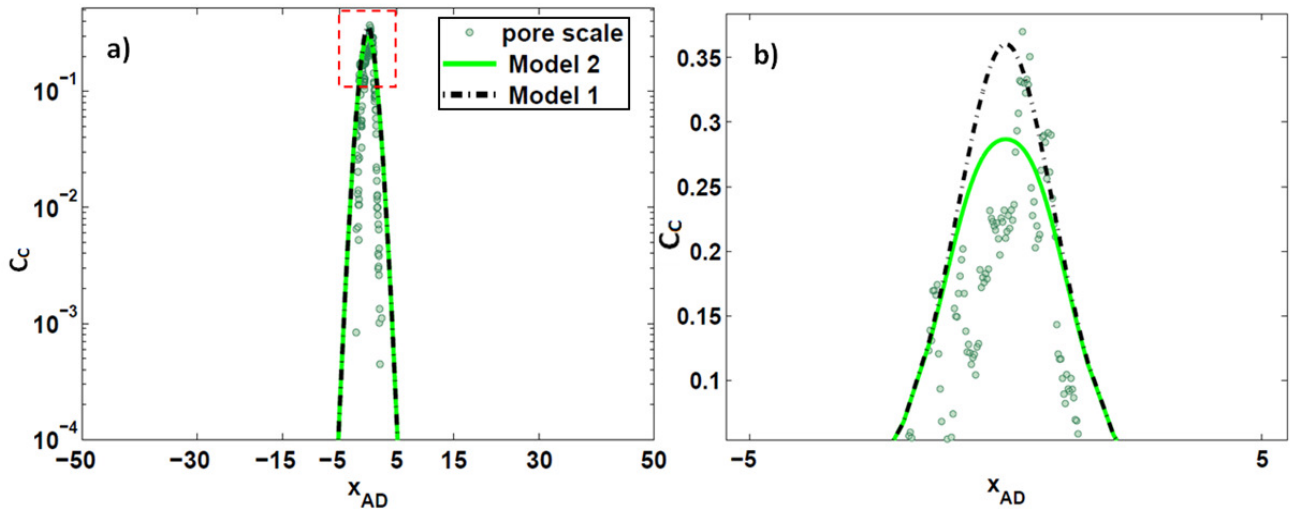

Figure 3.11 a) Product concentration profiles given by Model 1 and Model 2 at t=1.93 in logarithmic scale compared to pore-scale cross sectional averaged data. b) a zoomed image of product peack delimitated in figure a) by dashed red line in linear scale.

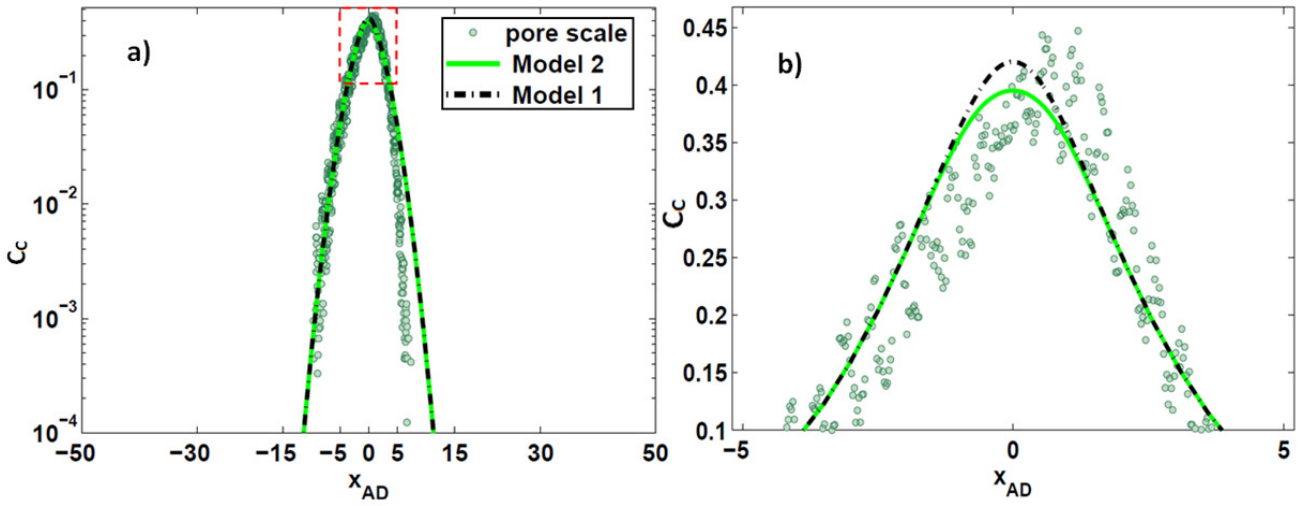

Figure 3.12 a) Product concentration profiles given by Model 1 and Model 2 at at t=9.63 in logarithmic scale compared to pore-scale cross sectional averaged data. b) a zoomed image of product peack delimitated in figure a) by dashed red line in linear scale.

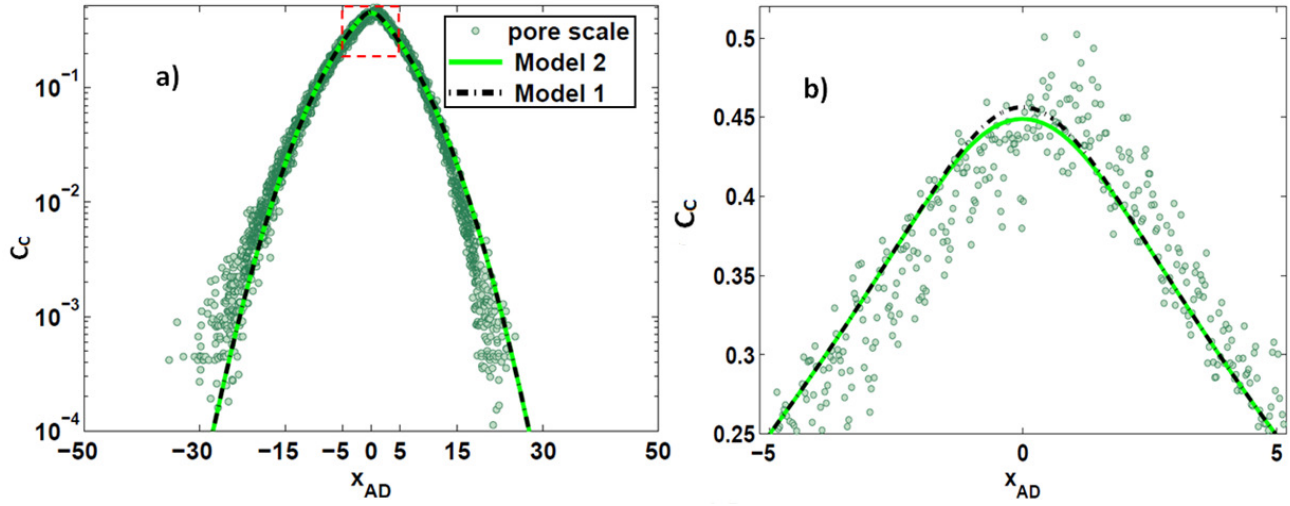

Figure 3.13 a) Product concentration profiles given by Model 1 and Model 2 at at t=57.77 in logarithmic scale compared to pore-scale cross sectional averaged data.b) a zoomed image of product peack delimitated in figure a) by dashed red line in linear scale.

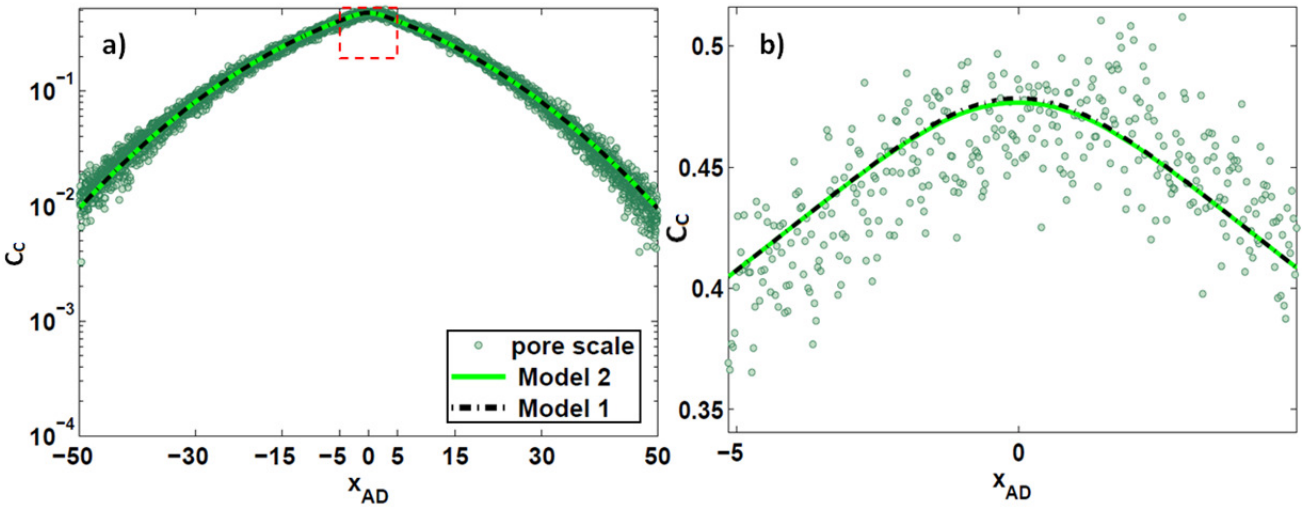

Figure 3.14 a) Product concentration profiles given by Model 1 and Model 2 at at t=481.40 in logarithmic scale compared to pore-scale cross sectional averaged data.b) a zoomed image of product peack delimitated in figure a) by dashed red line in linear scale.

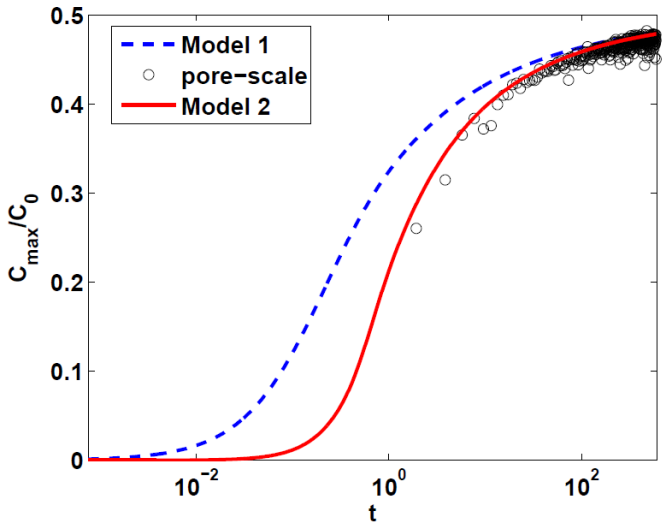

Figure 3.15 Comparison between pore-scale cross sectional averaged data product concentration peak and product peak evolution yieleded by Model 1 and Model 2.

3.4 Model 1 and Model 2 assessment

In this section a quantitative assessment of the two model performances is provided. This is perfomed through the objective functions f_1 (see Eq. (2.51)), f_2 and f_3 introduced in section 2.6.

The data considered for the computation of f_1 are selected according to the following criteria:

- Concerning C_C, we do not consider the part of domain where pore-scale data are equal to zero;

- Concerning C_B, we do not include the part of domain where pore-scale data are equal to zero and where pore-scale data fluctuate around the mean value of one.

Figure 3.16 exemplifies C_B data selection for the computation of f_1. In Figure 3.16, C_B pore-scale cross sectional data at t=57.77 are plotted: the selected data are highlighted through a darker color.

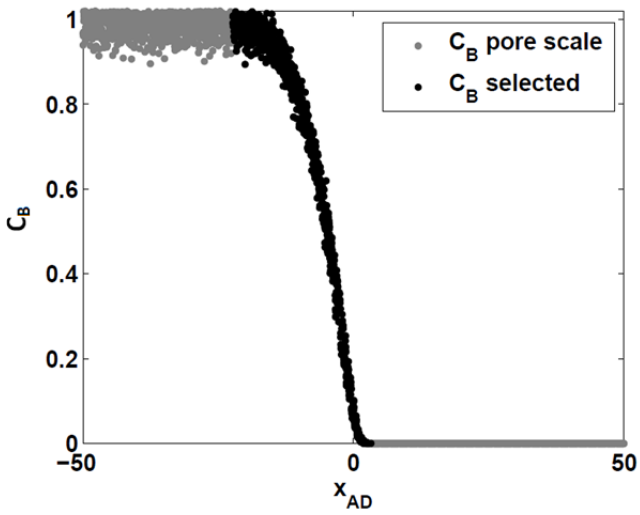

Figure 3.16 An exemple of C_B pore-scale data selection at t=57.77 for Eq. (2.51).

We neglect here C_A concentration profiles as they exhibit an oscillatory behavior in the mixing zone, which does not allow to discriminate between the two model performances.

The function f_2 allows to stress the error committed on the concentration tails approaching to zero. As shown in Figure 3.7-Figure 3.10, this is helpful to appreciate the differences between reactant Model 1 and Model 2 predictions in the crucial mixing zone, where the chemical reaction occurs. On the other hand, Eq. (3.4) emphasizes the tails of the distribution of C_C which are located outside the mixing region and consequently mainly influenced by the dispersive process (see Figure 3.11-Figure 3.14). Hence we expect the function $f_{2C\_k}(t)$ allows to assess the quality of the model performance in reproducing the dispersion of the reaction product concentration C_C (see Figure 3.11-Figure 3.14). The data considered for the computation of f_2 are selected according to the following criteria:

- Concerning C_C, we do not consider the part of domain where pore-scale data are equal to zero;

- Concerning C_B, we include only the part of domain in which mixing between reactant takes place, i.e. we exclude all the location in which $C_A C_B = 0$; indeed Model 1 and Model 2 predictions show a different behavior only in this region.

Figure 3.17 exemplifies the data selection of C_B for the computation of f_2. In Figure 3.17, C_B pore-scale cross sectional data at t= 57.77 are plotted: the selected data are highlighted in black. C_A data are plotted with the illustrative purpouse to dispay where both C_A and C_B assume non-zero values.

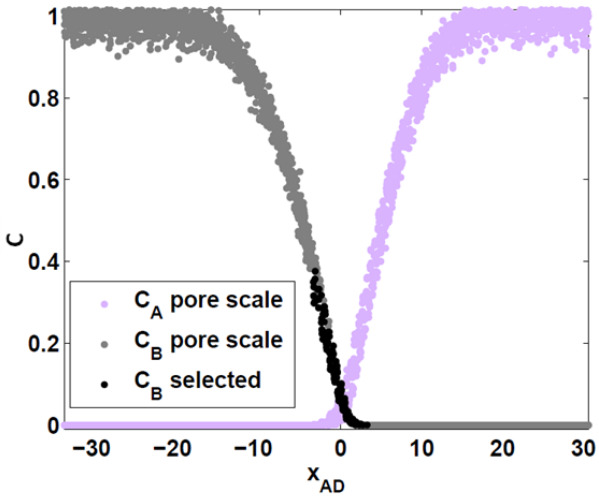

Figure 3.17 An exemple of C_B pore-scale data selection at t=57.77 for Eq. (2.53). The C_A pore-scale cross sectional averaged data are reported to highlight where both C_A and C_B are non zero values.

Finally, we compute the third objective function (f_3) which is expected to emphasize the model performances in predicting the product peak height and the two reactants dispersion outside the mixing zone. For this pourpose, we first conmpute the survival function (SF)

The survival function provides the complement to one of the chemical concentration profiles. An example is shown in Figure 3.18 where f_3 is applied to Model 1 and 2 solutions and to pore-scale cross-sectional averaged concentrations. Figure 3.19 and Figure 3.20 show that the survival functions in logarithmic scale allow to highlight the importance of the values close to the product concentration peak for C_C (Figure 3.19) and the two reactant tails outside the mixing zone as exemplified in Figure 3.20.

The data considered for the computation of f_3 are selected according to same criteria used for f_1.

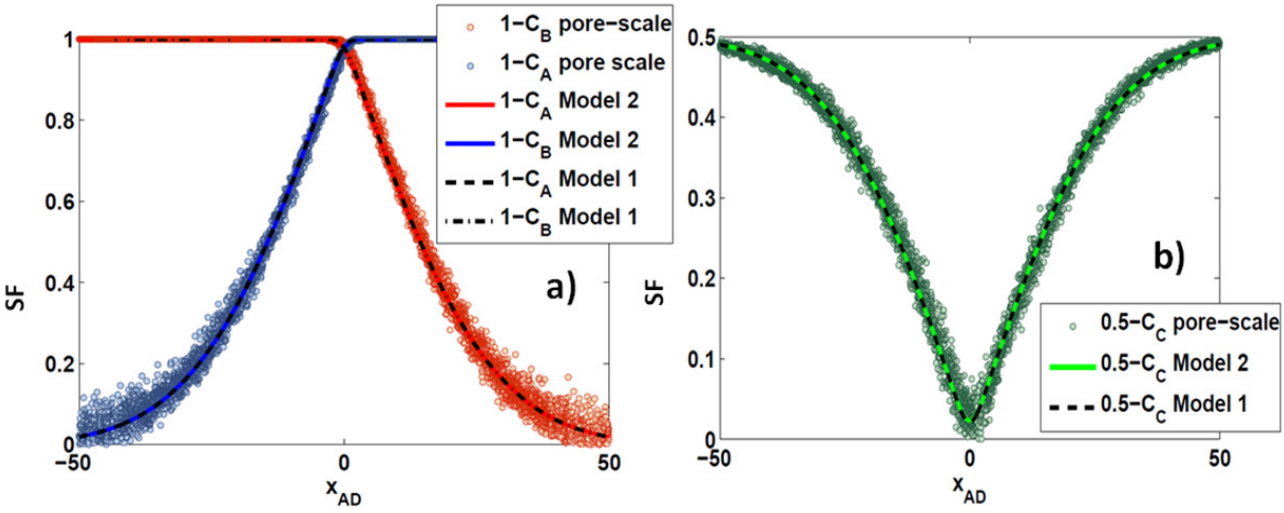

Figure 3.18 Survival functions of a) reactants concentration profiles and b) product concentration profile yielded by Model 1, Model 2 and pore scale cross sectional averaged data at t=481.40.

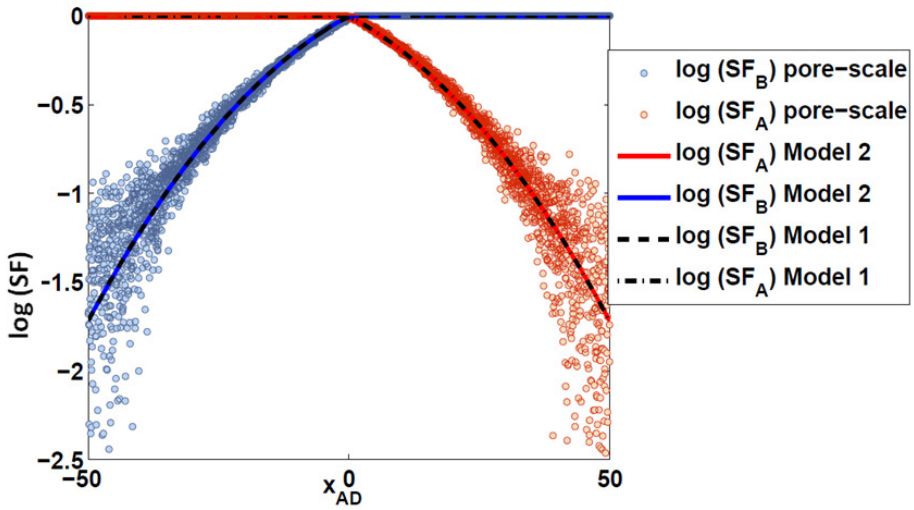

Figure 3.19 Logarithmic value of survival functions of reactants concentration profiles yielded by Model 1 and Model 2 and pore-cale cross sectional averaged data at t=481.40.

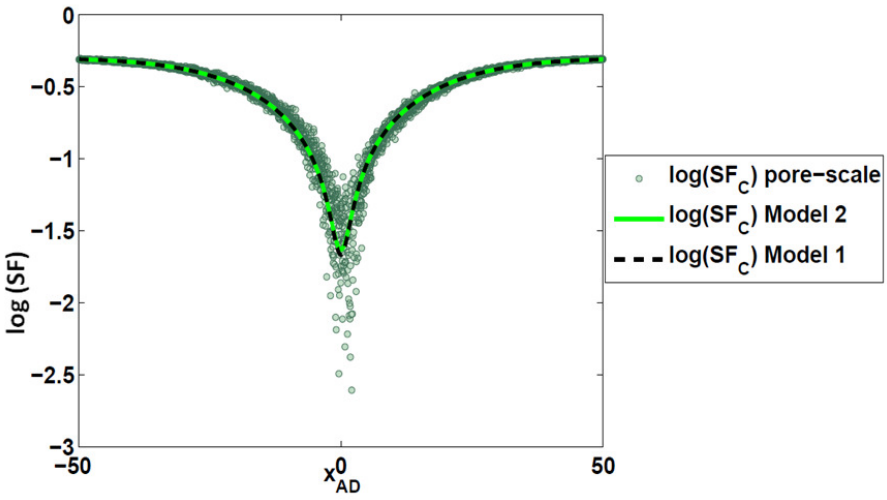

Figure 3.20 Logarithmic value of survival functions of product concentration profiles yielded by Model 1 and Model 2 and pore-cale cross sectional averaged data at t=481.40.

The functions f_1, f_2 and f_3 are evaluated at different times (comprised between 1.93 and 481.40) in order to identify which one of the two models minimizes the objective functions and, as a consequence, better predicts the pore-scale averaged data.

Figure 3.21a-Figure 3.23a depict the results related to the concentration of the reactant B. In particular Figure 3.21a shows the comparison between f_{1B_1} and f_{1B_2}. The two functions show a decreasing trend, in particular they both assume a value of 0.35 at the first considered time and then decrease to negligible values (0.032). This is consistent with the observation of Figure 3.7b and Figure 3.11b, which show that both models fail to reproduce the early behavior of the distribution of C_B. The comparison of the two curves displayed in Figure 3.21a does not disclose any meaningful result, since the difference between the two model results is hardly detectable . This result is consistent also with the observation that the results of the two models appear undistinguishable when we consider the full concentration profiles in a linear scale. Figure 3.22a shows the comparison of the two model performances evaluated through the logarithmic function f_{2B}. Here we observe a clear difference between the two model results: Model 2 better predicts B profile, as $f_{2B\_2} < f_{2B\_1}$ besides the first point (t=1.93) for which the both functions assume the maximum value. The latter result is consistent with the qualitative discussion provided in section 3.2, showing that both the models do not capture C_B concentration tail at t=1.93 (Figure 3.7). The comparison between the time evolutions of the two

functions f_{3B_1} and f_{3B_2} is shown in Figure 3.23a. The two functions decrease in time and are basically superimposed. This result is justified observing that these functions tend to emphasize the model results outside the mixing region, i.e. where the concentration profile tend to 1. Hence, this result confirms that the performance of the two models is basically identical outside the mixing region, as already suggested by Figure 3.23a

Figure 3.21b-Figure 3.23b display the same type of results, but computed by means of the product concentration C_C. The comparison between f_{1C_1} and f_{1C_2} (Figure 3.21b) suggests that Model 2 better predicts product concentration profile (Figure 3.21b). On the contrary the curves which describe the time evolution of f_{2C_1} and f_{2C_2} are superimposed for the whole considered time window. This is consistent with the observation that this function emphasizes the errors related to the prediction of the two tails of C_C distribution. This behavior is linked to the dispersive process, which is treated in the same way in the two considered models. The comparison between f_{3C_1} and f_{3C_2} is reported in Figure 3.23b. We recall that function f_{3C_k} is designed to emphasize the error in correspondence of the mixing zone, where the peak of C_C is located. As such, our result provides a quantitative assessment of the qualitative results discussed in previous section, in that Model 2 is significantly more accurate than model 1 for early times and then the two models reach a similar asymptotic behavior at long times. The increment of both f_{3C_1} and f_{3C_2} for long times is due to the presence of intense peak oscillations appearing for long times in pore-scale averaged data. In general, the results presented in Figure 3.21-Figure 3.23 show that (i) model 2 better predicts pore-scale averaged data in the mixing region, (ii) the two models provide the same results outside the mixing region.

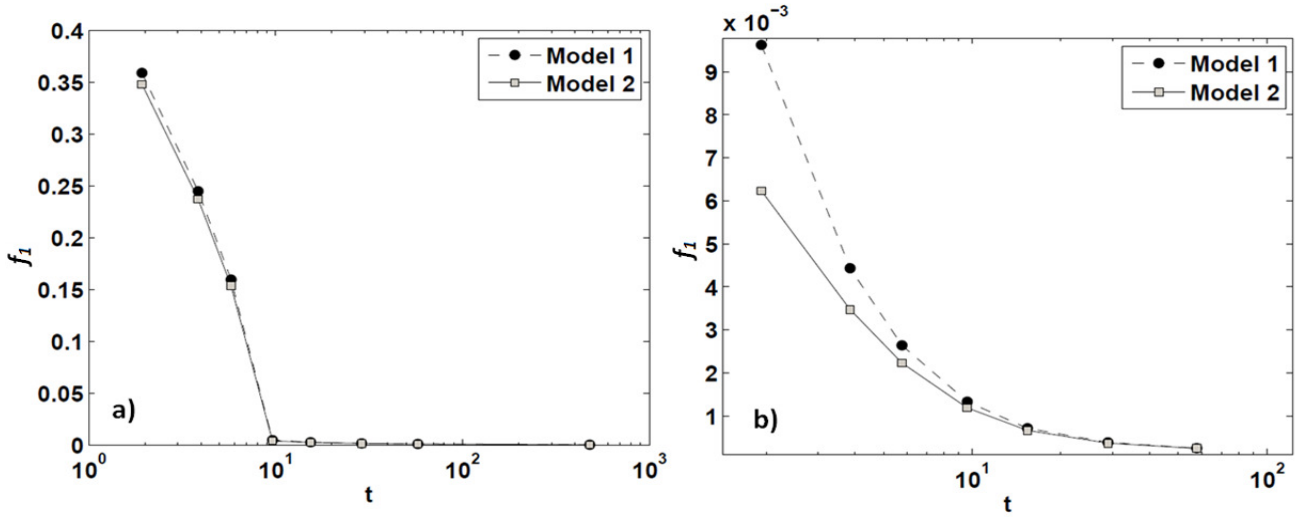

Figure 3.21 The figure shows *f1* computed for Model 1 and Model 2 on a) C_B concentration profiles and a) C_C concentration profiles.

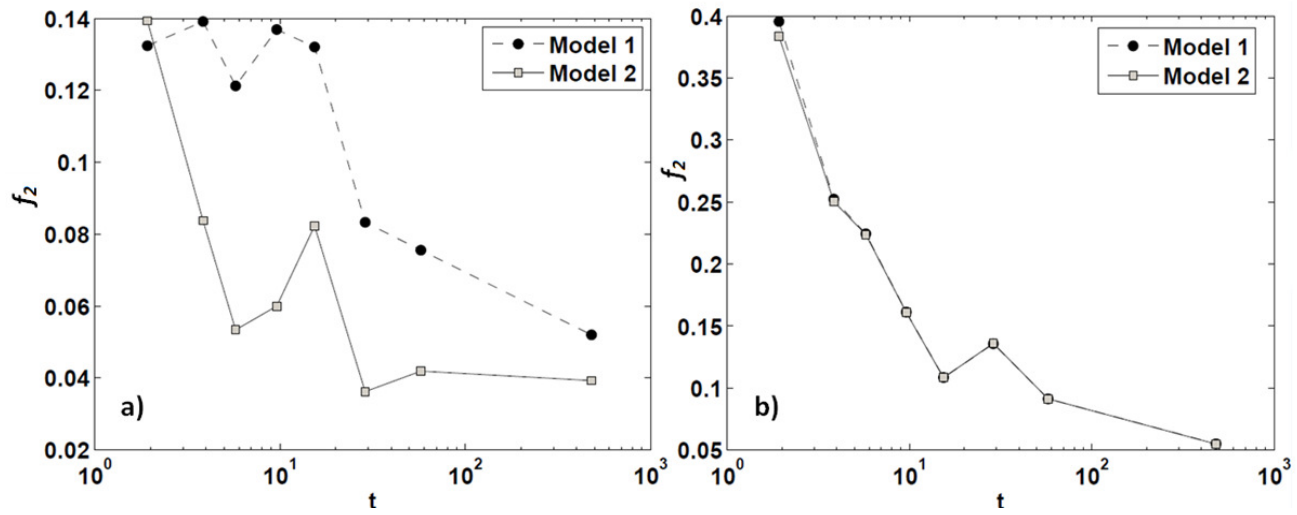

Figure 3.22 The figure shows f_2 computed for Model 1 and Model 2 on a) C_B concentration profiles and a) C_C concentration profiles.

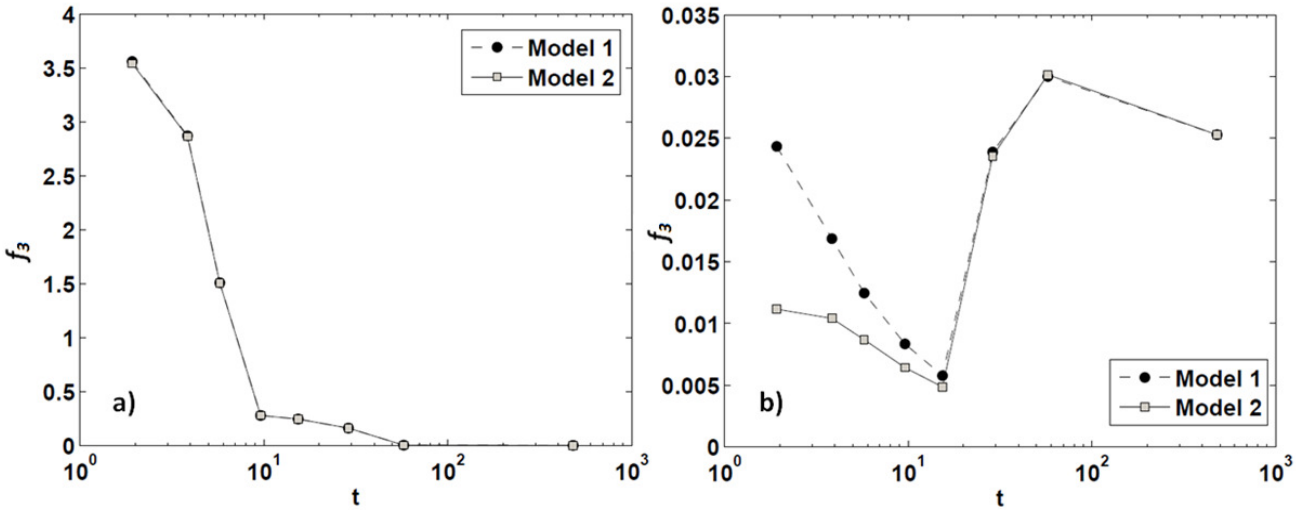

Figure 3.23 The figure shows f_3 computed for Model 1 and Model 2 on a) C_B concentration profiles and a) C_C concentration profiles.

3.5 Results discussion

The results shown in this Chapter move from the analysis provided in *Porta et al.(2013)*. In particular our aim is to compare the results yielded by continuum models and pore-scale simulations for a very simple pore scale geometry. Our results show that the evolution of global quantities, such as the global mass of *C* generated by the reaction, is governed by dispersion and poorly influenced by incomplete mixing. *Porta et al.(2013)* showed that incomplete mixing always takes place at the pore scale, but the presented results show that its effect on continuum scale models is negligible in the presence of this simple geometrical configuration. As a consequence both Model 1 and Model 2 capture global quantities behavior, in spite of the different formulation assumed for the reaction and transport terms inside the mixing region (see Eq.(2.18) and Eq. (2.7)). We emphasize that in this simple pore-scale setting the ADRE accurately reproduces the phenomenon, even in conditions where it should not be reliable according to theoretical up-scaling (*Battiato et al.,2011; Porta et al. 2012a*).

A detailed inspection of cross-sectional averaged quantities as chemical concentration profiles allows to observe that incomplete mixing effect can be identified by focusing on the reactant concentration tails in mixing zone and in the predicted product peak height. Qualitative analyses and errors assessment shows that Model 2 implementation leads to a better prediction of pore-scale cross sectional averaged data. This result is quantitatively assessed upon considering different objective functions, i.e., different ways of quantifying the model error. In particular our results show that the difference of the

continuum models prediction within the mixing zone is emphasized when the concentrations are compared in a logarithmic scale, i.e. focusing on the small values assumed by concentration in the mixing region. Both the models appear not to capture reactive transport evolving dynamics for short times overestimating:

- Concentration profiles dispersion (Figure 3.7)
- Product peak concentration (Figure 3.15).

This discrepancy between initial actual dispersion of pore-scale data and continuum model prediction one can be ascribed to the fact that nonlocal effects are neglected while computing the dispersive and reactive terms. The over-prediction of Model 1 product peak concentration must be identified with the absence of an incomplete mixing term that quantifies the local degree of mixing between reactants. Model 2 improves the product peak concentrations prediction getting closer to pore-scale averaged data. However a peak overestimation is registered for initial times. This porous medium setting, due to its simplicity, does not provide decisive evidences to demonstrate how Model 2 allows an advancement in predicting reactive transport compared to the standard formulation provided by Model 1.

However, since different authors prove that Model 1 generally over-predicts the amount of global product and product concentration for mixing limited systems (e.g. *Gramling et al. 2002, Raje and Kapoor 2000*), Model 2 is showing here promising results and encouraging further investigations in more complex scenarios, which are analyzed in detail in Chapter 4.

Chapter 4 RESULTS 2: POROUS MEDIUM SCENARIO 2

In this Chapter we present and discuss models assessment referring to porous medium scenario 2 (see section 2.2). We focus on a single dataset, obtained by the combination of the largest *Pe* and *Da* available from pore-scale simulations. Indeed, as anticipated in Chapter 3, these are the conditions in which incomplete mixing effect is relevant. The characteristics of the simulation considered are reported in Table 4.1.

Table 4.1 Numerical pore-scale simulation conditions considered in porous medium scenario 2.

Pe	24
Da	1038
ϕ	0.6
$\hat{D}_m$	2.0000e-9 [m^2/s]
$\hat{w}$	8.0000e-005 [m]
$\langle \hat{u} \rangle^l$	6.2220e-004 [m/s]
$\hat{k}$	324.38[m^3/(mol s)]

We first present a qualitative analysis of reactive transport evolving features observed in pore-scale simulation with the aim of providing a preliminary investigation which supports the following model assessments and discussion. Then, the criteria for choosing datasets for model assessment are presented and the datasets chosen are illustrated. The last part of the Chapter is dedicated to model assessment, i.e. the model performance are evaluated comparing model solutions to pore-scale dara and assuming range of variations for the models parameters. In this part the models analysis is presented divided in two different sections: the first one related to single continuum models and the second one dedicated to DRMT model. For the latter, only a preliminary analysis of chemical profiles and global product sensitivity to different parameters is performed since the numerical computation of Model 5 solution is particularly time consuming compared to the single continuum Models 1-4. The different models features will then compared and discussed in Chapter 5 on the basis of results presented herein.

4.1 Qualitative analysis of pore-scale simulation

We present here a first qualitative analysis of different quantities evolutions observed in pore-scale simulation. This allows identyfing the main evolving dynamics of reactive transport in the specific conditions considered (see Table 4.1). This preliminary investigation helps in defining criteria for selecting datasets used in the following model assessment and in interpreting models assessment results.

Pore-scale simulation data are investigated referring to the quantities definited in Chapter 2: global mass of the reaction product (G_C) indicated in Eq. (2.48), chemical concentration profiles (C_A, C_B, C_C) definted in Eq. (2.47). The global reaction rate (R_C), instead, is no longer included in the following analysis since it is simply computed deriving global product in time. This means that it does not add significant contribution to the discussion since it contains the same information of global product time-evolution.

Relying on non-reactive transport simulation performed in porous scenario 2, we derive the non-reactive dispersion coefficient according to the following procedure. Particle tracking simulation allow knowing the exact position of each one of the particle as function of time. Thanks to this information, it is possible to compute the square averaged particle displacement as function of time. This quantity is linked to dispersion value according to the following equation:

$$\left\langle (\hat{x} - \langle \hat{x} \rangle)^2 \right\rangle = 2\hat{D}\hat{t} \tag{4.1}$$

The dimensionless dispersion value is computed dividing $\hat{D}$ to molecular diffusion ($\hat{D}_m$). Figure 4.1 illustrates the time-evolution of dimensionless dispersion *D* as function of time. We observe that, at t=57 s which corresponds to the duration of reactive transport simulated, the system hasn't reached the asymptotic regime. Indeed the dispersion value has not reached a constant value. The crossing point of the two solid black lines indicates the value of dimensionless dispersion at t=57s which is equal to 741.

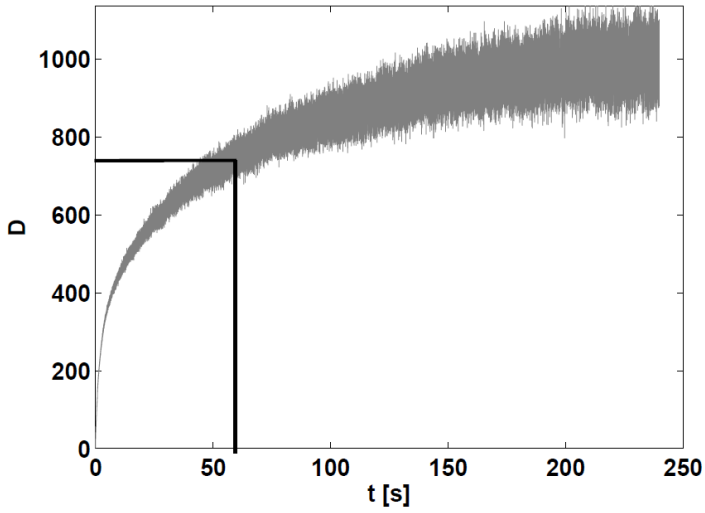

Figure 4.1 Dimensionless dispersion evolution as function of time computed square averaged particle displacement of non-reactive particle tacking simulation.

Figure 4.2 depicts the global product computed on product pore-scale cross sectional averaged concentrations. According to *Porta et al (2012b)*, in asymptotic regime, the global product time evolution is proportional to the square root of time ($G_C \propto \sqrt{t}$). This asymptotic trend is represented by a solid black line in Figure 4.2. Comparing pore-scale global product time-evolution and the expected asymptotic trend for long time, Figure 4.2 confirms numerical findings showed in Figure 4.1. Indeed, we observe that the system has not reached the asymptotic regime yet but global product shows to increase faster than the expected asymptotic behavior for the longest available time steps.

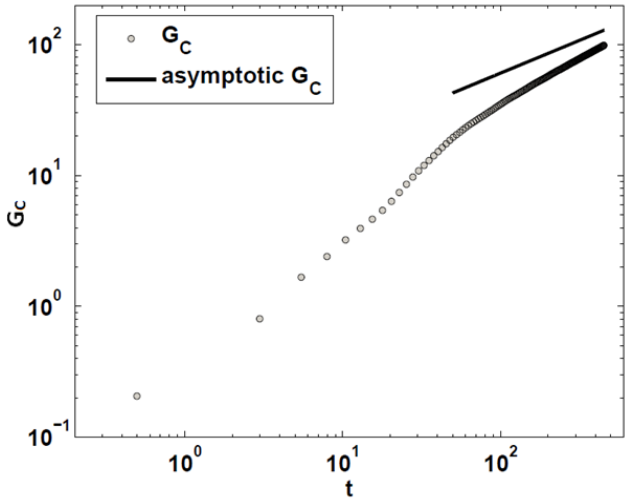

Figure 4.2 Global product time-evolution obsedved in pore-scale simulations compared to the asymptotic behavior.

We provide now a brief analysis of the time-evolution of chemical species concentration profiles. In Figure 4.3-Figure 4.5 we report the pore-scale cross-sectional averaged concentration of A and B at three different times ($t = 24.89; 223.96; 447.93$) in order to synthetically illustrate reactant concentration history. For each considered time level, a zoomed image of the mixing zone is reported where reactants concentrations are plotted in logarithmic scale. This allows highlighting the region close to the reaction where the reactant concentration values are close to zero. In general, we observe in Figure 4.3-Figure 4.5 that the initial steep reactants profile progressively smooth due to dispersion process. Looking at Figure 4.3a and Figure 4.5a, we observe that C_A and C_B show an oscillatory behavior manly concentrated on the backward tail, i.e. x_{AD}<0. In particular C_A profiles present relevant peaks and localized increase of concentration. On the contrary, C_B profiles present the opposite behavior showing localized decrease of section averaged concentration. These oscillations are due to the presence of immobile regions inside the domain due to system geometry, which includes cavities where the solute A is trapped. Notice that the oscillations are periodic reflecting the periodical structure of the domain (see section 2.2). Since at the beginning the porous medium is fully saturated with C_A solution, solute, which is initially located in dead end pores or slow velocity fluid regions, tends to remain trapped in them. This solute slowly transfers to high velocity fluid channels manly because of diffusion. On the other hand, C_B solution, which is injected into the domain, preferably occupies high velocity throats and slowly diffuses into almost immobile zones. Figure 4.4a and Figure 4.5b put in evidence that C_A is not the mirror image of C_B and vice versa. Indeed, C_A profiles appear to be steeper than C_B ones. Since the steepness intensity of the concentration profile typically depends on the dispersion process, we can deduce that C_B disperses quicker than C_A shaping a smoother profile. This may be explained by the fact that C_B preferentially occupies mobile zone rather than almost-immobile ones and, moving fast, it undergoes to a faster spreading process. Looking at Figure 4.3b-Figure 4.5b, where the logarithmic scale emphasizes reactant profiles in mixing zone, we can analyze the time-evolution of the reactive front location (indicated through dotted line in Figure 4.3b-Figure 4.5b). We identify the front location with the point in which C_A and C_B profiles cross each others. We observe that the reactive front location is not coincident with advective front, i.e. it is not located at $x_{AD} \approx 0$, as observed in th case of the simple Scenario 1 (see Chapter 3, Figure 3.7-Figure 3.10). Figure 4.3b-

Figure 4.5b display a different behavior, i.e. the two reactant concentration profiles cross each other in a location translated respect to x_{AD}=0. A comparison between reaction front positions in Figure 4.3b-Figure 4.5b shows that the distance between the reaction front and the mean traveled distance computed according to the average fluid velocity x_{AD} increases as the time increases. This result shows that the reactive front moves faster than the mean advective velocity.

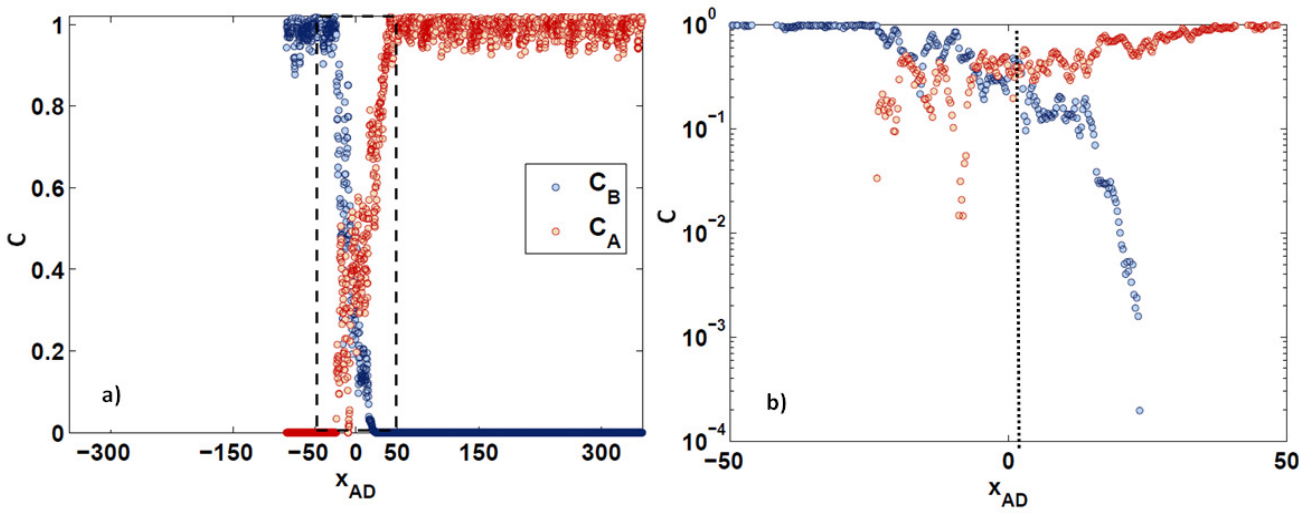

Figure 4.3 a) Reactant concentration profiles at t =24.89. Figure b) provides zoomed image of the reactant mixing front evidenced in figure a) through a dashed black line at t=24.89. The dotted line in figure b) indicates the position of the reactive front.

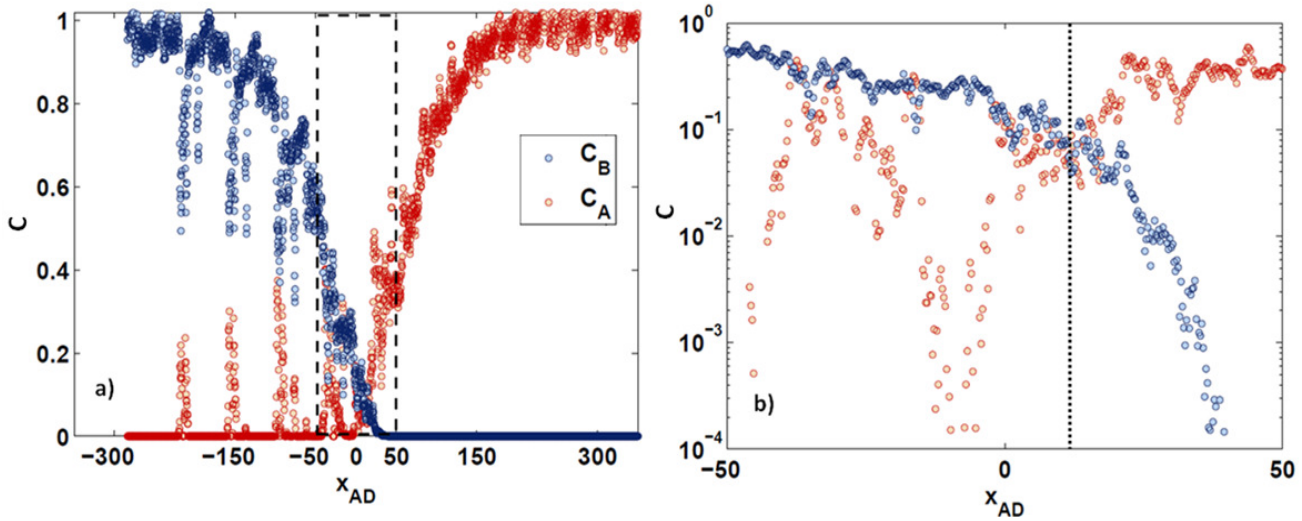

Figure 4.4 a) Reactant concentration profiles at t=223.97. Figure b) provides zoomed image of the reactant mixing front evidenced in figure a) through a dashed black line at t=223.97. The dotted line in figure b) indicates the position of the reactive front.

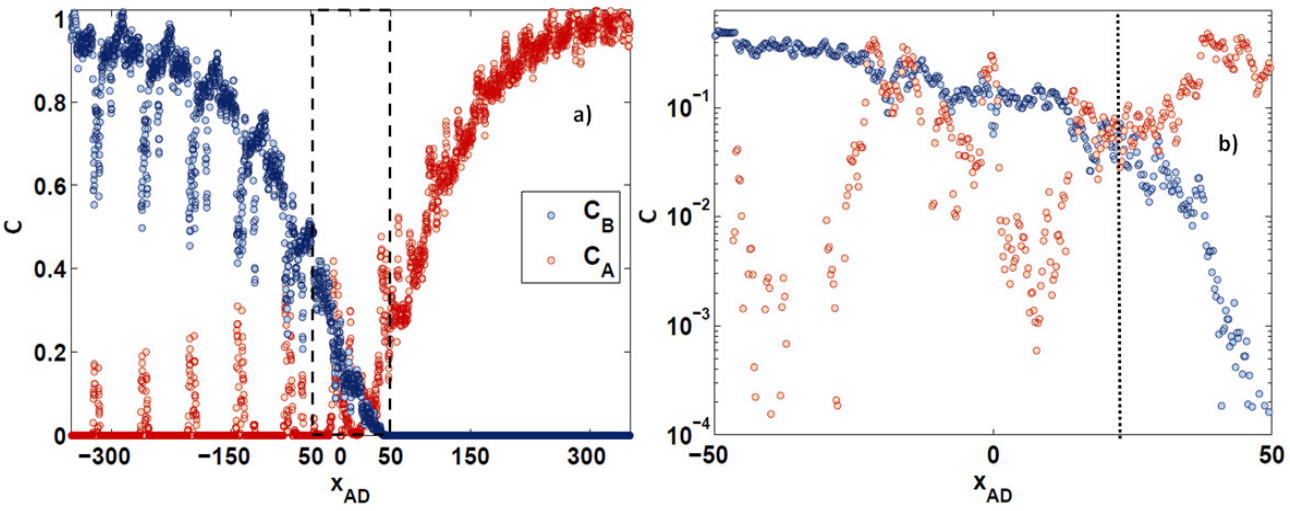

Figure 4.5 a) Reactant concentration profiles at t=447.93. Figure b) provides zoomed image of the reactant mixing front evidenced in figure a) through a dashed black line at t=447.93. The dotted line in figure b) indicates the position of the reactive front.

In Figure 4.6-Figure 4.8 we provide a synthetic history of C_C concentration profiles evolution at the same times considered in Figure 4.3-Figure 4.5. At each time, we report the product concentration plotted in both logarithmic and linear scales. Product concentration profiles share some features with reactant profiles confirming the observations done previously.

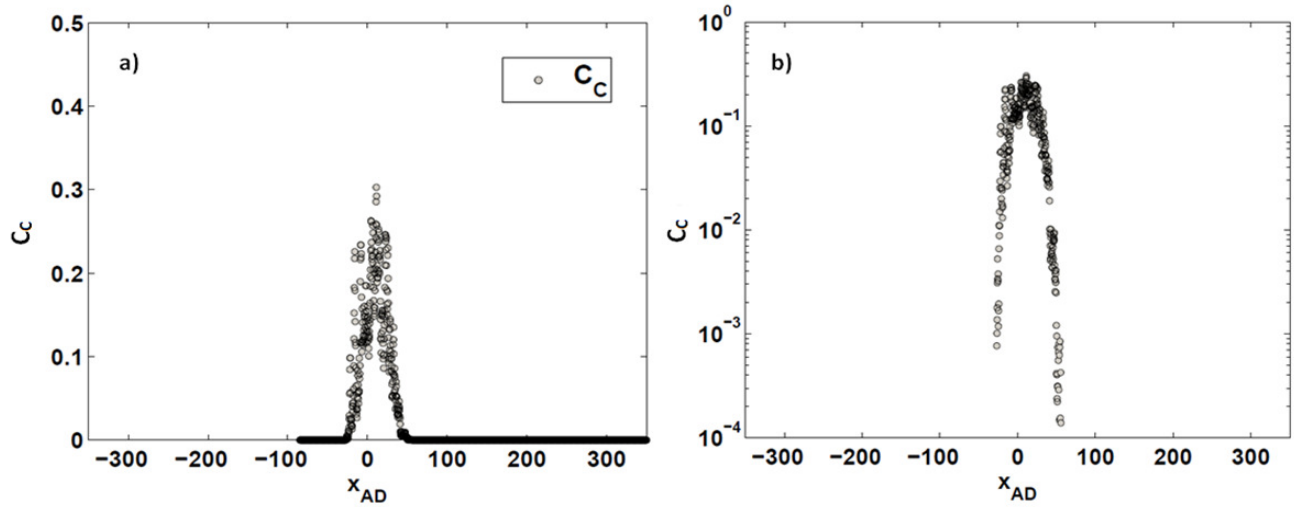

Figure 4.6 Product concentration profile in a) linear and b) logarithmic scale recorded at t=24.89.

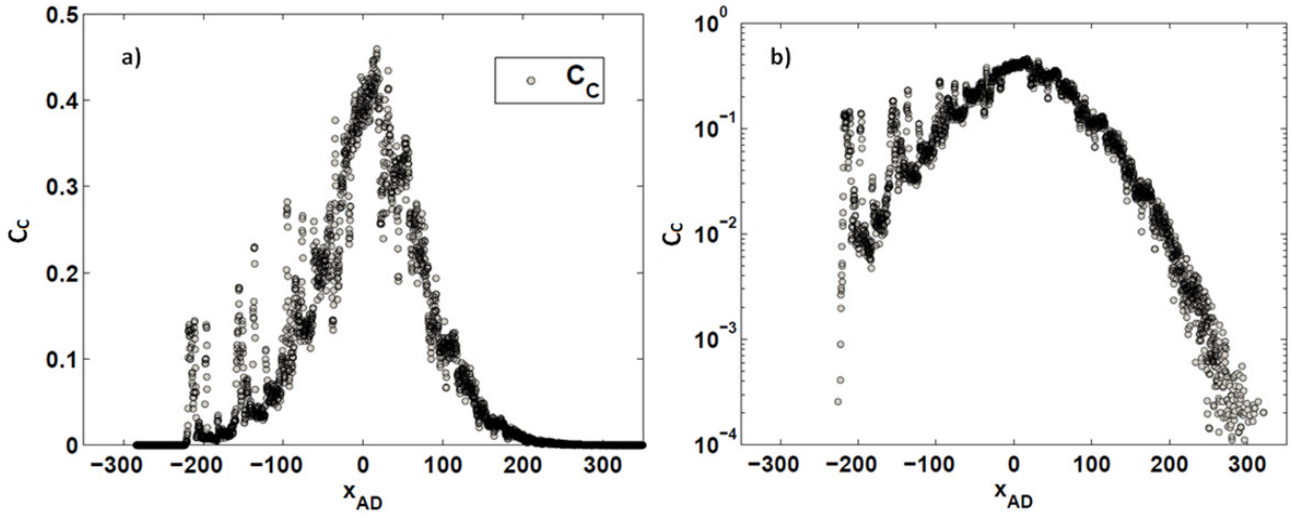

Figure 4.7 Product concentration profile in a) linear and b) logarithmic scale recorded at t=223.97.

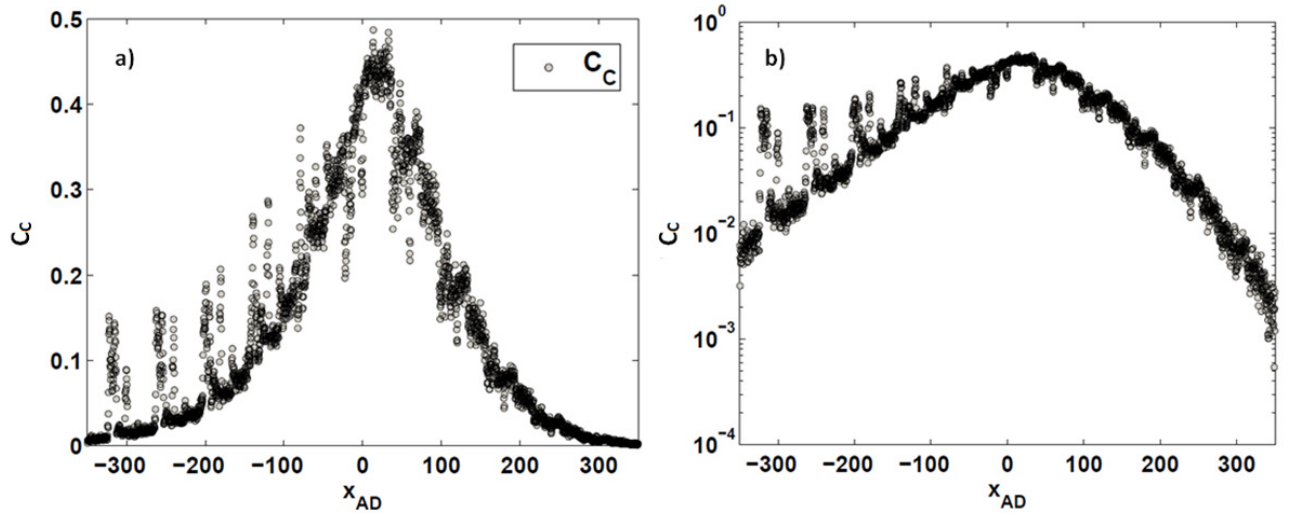

Figure 4.8 Product concentration profile in a) linear and b) logarithmic scale recorded at t=447.93.

Figure 4.6-Figure 4.8 display that C_C profile width increases with time due to dispersion process and the peak height significantly increments between t=24 and t=223 and then continues to raise slower until t=447. Focusing on C_C profile shape, Figure 4.6a-Figure 4.8a show that C_C presents peaks of high concentration on the tail slower than the reactive front (for x_{AD}<0), similarly to C_A. We can interpret these oscillations as the an amount of reaction product generated in immobile regions which remains entrapped for long times in these zones. In Figure 4.6b-Figure 4.8b, the logarithmic scale

evidences that C_C profiles are not symmetric with respect to the peak concentration. Product tail slower than advective front is less steep compared to the faster one. Moreover, we can observe that product concentration peak position is translated if compared to advective front position, similarly to the reactive front identified in Figure 4.3-Figure 4.5. Figure 4.9 evidences the correspondence between C_C peak and reactive front location at t=447: C_A, C_B C_C profiles are plotted and a vertical black arrow connects the advective front and the product peak. This result shows that the peak position of C_C profile tends to move faster than the advective front, reflecting the reactive front displacement.

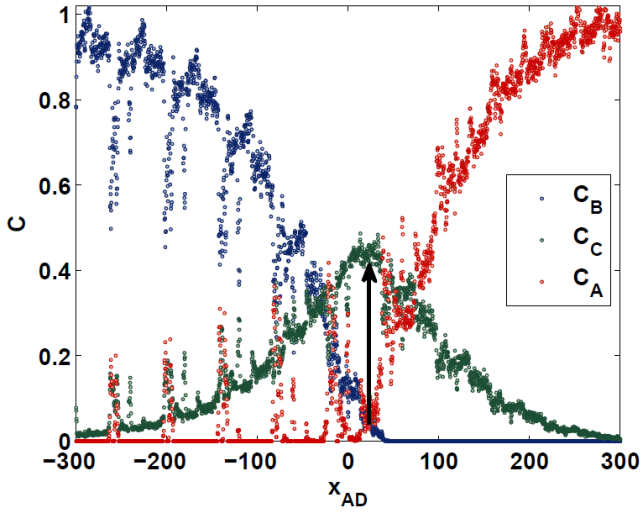

Figure 4.9 Pore-scale averaged data of CA, C_B and C_C concentration at t=447. The black arrow evidences that the peak position corresponds to the reactive front one.

We clarify the latter observation in Figure 4.10 where the product concentration peak position (i.e. the reactive front) as function of dimensionless time is compared to the advection front position. Advection front position linearly evolves in time since the average fluid velocity is constant. Since the peak concentration is affected by oscillations (see Figure 4.6-Figure 4.8), its position does not linearly evolve with time. However, a linear fit of the product concentration peak position as function of time allows evidencing the averaged trend. The slope of product concentration peak position fitting line and advection front position line quantifies the velocity of peak displacement and advective front respectively. Figure 4.10 shows that the peak position fitting line is characterized by an higher slope compared to advection front position one meaning that concentration peak and reactive front move faster that the advective front as observed in Figure 4.6b-Figure 4.8b.

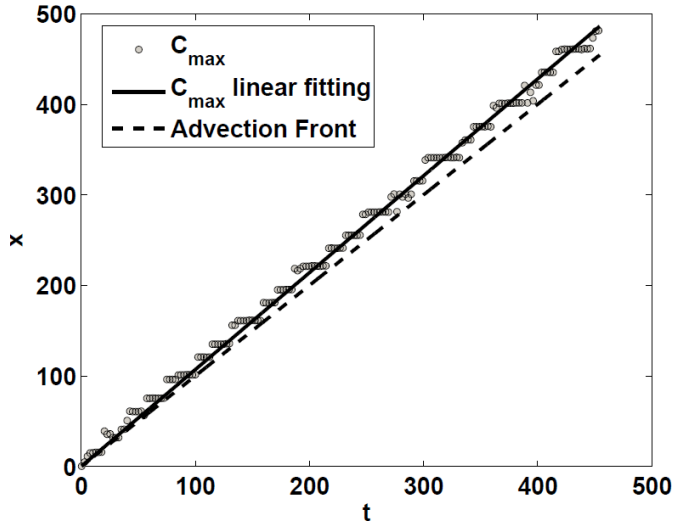

Figure 4.10 Time-evolution of product concentration peak position recorded in pore-scale cross sectional averaged data is compared to time-evolution of advective front position.

We remark that, by definition, single continuum models assume that reaction front coincides with advection front and that the reaction front advances at the average fluid velocity. Figure 4.11, for illustrative purposes, compares chemical cross-sectional averaged data to ADRE model (Model 1) prediction assuming *D*=450 (manually calibrated) at t=447. A solid red line evidences the ADRE reactive front position (coincident to advective front) while a red dashed line indicates the reactive front position observed in pore-scale simulation.

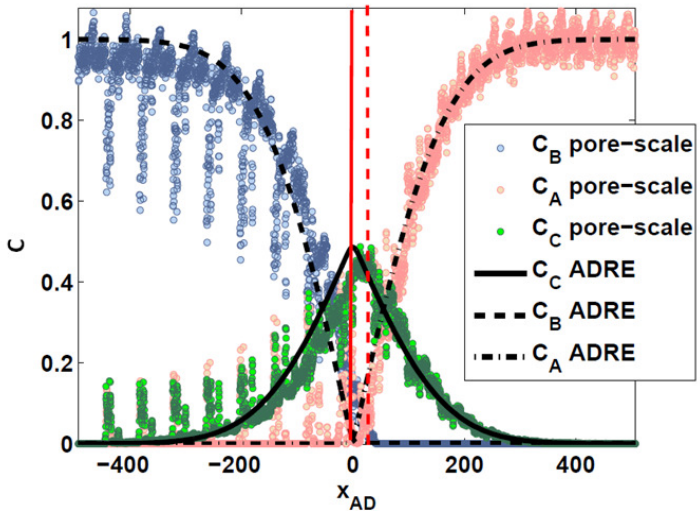

Figure 4.11 Pore-scale averaged data concentration at t=447 compared to Model 1 solution solved with *D*=450 (manually calibrated). The solid and dashed red lines indicate the position of advective front and reaction dront position , respectively.

Even if the discrepancy between the predicted and the actual reactive front could appear negligible, we can not ignore it in the following model assessment. Indeed this would lead to a systematic error, which would prevent a detailed analysis of the reactants concentration tails in the vicinity of the reaction front.

For this reason in all the single-continuum model assessment we assume that the solutes are transported by averaged reaction front velocity observed in pore-scale simulation (u_p). The latter is estimated from the slope of peak position fitting line plotted in Figure 4.10. The dimensional and dimensionless reaction front pore scale averaged velocities are reported in Table 4.2 compared to averaged advection velocity.

Table 4.2 Comparison between dimensional and dimensionless reaction front and advective velocities.

u_p	1.0560
$\hat{u}_p$	6.5702e-004[m/s]
$\langle u \rangle^l$	1
$\langle \hat{u} \rangle^l$	6.2220e-004[m/s]

4.2 Dataset selection for models assessment

For model assessment, we do not consider all the pore-scale cross sectional averaged data available for this scenario. Indeed, for each quantity considered, introduced in section 2.6, we selected only a limited number of data (from 10 up to 40) that allow capturing the overall behavior of the quantity analyzed excluding the noise due pore-scale cross-sectional data fluctuations and zero data.

Concerning to G_C, we select ten data equally distributed in time. The selection is illustrated in Figure 4.12. In the following, the selected data of G_C will be referred as $G_C 1$.

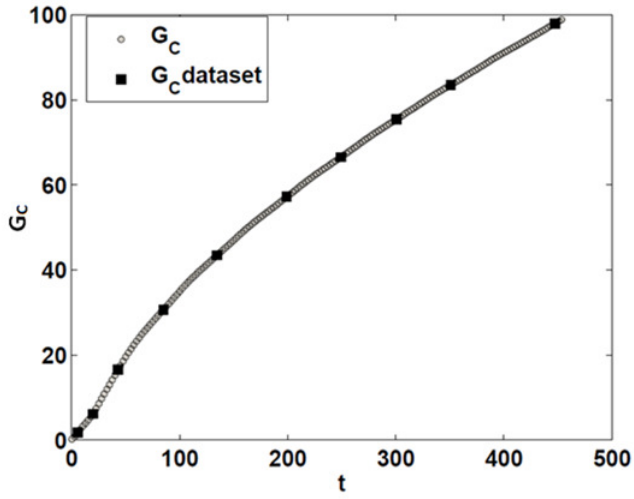

Figure 4.12 On the global product evolution observed in pore-scale simulation, the data chosen for the model assessment are evidenced.

Regarding the chemical concentration profiles, we define, instead, different datasets according to diverse criteria depending on the different models characteristics. The criteria, explained in the following, are based on the considerations done in section 4.1.

As observed in section 4.1, C_A, C_B and C_C are characterized by concentration fluctuations due to the presence of immobile regions, where local velocities are negligible. Single continuum models, due to their mathematical definition, are not able to capture and predict the amount of solute trapped in immobile regions since all the solutes is assumed to move under the effect of a single averaged advective velocity. As a consequence, single porosity models always predict symmetric C_C profiles with respect to peak position and C_A profile prediction is always the mirror image of C_B one with respect to reactive front. Because of that, in choosing a suitable datasets for single porosity models, the concentration oscillations appearing on the backward tails have been excluded.

Moreover, single continuum models presented in section 2.3 can be distinguished in: i) Model 1, Model 2 and Model 4 group where the reaction terms include time-independent parameters and ii) Model 3 where the reaction parameter is time-dependent. In chosing dataset for the first group of models we consider two profiles for each chemical both at late time ($t = 398.16$ and $t = 447.93$) on the hypothesis that the value of reaction and dispersion parameters are more established for long time. For Model 3, instead, we consider two profiles for each chemical species: the first one at $t = 24.88$ and the

second one at $t = 447.93$; the times selected are, on purpose, very far with respect to each other in order to generate a dataset sensitive to reaction parameter time-evolution. In both cases, we select 20 points for each profile considered leading to a dataset composed of 40 for each chemical species. In the following, the data selected for of C_A, C_B and C_C pore-scale data will be referred as indicated in Table 4.3. In Figure 4.13-Figure 4.15 the data selected are plotted compared to all profile data.

Table 4.3 Concentration profile dataset labels definitions.

Concentration Profile	Dataset label
C_i at t=24.88 (i=A,B,C)	C_i1 (i=A,B,C)
C_i at t=398.16 (i=A,B,C)	C_i2 (i=A,B,C)
C_i at t=447.93 (i=A,B,C)	C_i3 (i=A,B,C)

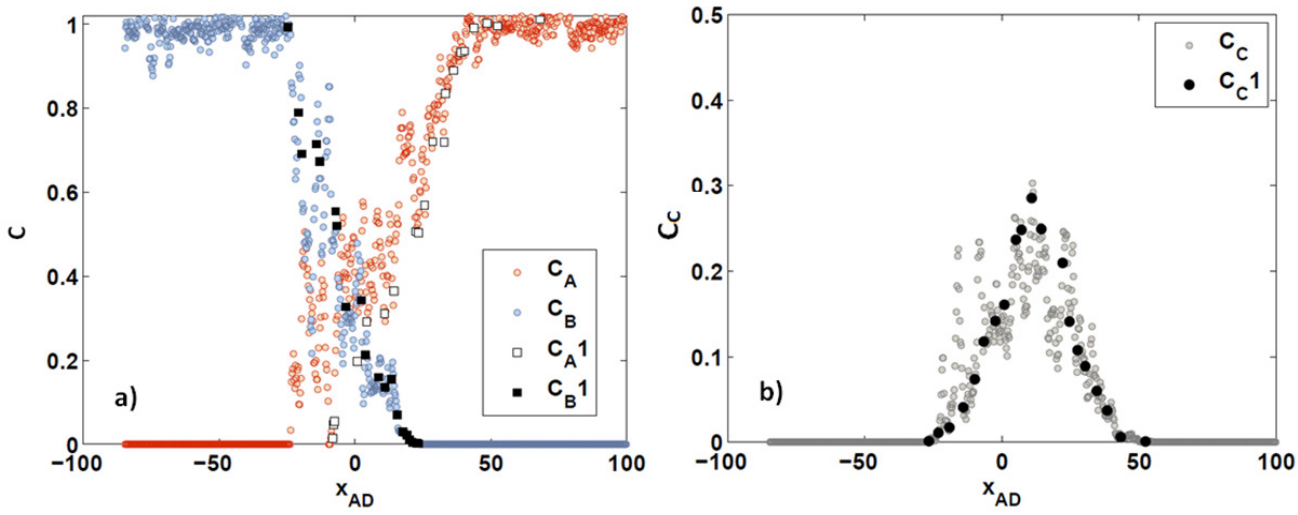

Figure 4.13 Comparison between pore-scale averaged concentrations data and selected datasets for a) reactant profiles and b) product profile at t=24.88.

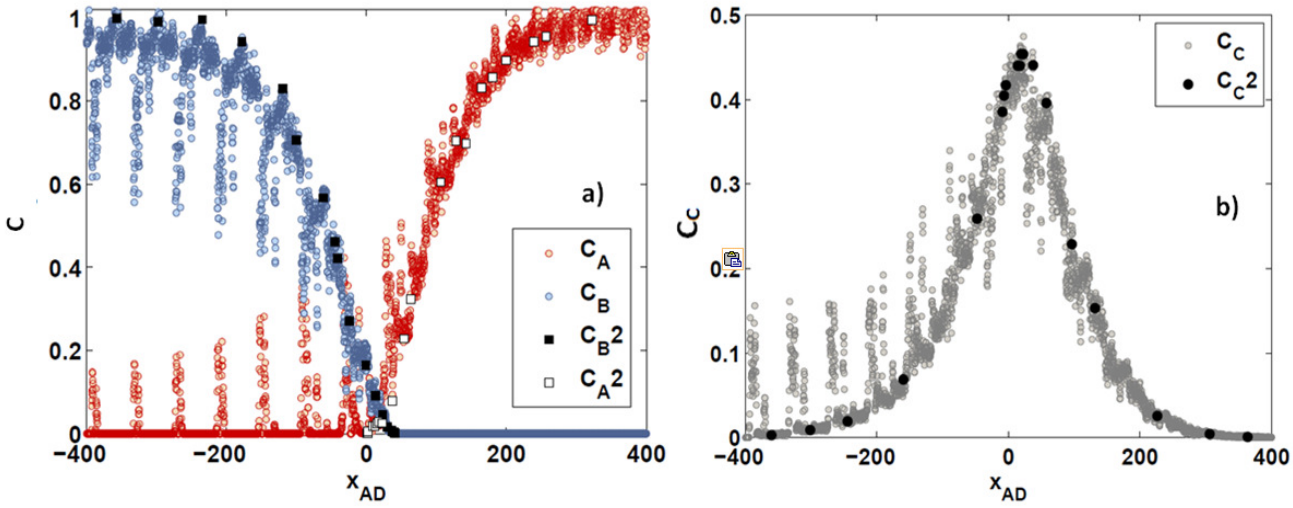

Figure 4.14 Comparison between pore-scale averaged concentrations data and selected datasets for a) reactant profiles and b) product profile at t=398.16.

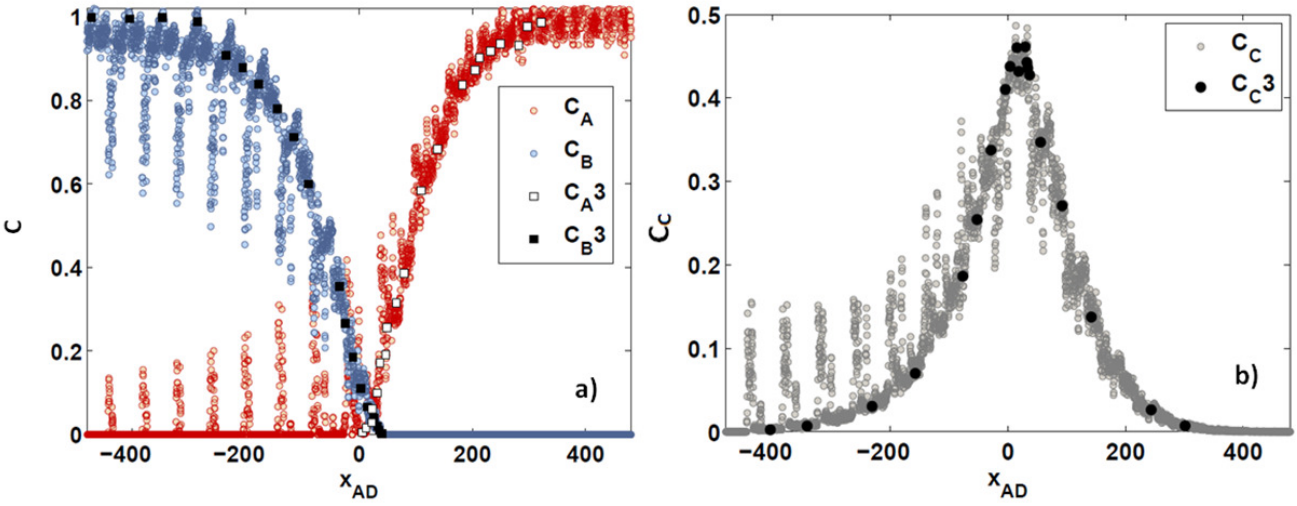

Figure 4.15 Comparison between pore-scale averaged concentrations data and selected datasets for a) reactant profiles and b) product profile at t=447.93.

For Model 5 (DRMTM) assessment, instead, different data are selected. As shown in section 2.4, the DRMT Model allows interpreting , on average, time and spatial evolution of solute entrapped in immobile regions. Hence we define a new dataset, specific for DRMT Model, including concentration oscillations appearing on backward tails of concentration profile, corresponding to dissolved matter moving slower than the advective front. We consider profiles at $t = 398.16$ and $t = 447.93$. Similarly to single continuum models, we select 20 data for each chemical profile. In the following, the specific

data selected on C_A, C_B and C_C profiles for Model 5 will be referred as reported in Table 4.4. In Figure 4.16 and Figure 4.17 the data selected are presented against all profile data.

Table 4.4 Defintion of labels for concentration datasets.

Concentration Profile	Dataset label
C_i at t=398.16 (i=A,B,C)	C_i4 (i=A,B,C)
C_i at t=447.93 (i=A,B,C)	C_i5 (i=A,B,C)

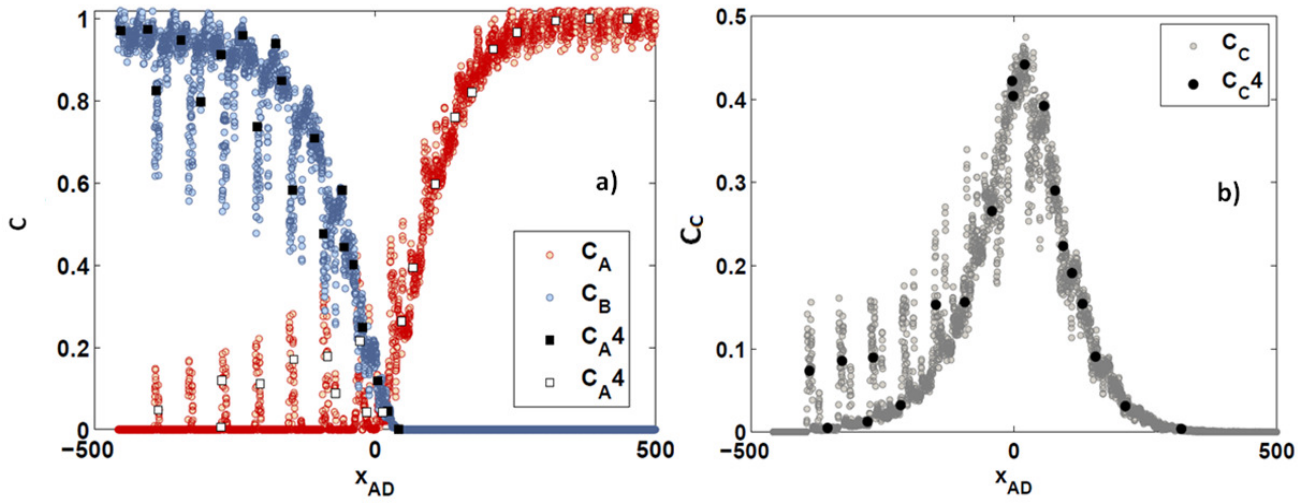

Figure 4.16 Comparison between pore-scale averaged concentrations data and selected datasets for a) reactant profiles and b) product profile at t=398.16 for DRMT Model.

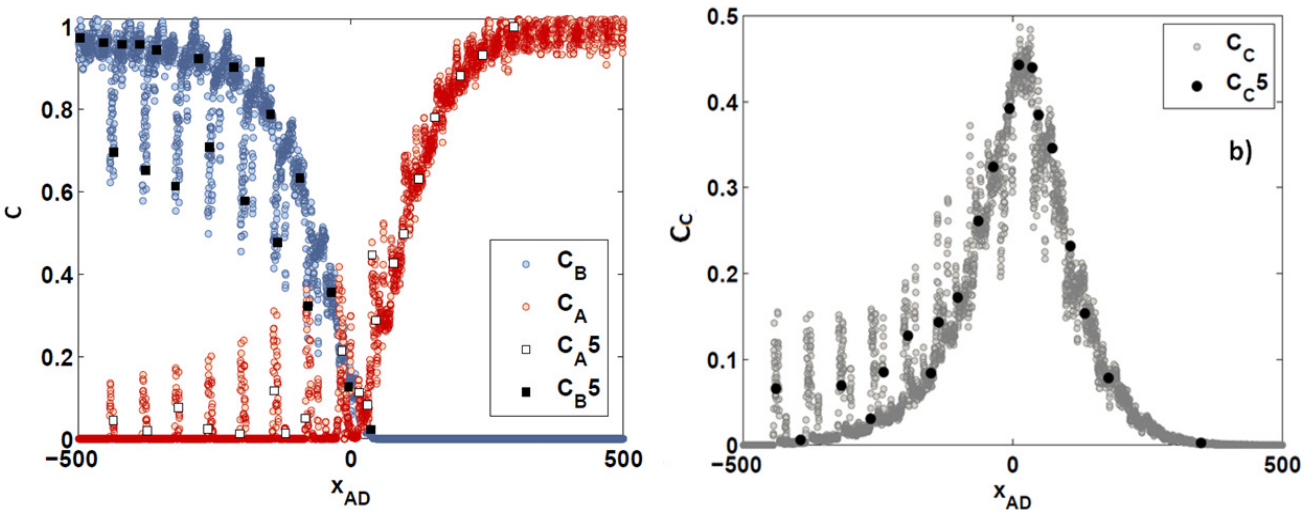

Figure 4.17 Comparison between pore-scale averaged concentrations data and selected datasets for a) reactant profiles and b) product profile at t=447.93 for DRMT model.

We summerize the different data selected for the diverse types of models in three dataset indicated in Table 4.5.

Table 4.5 Datasets summarizing table.

DATASET 1 (Single contiuum model; time-independent reaction paramenter: Model 1,2,4)	$G_C 1$ $C_A 2, C_B 2, C_c 2$ $C_A 3, C_B 3, C_c 3$
DATASET 2 (Single contiuum model; tme-dependent reaction parameter: Model 3)	$G_C 1$ $C_A 1, C_B 1, C_c 1$ $C_A 3, C_B 3, C_c 3$
DATASET 3 (DRMT: Model 5)	$G_C 1$ $C_A 4, C_B 4, C_c 4$ $C_A 5, C_B 5, C_c 5$

4.3 Single continuum models assessment

In this section we present the results related to single continuum models assessment. Each model depends on one or more parameters. For each parameter we define a range where the optimum parameter value is expected to be included. This identifies a region of interest, i.e. the so-called parameters space. The parameters ranges are then discretized and the model solution is computed for a grid of selected parameter combinations. Model solutions are used to evaluate the ability of each

combination of parameters in approximating concentration profiles and the global product time evolution observed in pore-scale simulation, i.e. the results identified in Figure 4.12-Figure 4.17. This evaluation is performed through the computation of the objective functions defined in section 2.6 in order to quantify the error committed by the model predictions compared to datasets presented in section 2.6.

In this section we compute the evolutions of f_2 (see Eq. (2.53)), f_3 (see Eq.(2.56)) and f_4 (see Eq. (2.57)).

We do not consider f_1 (see Eq.(2.51)) for concentration profiles analyses since this linear criterion has shown to be little sensitive to concentration tails which are in our case crucial zones, as explained in Chapter 3. We implement f_1 only for comparing global production time evolution predictions against G_C1 dataset (see Eq. (2.52)).

In the following, for each one of the single continuum models, we analyze the distribution of the objective functions within the selected paramente spaces. In this analysis we investigate if:

- the objective function used is a suitable candidate for the parameters estimation and models calibration procedures; indeed calibration algorithms are based on the minimization of an objective function and the calibration algorithm capability to correctly and precisely estimate the model parameters strongly depends on the evolution of objective function itself. In order to be suitable for e process, the objective function should be characterized by: i) the presence of only one minimum in the parameter space since the presence of local minima can lead to a wrong parameter estimation ii) a gradient close to zero only around the minimum value since this allows providing a more precise parameters estimation (*Carrera and Neuman, 1986*).
- the objective function chosen leads to a correct interpretation of the reactive transport process.

This analysis also provides a first estimation of dispersion and incomplete mixing parameters which allows comparing goodness of the different models at describing reactive transport. This comparison will be discussed in Chapter 5. In this sense the analysis proposed here provides a preliminary investigation for optimal calibration of the selected continuum models.

4.3.1 MODEL 1:ADRE

As explained in section 2.3.1, Model 1 formulation depends only on a single effective parameter: dispersion (D). According to the hypothesis that reactants are completely well-mixed, the reaction term (see Eq.(2.7)) depends only on the intrinsic constant reaction rate. The averaged solute transport velocity is fixed and assumed equal to u_p as explained in section 4.1. The value of dispersion may exhibit large variations depending on the system transport conditions (the *Pe* number) and on pore-scale geometry. The longitudinal coefficient D at least is equal to zero meaning that the mechanical dispersion is negligible and spreading is only governed by molecular diffusion. No upper boundaries of D can be defined since it can assume very high values depending on the porous medium geometry and associated flow field. As a consequence, dispersion parameter range varies from zero up to infinite.

Upon preliminary tests, we limit the wide parameter space to a smaller range $D \in [200, 800]$ for the problem at the hand. We recall that *D* is here a dimensionless parameter expressing the magnitude of the dispersion coefficient normalized by molecular diffusion,

To evaluate the model performance, we follow a three-step procedure: i) we sample D in the range considered as reported in Table 4.6; ii) we solve Model 1 for each dispersion value sampled; iii) we compute the objective functions using DATASET 1 for each solution performed in order to study the evolution of objective functions in the parameter space.

Table 4.6 Sampled value of dispersion parameter within 200 and 800.

D sampled value											
200	300	350	400	450	500	550	600	650	700	750	800

As shown in literature (i.e. *Gramling et al. 2002; Raje and Kapoor 2000; Sanchez-Vila et al. 2010*), Model 1 generally overestimates the product peak height and the reaction product concentration. This is due the assumption of completely well-mixed reactant mixing zone and leads to an overestimation of reaction rate. However, as shown in Chapter 3, Model 1 can provide a good fit of concentration profiles outside the mixing zone since dispersion is the prevalent process which governs solute transport in this zone.

In Figure 4.18 f_{3A_1}, f_{3B_1} and f_{2C_1} evolutions are plotted as function of dispersion. As shown in Chapter 3 these objective functions provide meaningful information for the characterization of the dispersion coefficient.

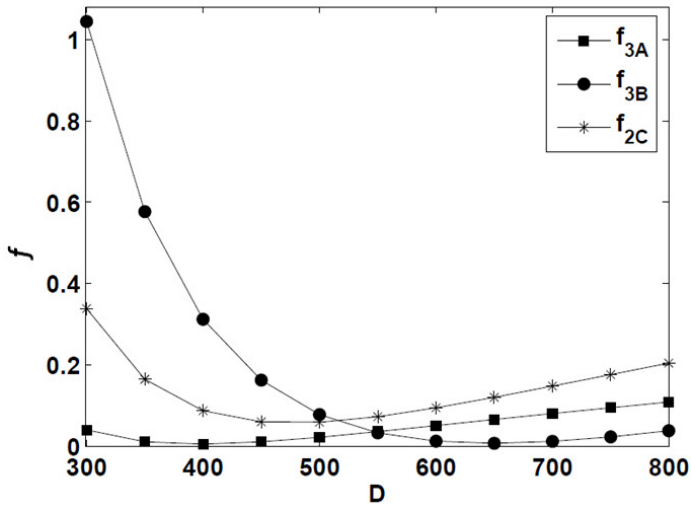

Figure 4.18 Evolution of f_{3A_1}, $f3B\_1$ and f_{2C_1} in Model 1 as function of *D*.

The functions f_{3A_1}, f_{3B_1} and f_{2C_1} present a similar behavior approaching a minimum for the considered values of *D*. However the three function identify three different optimum dispersion values: f_{3A_1} approaches its minimum (0.0056) for *D*= 400; f_{3B_1} reaches the minimum (0.0075) in *D*=650 and f_{2C_1} presents a higher minimum (0.059) in *D*=500. This result is consistent with the observations done in section 4.1. Indeed, since C_B preferentially occupies fast velocity region, this solute tends to spread quicker compared to C_A. The higher value of *D* suggested by f_{3B_1} compared to the one indicated by f_{3A_1} reflects this physical process. In section 4.1, we also observe that the two C_C profile tails present different dispersion behavior. The function f_{2C_1} identifies *D*= 500 which is an intermediate value among C_A dispersion and C_B dispersion, capturing an averaged behavior between the two tails. These observations are confirmed in Figure 4.19, where product concentrations at t=447 for different values of dispersion are compared against C_C3 data in logarithmic scale. We observe that the left tail tends to be well fitted by *D*=650 while the right one by *D*=400. This result is in agreement with finding of section 3.3 evidencing the asymmetric behavior of C_C. As a consequence, the

minimum observed value of the error function is found for an intermediate value of the parameter. Indeed, *D*=500 is suggested by criterion f_{2C_1} as the best fitting parameter for C_C profiles. In Figure 4.20, the survival functions of C_A and C_B Model 1 solutions for different dispersion values are compared to the survival functions of $C_A 3$ and $C_B 3$. Figure 4.20 shows that f_{3A_1} and f_{3B_1} correctly estimate the dispersion value since the $C_A 3$ and $C_B 3$ are well fitted with *D*=400 and *D*=650 respectively. Finally, Figure 4.21 depicts a zoomed image of reactants concentration in logarithmic scale near to the reactive front at t=447. Figure 4.21 shows that Model 1 is not able to capture concentration profiles in the mixing zone. Indeed, profiles are almost insensitive to dispersion value where the two reactants overlap and all the solutions plotted largely underestimated the $C_A 3$ and $C_B 3$ datasets.

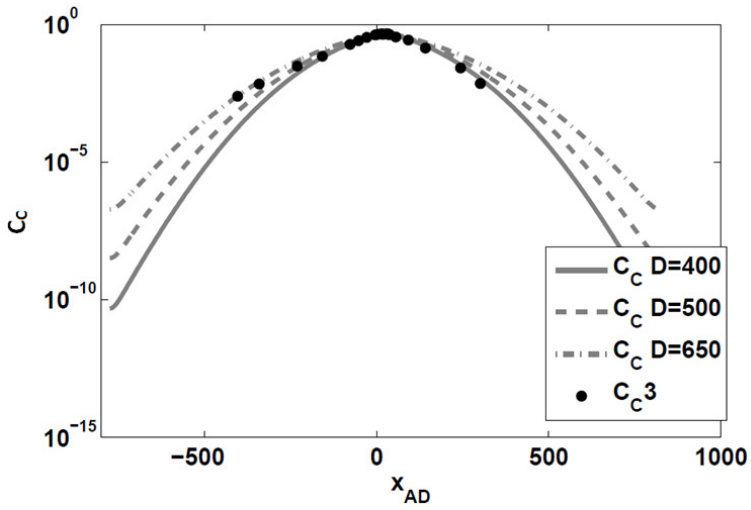

Figure 4.19 Product concentration profiles predicted by Model 1 for different dispersion value in logarithmic scale at t=447 compared to *$C_C 3$* dataset.

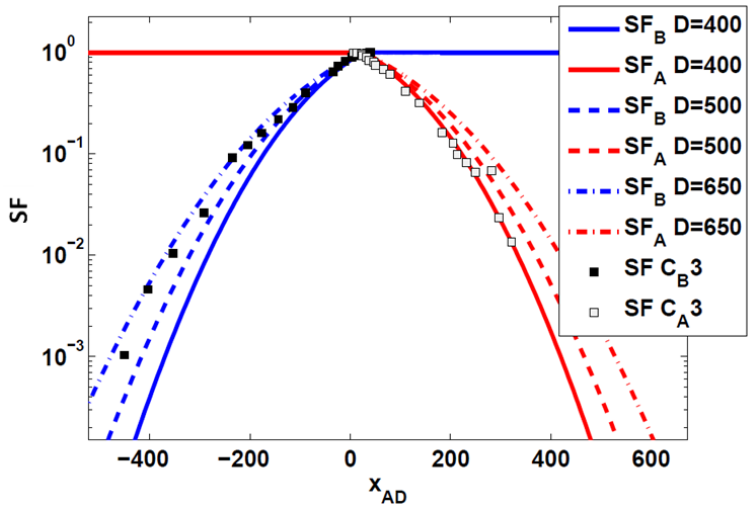

Figure 4.20 Survival function (SF) of Model 1 reactant profiles solution performed for different values of *D* at t=447 in logarithmic scale compared to survival function of C_B3 and C_A3 data.

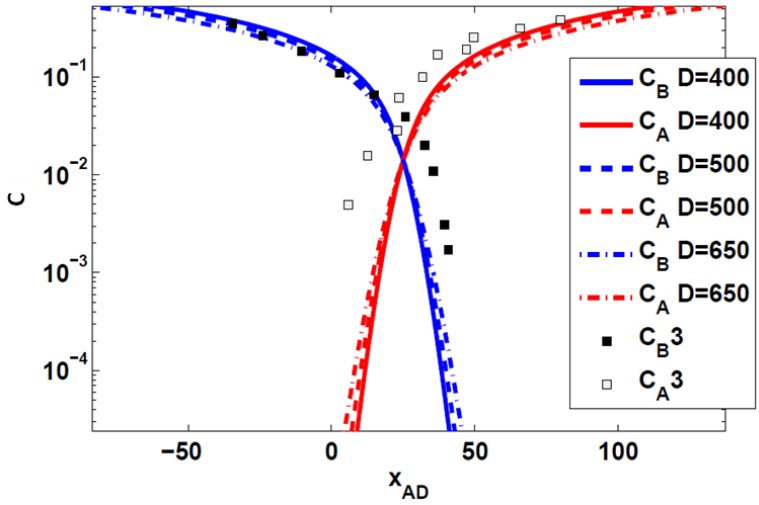

Figure 4.21 Model 1 reactant profiles solutions zoomed to the mixing zone computed for different values of *D* at t=447 are reported against C_B3 and C_A3 data in logarithmic scale.

In Figure 4.22, we report the evolution of f_{1GC} as function of *D*. The function f_{1GC} clearly identifies a global minimum in correspondence of *D*=350 which is smaller than the corresponding values found with f_{3A_1}, f_{3B_1} and f_{2C_1}. In order to investigate the reliability of this value, in Figure 4.23 we compare the global product time-evolution predicted by three different Model 1 solutions (S1, S2, S3) computed for different values of *D*. The values of *D* corresponding to S1, S2 and S3 are indicated in

Figure 4.22 by dashed black lines. Notice that S2 corresponds to D=350 which is the value estimated by f_{1GC}.

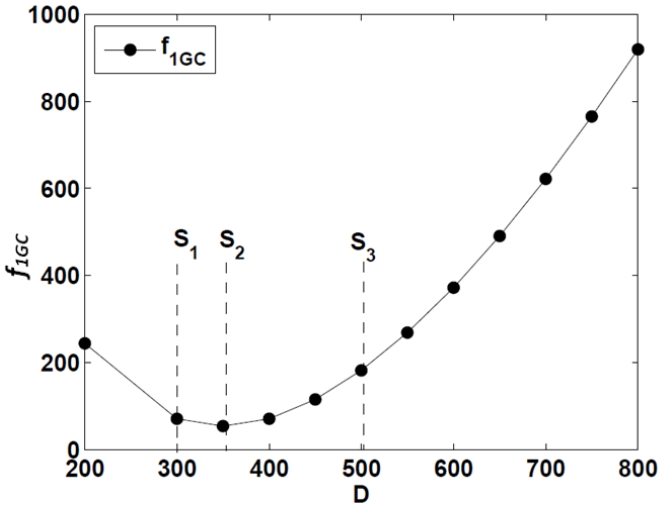

Figure 4.22 f_{1GC} Evolution as function of D computed for Model 1 solutions. The dashed black lines indicate the solutions plotted in Figure 4.23

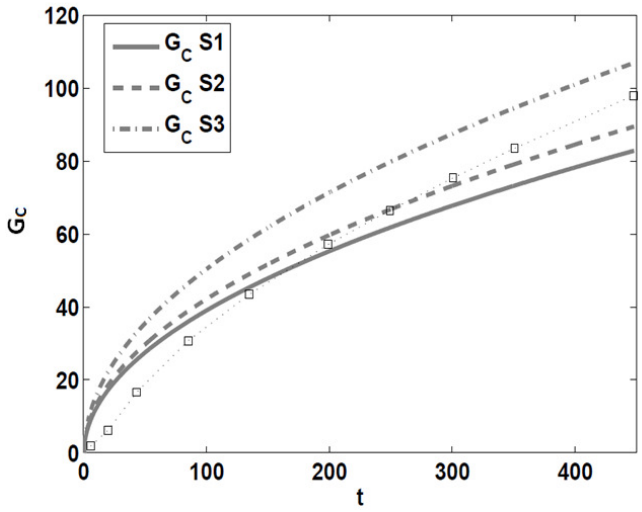

Figure 4.23 Global product evolution predicted by three Model 1 solutions relying on different dispersion value compared to G_{CI} data. The dispersion values corresponding to S1, S2 and S3 are indicated bydashed black lines in Figure 4.22.

In Figure 4.23, we observe that the solution S2 which appears to minimize the error function f_{1GC} actually is not correctly interpreting the data. Indeed S2 global product overestimates data for short times and underestimates them for long times. That means that D=350 does not capture the asymptotic behavior through which the global product observed simulation trends. Since global product evolution

is mainly governed by dispersion process, this result suggests that the dispersive process does not reach the asymptotic behavior for the problem at the hand. This is consistent with the previous theoretical and numerical results. Indeed, as shown in Figure 4.1 in previous section, the duration of pore-scale reactive transport simulated is too little to reach the asymptotic dispersion value. The analysis of pore-scale global product evolution (Figure 4.2) confirms that, at late time, it does not evolve as the square root of time which identifies the theoretically expected trend in asymptotic regime (*Porta et al. 2012b*). From this analysis we can conclude that f_{1GC} does not provide good estimation of asymptotic dispersion parameter for the ADRE model.

4.3.2 MODEL 2: Porta et al. (2012)

As explained in section 2.3.2, Model 2 formulation includes two parameters: the hydrodynamic dispersion coefficient *D* which models the dispersion and mixing processes and *B* which embeds the effect incomplete mixing between reactants according to Eq.(2.18) which is here recalled:

$$s = -\frac{Da}{Pe}\left[\left\langle C_B\right\rangle^l\left(\left\langle C_B\right\rangle^l - \left\langle C_D\right\rangle^l\right) + M\left(M-1\right)B\left(\frac{\partial\left\langle C_D\right\rangle^l}{\partial x}\right)^2\right]$$

As shown in Chapter 3, the relevant differences between Model 1 and Model 2 predictions appears in the reactant mixing zone where the reaction takes place. Far from the reaction front, the two models show a similar behavior. For this reason, we investigate the evolution of objective functions on a similar range of *D* values considered in Model 1 ($D \in [300,820]$). This range is discretized as reported in Table 4.7.

The parameter *B* is defined positive meaning that it cannot assume negative values but, in principle, it does not present an upper boundary. Note that parameter *B* can be estimated by pore-scale solution to closure problem, as mentioned in Chapter 3. Here this parameter is assumed to be unknown, since the pore-scale solution of the closure problem is not available for the geometry at the hand. The results in Chapter 3 show that the influence of parameter *B* is almost limited to the mixing zone. Upon preliminary simulations we limit the *B* range to the interval [110,500]. The latter is discretized as

reported in Table 4.7. Note that the solution of the model is provided on a grid of 14×14=196 combinations.

Table 4.7 Sampled values of dispersion (*D*) and incomplete mixing parameter (*B*).

D sampled values													
300	340	380	420	460	500	540	580	620	660	700	740	780	820
B sampled values													
110	140	170	200	230	260	290	320	350	380	410	440	470	500

According to what observed in section 4.1, the averaged solute transport velocity is fixed and assumed equal to u_p.

Figure 4.24a and Figure 4.24b represent the contour plots of the logarithmic error functions f_{2A_2} and f_{2B_2} within the parameters space identified in Table 4.7.

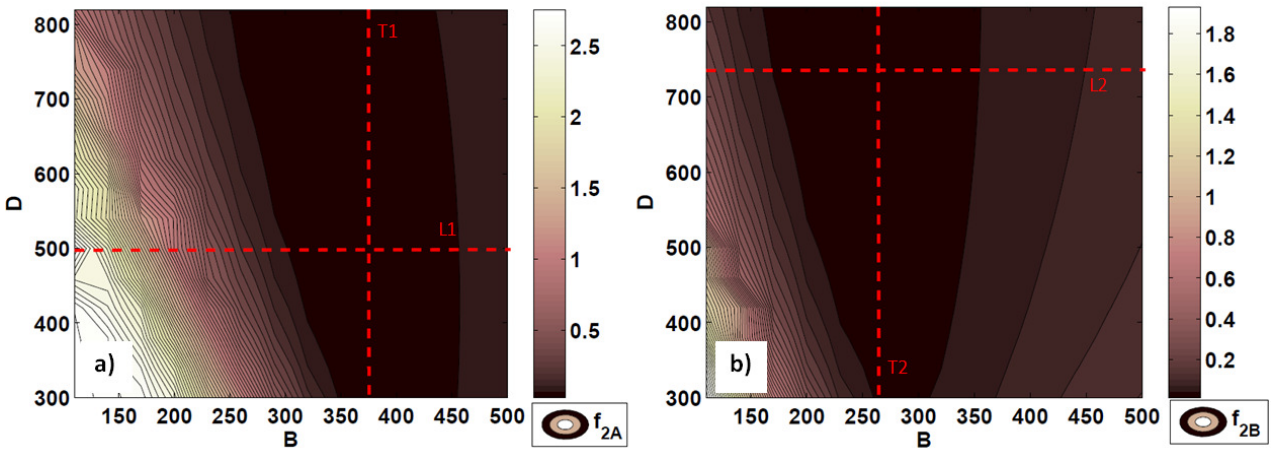

Figure 4.24 Evolution of f_{2A_2} a) and f_{2B_2} b) as function of *B* and *D*. The dashed red lines labeled T1, T2, L1 and L2 indicate the four cross sections of f_{2A_2} and f_{2B_2} depicted in Figure 4.25.

Figure 4.24 allows understanding the qualitative evolutions of f_{2A_2} and f_{2B_2} as function of different combinations of *D* and *B*. We can notice that f_{2A_2} and f_{2B_2} are sensitive to *B* parameter. The darker color (corresponding to smaller errors) is associated only to a limited range of *B* values. Concerning f_{2A_2}, it reaches its lower value for $B \in [300,450]$ while f_{2B_2} is minimized for $B \in [200,350]$.

On the other hand, it appears that f_{2A_2} and f_{2B_2} show a mild dependence on *D*. Indeed, chosen a value of *B*, f_{2A_2} and f_{2B_2} seem indifferent to a change in *D* value. However this is not true since, analyzing the specific values assumed by the functions for each combination of *D* and *B*, a global minimum does exist for a specific value of dispersion (*D*= 500 for f_{2A_2} and *D*= 740 for f_{2B_2}). This can be shown by analyzing the values assumed by the two functions along different cross sections within the parameters space. Figure 4.25 depicts vertical (T) and horizontal (L) sections of f_{2A_2} and f_{2B_2}. The sections depicted in Figure 4.25 are indicated in Figure 4.24 by the two red dashed lines labeled as T1 and L1 for f_{2A_2} and as T2 and L2 for f_{2B_2}. The cross-section positions of T1, T2, L1 and L2 are chosen depending on the locations of f_{2A_2} and f_{2B_2} minima, i.e. their crossing point of T1 and L1 identifies the parameters combination in which f_{2A_2} is minimized (Figure 4.24a) and, similarly the crossing point of T2 and L2 indicates the location of f_{2B_2} minimum (Figure 4.24a).

Figure 4.25a allows indentifying the optimum value of dispersion coefficient while Figure 4.25b allows detecting the value of *B* that minimize f_{2A_2} and f_{2B_2} (*B*=350 and *B*= 230 respectively). Figure 4.25a and Figure 4.25b show that both the parameters influence the function value but that the criteria considered are strongly sensitive to *B* and slightly to *D*. Figure 4.25a evidences that, even if minima are detected, f_{2A_2} and f_{2B_2} display small variations for a large interval of *D* values. As explained in section 4.3, this feature is not desirable for an objective function involved in the calibration process, since it would lead to parameters estimates plagued by considerable uncertainty. On the other hand, Figure 4.25b shows that f_{2A_2} and f_{2B_2} are reliable functions for incomplete mixing parameter estimation: the global minima are easy detectable since the function gradients increase rapidly also for little displacement of *D* from the minimum. This different sensitivity to *B* and *D* is due to formulation of f_2 (see Eq. (2.53)). Investigating the logarithmic values of concentration, f_2 gives more relevance to reactant tails in the mixing zone where the curves are largely influenced by the incomplete mixing local reaction parameter and only slightly by dispersion. Indeed, the errors performed on data far from the reactive front, which are affected by dispersion values (*D*), poorly influence the f_{2A_2} and f_{2B_2} evolutions.

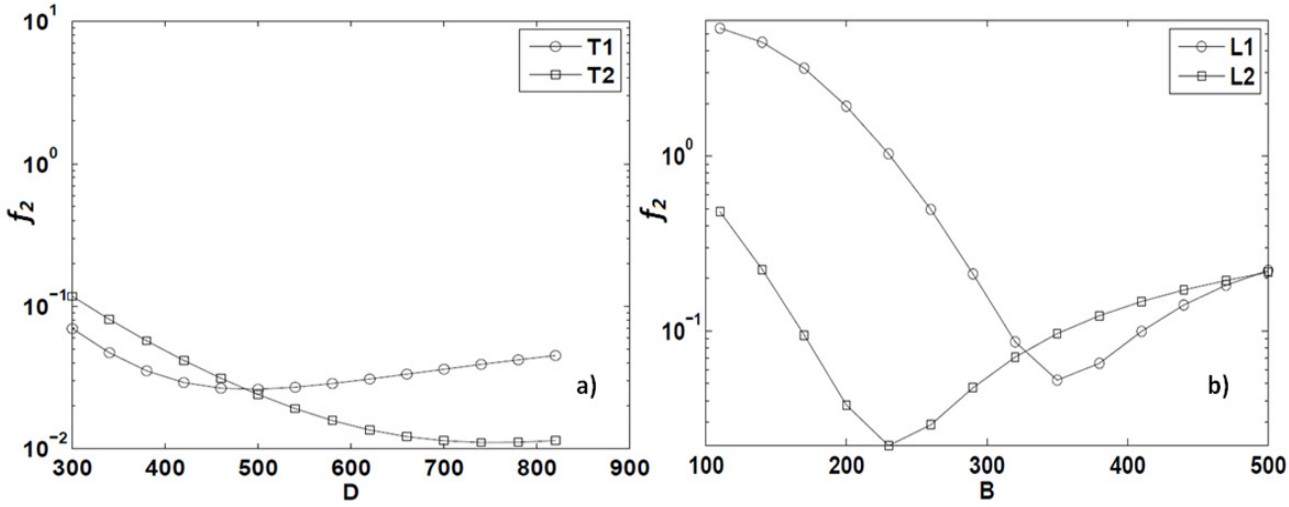

Figure 4.25 Evolution of a) f_{2A_2} and b) f_{2B_2} as function of *D* and *B* along the sections T1, T2 and L1, L2 indicated in Figure 4.24 through red dashed lines.

The lowest reached values of f_{2A_2} and f_{2B_2} and the corresponding combination of the parameters *B* and *D* for which they are reached are reported in Table 4.8.

Table 4.8 f_{2A_2} and f_{2B_2} minimum values and the combination of *B* and *D* for which they are reached

Function	Minimum	(D;B)
f_{2A}	0.026	(500;350)
f_{2B}	0.011	(740;230)

Confirming what observed in Model 1 analysis, the two reactants are characterized by different behaviors and as a consequence f_{2A_2} and f_{2B_2} identify two diverse combinations of values as optimal (Table 4.8). Moreover we note that the minimum computed value of f_{2A_2} is approximately double the minimum value attained for f_{2B_2}, i.e. in general the error associated to prediction of C_B is smaller than that associated to C_A.

In order to test the parameter estimations performed, in Figure 4.26, we plot the survival function of reactant profiles solutions (at t=447) computed with the two combinations of *D* and *B* reported in Table 4.8. These solutions are compared to the datasets $C_A 3$ and $C_B 3$. We observe that *D*=740 overestimates the longitudinal dispersion observed for $C_B 2$ and, similarly, *D*=500 for $C_A 2$.

In Figure 4.27 a zoomed image of reaction zone is presented and chemical concentrations are represented in a semi-logarithmic scale. The C_A2 data present an oscillatory behavior. However imposing *B*=350, Model 2 is able to capture the averaged trend of C_A2 data. The data of C_B2 datasets are characterized by smaller oscillations and are particularly well predicted by Model 2 solution with *B*=260 since Model 2 solution and C_B2 data are really close. The absence of strong oscillations on C_B2 data explains why the f_{2B_2} minimum value is consistently lower than f_{2A_2} one (see Figure 4.25 and Table 4.8).

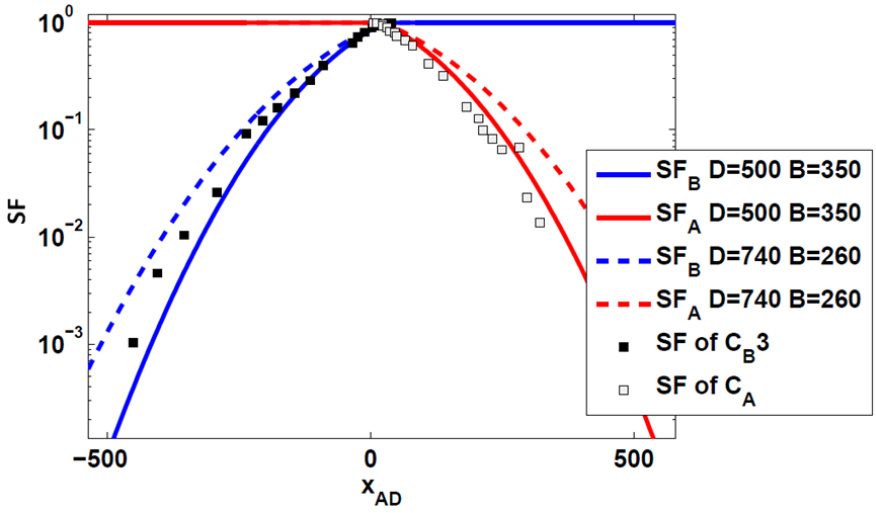

Figure 4.26 Survival function (SF) of reactant profiles given by the two Model 2 relying on different *D* and *B* values compared to survival function of C_A3 and C_B3 data.

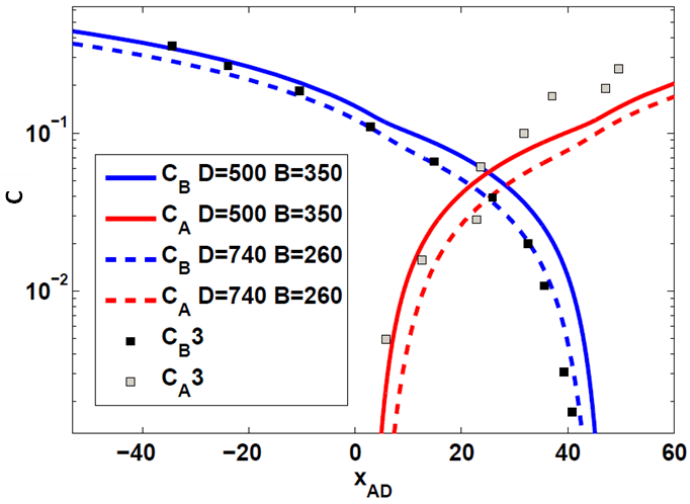

Figure 4.27 Reactant profiles in the mixing zone given by two Model 2 solutions relying on different *D* and *B* values compared to survival function of C_A3 and C_B3 data.

On the basis of the results presented above, we analyze the distribution of f_4 evolution as function of parameters to improve the estimation of longitudinal dispersion. In the following we analyze the evolution of f_{4A_2} (Figure 4.28a), f_{4B_2} (Figure 4.28b) and f_{4C_2} (Figure 4.30) as function of *D* and *B*.

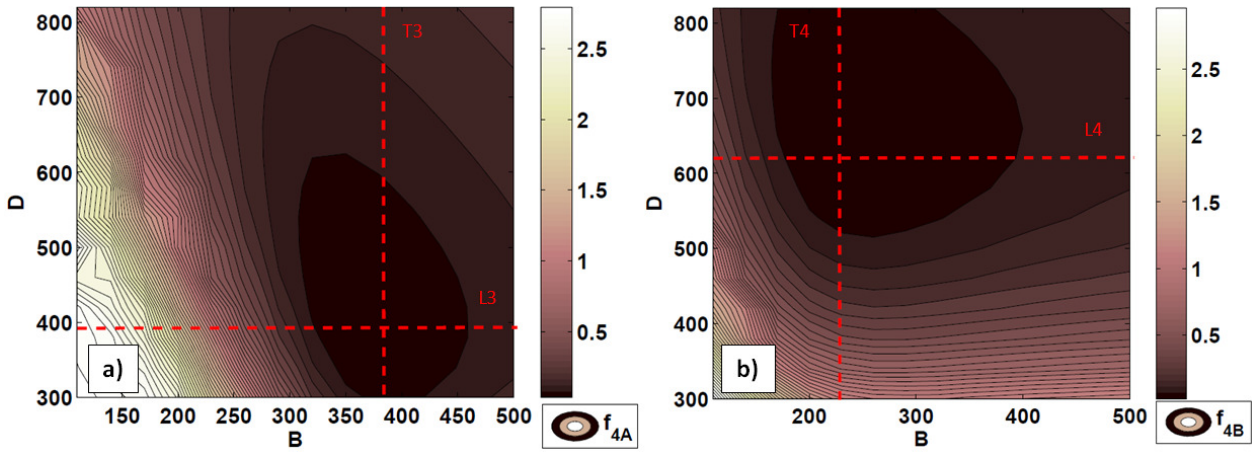

Figure 4.28 Evolutions of f_{4A_2} (a) and f_{4B_2} (b) as function of *B* and *D*. The dashed red lines labeled as T3, T4, L3 and L4 indicate the four cross sections of f_{4A_2} and f_{4B_2} depicted in Figure 4.29-.

The functions f_{4A_2} and f_{4B_2} show common features: the contour lines shape shows that of f_{4A_2} and f_{4B_2} exhibit a convex shape and are characterized by a single minimum. As a consequence, we can affirm that f_{4A_2} and f_{4B_2} are sensitive to both *B* and *D* values identifying a global minimum for a

single combination of parameters. Analyzing the single values that f_{4A_2} and f_{4B_2} assume for all the different combination of *B* and *D* we observe that:

- f_{4A_2} reaches its minimum (equal to 0.0664) where *D*=380 and *B*=380;
- f_{4B_2} is minimized if *D*=660 and *B*=230; its lowest value is 0.0399.

In Figure 4.28 f_{4A_2} and f_{4B_2} minimum locations are identified by the crossing points of two couples of red dashed lines labeled T3 and L3 in Figure 4.28a and T4 and L4 in Figure 4.28b.

To evidence the evolution of f_{4A_2} and f_{4B_2} and the minima reached, in Figure 4.29a we analyze the trends of f_{4A_2} and f_{4B_2} along T3 and T4 respectively as function of *D*. Similarly, f_{4A_2} and f_{4B_2} evolutions are investigated along L3 and L4 respectively as function of *B* in Figure 4.29b.

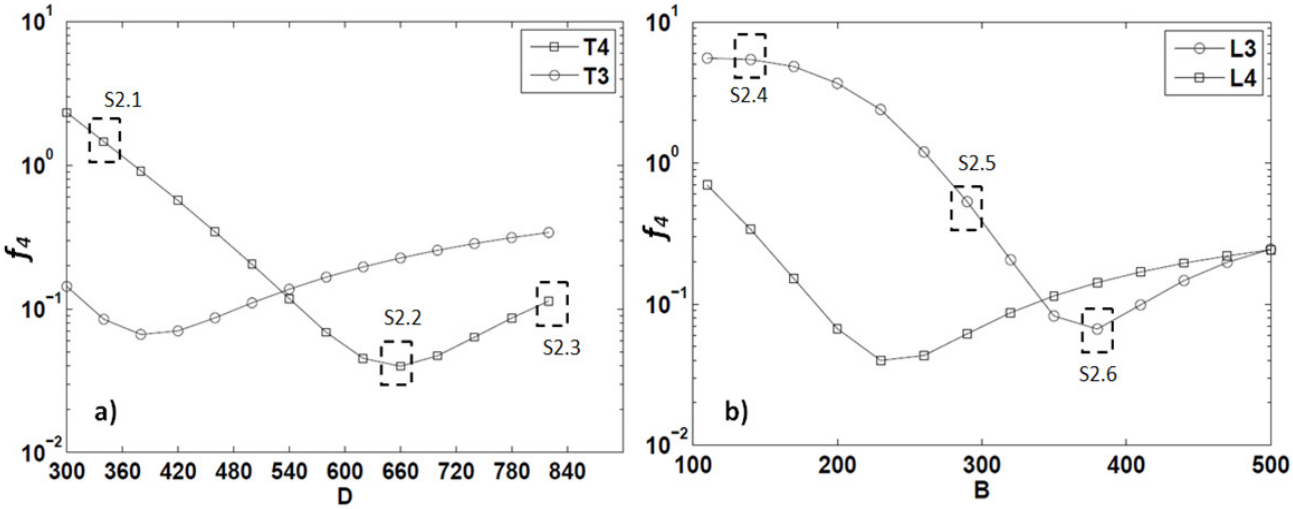

Figure 4.29 Evolution of a) f_{4A_2} and b) f_{4B_2} as function of *D* and *B* along the sections T3, T4 and L3, L4 indicated in Figure 4.28 through red dashed lines.

Comparing Figure 4.29a to Figure 4.25a, we can observe that f_{4A_2} and f_{4B_2} present a more general gradient as a function of *D* if compared to f_{2A_2} and f_{2B_2} (compare Figure 4.25 to Figure 4.29). As previously observed f_{2A_2} and f_{2B_2} are practically flat characterized by a gradient close to zero for a large range of dispersion values. As a consequence, f_{4A_2} and f_{4B_2} are more sensitive to dispersion parameter and more suitable for the estimation of dispersion parameter than f_{2A_2} and f_{2B_2}.

Increasing the sensitivity to D does not lead to depletion in function sensitivity to B. Indeed, Figure 4.29b shows that the optimum value of B is clearly identified for values similar to those obtained through the criteria f_{2A_2} and f_{2B_2}. As already observed, Figure 4.29 evidences that performing estimations on C_A and C_B profiles separately, leads to different parameter estimations. In agreement with previous results in section 4.3.1and section 4.1, C_A profiles are characterized by a steeper gradients as compared to C_B ones, which lead to the identification of a smaller optimal dispersion coefficient for C_A than for C_B. The dispersion parameter estimations are close to ones obtained for Model 1.

In Figure 4.30 we present f_{4C_2} evolution as function of parameters and the crossing point of the two red dashed lines (L5 and T5) illustrates f_{4C_2} minimum position (D=460 and B=290). For similar reasons presented for criteria f_{4A_2} and f_{4B_2}, the function f_{4C_2} configures as a valuable objective function for the calibration of the two selected parameters, B and D. We observe that f_{4C_2} identifies a third different combination of D and B as optimum which corresponds to an intermediate solution between f_{4A_2} and f_{4B_2} parameter estimations (compare Figure 4.30 to Figure 4.28).

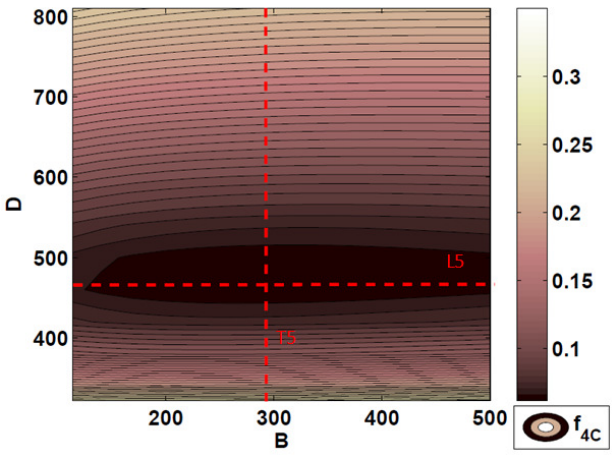

Figure 4.30 Evolution of f_{4C_2} as function of B and D. The dashed red lines labeled T5 and L5 indicate the position of the function minimum value.

To conclude this analysis, we select different Model 2 solutions along the section T4 and L3 in order to investigate the behavior of the corresponding predicted chemical concentrations as function of the two unknown parameters. The combinations of parameters chosen are indicated in Figure 4.29 through

dashed black lines and by a label. For the sake of clarity, all the solutions considered are listed in Table 4.9 and identified in Figure 4.31 with the corresponding labels and parameter combinations.

Table 4.9 Combination of parameter of Model 2 solutions analyzed in Figure 4.32 and Figure 4.33 with associated labels.

Label solution	(D;B)
S2.1	(340;230)
S2.2	(660;230)
S2.3	(820;230)
S2.4	(380;140)
S2.5	(380;290)
S2:6	(380;380)

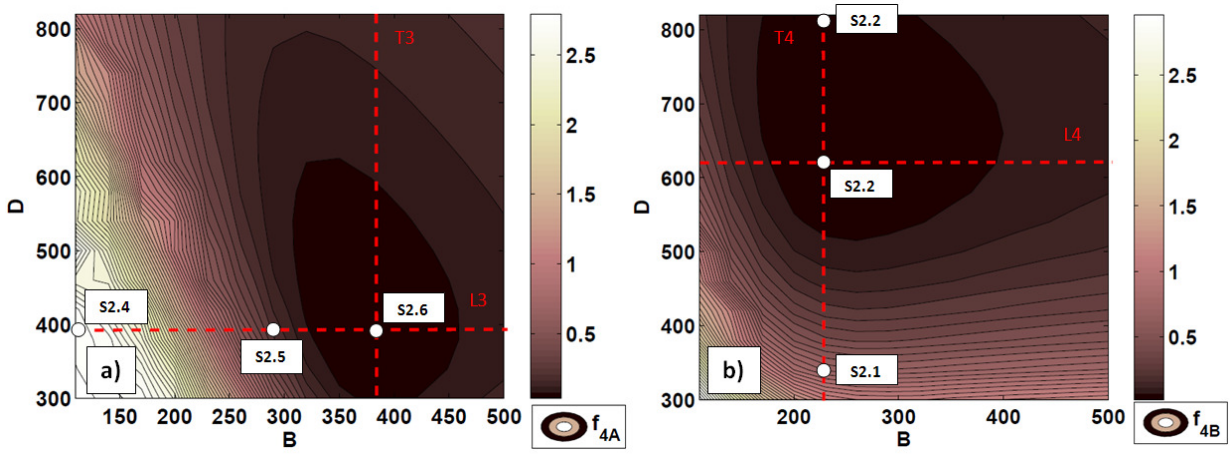

Figure 4.31 Evolution of f_{4A_2} (a) and f_{4B_2} (b) as function of *B* and *D*. The dashed red lines labeled as T3,T4, L3 and L4 indicate the four cross sections of f_{4A_2} and f_{4B_2} depicted in Figure 4.29. White dots indicate the solutions reported in Table 4.9 within the space of the parameter and the correspondent labels.

In Figure 4.32 and Figure 4.33 different Model 2 solutions are compared to C_A3 and C_B3 data in order to allow performing a qualitative sensitivity analysis of chemical profiles to parameters.

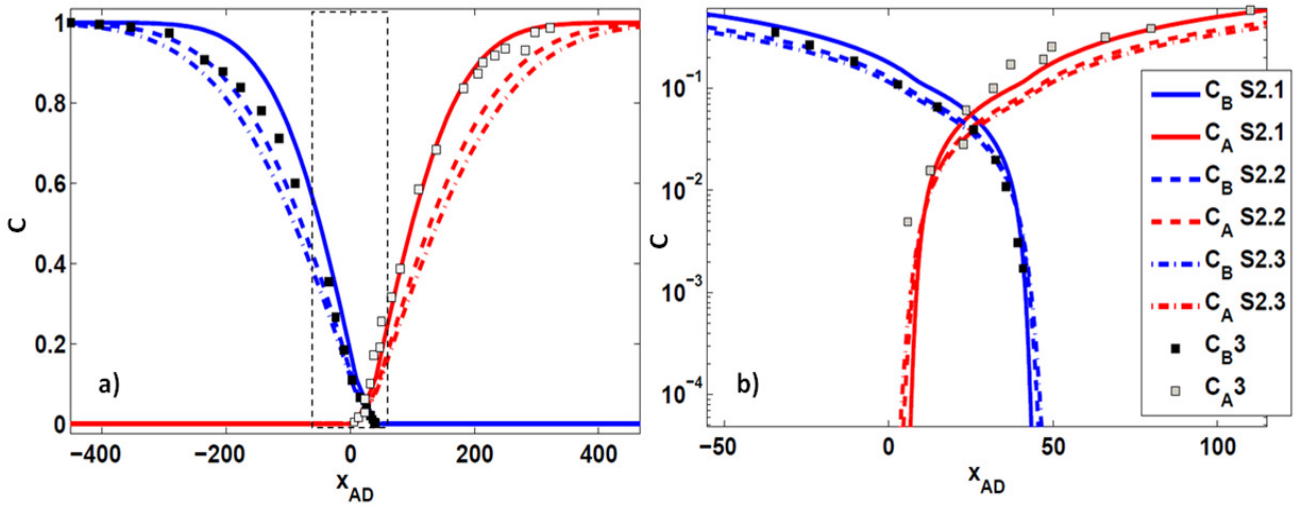

Figure 4.32 a) Reactant profiles yielded by S2.1, S2.2 and S2.2 compared to C_A3 and C_B3 data at t=447. Figure b) provides a zoomed image of reactive zone delimitated in figure a) by dashed black line.

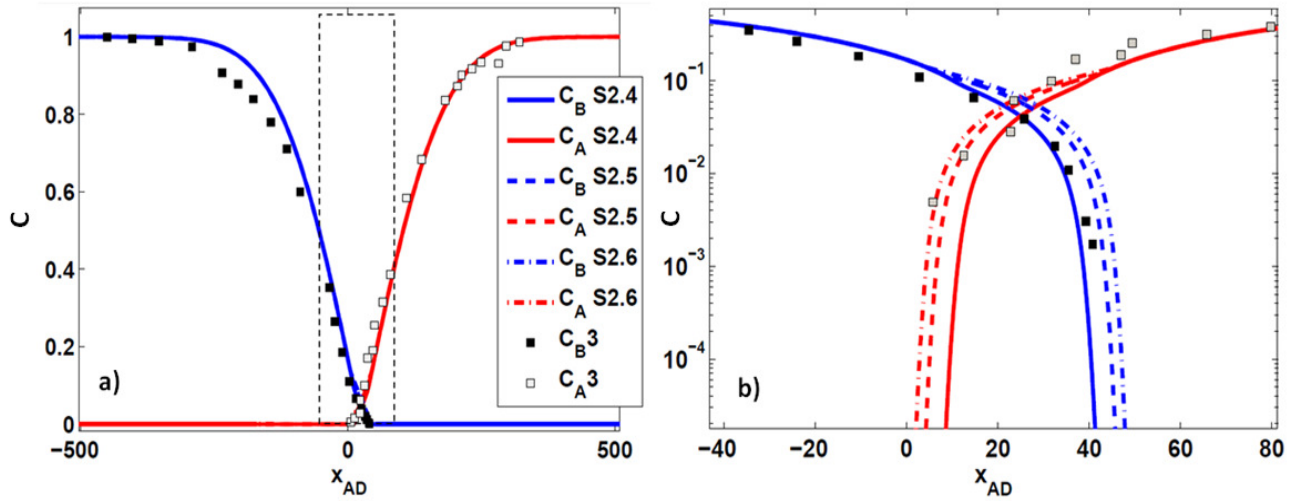

Figure 4.33 a) Reactant profiles yielded by S2.4, S2.5 and S2.6 compared to C_A3 and C_B3 data at t=447. Figure b) provides a zoomed image of reactive zone delimitated in figure a) by dashed black line.

In Figure 4.32 we compare S2.1, S2.2 and S2.3 reactant profiles predictions at t=447 against C_A3 and C_B3 data. Figure 4.32b is a zoomed image of reactant mixing zone delimitated by black dashed line in Figure 4.32a. We observe that the dispersion coefficient strongly influences the chemical profiles only outside the mixing zone confirming previous findings of Chapter 3. Figure 4.33, instead, reports S2.4, S2.5 and S2.6 reactant profiles predictions at t=447 against C_A3 and C_B3 data. Figure 4.33b is a zoomed image of reactant mixing zone delimitated by dashed line in Figure 4.33a. Figure 4.33a shows

that parameter *B* does not influence the solution outside the mixing zone (for $x_{AD}<0$ and $x_{AD}>60$) and its effect is visible only within the reaction zone ($0<x_{AD}<60$): if *B* increases, reactant concentration profiles assume larger values. This allows modeling incomplete mixing effects, i.e. the inhibition of the reaction process due to pore-scale segregation of reactants. In Figure 4.32b, it appears that reactant profiles sensitivity with respect to dispersion coefficient is quite limited. However, an important influence does exist and it is disclosed on product profiles. Figure 4.34a depicts different Model 2 product profile solutions at t=447 for different values of *D* while *B* is fixed equal to 230. Here we observe that, as expected, increasing dispersion leads an increment of product profile spreading and on the maximum observed product concentration. In Figure 4.34b we present a zoomed imaged of the product concentration peak indicated by a dashed red line in Figure 4.34a. For fixed *B* and time, the product concentration peak is proportional to *D* meaning that incomplete mixing affects the product generation with less intensity. This influence can be explained looking at Model 2 reaction term mathematical formulation. Looking at Eq. (2.18), we can notice that the source term s embedding the incomplete mixing effect depends on $\frac{\partial \langle C_D \rangle^l}{\partial x}$, i.e. on the longitudinal gradient of the conservative component *D*. The time evolution of this gradient is in turn dependent on dispersion parameter. That means that when dispersion increases, $\langle C_D \rangle^l$ spreads quicker and its gradient along *x* rapidly smoothes with time in the mixing zone. As a consequence the incomplete mixing effect decreases rapidly proportional to the decrement of conservative component C_D gradient with time allowing to higher product concentration peak and lower reactants concentrations in the mixing zone independently from *B* value.

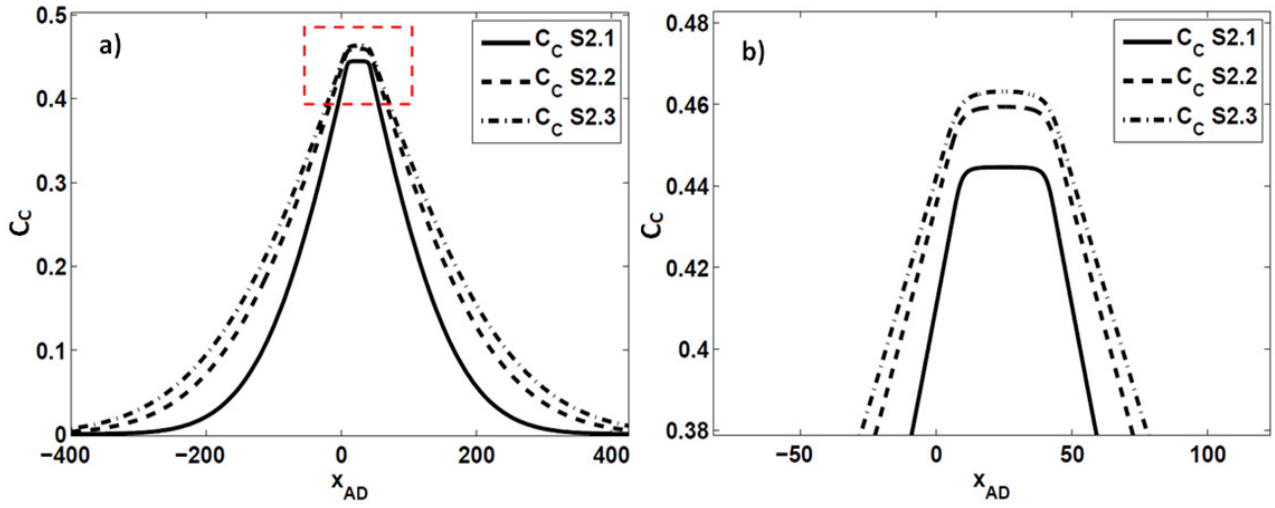

Figure 4.34 a) Product profiles yielded by S2.1, S2.2 and S2.2 at t=447. Figure (b) provides a zoomed image of peak zone delimitated in figure a) by dashed red line.

Figure 4.35 depicts the f_{1GC} evolution as function of the two parameters. Figure 4.35 evidences that f_{1GC} shows its lower value for *D*=380. This value is very close to the one estimated in Model 1 for the same objective function considering the same dataset (see Figure 4.22). According to the considerations done in section 4.3.1, we recall that *D*=380 is an incorrect estimation of the dispersion parameter not capturing chemical real spreading process.

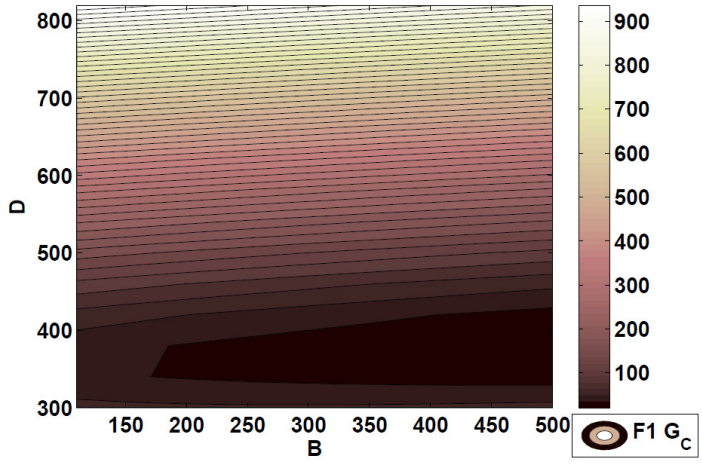

Figure 4.35 Evolution of f_{1GC} as function of B and D.

4.3.3 MODEL 3: Sanchez-Vila et al. (2010)

As shown in section 2.3.3, Model 3 depends on three effective parameters: D, $\hat{\beta}_0$ and m. Notice that $\hat{\beta}_0$ is dimensional while D and m are dimensionless according to Eq. (2.24) and Eq. (2.23). The formulation of Model 3 dispersive term (Eq. (2.25)), which includes the parameter D, is similar to Model 1 and Model 2. Indeed in all the three model dispersion process is assumed to be Fickian. For this reason, Model 3 is expected to have a behavior similar to Model 1 and Model 2 outside the mixing zone, where the incomplete mixing does not affect the solution (see Chapter 3 and section 4.3.2). As a consequence we can assume that dispersion estimation in Model 3 would lead to similar values estimated for Model 1 and Model 2. Then we select only three fixed values of dispersion (D=400, D=500, D=600) and focus the analyses on the role of $\hat{\beta}_0$ and m which affect profile solutions close to reactive front. The choice of the three dispersion values is based on the estimations performed for Model 1 (see section 4.3.1) and for Model 2 (see section 4.3.2). According to these results, it possible to conclude that: i) a dispersion value close to 400 can depicts C_A profiles; ii) a dispersion value close to 600 fits C_B concentration profiles; ii) a dispersion value close to 500 captures the C_C average spreading.

The two parameters $\hat{\beta}_0$ and m are included in Model 3 reaction rate described by Eq. (2.22)-(2.23) here recalled:

$$s = \hat{\beta}\langle C_A\rangle^l \langle C_B\rangle^l = \hat{\beta}_0 t^{-m} \langle C_A\rangle^l \langle C_B\rangle^l$$

Those are both positive and no upper boundaries are identified. This means that $\hat{\beta}_0$ and m can assume any positive value. Upon preliminary solutions of Model 3, we have limited the theoretically infinite parameter space to finite domain in which the combination of fitting parameters is included for the problem at the hand. The value of $\hat{\beta}_0$ varies in [0.0324,649] and m in $[0,1]$. These intervals are then discretized as shown in Table 4.10 and a Model 3 solution is numerically computed for each one of the 77 parameters combinations.

Table 4.10 Value of Model 3 parameter sampled for objective function evolution analysis.

$\hat{\beta}_0$ sampled values								
0.03	3.24	9.73	19.46	32.43	97.31	194.62	324.37	421.68
m sampled values								
0.005	0.010	0.030	0.060	0.100	0.500	0.800	1.000	

The results in section 4.3.2 show that the objective function f_2 should provide a reliable criterion for the identification of optimal parameters which governs the reaction process in the mixing region. The f_{2A_3} and f_{2B_3} evolutions are investigated in the following. Here we also present the function f_{3C_3}. As shown in Chapter 3, it allows stressing the discrepancy between C_C predictions and concentration observed in pore-scale data only in the region centerd on the peak. Indeed, C_C profiles far from the reaction front are not interesting in this analysis since it is governed practically by dispersion alone which is constant. For objective function computation, we use DATASET 2 (see Table 4.5) for the reasons explained in section 4.2.

In the following, only function evolutions computed with *D*=500 are reported and commented since results for *D*=600 and *D*=400 are analogous and lead to similar considerations.

In Figure 4.36a, Figure 4.36b and Figure 4.37, we depict f_{2A_3}, f_{2B_3} and f_{3C_3} evolutions as function of the two parameters $\hat{\beta}_0$ and m logarithmic values. The locations of lower values (i.e. the darker areas in Figure 4.36a, Figure 4.36b and Figure 4.37) and the contour lines shape, suggest that f_{2A_3}, f_{2B_3} and f_{3C_3} evolutions in parameter space are "U-shaped". Indeed, the three function reach their lower values along a strip centered in $\log(\hat{\beta}_0)=1$ for f_{2A_3} and f_{2B_3} and in $\log(\hat{\beta}_0)=0.5$ for f_{3C_3}. That means that the three functions are sensitive to the parameter $\hat{\beta}_0$. As a consequence, f_{2A_3}, f_{2B_3} and f_{3C_3} represent good objective functions for the estimation of $\hat{\beta}_0$.

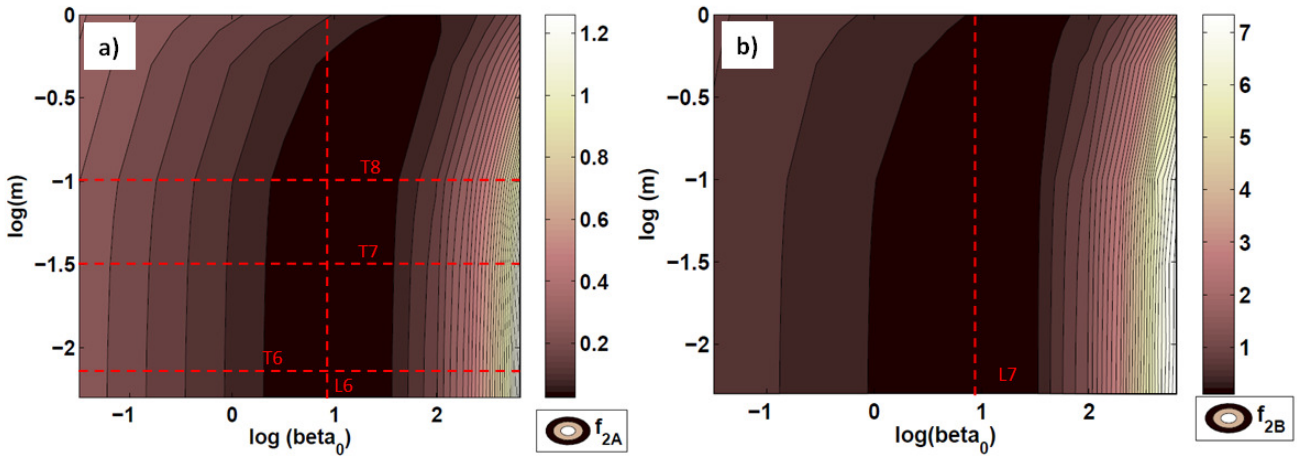

Figure 4.36 Evolutions of a) f_{2A_3} and b) f_{2B_3} as function of parameters. The red dashed lines indicate the position of function sections reported in Figure 4.38 and Figure 4.39.

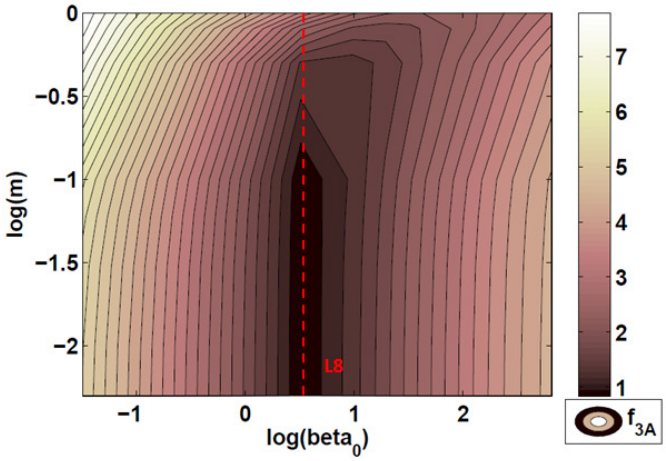

Figure 4.37 Evolution of f_{3C_3} as function of parameters. The red dashed line labeled as L8 indicates the position of the function section reported in Figure 4.39.

In Figure 4.38 we depict the evolution of f_{2A_3} as function of $\log(\hat{\beta}_0)$ along three sections T6, T7 and T8 indicated by red dashed lines in Figure 4.36a. Figure 4.38 confirms that f_{2A_3} an easily detectable minimum for $\hat{\beta}_0$ exists since the three curves all present a marked concavity. The three sections considered correspond to diverse values of m as shown in Figure 4.36a. As a consequence, the minimum reached by f_{2A_3} appears to be almost independent of the assumed m value. Similar investigations on Figure 4.36 and Figure 4.37 lead to analogous considerations on f_{2B_3} and f_{3C_3} behaviors. Then, to better understand the influence of m, the trends of f_{2A_3}, f_{2B_3} and f_{3C_3} are analyzed as function of m along three longitudinal sections L6, L7 and L8. The longitudinal sections

considered are indicated in Figure 4.36 and Figure 4.37 using dashed red lines and correspond to optimum value of $\hat{\beta}_0$ identified by each function. Figure 4.39 reports f_{2A_3}, f_{2B_3} and f_{3C_3} along L6, L7 and L8 respectively. The functions f_{2A_3}, f_{2B_3} and f_{3C_3} show a common behavior: as m decreases, the functions value decrease. However, for values of m smaller than 0.06 (corresponding in Figure 4.39 to log (m) =-1.22) the three curves assume a constant value and the three criteria are insensitive to m value. Parameter m quantifies the dependence of reaction rate on time (Eq. (2.22)-(2.23)). Our results suggest, instead, that the dependence on time of the reaction constant as formulated in Model 3 does not provide a significant improvement in fitting concentration profiles observed in pore-scale simulations. As a consequence, Model 3 tends to assume a formulation close to the ADRE model one where the reaction term is proportional to an effective reaction rate smaller than the intrinsic one.

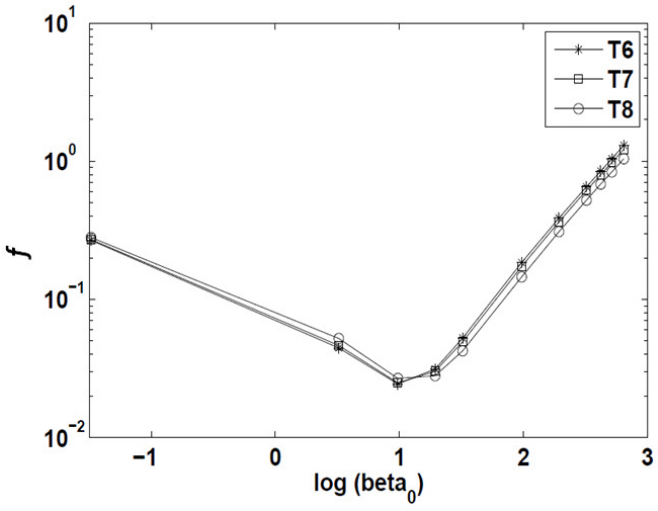

Figure 4.38 Evolution f_{2A_3} as function of log (β_0) along the three traverse sections T6, T7 and T8 indicated in Figure 4.36a through red dashed lines.

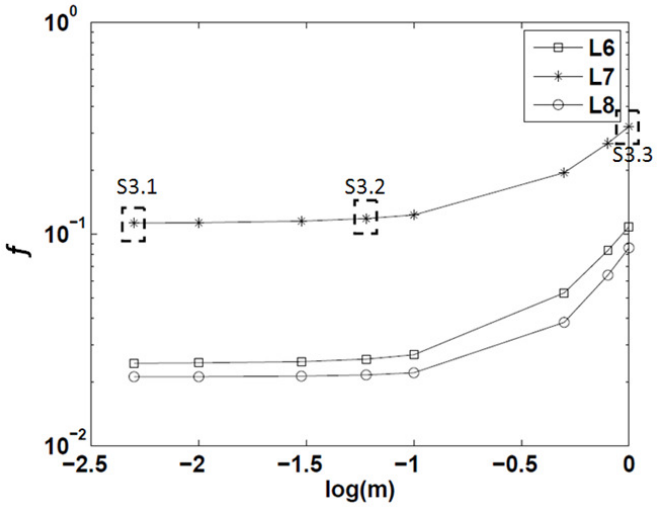

Figure 4.39 Evolutions of *f2A_3*, *f2B_3* and *f3C_3* as function of *m* along the longitudinal cross sections L6, L7 and L8 respectively. The locations of L6, L7 and L8 are indicated in Figure 4.36 and Figure 4.37.

The negligible influence of *m* can be highlighted also analyzing concentration profiles. We select three Model 3 solutions (labeled as S3.1, S3.2 and S3.3) computed for a fixed value of $\hat{\beta}_0$=9.73 and different values of *m*. The solutions selected are indicated in Figure 4.39 through black dashed lines. For the sake of clarity, we report the three solutions selected with the corresponding parameter combinations and labels in Table 4.11 and Figure 4.40.

Table 4.11 Combination of parameter of Model 3 solutions analyzed in Figure 4.42 and Figure 4.42 with the corresponding labels.

Solution label	(D, $\hat{\beta}_0$, m)
S3.1	(500, 9.73,0.005)
S3.2	(500, 9.73,0.06)
S3.3	(500, 9.73,1)

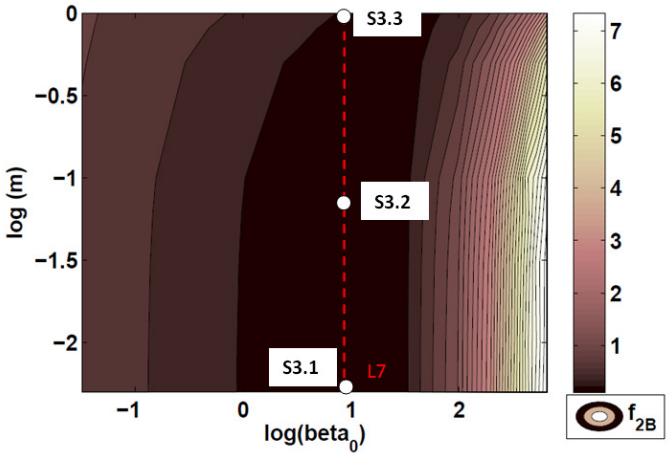

Figure 4.40 Evolution of f_{2B_3} as function of parameters. The red dashed lines indicate the position of function sections reported in Figure 4.38 and Figure 4.39. The white dots indicate the Model 3 solutions investigated in Figure 4.42 and Figure 4.42 and the corresponding labels.

The chemical species profiles at t=447 corresponding to S3.1, S3.2 and S3.3 are plotted in Figure 4.41 and Figure 4.42 and are compared to pore-scale averaged concentrations. In particular, Figure 4.41 depicts the reactant profiles: we observe that even as *m* changes its value, no influence is visible on reactant concentrations and S3.1, S3.2 and S3.3 are practically coincident. Similar considerations are derived looking at Figure 4.42a where the three product profile predictions corresponding to S3.1, S3.2 and S3.3 are illustrated and compared to $C_A 3$ and $C_B 3$. Indeed, since the overall profiles are mainly influenced by dispersion, as shown in section 4.3.2, the parameter *m* is expected to influence only the mixing zone and the height of the peak of the CC concentration profile. In Figure 4.41b, we present a zoomed image of the reactive zone delimited in Figure 4.41a through a black dashed line. Slight sensitivity to *m* is registered on reactant profiles in the mixing zone. Indeed as *m* decreases, profiles get closer to pore-scale data coherently to curves presented in Figure 4.39 suggesting that a lower value than 0.005 would lead to a slight improvement of data fitting. Figure 4.42b zooms in the product profiles centered on the peak as indicated in Figure 4.42a through red dashed line. Figure 4.42b underlines that a decrement of *m* value of two hundred of times (from 1 to 0.005) leads to almost imperceptible increment (approximately 1%) of peak height. The latter consideration is an additional confirm of the negligibility of time-dependence of reaction term.

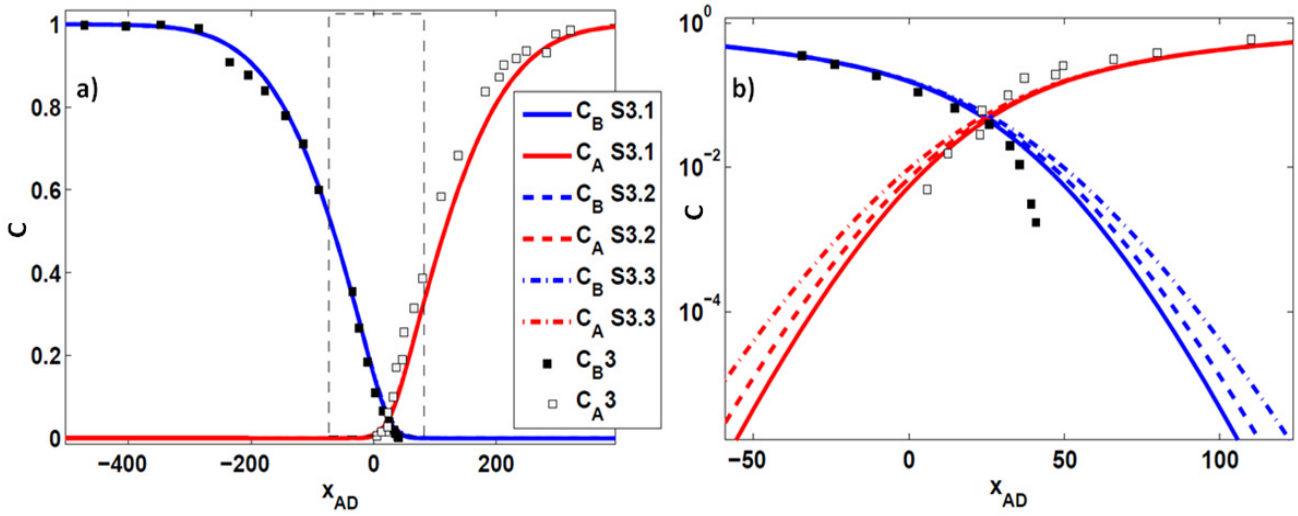

Figure 4.41 a) Reactant profiles given by S3.1, S3.2 and S3.2 at t=447. Figure(b) provides a zoomed image of mixing zone delimitated in figure a) by dashed black line.

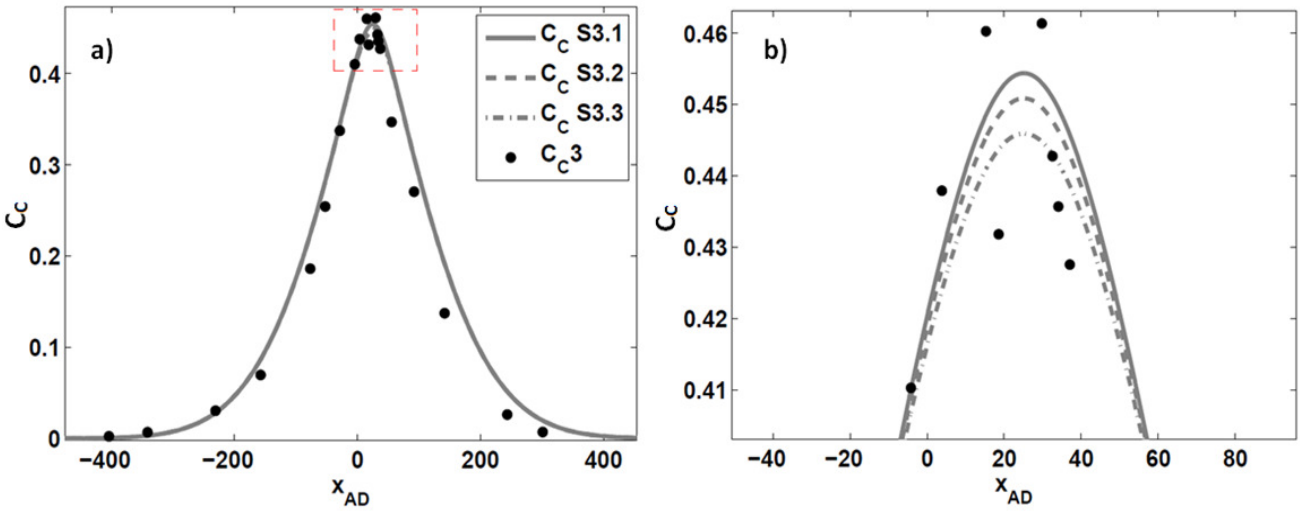

Figure 4.42 a) Product profiles given by S3.1, S3.2 and S3.2 at t=447. Figure(b) provides a zoomed image of peak zone delimitated in figure a) by dashed red line.

On the other hand, the criteria f_{2A_3}, f_{2B_3} and f_{3C_3} attribute to $\hat{\beta}_0$ an important role in fitting profile concentrations. In Figure 4.43 and Figure 4.44 we investigate the concentrations profile solutions at t=447 given by the three different values of $\hat{\beta}_0$ listed in Table 4.12 while *m* is fixed to 0.005. The predictions are compared to C_A3, C_B3 and C_C3 data. Since the time-dependence of reaction rate is negligible, S3.6 is practically coincident to ADRE solution since $\hat{\beta}_0 = \hat{k}$.

Table 4.12 Labels assigned to three different solutions of Model 3 computed for different values of β_0.

Solution Label	$\hat{\beta}_0$
S3.1	3.24
S3.4	97.31
S3.5	324.37

In Figure 4.43a reactant profiles (C_A, C_B) corresponding to S3.1, S3.4, S3.5 are plotted at t=447 against C_A3, C_B3 while Figure 4.44b depicts the concentration C_C. No differences are visible between the diverse solutions. Indeed, since parameter $\hat{\beta}_0$ is linked to reaction process and not to dispersion, its influence is limited to reaction zone, in agreement to previous findings. The reactants and product profiles sensitivity to $\hat{\beta}_0$ in mixing zone is presented in Figure 4.43b and Figure 4.44b, respectively. Figure 4.43b illustrates S3.1, S3.4,S3.5 reactant profile solutions zoomed in the mixing zone delimitated by black dashed line in Figure 4.43a. As $\hat{\beta}_0$ increases reactants concentrations decrease.

Note that the value of $\hat{\beta}_0$ can be associated to the degree of mixing observed at the pore-scale. As a consequence the reaction takes place faster leading lower values of non-reacted reactants in the mixing zone. For $\hat{\beta}_0 = \hat{k}$ reactants data are evidently underestimated. We observe instead that the effective reaction rate, which provides a better estimation of reactant concentrations, is approximately 9.73, i.e. almost 30 times lower than the intrinsic one (324), in agreement to previous works shown in Chapter 1. However, in Figure 4.43b, it seems that Model 3 is not well reproducing C_A3 and C_B3 trends since it is not able to capture the rapid decrement that characterizes the tails of pore-scale data for x_{AD}>0. In Figure 4.44b, the sensitivity of peak height to $\hat{\beta}_0$ is disclosed. We can observe that as $\hat{\beta}_0$ decreases, the peak height reduces.

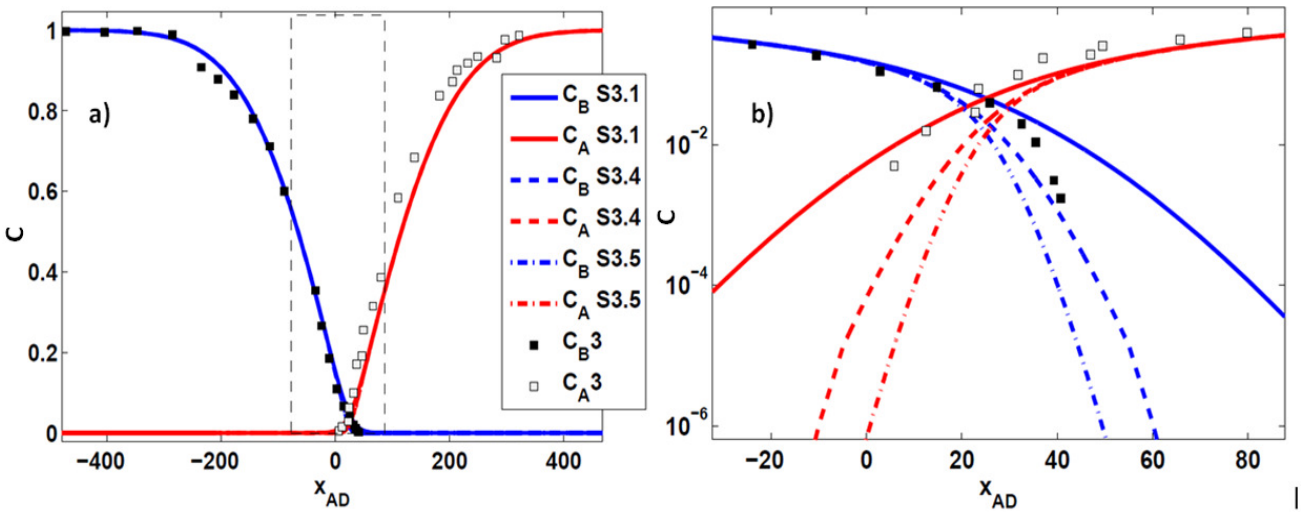

Figure 4.43 a) Reactant profiles given by S3.1, S3.4 and S3.5 at t=447. Figure b) provides a zoomed image of reaction front delimitated in figure a) by dashed black line.

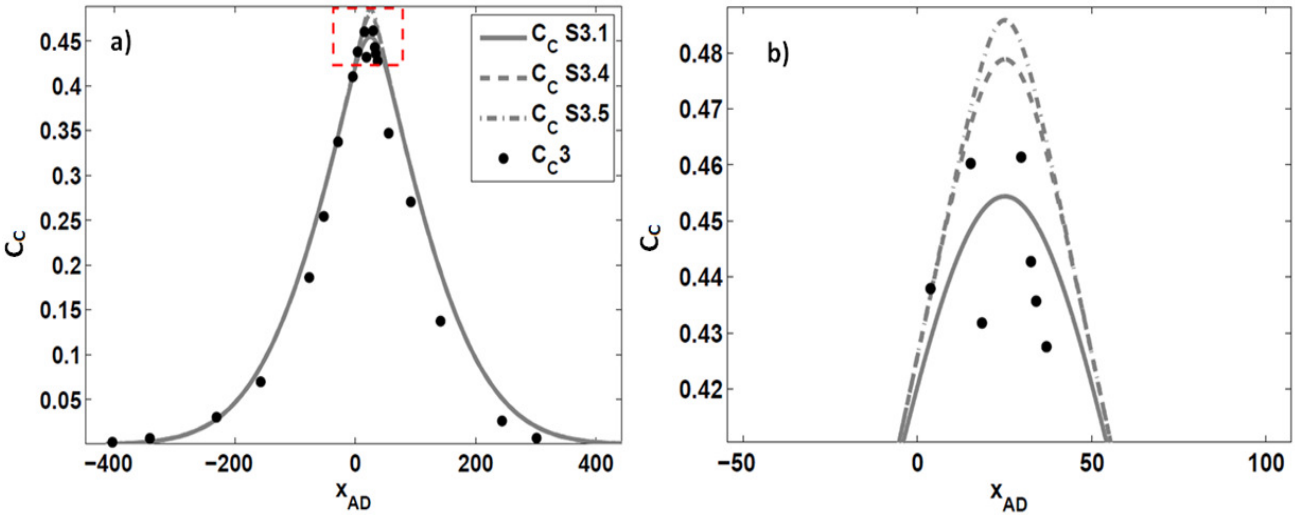

Figure 4.44 a) Product profiles predicted by S3.1, S3.4 and S3.5 at t=447. Figure b) provides a zoomed image of peak zone delimitated in figure a) by dashed red line.

We do not present the analysis of the error related to the global mass of reaction product since this would lead to the same results already discussed in section 4.3.1and section 4.3.2.

4.3.4 MODEL 4: Hochstetler and Kitanidis (2013)

As shown in section 2.3.4, Model 4 depends on three effective parameters: D, λ and γ. In *Hochstetler and Kitanidis (2013)* the dispersion parameter of reactive species is supposed to be equivalent of tracers one. Since our system hasn't reached the asymptotic behavior, as shown in section 4.1 (Figure

4.1 and Figure 4.2), the dispersion coefficient is assumed equal to 741 which is the value computed with a non-reactive numerical simulation at t=59 s corresponding to the duration of simulated reactive transport (see Figure 4.1) analyzed in this Chapter.

As dispersion parameter is fixed, the following analysis aims to investigate only λ and γ roles. As shown in section 4.3.1and 4.3.2, parameters included in reaction term tends to have an influence limited to reactant mixing zone and that f_2 provides a good estimation of them. As a consequence we chose to rely λ and γ estimations on f_{2A_4} and f_{2B_4} computation which stress reactant prediction errors committed near the reactive front. Reactant profiles outside the mixing zone are not interesting in this case since their trends are governed mainly by dispersion which is fixed in this analysis.

Both the parameters are defined positive. While λ can vary from zero to infinite, the authors limited γ domain between zero and one. Upon preliminary simulations with different values of λ, we delimite the parameter space to a small interval [100,700]. The two intervals are discretized as shown in Table 4.13 and a numerical solution of Model 4 is computed for each of the 35 identified combinations of parameters.

Table 4.13 Values of γ and λ sampled for objective function computation.

γ sampled values						
0.2	0.4	0.6	0.8	1		
λ sampled values						
100	200	300	400	500	600	700

Figure 4.45 shows the distributions of f_{2A_4} and f_{2B_4} as function of parameters. The contour line shapes and darker colored areas highlight that f_{2A_4} and f_{2B_4} present different local minima. To verify if a global minimum exists, we compare the functions f_{2A_4} and f_{2B_4} evolutions along the sections indicated in Figure 4.45 through dashed red lines.

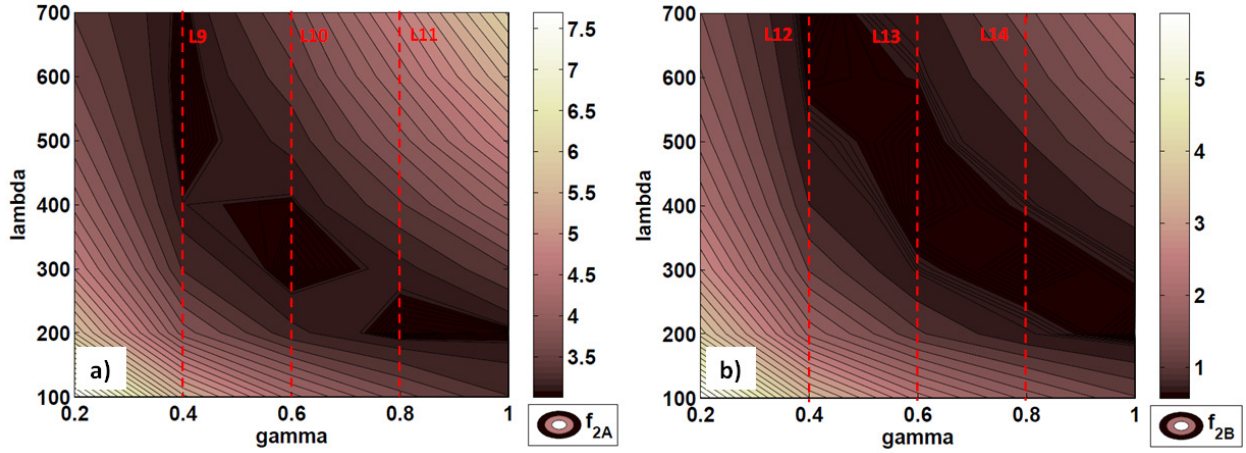

Figure 4.45 Evolutions of a) f_{2A_4} and b) $f_{2\_B\_4}$ as function of parameters. Red dashed lines indicate the positions of the sections reported in Figure 4.46.

In Figure 4.46a f_{2A_4} evolutions along L9, L10 and L11 (indicated in Figure 4.45a) are illustrated as function of λ. The value of f_{2A_4} is reported in logarithmic scale in order to exalt eventual differences when function values approach to zero. The three minima, however, are undistinguishable. Analogous considerations are valid for Figure 4.46b where the evolution of f_{2B_4} along L12, L13 and L14 (indicated in Figure 4.45b) are shown as function of λ. The results show that λ and γ are correlated and that infinite combinations of these two parameters can be estimated that lead to equivalent Model predictions. Then it is no possible to estimate λ and γ relying on chemicals profiles information. This is consistent with formulation of effectiveness factor (Eq. (2.29)) proposed by *Hochstetler and Kitanidis (2013)* here recalled:

$$E = \frac{\gamma\lambda}{\lambda + Da}.$$

Looking at this formulation, as E value is fixed, for each value of chosen value of γ exists a value of λ which allows obtaining the fixed value of E.

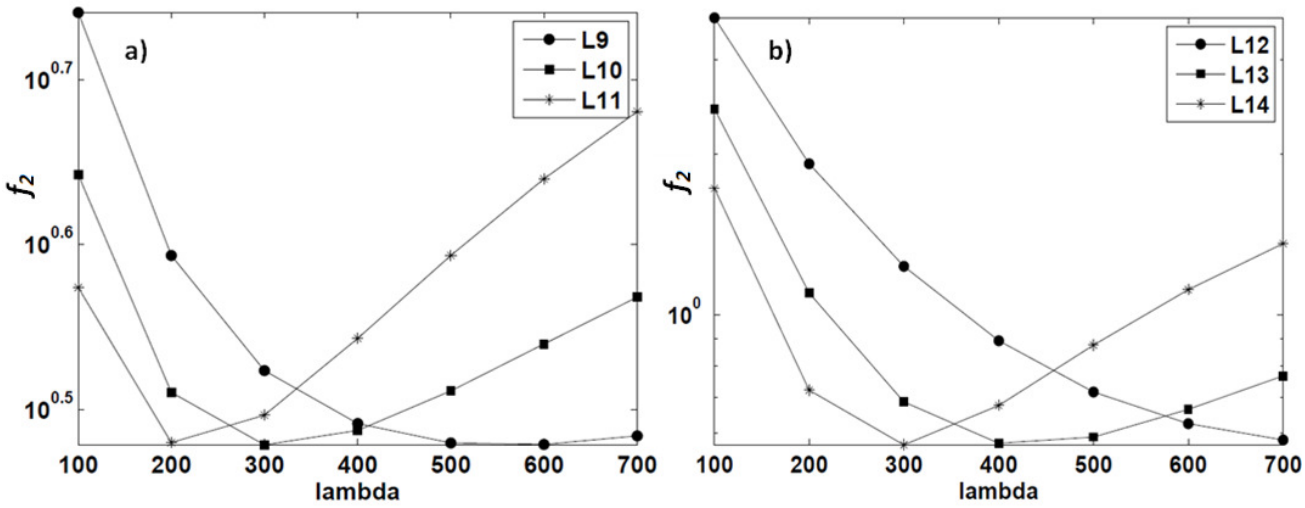

Figure 4.46 Evolutions of a) f_{2A_4} along L9, L10 and L11 sections indicated in Figure 4.45a and b) $f_{2\_B\_4}$ along L12, L13 and L14 sections indicated in Figure 4.45b.

In Figure 4.47 the survival functions *SF* of reactants profiles predicted for different combinations of parameter indicated in Table 4.14. These solutions are compared to the survival function *SF* (C_A3) and *SF* (C_B3). Figure 4.47 shows that, (i) the values of λ and γ do not affect the solutions outside the mixing zone, ii) the dispersion parameter assumed according to the procedure proposed in *Hochstetler and Kitanidis (2013)* appears to be overestimated for both C_A3 and C_B3 profiles. As shown in section 4.3.1 and section 4.3.2, C_C profile is characterized by an intermediate value of dispersion between A and B ones. As a consequence, D=741 overestimates C_C profile dispersion too. This suggests that the dispersion parameter cannot be estimated independently from reaction process.

Table 4.14 Model 4 solutions plotted in Figure 4.47

Solution label	(λ; γ; D)
S4.1	(200;0.2;741)
S4.2	(500;0.6;741)
S4.3	(600;0.4;741)

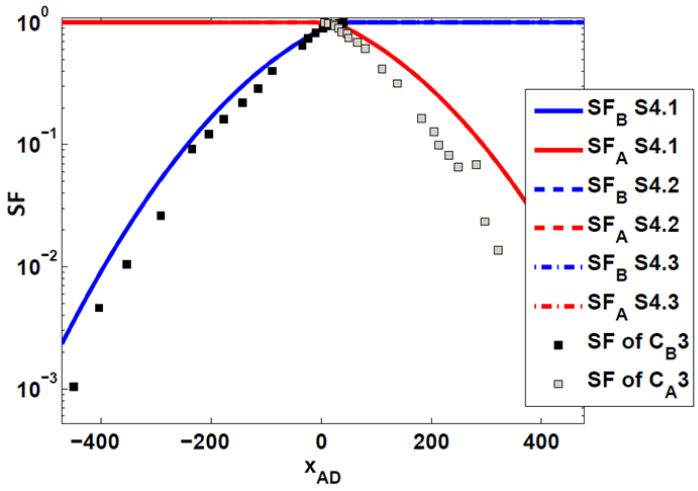

Figure 4.47 Survival function (*SF*) of reactant profile solutions computed for different combinations of parameter reported in Table 4.14.

To overcame this limitation in the following we fix γ=1 (following an alternative formulation of *E* proposed by *Hochstetler and Kitanidis (2013)*) and reintroduce *D* as a calibration parameter. In this case, we implement f_{4A_4}, f_{4B_4} and f_{4C_4} which allow to characterize both the dispersive and reactive processes as discussed in section 4.3.2. The dispersion and λ values investigated this analysis are reported in Table 4.15. A total of 60 parameters combinations have been considered for this analysis.

Table 4.15 Sampled values of *D* and λ for objective function evolution analysis.

D sample values									
300		400		500		600		700	800
λ sample values									
10	20	30	50	100	200	300	350	400	500

Figure 4.48 and Figure 4.49 display the evolution of f_{4A_4}, f_{4B_4} and f_{4C_4} as function of the two parameters are reported. The contour lines show that a global minimum can be identified for each one of the three functions. This proves that f_{4A_4}, f_{4B_4} and f_{4C_4} are sensitive to both parameters investigated and may provide a reliable criterion for model calibration. In Figure 4.48 and Figure 4.49, the crossing points of the red dashed lines located the position of the minima.

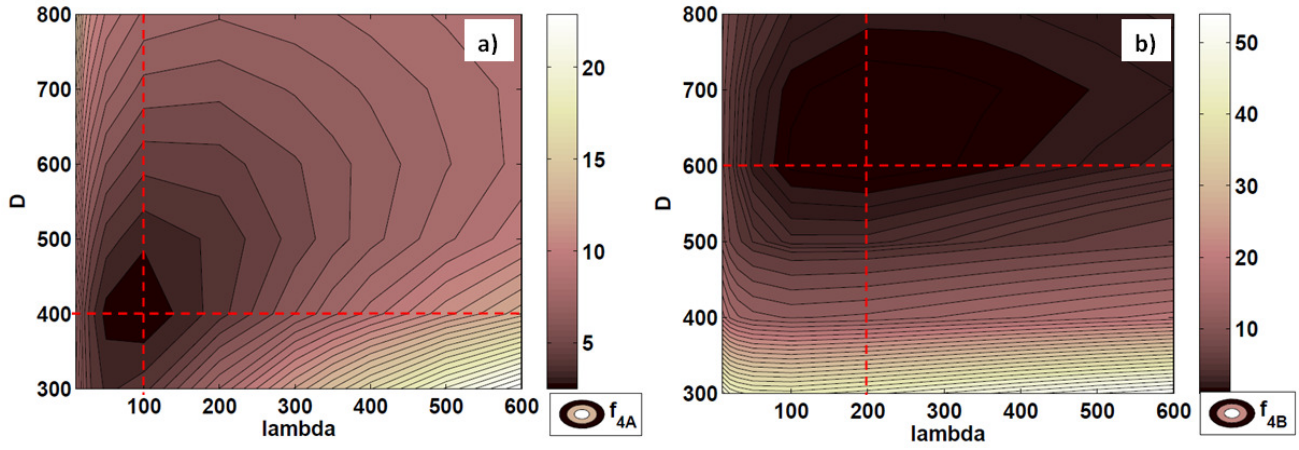

Figure 4.48 Evolutions of a) f_{4A_4} and b) $f_{4\_B\_4}$ as function of parameters *D* and λ. Red dashed lines indicate the positions of the minima reached by each function.

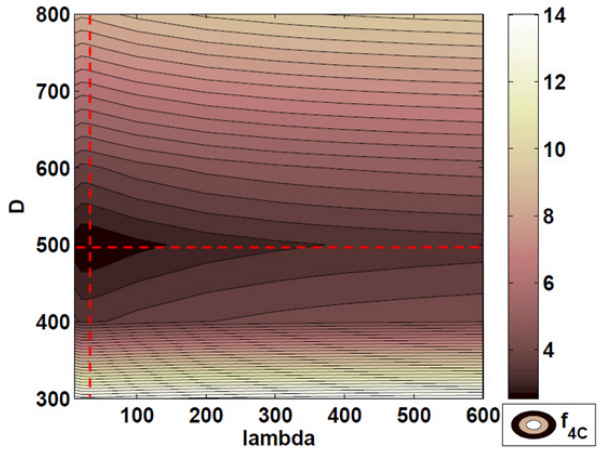

Figure 4.49 Evolutions of f_{4C_4} as function of parameters *D* and λ. Red dashed lines indicate the position of the minimum reached by the function.

Figure 4.48 and Figure 4.49 evidence that f_{4A_4}, f_{4B_4} and f_{4C_4} indicate three different combinations of parameters (reported in Table 4.16) as optimum.

Table 4.16 Combinations of parameters that optimize *f4A_4*, *f4B_4* and *f4C_4*.

Function	Parameters estimate (D; λ)
f_{4A_4}	(400;100)
f_{4B_4}	(500;20)
f_{4C_4}	(600;200)

The difference observed between the three dispersion estimations confirms the findings of section 4.1-4.3.1-4.3.2. In order to explain the significant differences observed in λ estimations, we investigated the sensitivity of concentration profiles with respect to λ. Figure 4.50 shows the reactant concentration profiles computed with different values of λ (20; 100; 200) and D=500 at t=447. The solutions are compared to C_A3 and C_B3 data. We observe that, consistently with findings of Chapter 3, reactant profiles outside the mixing zone (x_{AD}< 20 and x_{AD}>60) are not sensitive to λ which influences only reaction term and not to dispersion process. The influence of λ is instead detectable in Figure 4.50b, which is a zoomed image of reactant concentration profiles in mixing zone, and in Figure 4.51b, where an enlarged image of product peak zone is depicted.

As λ decreases, the reactant concentrations values tend to increase, meaning that when λ tends to zero the incomplete mixing effects increases. This finding is in agreement with reactive term defined in Model 4 (see Eq.(2.27)-(2.29)): as λ gets closer to zero, the effective reaction rate $\hat{k}_{eff}$ assumes a smaller value compared to intrinsic reaction rate. However, Model 4 appears not to well-captures the concentration evolution in reactive zone, in particular for C_B3 data. If C_B3 data show a steep decrement to zero, Model 4 solution tends to be smoother and it shows a flatter profiles. For this reason C_B3 data are in part well-fitted imposing λ=100 and in part imposing λ=200 but a unique value of λ cannot reproduce the full C_B3 data trend. Looking at Figure 4.51b, we observe that the peak of C_C profile is higher when λ increases. Figure 4.51b compares C_C3 data and the three product solutions at t=447 in the peak zone delimitated by read broken line in Figure 4.51a. This shows that the lower value obtained through f_{4C_4} for λ= 20 are essentially due to pore-scale data selected that are characterized by oscillations. The results in Figure 4.51b show that all three λ estimations can be considered feasible and no one of the value proposed seems to provide a better interpretation of concentration peak data compared to the others.

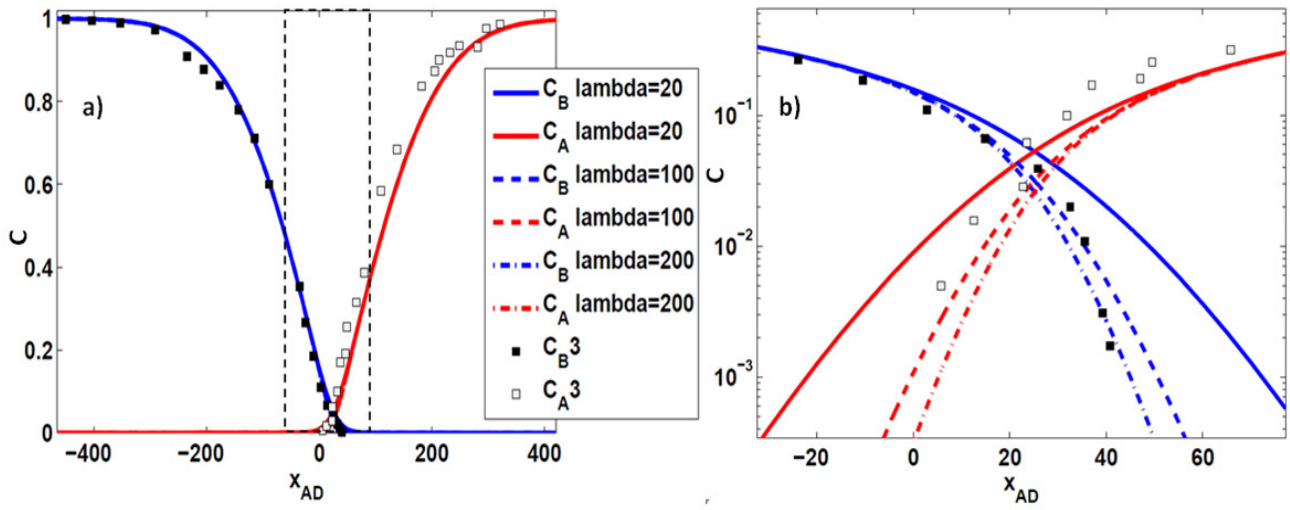

Figure 4.50 a) Reactants concentration profiles yielded by Model 4 for different values of λ, *D*=500 and γ=1 at t=447 compared to C_A3 and C_B3. Figure b) is a zoomed image of reactant mixing zone delimited by dashed black line in figure a).

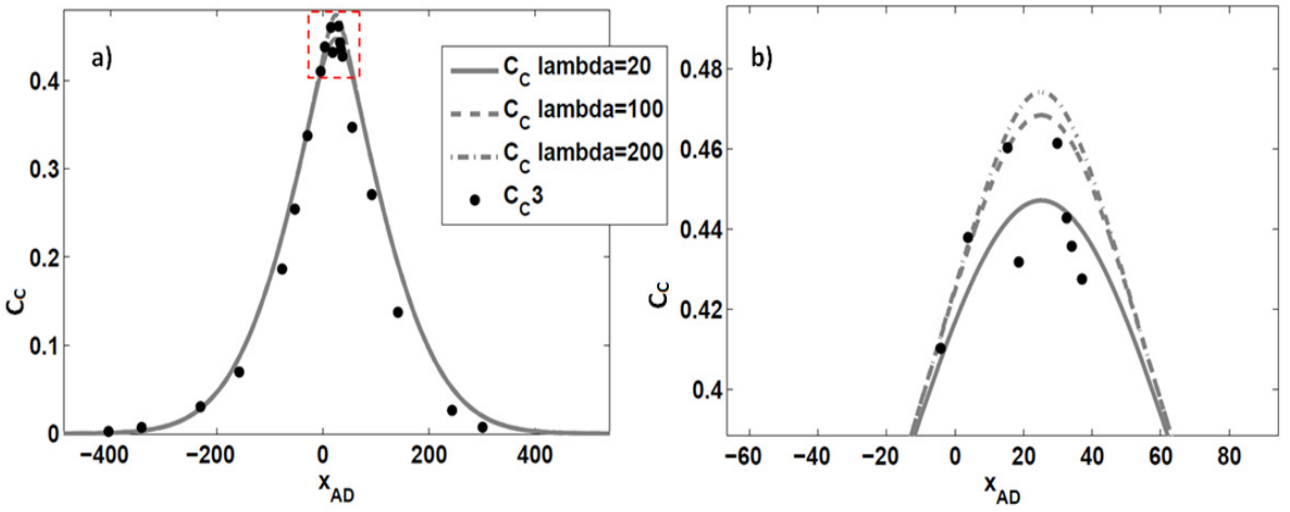

Figure 4.51 a) Product concentration profiles yielded by Model 4 for different values of λ, *D*=500 and γ=1 at t=447 compared to C_C3 data. Figure b) is a zoomed image of concentration peak delimited by dashed red line in figure a).

4.4 MODEL 5: DRMT Model

The numerical solution of Model 5 involves significantly larger computational costs and for this reason we do not provide here a complete investigation of the model performance as function of the model parameters. However, since this type of model has never been implemented for the case of homogeneous irreversible bimolecular reaction in porous media, a qualitative sensitivity analysis of evolving features dynamics to parameters is performed.

As shown in section 2.4, Model 5 depends on three different parameters: D_{Mob}, β_{IM} and Z. In section 2.4 we underline that ϕ_m is linked to the velocity of solute located in the mobile region ($\langle v_m \rangle$) through advective velocity and porous medium porosity (Eq. (2.36)). As a consequence, since the porosity of the system and the advective velocity are constant, a unique value of $\langle v_m \rangle$ is associated for each possible value of ϕ_m. Once that ϕ_m is known, β_{IM} is immediately derived as:

$$\beta_{IM} = \frac{\phi - \phi_m}{\phi_m} \tag{4.2}$$

According to what presented above, a first estimation of β_{IM} is possible assuming that $\langle v_m \rangle$ is equal to reactive front velocity (u_p) observed in pore-scale simulation (see section 4.1). The parameters values and results of this first estimation are reported in Table 4.17.

Table 4.17 Results of first estimation of β_{IM}.

$\langle u \rangle^l$	1
$\langle v_m \rangle = u_p$	1.0560
ϕ	0.6
ϕ_m	0.57
ϕ_{im}	0.03
β_{IM}	0.052

We can observe that, in these conditions, the immobile region corresponds to a little fraction (5%) of the pore space. We then solve Model 5 with different combinations of D_M and Z. Labels and parameters combination corresponding to each solution are indicated in Table 4.18.

Table 4.18 Solutions computed for different parameters combination and corresponding labels.

Label solution	D_M	Z	β_{IM}
S5.1	250	0.001	0.052
S5.2	450	0.001	0.052
S5.3	600	0.001	0.052
S5.4	450	0.005	0.052
S5.5	450	0.008	0.052

In Figure 4.52, reactant profiles of solutions S5.1,S5.2 and S5.3 are plotted at t=447 compared to C_A5 and C_B5 data, which include also data depicting chemical species concentrations oscillations observed in Figure 4.3-Figure 4.8, differently from the data used for single continuum models assessment. In Figure 4.52 we can observe that, even as A and B are characterized by the same D_{Mob} value they exhibit large differences between each other. Introducing an immobile phase, where solutes do not move by advection, delays part of the solute mass. Concerning C_B, the effect of delayed solute is visible for x_{AD}<0. Here the concentrations values are lower than expected since a percentage of the solute mass is trapped in the inlet zone. Concerning C_A, instead, concentration profile shows a long backward tail slower than the advective front. This tail represents the amount of C_A solute entrapped in the immobile zone and it exhibits a slowly decreasing trend. However, independently from solute shapes, the profiles show a similar sensitivity to dispersion. Indeed a decrement of dispersion value leads to a steeper concentration curve since the spreading process in mobile phase is slower. Moreover Figure 4.52 shows that C_A tail distribution is not affected by dispersion value as well as the position of the reactive front, i.e. of the points where the two reactants profile cross each other. This is consisted with Model 5 formulation (Eq. (2.37)), i.e. D_{Mob} value does not appear in immobile phases equations nor in the exchange term that links the mobile-immobile region concentrations. The large oscillations that characterize all C_B curve dataset do not allow visually selecting an optimal value for dispersion coefficient, since all the three solutions are feasible for C_B profile interpretation. The C_A profile, which presents oscillations only on the immobile tail not affected by dispersion, carries meaningful

information for preliminary estimation of dispersion. Indeed solution S5.2 (D=450) matches well C_A5 data.

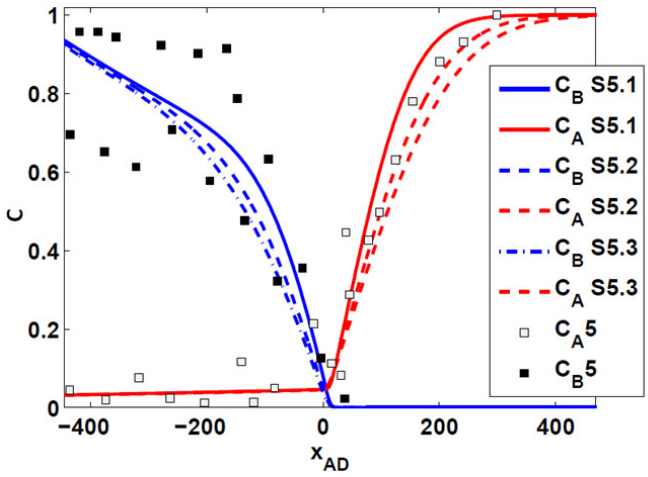

Figure 4.52 Reactant profiles given by S5.1, S5.2 and S5.3 at t=447 compared to C_A5 and C_B5 data.

In Figure 4.53 product profiles of solutions S5.1, S5.2 and S5.3 are plotted at t=447 compared to C_C5. The immobile concentration is visible in C_C profile in its asymmetric shape around the peak. A longer tail characterized the part of concentration slower than the reactive front (x_{AD}<0) due to the reaction taking place in immobile phase. However the asymmetry importance is not affected by dispersion as peak height and position. Similarly to reactant profiles, dispersion influences the spreading of the concentration in longitudinal direction. Confirming what observed for C_A profile, D=450 appears to be the best fit for C_C well matching the forward tail of C_C5 among the ones investigated.

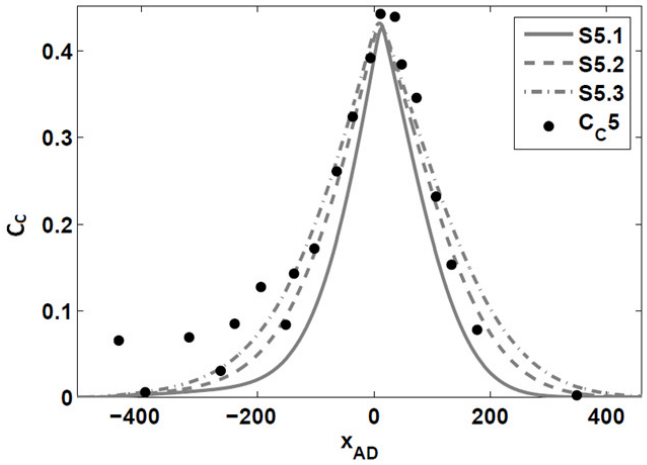

Figure 4.53 Product profiles concentration predicted by S5.1, S5.2 and S5.3 at t=447 compared to C_C5 data.

In Figure 4.54 reactant profiles yielded solutions S5.2, S5.4 and S5.5 are plotted at t=447 compared to C_A5 and C_B5 data while Figure 4.55 depicts product profiles given by solutions S5.2, S5.4 and S5.5 at t=447 against C_C5 data. Dispersion is fixed at 450 and the solutions are computed with different Z values. The parameter Z has physical meaning which has been introduced in section 4.4. In particular, the dimensionless parameter $\hat{Z}$ is proportional to the velocity of mass transfer between the immobile and the mobile phases. According to the formulation proposed in section 2.4, we can define a characteristic transfer time-scale as the inverse of the mass transfer rate $\hat{Z}$. This quantifies the mean time necessary for solute mass transfer to take place between mobile and immobile regions. As a consequence, according to the definition provided in section 2.4, the dimensionless Z represents ration between the characteristic time scale of the mass transfer process and the advective time scale. This means that fixed the average advection velocity and, as consequence the advective time scale $\hat{t}_a$, an increment of Z implies a faster mass transfer process. Looking at Figure 4.54 and Figure 4.55, we can observe that: when the mass transfer process is quick (i.e. large values of Z) chemicals profiles are smoother. Indeed, the rapid transfer from mobile region to immobile one and vice versa tends to homogenize the mass spreading along the domain leading to more stretched and flattened concentration profiles. This also yields a reduction in product concentration peak, as shown in Figure 4.55. In Figure 4.54, parameter Z shows a significant influence on C_A slow long tail. For S5.2 (Z=0.001) concentration on the tail is almost constant while it tends to decreases in space for S5.4 (Z=0.005) and S5.5 (Z=0.008). From a physical point of view, this means that when the transfer process is slow,

immobile and mobile solutes tend to remain segregated in the two distinct phases: the mobile solute moves along x due to advection while the immobile one is entrapped and generates the long concentration tail. On the other hand, when Z increases and the mass transfer process is quick, the C_A tail vanishes rapidly since the solute residing in the immobile phase rapidly transfers to the mobile region. For the same reason we observe a delayed peak for lower Z values in Figure 4.55. For low values of Z, solute is constantly displaced by $\langle v_m \rangle^l$ and the mobile concentration advances fast while the solute in the immobile region is not moving. Instead, if the solute mass easily transfers to immobile region, it advances discontinuously generating a slowing down of reaction front and peak position. In this case, looking at Figure 4.54, the mass transfer appears to be quite slow since the $C_A 5$ data describe a long and evident tail slower that reaction front.

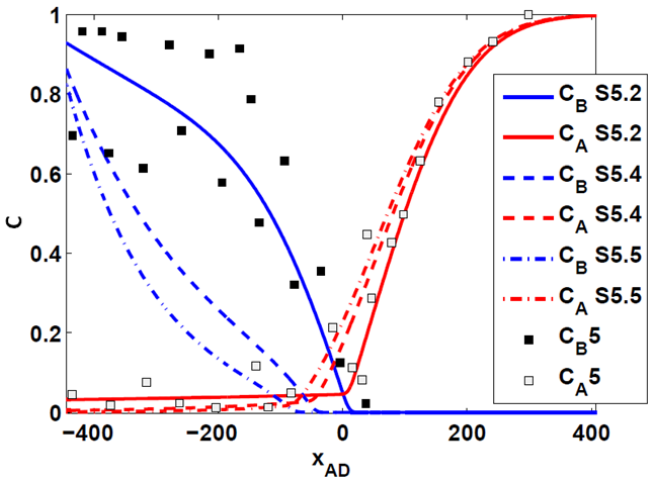

Figure 4.54 Reactant profiles given by S5.2, S5.4 and S5.5 at t=447 compared to C_A5 and C_B5 data.

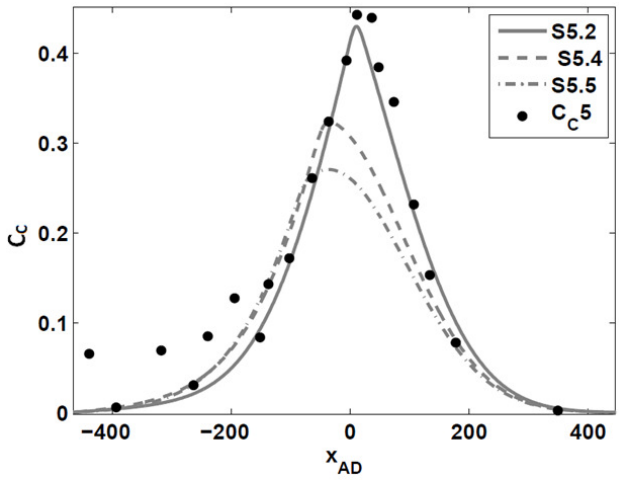

Figure 4.55 Product profiles given by S5.2, S5.4 and S5.5 at t=447 compared to C_C5.

To complete the analysis, we analyze different solutions where the immobile porosity is increased compared to our first estimation. In the following three different solutions, listed in Table 4.19, are compared against C_A5, C_B5 and C_C5 data.

Table 4.19 Solutions computed for different parameters combination and corresponding labels.

Label solution	D_M	Z	β_{IM}
S5.2	450	0.001	0.052
S5.6	450	0.001	0.078
S5.7	450	0.001	0.15

In Figure 4.56 reactant profiles given by solutions S5.2, S5.4 and S5.5 are plotted at t=447 compared to C_A5 and C_B5 data while Figure 4.57 illustrates product profiles yielded by solutions S5.2, S5.4 and S5.5 at t=447 against C_C5 data. In Figure 4.56, we can observe that an increment in β_{IM} value leads to an increment of C_A concentrations in the backward tail. Indeed β_{IM} establishes the importance of the immobile region compared to immobile one, by definition. If β_{IM} is small the amount of solute mass that at each time is located in the immobile region is negligible and mobile solute practically determinates the profile shape. As β_{IM} increases, the immobile solute concentration acquires importance and it contributes to define concentration evolution in space . Figure 4.57 puts in evidence

another important aspect: when β_{IM} increases, the overall product profile appears to move slower, in particular the peak. Indeed, as explained above, β_{IM} is linked to mobile region velocity. As a consequence, changing β_{IM} we implicitly change the mobile region velocity accordingly. For this reason, the concentration profiles appear to move faster compared to advection front. Actually the increased mobile region velocity is balanced by the long backward tails and, on average, the overall velocity of solutes is the same for all the solutions.

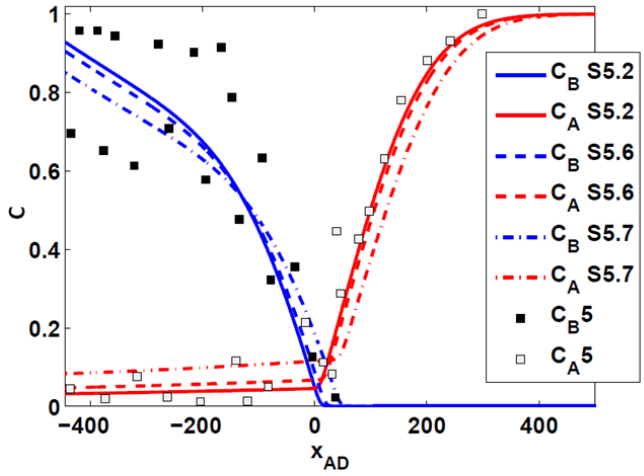

Figure 4.56 Reactant profiles given by S5.2, S5.6 and S5.7 at t=447 compared to C_A5 and C_B5 data.

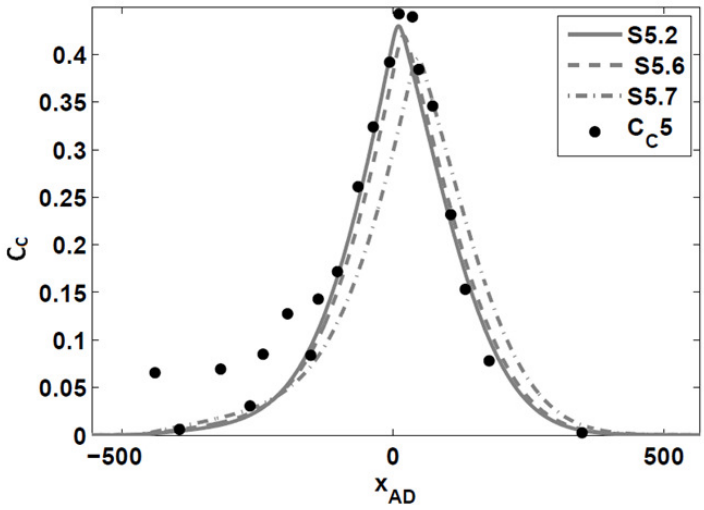

Figure 4.57 Product profiles given by S5.2, S5.6 and S5.7 at t=447 compared to C_C5.

Differently from single continuum models, the parameters appear to be linked one to another, since they appear to contribute to characterized a single profile aspect: for example spreading is regulated

contemporary by D_{Mob} and Z while reactive front position by Z and β_{IM}. For this reason it is expected that also global product evolution may be significantly influenced by all the parameters and mainly by dispersion and mass transfer rate which govern longitudinal solute spreading process.

In Figure 4.58a global product evolutions yielded by S5.1, S5.2 and S5.3 are plotted against G_C1 dataset. Similarly to single continuum models, dispersion, even if limited to mobile zone, significantly affects global product evolution. In particular, dispersion also affects the velocity of product generation from the very beginning since the curves characterized by higher dispersion grow faster. A different influence is instead observed for Z. In Figure 4.58b global product evolutions predicted by S5.2, S5.4 and S5.5 are plotted against G_C1 dataset. For short time, global product is insensitive to Z: its value only affect product evolution for late times.

In Figure 4.59 global product evolutions yielded by S5.2, S5.6 and S5.7 are plotted against G_C1 dataset. Previous profiles analysis has shown that β_{IM} is not directly linked to the solute spreading process. As a consequence, its influence on global product evolution which is marginal, since this output is mainly governed by dispersion mechanism.

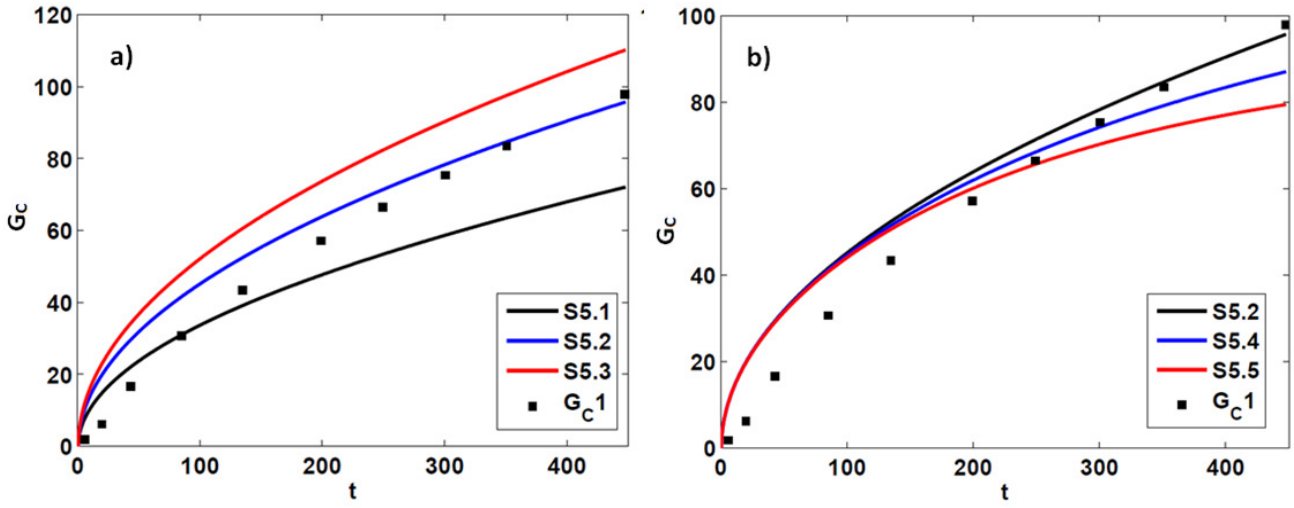

Figure 4.58 Global product evolutions predicted by a)S5.1, S5.2 and S5.3 and b) S5.2, S5.4 and S5.5 at t=447 compared to *G_C1* data.

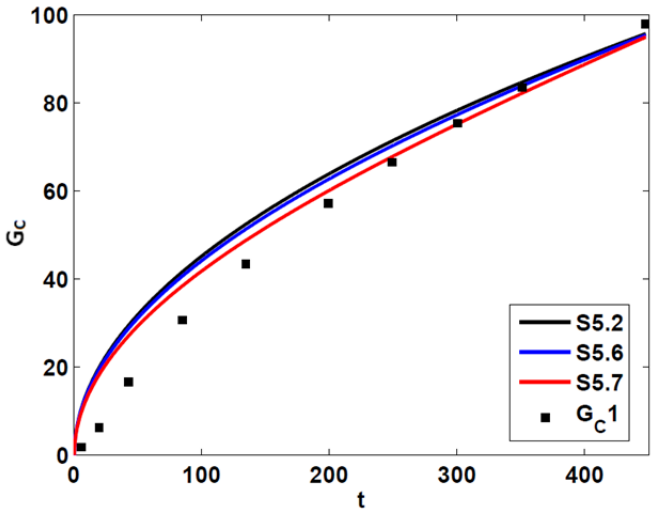

Figure 4.59 Global product evolutions predicted by S5.2, S5.6 and S5.7 at t=447 compared to G_C1 data.

4.5 Summary of results

In this section we briefiely summarize the main results presented in this Chapter:

- We demonstrate that the system analyzed has not reached the asymptotic behavior from both numerical and theoretical point of view. Pore-scale simulation analysis allows detecting the effects of immobile region on solutes distributions along the longitudinal direction: i) backward C_A concentration tail is characterized by significant oscillations due to solute entrapped in immobile region; ii) C_A and C_B concentration profiles are characterized by different spreading processes; iii) C_C concentration profiles are not symmetric; vi) the reactive front, i.e. the crossing point between C_A and C_B profiles, is not well characterized by the averaged fluid velocity.
- Since the ADRE model does not include a parameter for the quantification of incomplete mixing effect, it leads to poor predictions of the reactants concentrations inside the mixing region. However, we can obtain a good fit of concentration profiles outside the mixing region, where dispersion is the dominant process. The functions f_{3A}, f_{3B} and f_{2C} provide a feasible but different optimal dispersion parameters due to the fact that the three solutes are characterized by different shapes of the concentration distributions along the longitudinal direction. To overcome this inconsistence, a possible solution is to assume C_C dispersion for characterizing, which allows describing an intermediate behavior of the system. On the contrary, this analysis

suggests that the model is not capable of reproducing the dynamics of the global product of the reaction. This is due to the fact that the dispersive process does not attain an asymptotic behavior in the scenario analyzed

- Concerning Model 2 analysis, we can observe that the introduction an incomplete mixing parameter is necessary for capturing system features and concentration profiles both inside and outside the mixing zone. The definition of a suitable objective function is fundamental for approaching a correct estimation of parameters. In this section, we show that f_2 configures as a useful objective function for estimating parameter affecting the reaction rate and the effects of pore-scale reactants segregation (i.e. incomplete mixing), but it is scarcely sensitive to the dispersion parameter. As a consequence, criteria f_2 can give reliable results in calibrating reaction parameters when dispersion is already known or previously calibrated. The criterion f_4, instead, can be implemented when both dispersive and reactive parameters, are unknown due to its sensitivity to both *D* and *B*. Finally we underline that, in analogy to Model 1, the criterion f_{1GC} leads to identify unreliable parameters combinations, when compared to the time evolution of the reactive transport process. In particular it appears that asymptotic dispersion value estimation is not possible relying on the available time history of the global mass of generated product.
- The results presented for Model 3 suggest that the criteria used for parameters estimation are not able to disclose the time-dependence of the reaction constant. The parameter *m*, which establishes relation between the constant reaction rate and time, tends to zero-value. This suggests that Model 3 assumes a formulation close to the ADRE model where the intrinsic kinetic constant is replaced by a lower effective reaction rate.
- The results concenrning Model 4 suggest that the effectiveness factor (*E*) formulation proposed by *Hochstetler and Kitanidis (2013)* cannot be fully calibrated relying only on profile concentration profiles related to a single *Da* number. More information are needed to perfom the estimation of the two parameters λ and γ. Moreover we highlight that the estimation of dispersion coefficient relying on conservative tracer transport leads to overestimated of it.
- DRMTM shows an interesting potential in capturing peculiar aspects of reactive transport that encourage further investigations about its pertinence for homogeneous reactive transport description which is still an unexplored field. Even as the analysis provided is qualitative, it

evidences in particular that DRMT Model is able to captures the asymmetrical trends of concentration profiles and the effects of almost immobile regions due to porous medium heterogeneities. These aspects make the DRMTM solutions significantly different from single continuum model ones. A direct comparison between them, which helps in disclosing the differences, will be discussed in section 5.2.

Chapter 5 MODELS COMPARISON AND DISCUSSION

In this chapter, we provide a quantitative comparison between solutions yielded by the five models analyze individually in Chapter 4. In the first section, we focus on the single continuum models in order to highlight similarities and differences between models characterized by a common approach. Limitations of the single continuum approaches and possible solutions are also illustrated. In section 5.2, instead, we qualitative compare Model 2 to DRMTM in order to highlight the differences existing between the two approaches and their peculiarities.

5.1 Quantitative single continuum models comparison

For all the models presented, parameters estimation has been performed relying on four different types of data: C_A profiles, C_B profiles, C_C profiles and global product evolution. As shown in sections 4.3.1-4.3.2-4.3.3-4.3.4, according to the chemical species used for estimating parameters, we approach to a different estimations of dispersion and reaction parameters.

In particular, as shown in sections 3.3 and 4.1, the forward tail of C_B profiles, which falls into the crucial mixing zone, shows limited oscillations of pore scale data with respect to the corresponding C_A profiles. As concentration fluctuations generate uncertainties in dataset selection and increase the difficulty in discriminate between model performances, we limit models comparison to C_B profiles. As a consequence, among the different optimal combinations of parameter identified for each model, we select the ones which maximize models performances in fitting C_B profiles. In Table 5.1 we report the parameter estimations performed for each model in Chapter 4. For each model, we report in Table 5.1 three different objective function values: f_{2B}, f_{3B} and f_{4B} (see section 2.6). These are computed relying on C_B3 and C_B2 datasets (see Figure 4.14 and Figure 4.15) . As shown in Chapter 3 and Chapter 4, each function allows evaluating the performances of the four models referring to a specific pirtions of the C_B profile: f_{2B} emphasizes the five models performances within the mixing zone, while f_{3B} outside the mixing region. The criterion f_{4B} is given by the sum of f_{2B} and f_{3B} and evaluates the model performances on the overall C_B profile.

Table 5.1 parameters estimated for each Model and correspondent error computed on C_B2 and C_B3 data using f_{4B}.

Model	Parameters	f_{2B}	f_{3B}	f_{4B}
Model 1	D=650	0.399	0.013	0.386
Model 2	D=660; B=230	0.012	0.008	0.020
Model 3	D=600; m=0.05; $\hat{\beta}_0$=9.73	0.040	0.044	0.084
Model 4	D=600;γ=1;λ=200	0.012	0.044	0.056

We can observe that consistent differences are registered among f_{4B} values. Model 1 presents the highest error. A shown in section 4.3.1, the absence of a parameter for embedding incomplete mixing effect disadvantages this model, since the concentration profiles within the mixing region result evidently underestimated independently from the dispersion value chosen (Figure 4.19). This is consistent with objective functions values reported in Table 5.1. The value of f_{3B}, which enphatizes the model performances outside the mixing region, is similar for the four models, while the value of f_{2B} is much larger for Model 1 meaning that its solution badly performs within the mixing region. As explained above, this means that the most significant discrepancy between Model 1 (ADRE) solution and pore-scale cross-sectional averaged data is localized within the mixing zone. Introducing a quantification of incomplete mixing through effective parameters leads to a crucial improvement in C_B profile fit leading to a lower error committed by the model solutions. In particular we observe the lowest f_{2B} values associated to Model 2 and Model 4. Limiting the analysis to error computation would lead to the conclusion that Model 2 and 4 both allow to equivalently well-predicting concentration profiles at t=398 and t=447. Further investigations on C_B profile solution shapes, presented in the following, disclose instead that significant differences exist between the two model performances. In Figure 5.1 C_B profiles yielded by the four models at t=447 and t=398 are compared to C_B3 and C_B2 data.

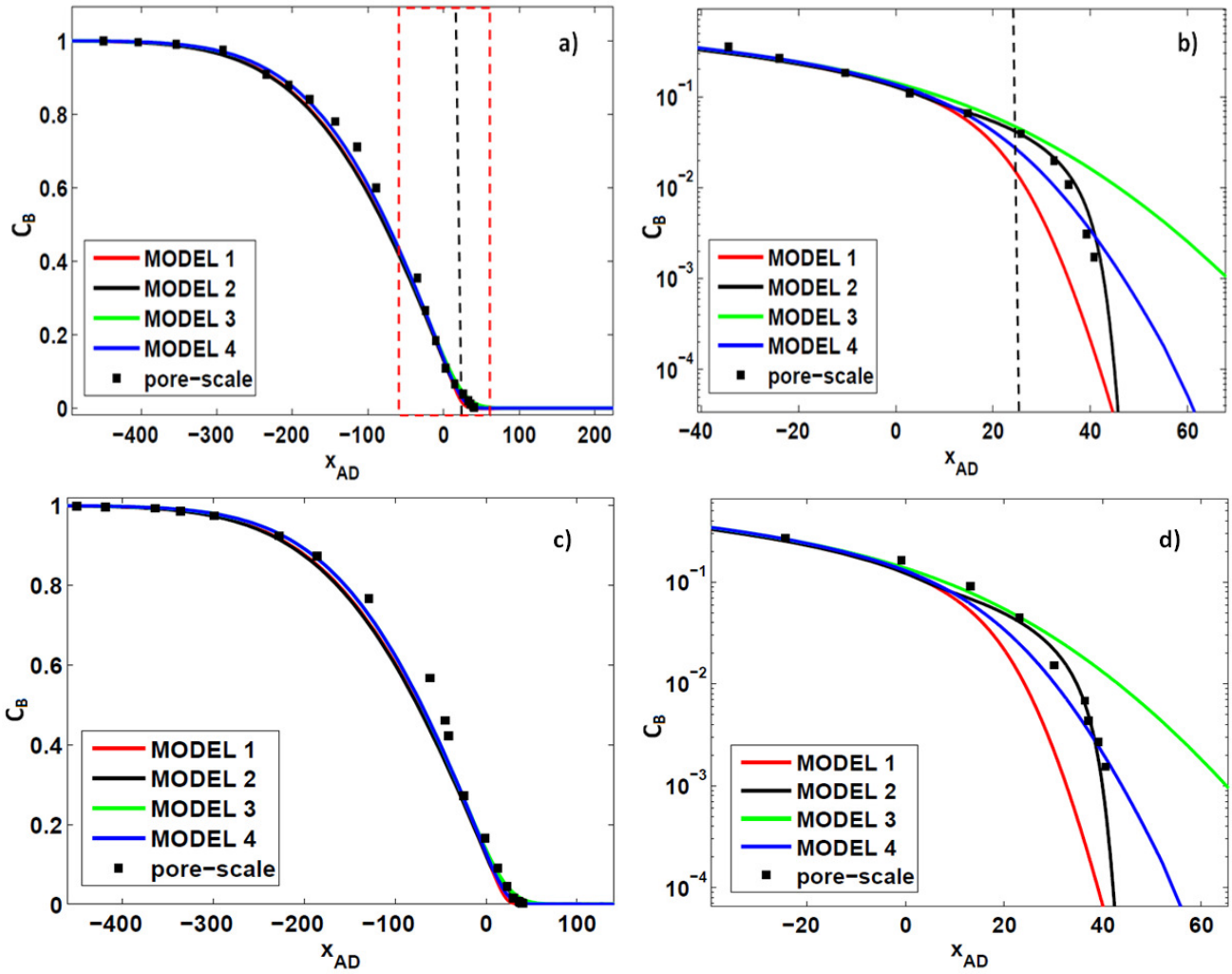

Figure 5.1 a) and c) depict C_B profiles given by Model 1-4 computed with the combination of parameters estimated in Chapter 4 and reported in Table 5.1 at t=447 and t=398, respectively. b) and d) are a zoomed image of C_B profiles at the reactive zone delimited by red broken line in figure a) and c). The exact position of the reactive front is indicated by a black dashed line. The solutions are compared to C_B3 data in a) and b) and to C_B2 data in c) and d).

In Figure 5.1a and c model curves are almost undistinguished yielding to very similar trends outside the mixing zone. Indeed, as shown in Chapter 4, the different reaction term modeling approaches included in the four models practically do not affect concentration profiles outside the mixing zone (delimited by dashed red lines in Figure 5.1a and c , i.e. where dispersion process governs the solute transport. Indeed the four models present identical dispersion term modeling approach in this region. This explains why models yield to almost identical profiles outside the mixing zone and the dispersion parameter estimations assume very similar values. This is consistent with f_{3B} values registered (Table 5.1): all the models show low and comparable errors outside the mixing zone. In particular Model 3 and 4 show

exactly the same f_{3B} value and are characterized by the same dispersion parameter estimations (D=600). This suggests that the slight difference observed between f_{3B} values is due to the different estimated dispersion which do not lead to significant discrepancy between fitting models performances, as observed in Figure 5.1a and c). However, looking at f_{2B} values reported in Table 5.1, we can notice that a large discrepancy between the four model solutions does exist and it is localized within the mixing zone. This result is embedded in criterion f_{4B}. This discrepancy is imputable to the different model trends in the mixing zone close to the reactant front (the position of which is indicated in Figure 5.1 by black dashed line). Figure 5.1b an d depict a zoomed image of the mixing zone indicated Figure 5.1a through black dashed line. Figure 5.1b an d disclose the different model performances in the reactive zone. As expected the ADRE model (Model 1) leads to a strong underestimation of concentration due to the assumption of complete mixing between reactants which does not occur at pore-scale. Model 2, 3 and 4 incomplete mixing terms allow reducing the underestimation showed by Model 1 as already observed according to f_{2B} values. Model 3 and 4 are both able to capture the data evolution preceding the position of the reactive front (x_R which is indicated by a dashed black line in Figure 5.1) but they do not capture the behavior of the tail for longitudinal positions larger than the reaction front position. Indeed, the C_B3 data are characterized by a slow decreasing trend for $x<x_R$ the reactive front, while C_B3 data change completely behavior, i.e. the concentrations decrease fastly assuming almost a vertical trend. Model 3 and 4, instead, show smooth variation of concentration maintaining a slow decrement in space for $x>x_R$. Note that Model 3 and 4 show exactly the same qualitative behavior even as their different reactive term modeling approaches. Actually, according to the findings of section 4.3.3, the parameter m, appearing in Model 3 formulation, tends to zero meaning that Model 3 effective reaction rate is practically constant in time. As a consequence, for this specific problem, Model 3 and Model 4 reactive term formulations are practically identical, i.e. the incomplete mixing effect is embedded in a constant effective kinetic rate smaller than the intrinsic one. However, in Figure 5.1b and c, they show a significant quantitative difference, even as they represent the practically same model. This is due to fact that only discrete values in parameter space have been analyzed for parameter estimations. A more precise calibration process for the two models would probable lead to two different λ and $\hat{\beta}_0$ estimated values that, however, determine the same effective constant rate. In general, Figure 5.1b and d suggest that embedding the incomplete mixing effect in a

constant effective reaction rate, lower than intrinsic one, allows improving the results yielded by the ADRE (Model 1) but does not yield a fully accurate interpretation of concentration tails observed in pore-scale simulation cross sectional averaged data.

An outstanding and promising performance is instead shown by Model 2. Indeed even as Model 4 and Model 2 given solutions are affected by comparable errors within the mixing zone (see Table 5.1), the qualitative trend of C_B is significantly different in Figure 5.1b. Model 2 is able to capture the rapid decrement that characterizes the reactive front forward data (for $x>x_R$). The slight data overestimation is still detectable for the lowest values of concentration. This is probably imputable to approximated estimations performed in this work. Future models calibration is, then, needed for a precise estimation. Model 2 peculiarity must be researched in its reaction term definition (Eq. (2.18)). Indeed the incomplete mixing quantification depends on the square value of $\frac{\partial C_D}{\partial x}$ which establishes a relation between the reaction and the dispersive processes. The comparison between model solutions and pore-scale data showed in Figure 5.1 is performed at t=447. The pore-scale averaged data at this time level have also been used in the estimation parameter process. As validation of results, we now compare model solutions against C_B pore-scale averaged data at two different times level (t=99.54 and t=373) not used for parameter estimations.

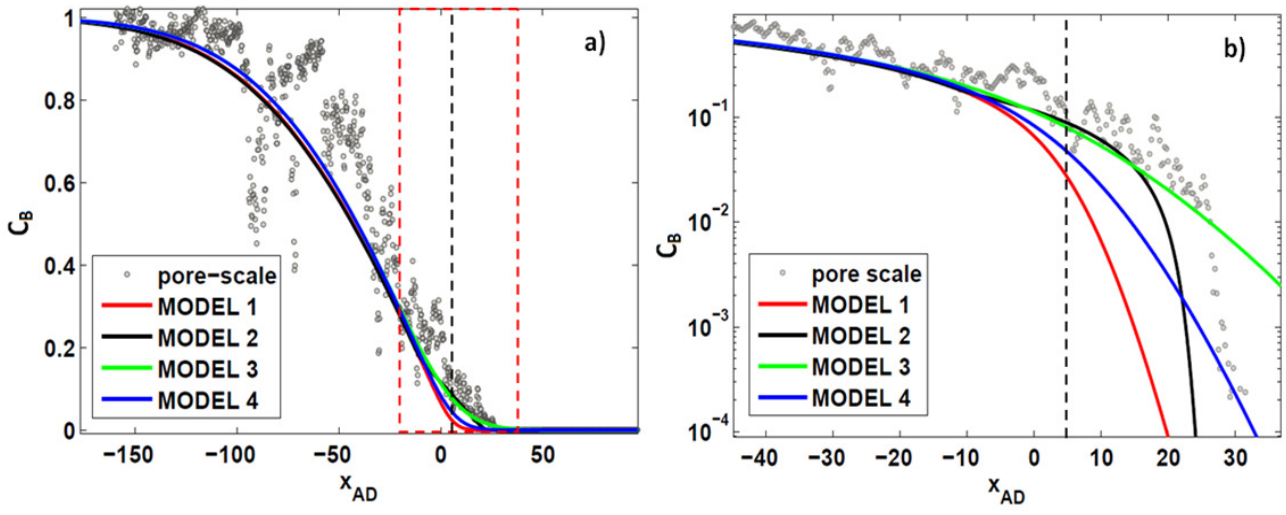

Figure 5.2 a) C_B profiles yielded by Model 1-4 computed with the combination of parameters estimated in Chapter 4 and reported in Table 5.1 at t=99.54. Figure b) is a zoomed image of C_B profiles at the reactive zone delimited by red broken line in figure a. The exact position of the reactive front is indicated by a black dashed line. The solutions are compared to pore-scale cross sectional averaged data.

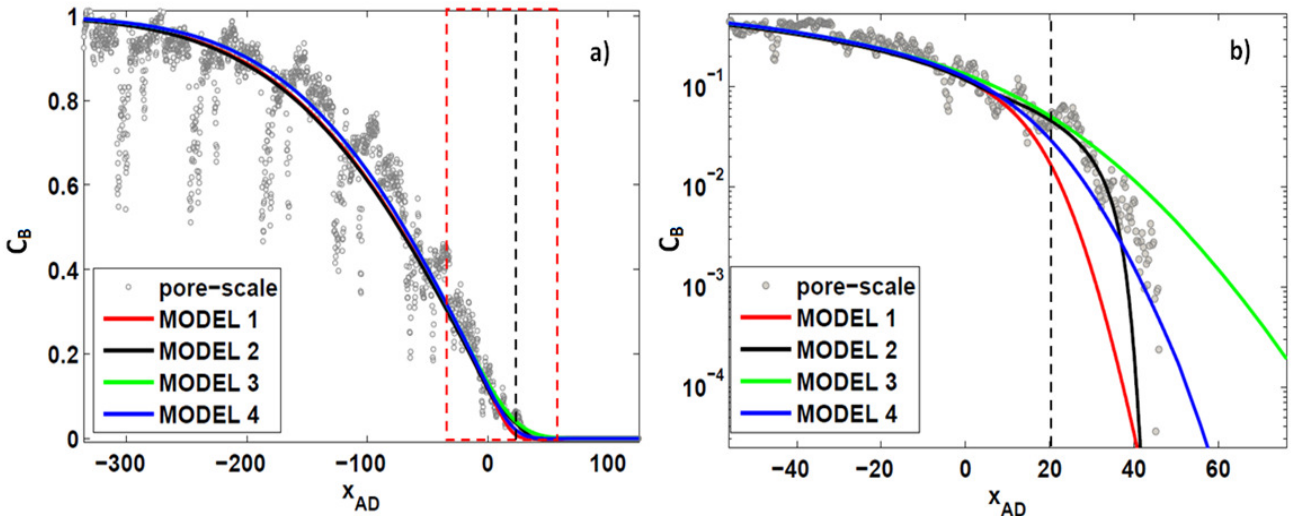

Figure 5.3 a) C_B profiles yielded by Model 1-4 computed with the combination of parameters estimated in Chapter 4 and reported in Table 5.1 at t=373. Figure b) is a zoomed image of C_B profiles at the reactive zone delimited by red broken line in figure a. The exact position of the reactive front is indicated by a black broken line. The solutions are compared to pore-scale cross sectional averaged data.

In Figure 5.2 and Figure 5.3, C_B profiles given by the four models are plotted at t=99.54 and t=373, respectively. Model solutions are compared to pore-scale cross sectional averaged data observed at the same time. Figure 5.2a shows that all the models do not capture the overall C_B curve at t=99.54. A possible cause of this inaccuracy is the overestimation of spreading process. Outside the mixing zone, the transport is mainly ruled by dispersion parameter and, as a consequence, a possible explanation is that dispersion parameter estimated for late times does not capture dispersion process in early times, i.e. the curves yielded by continuum models exhibit a smaller longitudinal gradient with respect to the pore-scale data. As already discussed, dispersion should be treated through time nonlocal formulations, to capture this behavior. Disregarding such time dependence compromises the reliability of models for short times when the dispersion is strongly affected by non-local effects. Figure 5.2b and Figure 5.3b depict a focus of mixing zone delimited in Figure 5.2a and Figure 5.3a, respectively, by red dashed lines. Independently of the time considered, we can observe the qualitative different trend, which characterized Model 2 solution at t=447 (Figure 5.1b), is detectable also at t=99.54 and t=373 (Figure 5.2b and Figure 5.3b). Since dispersion slightly influences mixing zone profiles, as shown in Chapter 4, the Model 1-3-4 qualitative different trends compared to pore-scale data can be ascribe only to reaction term mathematical formulation. Model 2 instead depicts a parallel curve to pore scale data both in Figure 5.2b and Figure 5.3b. However those are not well-fitted by Model 2 with the chosen estimated parameters. This can be ascribed to fact that all the effective parameters, in general, do not show

constant values in time but they depend on the time at which they are estimated. The substantial difference, observed in Figure 5.1b-Figure 5.3b, between Model 1-3-4 and Model 2 is that as Model 2 qualitatively reproduces the data trend, this is not true for the ADRE-based models. Figure 5.1b-Figure 5.3b suggest that a focused change in Model 2 parameters would probably allow to fit pore-scale data. On the contrary, a change in ADRE-based model parameters would translate the curves without capturing pore-scale trend.

The parameter values evolution in time is shown in *Porta et al. (2012a)-(2013)*. Indeed the model mathematical formulation proposed by *Porta et al. (2012a)* includes two convolution terms which indicates the non-local evolution of dispersion and incomplete mixing term. As consequence constant parameters are not good at capturing these evolutions. Hence, the negligence of those can lead to the failure in reproducing short times concentration profiles evolution in Model 2.

Figure 5.4 displys C_A profiles yielded by Model1-4 for the parameters values reported in Table 5.1 at t=373. Figure 5.4 shows that dispersion parameter for all the model is overestimated for C_A profiles. This is consistent with finding of Chapter 4. Indeed, dispersion estimation for all the models indicates a lower value of dispersion for C_A than C_B. Moreover, we can notice that none of the single continuum models is able to capture on average the backward tail oscillations ($x<x_{AD}$).

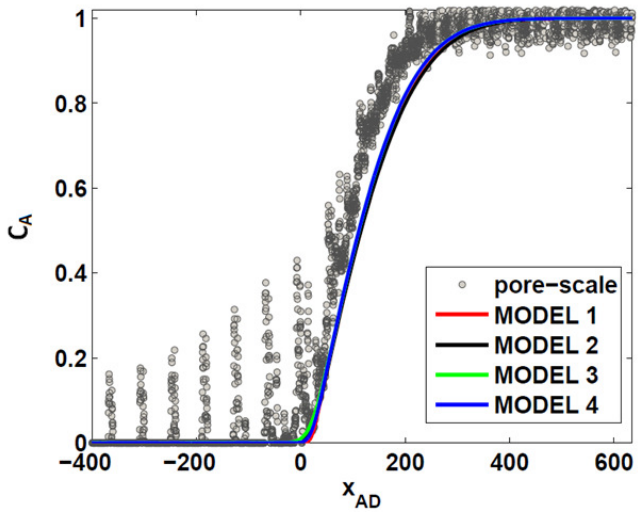

Figure 5.4 C_A profiles yielded by Model 1-4 computed with the combination of parameters estimated in Chapter 4 and reported in Table 5.1 at t=373.

In Figure 5.5 the global product evolutions in time given by the four models is compared to G_C1 data. All the considered models do not seem able to capture the pore-scale data trend. Indeed all the curves given by models significantly overestimate global product pore-scale evolution. As shown in Chapter 3, global quantities are poorly influenced by incomplete mixing effect, and because of that, Figure 5.5 suggests that the overestimation can mainly be ascribed to dispersion parameter value. Also in this case, the negligence of nonlocal effects in time may play a crucial role in capturing pore-scale data evolutions.

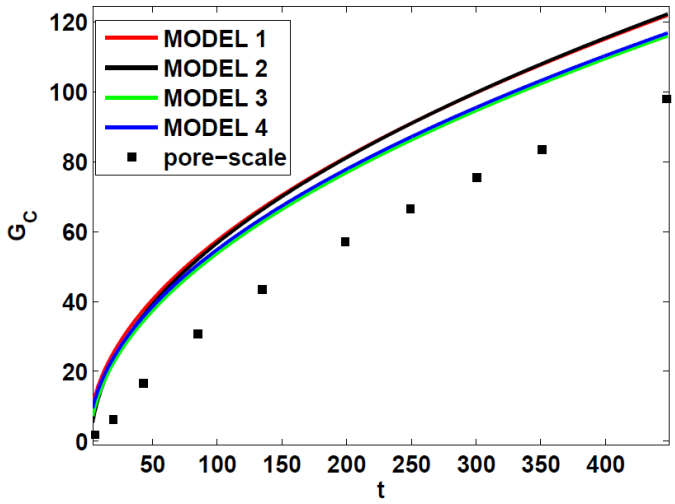

Figure 5.5 Global product evolutions given by Model 1-4 computed with the combination of parameters estimated in Chapter 4 and reported in Table 5.1. The solutions are compared to G_C1 data.

To test the importance of time-dependent parameter behavior, we propose here an exemplificative implementation of Model 2b presented in section 2.3.2. In this model the reactive and dispersive term convolutions are approximated by local time-dependent parameters expressed in Eq. (2.21)) and here recalled:

$$B(t) = B(1-\exp(-a_1 t))$$
$$D(t) = D(1-\exp(-a_2 t))$$

where B and D are assumed equal to the ones that optimize Model 2 solution while a_1 and a_2 appearing in Eq. (2.21) are manually estimated against G_C1 data. In Table 5.3 the parameter values estimated are reported.

Table 5.2 Parameters manually estimated against G_C1 data.

D	660
B	230
a_1	0.01
a_2	0.05

Figure 5.6 depicts the evolution with time of B and D exspressed by Eq. (2.21) computed with parameter values reported in Table 5.3. Figure 5.6 displays that the local time dependent parameters progressively increase with time and an asymptotic value is approached. The velocity through which the asymptotic value is reached depends on the values of a_1 and a_2.

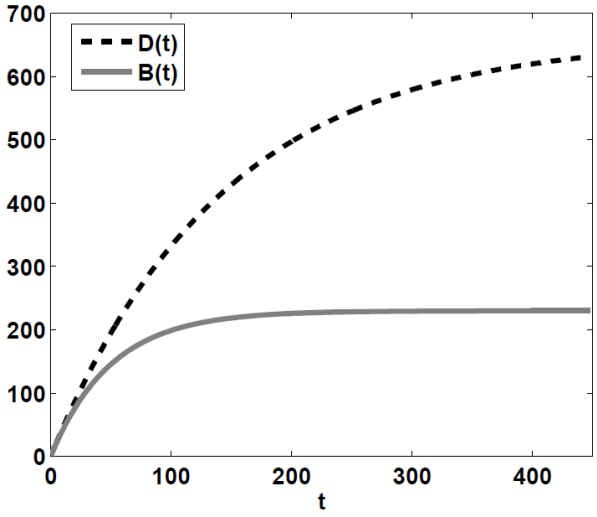

Figure 5.6 Evolution of *D* and *B* with time computed with Eq. (2.21) with parameter values reported in Table 5.3.

Figure 5.7 shows the global product evolution yielded by Model 2b and Model 2 solutions against G_C1 data. Model 2b is able to reproduce global product evolution since the very first times and the solution yielded by Model 2b remarkably reduces the overestimantion performed by Model 2. This clearly suggests that dispersion time-evolution dependence has a key role in reproducing global model evolution concentration for short time.

In Figure 5.8a C_B profile yielded by Model 2 and Model 2b are compared against pore-scale cross section averaged data at t= 99.54. Time-dependent dispersion allows improving the fit of pore-scale cross sectional averaged concentration for short times. By considering time-dependent effective parameters Model 2b well reproduces C_B profile at this early time and better interprets the dispersion process compared to Model 2 which, as noticed before, definitely over predicts profile spreading. Figure 5.8b provides a zoomed imaged of C_B profiles as indicated in Figure 5.8a through broken red line. The logarithmic concentration scale allows disclosing the differences between the two models solutions close to zero with the mixing zone. Figure 5.8b shows that Model 2b better interprets pore-scale cross sectional averaged concentration. However the forward tail is still not well fitted and further investigations are needed to analyze this result.

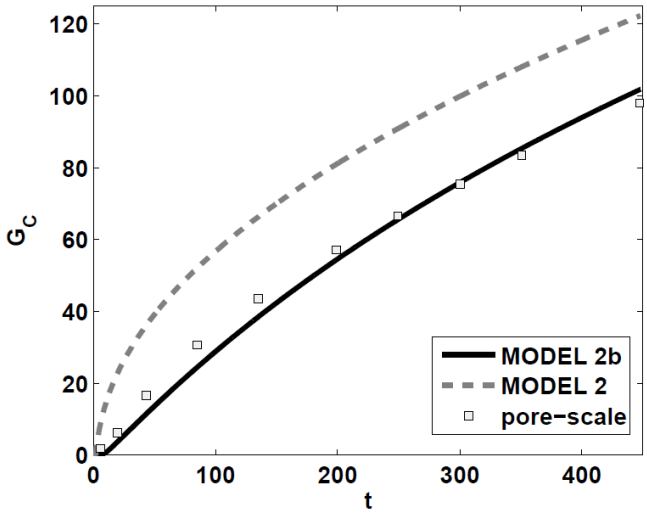

Figure 5.7 Global product evolutions given by Model 2b and Model 2 compared to G_C1 data.

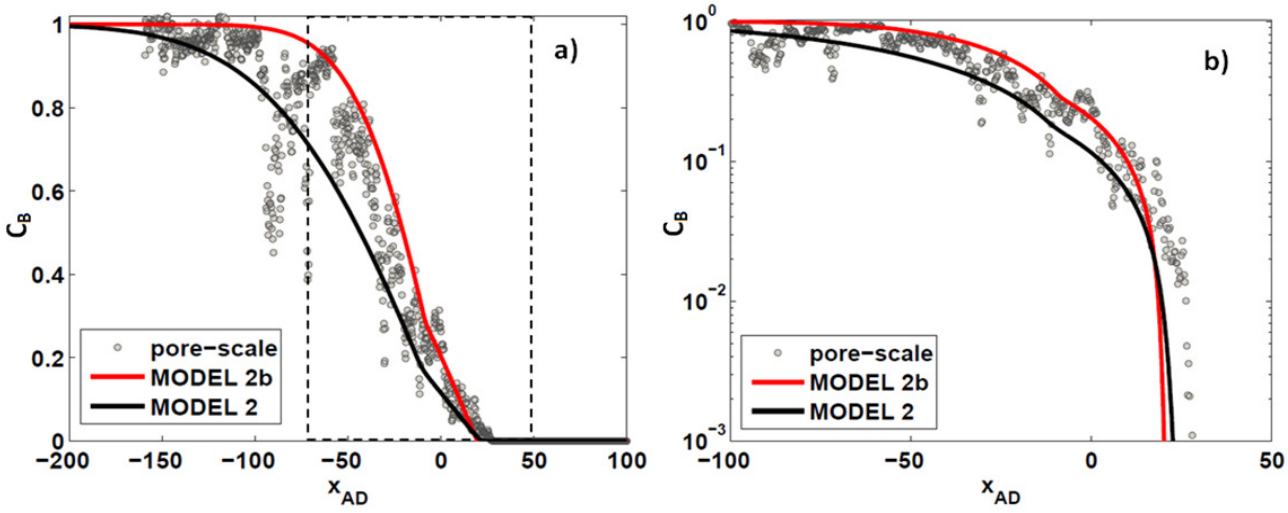

Figure 5.8 a)C_B profiles yielded by Model 2 and Model 2b at t=99.54 compared to pore-scale cross sectional averaged concentrations. b) zoomed image of C_B profiles within the mixing zone as indicated in figure (a) through black broken lines.

The quantitative Model comparison presented above allows inferring significant conclusions. The theoretically based Model 2 shows an outstanding behavior compared to effective models previously proposed in literature. Its implementation has shown remarkable improvement in profiles interpretation well-matching the tail concentration in the mixing region. However Model 2 is still affected by important limitations which characterized all the single continuum models analyzed. The analysis suggests that the assumption of constant asymptotic value for the dispersion parameter does not allow interpreting global product and concentrations profiles at short times. A possible solution to this limitation is to approximate nonlocal effects in time through convolution term and/or time-dependent local expressions, as shown above in Figure 5.7. However the appropriateness of approximating nonlocal effects to local terms requires further investigations. Another important limitation is represented by the impossibility of single continuum models to depict the influence of immobile zones which leads to long tails of delayed solute mass, asymmetric concentrations profiles and different dispersion process between solutes.

5.2 Qualitative model comparison between single continuum and DMRTM modeling features

The qualitative analysis presented in section 4.4 of DRMT model allows modeling solute long tails due the immobile-mobile regions exchanges. On the contrary, as evidenced in section 4.2 and section 5.1, through single continuum models these processes cannot be described. In this section we want to

provide a qualitative comparison between Model 2, which has shown the most promising characteristics among single continuum models analyzed, and DRMT Model aiming to compare the performances of the two types of models. In order to perform this comparison, we select the solution reported in Table 5.3.

Table 5.3 solutions of Model 2 and Model 5 for qualitative comparison.

S2	D=460, B=290
S5	D=450, Z=0.001, β_{IM} =0.078

The solution S2 corresponds to the best fit given by f_{4C_2} analysis relying on C_C data profiles. It represents an intermediate solution between the best fit of C_B and C_A profiles which we want to investigate contemporary. The solution S5 have been chosen on the basis of qualitative analysis proposed in section 4.4.

In Figure 5.9 C_A profiles predicted by S2 and S5 are plotted compared to pore-scale cross sectional averaged data at t=373. The two solutions present a significant difference only in the backward tail (for x_{AD}<0). Model 5 indeed shows the capability of describing the behavior of a solute entrapped in almost-immobile zone i.e. it captures in average the C_A pore-scale data oscillations. This feature is particularly interesting when dealing with reactive transport in natural porous media since it would allow capturing delayed reaction and related concentration plume tails which cannot be detected by single continuum models. The advantages of Model 2 highlighted in previous section appears here not relevant for correctly interpreting C_A profile due to the oscillations. Limiting the comparison to C_A it appears that DMRTM allows a better interpretation of the reactive transport processes. The C_B profiles given by Model 2 and Model 5 are shown in Figure 5.10.

In Figure 5.10a C_B profiles predicted by S2 and S5 are plotted compared to pore-scale cross sectional averaged data at t=373. Figure 5.10b provides a zoomed image of C_B forward tail delimited by red dashed line in Figure 5.10a. Figure 5.10a shows that, similarly to C_A, DRMT Model is able to reproduces on averaged the oscillations that characterize C_B profiles for x_{AD}<0. Figure 5.10b suggests

that Model 5 qualitative trend is very different from pore scale one within the reaction zone. Similarly to Model 1-3-4, C_B profile yielded by Model 5 does not reproduce qualitatively the fast decreasing trend that characterized simulation observed data. On the contrary, as shown in section 5.1, Model 2 qualitative well interprets the pore-scale data trend.

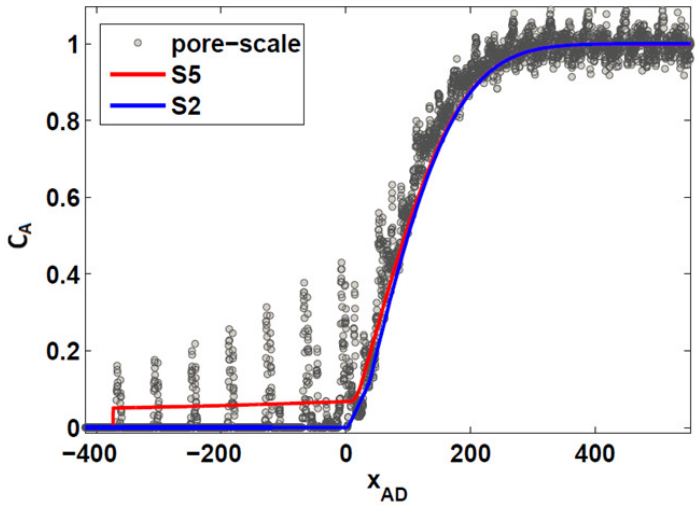

Figure 5.9 C_A profiles predicted by S2 and S5 at t=373 compared to pore-scale cross sectional averaged data.

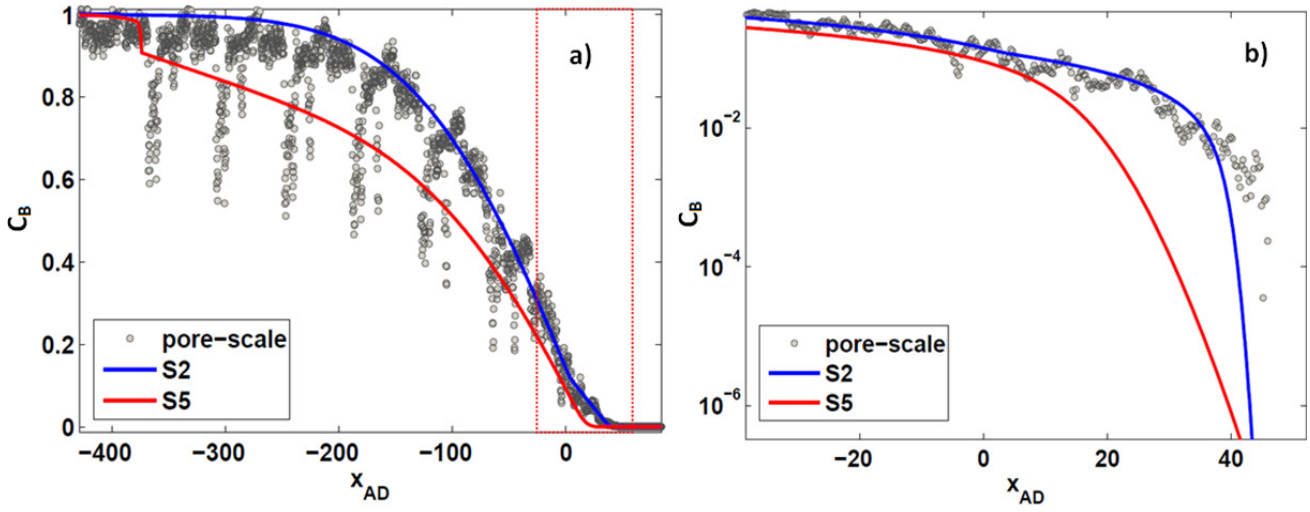

Figure 5.10 a)C_B profiles predicted by S2 and S5 at t=373 compared to pore-scale cross sectional averaged data. b) a zoomed image of C_B fast tail concentration delimited in a) by red broken line.

Figure 5.11 displays the global product evolutions as function of time given by S2 and S5 in both linear (Figure 5.11a) and logarithmic (Figure 5.11b) scale. Figure 5.11 shows that S2 and S5 similarly overestimates global product pore-scale data for short times. For late times, instead, the two curves are

distinguished and S5 shows a better fit of G_C1 data. Figure 5.11b allows comparing G_C1, S2 and S5 late time trends to the behavior associated to asymptotic regime. Figure 5.11b discloses that both S2 and S5 yield to recast the asymptotic behavior for late times considered.

However, as shown in section 4.4, furthers and detailed investigations are needed to precisely understand the key role of each parameter in Model 5. Indeed, DRMT model presents many degrees of freedom due to both its mathematical formulation and parameters included in it. We have provided only a preliminary analysis to highlight its promising features but it is not enough to clearly identify the potential of this model for the simulation of reactive transport processes.

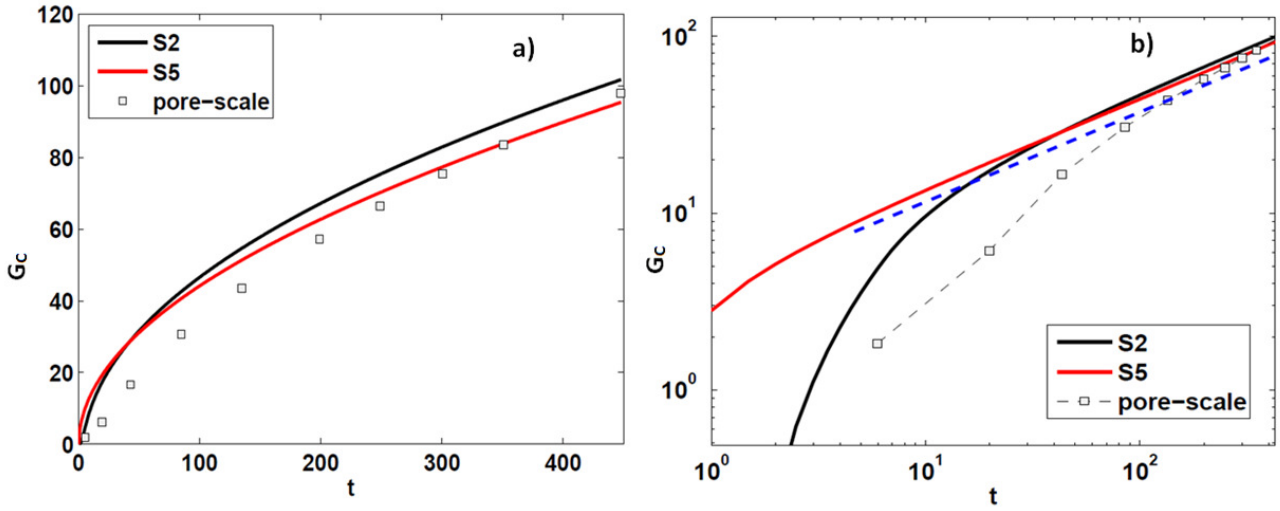

Figure 5.11 a) global product evolutions in time given by S2 and S5 compared to G_C1 data Figure b) is equivalent to a) but axes are expressed in logarithmic scale. The blue broken line depicts the global product asymptotic trend.

In conclusion, this preliminary analysis suggests that Model 2 and Model 5 are characterized by some advantages that can complete each other lacks. As a consequence, these preliminary results encourage further investigations on the potentiality of DRMT model implementation to bimolecular homogeneous reactive transport and eventually, the possible integration of these two models in a single one, i.e by modifying the structure of the reaction term in the DRMT model. This may ultimately lead to the formulation able to exploit the strengths of both models, which have been assessed in this Chapter.

Chapter 6 CONCLUSIONS AND FURTHER RESEARCH

Our work deals with the reactive transport modeling problem in porous media. We focus on a simple reaction pattern involving an irreversible homogeneous bimolecular reaction of the kind A+B→C which takes place in a fully saturated porous medium. Different authors have already investigated this specific problem setting proposing diversified approaches which constitute, currently, a varied state of the art. We select four single-continuum models proposed in literature which present different modeling approaches:

- the ADRE model which is the state of the art model for macro scale reactive transport simulation;
- *Porta et al. (2012a)* model which is, up to now, the only formualtion that is theoretically derived through a formal up-scaling technique in the presence of fast reaction;
- *Sanchez-Vila et al.(2010)* model which includes an effective time-dependent reaction kinetics;
- *Hochstetler and Kitanidis (2013)* model in which an effective constant reaction rate replaces the kinetic one.

In these models, the interaction between porous medium structure and coupled reaction and transport processes is embedded into effective parameters. However, each one of these models embeds a different strategy for representive effective reaction rates at continuum scale.

In addition to the four models listed above, we have also considered an alternative modeling approach still little explored for this problem setting: the Double Rate Mass Transfer Model (DRMTM). This model embeds local segregation of reactants concentrations assuming that the continuum domain can be split into two interacting continua, i.e. a mobile and an immobile phase. Solute mass exchange is assumed to take place between the two regions. Through this outline of the porous domain, the DRMTM is able to capture the influence of the local velocity field heterogeneities on solute concentrations evolution in space and time.

The conceptual and mathematical structures of these models are reviewed and numerically implemented in order to assess and compare different continuum-based strategies to model reactive transport in critical conditions characterized by high *Pe* and *Da* numbers. This comparative assessment relies on pore-scale numerical simulations which provide a detailed knowledge of local and averaged

quantities. We consider two different porous medium scenarios: in the first one pore space is constituted by ordered array of cylinders; in the second one more complex geometry is generated by disordered cylinders. The first scenario is used to compare solutions given by ADRE and *Porta et al (2012a)* models. In the second scenario each model is assessed singularly investigating the influence of parameters on model solutions, the appropriateness of model to describe the results observed in pore-scale numerical simulations. The models assessment is based on the definition of different criteria which quantify the difference between continuum and pore-scale model results. These selected criteria are investigated as possible objective functions for the future calibration process. On the basis of models assessment results, a quantitative comparison between single porosity models is performed in order to discriminate among the different model performances. Finally we provide a qualitative comparison between single continuum models and Double Rate Mass Transfer Model (DRMTM) in order to highlight the differences between the two diverse conceptual approach.

Our results allow to:

- Explore the influence of pore structure on models performances;
- Assess the appropriateness of different continuum-based strategies to capture key features of reactive transport at continuum scale in different disaggregated porous scenarios;
- Discriminate among different models performances
- Investigate the suitability of different criteria for the future model calibration process;

Concerning the first point, we conclude that the performance of a model in capturing reactive transport features strongly depends on the complexity of the considered porous medium geometry. In a perfectly homogeneous porous medium, even as flux and reaction conditions are critical and incomplete mixing effects are detectable at local level, averaged and global quantities are poorly affected by local concentration fluctuations. Moreover nonlocal effects vanish quickly and their influence on the reactive transport is negligible, i.e. transport and reaction parameters can be appropriately replaced by their asymptotic values. When the pore structure complexity increases, the local fluctuations of reactant concentrations are emphasized leading to detectable incomplete mixing effect in the mixing zone on concentration profiles and significantly affecting reaction evolution. Non local effects are no longer negligible since the system takes long time to recover the asymptotic behavior. In particular dispersion process is remarkably dependent on time and taking into account this dependency is crucial to capture

reactive transport features at short times. As a conclusion, the pore-scale structure significantly influences reactive transport evolution and the importance of nonlocal effects.

Since the complexity of reactive transport is function of the porous medium structure, continuum models may or may not capture the relevant features of the phenomena depending on the porous medium considered. Indeed, the ADRE model, which does not include any quantification of incomplete mixing, well interprets reactive transport dynamics in ordered pore spaces.

The need of including incomplete mixing effects arises when the geometry of the medium becomes more complex and notably embeds closed cavities and dead end pores, i.e. in the presence of an heterogeneous local velocity field. In such a case the standard ADRE model is no longer appropriate for reactive transport description. Our analysis allows concluding that including the incomplete mixing effects into continuum model formulation leads to improve reactive transport interpretation but the strategy used to embed this effect into model mathematical formulation has a crucial role for two main reasons:

- Correct interpretation of the actual processes evolution;
- Aptitude of model to calibration.

Considering both of the two aspects, our analysis allows to deduce that *Porta et al. (2012a)* model provides an innovative and better performance in predicting averaged pore scale data within the crucial mixing zone where the reaction occurs compared to *Sanchez-Vila et al. (2010)* and *Hochstetler and Kitanidis (2013)* formulations. Independently from the time considered, the trend of reactant profiles yielded by *Porta et al. (2012a)* model allows capturing the qualitative evolution of pore-scale cross-sectional averaged concentrations. This is due to the fact that this model is characterized by an innovative sensitivity to dispersion parameter compared to the other single continuum models analyzed (Figure 4.34). On the contrary, the effective formulations proposed in *Hochstetler and Kitanidis (2013)* and *Sanchez-Vila et al. (2010)* do not completely capture the overall behavior of the reactants concentrations which is yielded by pore scale simulations. Moreover, *Hochstetler and Kitanidis (2013)* and *Sanchez-Vila et al. (2010)* models exhibit difficulties in parameters identification based only on reactant and product profiles data requiring different or additional data. This can represent an important limitation for the two models implementation since normally a limited number and types of data are available for practical purposes.

Comparing DRMTM to single porosity model we can conclude that DRMTM is characterized by interesting and promising features which suggest further and detailed investigations. The different mathematical and conceptual structure attributes to the model a larger flexibility and allows capturing some reactive transport features observed in pore-scale simulation in disordered porous medium scenario: long reactant concentration tails entrapped in low mobility regions, asymmetrical concentration profile behaviors and the misalignment between reactive and advective fronts. Depicting these phenomena is instead impossible through single porosity models and this represents an important limitation of this approach. Thus, Double Rate Mass Transfer Model approach is a potential way for overcoming single continuum models limitations.

Our analysis leads to the conclusion that a cursory definition of the criteria (or objective functions) and choice of the type of data can lead to imprecise or wrong parameter estimation. Suitable modifications of criteria definition can bring a significant improvement of criteria sensitivity to parameter. Even as a criteria appears insensitive to a parameter, it does not imply that model solution is equally indifferent to the value of that parameter. In particular, this must be taken into account when dealing with incomplete mixing parameter estimations. The latter ones influence only a limited portion of concentration profile (within the mixing zone) which is even close to zero for reactants species. As a consequence, using a linear objective function (e.g. Eq. (2.51)), it is almost impossible to perform a feasible estimation of parameters that regulate the incomplete mixing due to the low importance that these data assume in the overall objective function value computed.

Moreover, our results show that the parameter estimations performed in model assessment with different types of data leads to different optimum parameter values. This is due to the fact that each type of data embeds different information on the process which we are investigating. Errors in calibration process arise when we try to estimate parameter with a dataset that does not contain the enough information about that specific parameter value we are looking for.

All these considerations contribute significantly to define and identify the most promising directions to explore in future researches. Our preliminary analysis has shown that the model formulation proposed by *Porta et al. (2012a)* can represent a significant advancement in reactive transport modeling. In particular we emphasize that this formualtion (i) is formally derived through theoretical up-scaling; ii) can qualitatively capture the concentration profile trend within the mixing zone without reducing the

performance in describing the dispersion process. However, important limitations, that have always characterized all effective continuum models, affect *Porta et al. (2012a)* model too. In particular we highlight that i) negliecting nonlocal effects for dispersion process prevents the continuum models analyzed from being reliable at short times; ii) single continuum models, by definition, do not allow capturing profiles asymmetries and trapped solutes in the immobile zones. Concerning the first limitation, we have provided a first attempt in which dispersion is assumed time dependent according to a local formulation. This shows that a time-dependent local term can be a possible approximation of non-local effects since it allows capturing short times profile shape and well-fitting the global product evolution in time (Figure 5.7 and Figure 5.8). This can be a promising starting point to investigate if nonlocal effects can be as well-approximated by a time-dependent local term. The validation of this correspondence would lead to important results of practical interest since it would allow interpreting parameter time-dependency avoiding the explicit computation of time convolutions, which is computationally very expensive.

On for the modeling of delayed transport in immobile zones, the DRMTM model has shown encouraging features. However, the actual role of each parameter included in it needs to be understood. Due to the close interconnection between parameter influences on the output solution, this is quite ambitious aim but it is crucial to confer manageability to this powerful modeling tool.

BIBLIOGRAPHY

Ames, W.F. (1992). Numerical methods for partial differential equations. 3rd edn. Academic Press, USA.

Anmala, J., & Kapoor, V. (2013). Dynamics of mixing and bimolecular reaction kinetics in aquifers. *Stochastic Environmental Research and Risk Assessment, 27*(4),1005-1020.

Audigane, P., Gaus, I., Czernichowski-Lauriol, I., Pruess, K., & Xu, T. (2007). Two-dimensional reactive transport modeling of CO2 injection in a saline aquifer at the sleipner site, north sea. *American Journal of Science, 307*(7), 974-1008.

Battiato, I., & Tartakovsky, D. M. (2011). Applicability regimes for macroscopic models of reactive transport in porous media. *Journal of Contaminant Hydrology, 120–121*(0), 18-26.

Bear, J., & Cheng, A. (2010). *Modeling groundwater flow and contaminant transport.* Springer, ISBN 978-1-4020-6681-8.

Berkowitz, B., Cortis, A., Dentz, M., & Scher, H. (2006). Modeling non-Fickian transport in geological formations as a continuous time random walk. *Reviews of Geophysics, 44*(2) , RG2003.

Berkowitz, B., & Scher, H. (2009). Exploring the nature of non-fickian transport in laboratory experiments. *Advances in Water Resources, 32*(5), 750-755.

Bijeljic, B., Muggeridge, A. H., & Blunt, M. J. (2004). Pore-scale modeling of longitudinal dispersion. *Water Resources Research, 40*(11), W11501.

Carrera, J., & Neuman, S. P. (1986). Estimation of aquifer parameters under transient and steady state conditions: 1. maximum likelihood method incorporating prior information. *Water Resources Research, 22*(2), 199-210.

Chaynikov, S. V. (2013). *Theoretical and Numerical Upscaling of Solute Transport in Porous Media,* Doctoral thesis, Doctoral Program in Environmental and Infrastructure Engineering, Politecninco di Milano, XXV CYCLE, 2013.

Chen, C., & Meiburg, E. (1998). Miscible porous media displacements in the quarter five-spot configuration. part 2. effect of heterogeneities. *Journal of Fluid Mechanics, 371*, 269-299.

Ciriello, V., Guadagnini, A., Di Federico, V., Edery, Y., & Berkowitz, B. (2013). Comparative analysis of formulations for conservative transport in porous media through sensitivity-based parameter calibration. *Water Resources Research, 49*(9), 5206-5220.

Citrini, D., & Noseda, G. (1987). IDRAULICA,2nd edn. casa ed. Ambrosiana, Milano.

Cortis, A., Chen, Y., Scher, H., & Berkowitz, B. (2004). Quantitative characterization of pore-scale disorder effects on transport in “homogeneous” granular media. *Physical Review E, 70*(4), 041108.

Crane, M. J., & Blunt, M. J. (1999). Streamline-based simulation of solute transport. *Water Resources Research, 35*(10), 3061-3078.

Danckwerts, P. (1952). The definition and measurement of some characteristics of mixtures. *Applied Scientific Research, Section A, 3*(4), 279-296.

De Anna, P. d., Jimenez-Martinez, J., Tabuteau, H., Turuban, R., Le Borgne, T., Derrien, M., et al. (2013). Mixing and reaction kinetics in porous media: An experimental pore scale quantification. *Environmental Science & Technology, 48*(1), 508-516.

Delshad, M., Asakawa, K., Pope, G. A., & Sepehrnoori, K. (2002). Simulations of chemical and microbial enhanced oil recovery methods. *SPE/DOE Improved Oil Recovery Symposium,* 13-17 April, Tulsa, Oklahoma.

Dentz, M., & Berkowitz, B. (2005). Exact effective transport dynamics in a one-dimensional random environment. *Physical Review E, 72*(3), 031110.

Dentz, M., & Castro, A. (2009). Effective transport dynamics in porous media with heterogeneous retardation properties. *Geophysical Research Letters, 36*(3).

Dentz, M., Le Borgne, T., Englert, A., & Bijeljic, B. (2011). Mixing, spreading and reaction in heterogeneous media: A brief review. *Journal of Contaminant Hydrology, 120–121*(0), 1-17.

Edery Y.,Scher H., & Berkowitz B. (2010). Particle tracking model of bimolecular reactive transport in porous media. *Water Resources Research, 46*(07),W07524.

Gramling, C. M., Harvey, C.F., & Meigs, L.C. (2002). Reactive transport in porous media: A comparison of model prediction with laboratory visualization. *Environmental Science & Technology, 36*(11), 2508-2514.

Haggerty, R., & Gorelick, S. M. (1995). Multiple-rate mass transfer for modeling diffusion and surface reactions in media with pore-scale heterogeneity. *Water Resources Research, 31*(10), 2383-2400.

Haggerty, R., Harvey, C. F., Freiherr von Schwerin, C., & Meigs, L. C. (2004). What controls the apparent timescale of solute mass transfer in aquifers and soils? A comparison of experimental results. *Water Resources Research, 40*(1), W01510.

Hochstetler, D. L., & Kitanidis, P. K. (2013). The behavior of effective rate constants for bimolecular reactions in an asymptotic transport regime. *Journal of Contaminant Hydrology, 144*(1), 88-98.

Huang, H., & Hu, B. X. (2000). Nonlocal nonreactive transport in heterogeneous porous media with interregional mass diffusion. *Water Resources Research, 36*(7), 1665-1675.

Huang, H., Hassan, A. E., & Hu, B. X. (2003). Monte carlo study of conservative transport in heterogeneous dual-porosity media. *Journal of Hydrology, 275*(3–4), 229-241.

Kapoor, V., Gelhar, L. W., & Miralles-Wilhelm, F. (1997). Bimolecular second-order reactions in spatially varying flows: Segregation induced scale-dependent transformation rates. *Water Resources Research, 33*(4), 527-536.

Kluck, C., & Achari, G. (2004). Chemical oxidation techniques for in situ remediation of hydrocarbon impacted soils. *Environmental Engineering,* Case Study.

Ogata, A., & Banks, R. B. (1961). A solution of the differential equation of longitudinal dispersion in porous media.

Partial Differential Equation Toolbox™ User's Guide, 2013

Porta, G. M., Riva, M., & Guadagnini, A.(2012a). Upscaling solute transport in porous media in the presence of an irreversible bimolecular reaction. *Advances in Water Resources, 35*, 151-162.

Porta, G., Thovert, J., Riva, M., Guadagnini, A., & Adler, P. (2012b). Microscale simulation and numerical upscaling of a reactive flow in a plane channel. *Physical Review E, 86*(3), 036102.

Porta, G. (2013). Numerical investigation of pore and continuum scale formulations of bimolecular reactive transport in porous media. *Advances in Water Resources, 62,243-253.*

Raje, D.S., & Kapoor,V.(2000). Experimental study of bimolecular reaction kinetics in porous media. *Environmental Science & Technology, 34*(7), 1234-1239.

Rubin, J. (1983). Transport of reacting solutes in porous media: Relation between mathematical nature of problem formulation and chemical nature of reactions. *Water Resources Research, 19*(5), 1231-1252.

Rubio, A.D., Zalts, A., & El Hasi, C.D. (2008). Numerical solution of the advection-reaction-diffusion equation at different scales. *Environmental Modelling & Software, 23*(1), 90-95.

Salamon, P., Fernàndez-Garcia, D., & Gómez-Hernández, J. J. (2006). A review and numerical assessment of the random walk particle tracking method. *Journal of Contaminant Hydrology, 87*(3), 277-305.

Salles, J., Thovert, J., Delannay, R., Prevors, L., Auriault, J., & Adler, P. (1993). Taylor dispersion in porous media. determination of the dispersion tensor. *Physics of Fluids A: Fluid Dynamics (1989-1993), 5*(10), 2348-2376.

Sanchez Vila, X., Fernandez-Garcìa, D., & Guadagnini, A. (2010). Interpretation of column experiments of transport of solutes undergoing an irreversible bimolecular reaction using a continuum approximation. *Water Resources Research, 46*(12), W12510.

Steefel, C. I., DePaolo, D. J., & Lichtner, P. C. (2005). Reactive transport modeling: An essential tool and a new research approach for the earth sciences. *Earth and Planetary Science Letters, 240*(3), 539-558.

Stehfest, H. (1970). Algorithm 368: Numerical inversion of laplace transforms [D5]. *Communications of the ACM, 13*(1), 47-49.

Van Genuchten, M. T., & Wierenga, P. (1976). Mass transfer studies in sorbing porous media I. analytical solutions. *Soil Science Society of America Journal, 40*(4), 473-480.

Van Schijndel, A. J. (2000). Application of HAMLab for whole building HAM response modeling, numerical methods,CMR-2651.

Whitaker, S. (1999). *The method of volume averaging.* Netherlands:Kluwer Academic Publishers.

Zheng, C., & Wang, P. P. (1999). *MT3DMS: A Modular Three-Dimensional Multispecies Transport Model for Simulation of Advection, Dispersion, and Chemical Reactions of Contaminants in Groundwater Systems; Documentation and User's Guide,* Contract Report SERDP-99-1, U.S. Army Engineer Research and Development.

Zheng, L., Apps, J. A., Zhang, Y., Xu, T., & Birkholzer, J. T. (2009). Reactive transport simulations to study groundwater quality changes in response to CO2 leakage from deep geological storage. *Energy Procedia, 1*(1), 1887-1894.